UNIVERSITÉ CATHOLIQUE DE LOUVAIN

MICROWAVE LABORATORY
ELECTROMAGNETICS, MICROWAVES & COMMUNICATIONS

Louvain-la-Neuve, Belgium

Propagation Modelling of Low Earth-Orbit Satellite Personal Communication Systems

Claude OESTGES

Thesis presented for the Ph.D. degree
in Applied Sciences

JURY

Prof. P. SOBIESKI (UCL) – Chairman
Prof. D. VANHOENACKER-JANVIER (UCL) – Supervisor
Prof. C. RIVA (Politecnico di Milano, Italy)
Prof. S.R. SAUNDERS (University of Surrey, UK)
Prof. L. VANDENDORPE (UCL)
Prof. A. VANDER VORST (UCL)

December 2000

I would like to devote these few lines to so many people who made the achievement of this work possible.

First, I am sincerely grateful to Prof. Danielle Vanhoenacker for her guidance, her precious support and, most of all, her kindness and understanding. It has been a real pleasure to work with her during these four years.

Then, I would like to thank Prof. André Vander Vorst, Head of the Microwave Laboratory UCL. I have greatly appreciated his generous collaboration and helpful comments. His pertinent questions have been a source of many interesting investigations.

I also express my gratitude to Prof. Carlo Riva, Prof. Simon Saunders, Prof. Piotr Sobieski and Prof. Luc Vandendorpe, for devoting a part of their time to review this dissertation. Their suggestions have been of great help in finalizing the text of this thesis.

I am grateful to the members of the mobile working group of COST Action 255. This project has really opened up new horizons for me. Especially, I would like to thank Prof. Simon Saunders, for his cheerful welcome at the University of Surrey. I keep a wonderful memory of the time I spent working with him in Guildford. Also, many thanks to Dr. Martin Döttling, in remembrance of our enlightening collaboration and e-mail discussions.

I thank all my colleagues from the Microwave Laboratory UCL, for their friendly support and professionalism and the highly pleasant atmosphere within the Laboratory. The former and present members of the propagation team deserve special acknowledgements, particularly Dr. Hugues Vasseur, for his kind help at the beginning of my doctoral research. I am also thankful to all undergraduate students whom I have been supervising, as an assistant lecturer, during their last-year research project. Their fresh and bright ideas have been mostly stimulating.

Finally, I would like to express my gratitude to my parents and family, for their continuous encouragement. I am also deeply grateful to my friends Anne, Jean, Jérôme, Laurent and "Léon", for their support and ever-distracting presence during all these years.

CONTENTS

INTRODUCTION

Scientific publications 5
List of common variables, symbols and abbreviations 8
References 12

CHAPTER 1 TROPOSPHERIC PROPAGATION FOR LOW EARTH-ORBIT LINKS

1.1 Introduction 13

1.2 Attenuation due to atmospheric gases 15
1.2.1 Physical background of gaseous absorption 15
1.2.2 Oxygen attenuation 15
1.2.2.1 Slant-path attenuation 15
1.2.2.2 Statistical distribution 17
1.2.3 Water vapour attenuation 18
1.2.3.1 Slant-path attenuation 18
1.2.3.2 Statistical distribution 20

1.3 Attenuation by hydrometeors 22
1.3.1 Scattering and aborption by particles 22
1.3.2 Attenuation due to clouds 22
1.3.2.1 Specific cloud attenuation 22
1.3.2.2 Statistical distribution 25
1.3.3 Rain attenuation 26
1.3.3.1 Models of rain attenuation 26
1.3.3.2 ITU-R specific attenuation and effective rain height 27
1.3.3.3 ITU-R slant-path rain attenuation statistics 28
1.3.3.4 EXCELL model 30
1.3.4 Attenuation by other hydrometeors 34

1.4 Scintillation 36
1.4.1 Definition 36
1.4.2 Physical and empirical models 36
1.4.2.1 Short-term variation 36
1.4.2.2 Long-term standard deviation of scintillation 38
1.4.3 Time distribution of the variance of scintillation 40
1.4.4 Cumulative time dsiribution of the signal variation 41

1.5 Combination of effects 42
1.5.1 Introduction 42
1.5.2 Mathematical background for combination of phenomena 42
1.5.2.1 Equiprobability summing 42
1.5.2.2 Convolution method 42
1.5.2.3 Disjoint summing 43
1.5.2.4 Square-root-sum combination 43
1.5.2.5 Coherent summing 43
1.5.3 Propagation methods of combination 44
1.5.3.1 ITU-R method 44
1.5.3.2 Castanet-Lemorton method 44

1.6 How to account for the specificity of non-geostationary orbit systems 46
1.6.1 Introduction 46
1.6.2 Statistical modelling 46
1.6.3 Time series modelling 48
1.6.3.1 A modelling problem 48
1.6.3.2 Short-term effects of hydrometeors 49

1.6.3.3 Short-term simulation of scintillation 52
1.6.3.4 Returning from short-term to long-term predictions 52

1.7 Summary 54

1.8 References 55

CHAPTER 2 NEW PROPAGATION MODELS FOR TRANSMISSION IN BUILT-UP AREAS

2.1 Introduction 59

2.2 Physical modelling 62
2.2.1 Introduction 62
2.2.2 The ray-tracing method 62
2.2.3 Material characteristics 66
2.2.4 Propagation mechanisms 67
2.2.4.1 Reflection 67
2.2.4.2 Edge diffraction 70
2.2.4.3 Diffuse scattering by rough surfaces 78
2.2.4.4 Attenuation by foliage 82
2.2.4.5 Simulation results 83
2.2.5 Wideband characterisation 87
2.2.6 Experimental validation 89

2.3 Physical-statistical modelling 92
2.3.1 The physical-statistical approach 92
2.3.2 Distribution of physical parameters 96
2.3.2.1 Building height 96
2.3.2.2 Street width 99
2.3.2.3 Elevation angle 100
2.3.2.4 Azimuth angle 102
2.3.2.5 Other parameters 104
2.3.3 Narrowband channel characterisation 105
2.3.3.1 Built-up and open areas 105
2.3.3.2 Relationships between physical and statistical parameters 107
2.3.4 Shadowing correlation model for satellite diversity 108
2.3.5 Wideband channel characterisation 114

2.3.6 Validation and applications 116
2.3.6.1 Fade statistics 116
2.3.6.2 Effect of foliage 124
2.3.6.3 Wideband parameters 125
2.3.7 Bit error probability 127
2.3.7.1 Prediction of the average BER 127
2.3.7.2 Non-selective channel 127
2.3.7.3 Selective channel 130
2.3.7.4 Simulation results 132

2.4 Summary 136

2.5 References 137

CHAPTER 3 EVALUATION OF SYSTEM IMPAIRMENTS AND PERFORMANCE PREDICTION

3.1 Introduction 141

3.2 Prediction of long-term performance for low earth-orbit satellite links 144
3.2.1 Outline 144
3.2.2 Fade distribution over time and area 144
3.2.3 BER prediction 147
3.2.4 Time series simulations 148
3.2.4.1 The COST 255 methodology 148
3.2.4.2 Link-level: coded BER calculation 149
3.2.4.3 System-level: evaluation of performance 151

3.3 Short-term performance and system strategies 154
3.3.1 Preamble 154
3.3.2 Fade compensation 154
3.3.2.1 Static compensation of free space loss 154
3.3.2.2 Dynamic fade mitigation 155
3.3.3 Satellite handoff diversity 160
3.3.4 Multi-satellite diversity 161

3.4 L band LEO-*N* voice transmission system 163
3.4.1 Land mobile satellite systems 163

3.4.2 System specifications 164
3.4.3 Feeder link 166
3.4.3.1 Modelling approach 166
3.4.3.2 Simulation results 166
3.4.4 Mobile user link: long-term performance 171
3.4.4.1 Physical-statistical analysis in built-up areas 171
3.4.4.2 Time series analysis in built-up areas 177
3.4.5 Mobile user link: shadowing correlation analysis 180
3.4.5.1 Statistics of elevation angles and azimuth separation 180
3.4.5.2 Simulation results 181
3.4.6 Mobile user link: short-term performance in canonical scenarios 185
3.4.6.1 Definition of canonical scenarios 185
3.4.6.2 Impact of system parameters 189
3.4.6.3 Performance for the long straight street case 194
3.4.6.4 Comparison between a long street and a crossroad 198

3.5 S band satellite IMT 2000 201
3.5.1 IMT 2000 and low earth-orbit satellites 201
3.5.2 System description 201
3.5.3 Long-term performance prediction 202
3.5.3.1 Simulation method 202
3.5.3.2 Performance for a pedestrian speed 202
3.5.3.3 High-speed scenarios 205
3.5.4 Shadowing correlation in dual-diversity schemes 207

3.6 Ka band multimedia satellite system 211
3.6.1 "Internet-in-the-sky" 211
3.6.2 System specifications 212
3.6.3 Statistical long-term performance 212
3.6.4 Short-term performance 213
3.6.4.1 Time series modelling 213
3.6.4.2 Preliminary results at Ka band 215
3.6.4.3 Simulation results 220

3.7 Stratospheric communication system 223
3.7.1 High-altitude platforms 223
3.7.2 System specifications 224
3.7.3 Performance prediction 225

3.7.3.1 Simulation approach 225
3.6.3.2 Distribution of physical parameters 225
3.6.3.3 Attenuation statistics for the V band multimedia service 226
3.6.3.4 Raw and coded BER prediction for IMT 2000 service 231

3.8 Summary 236

3.9 References 238

CONCLUSIONS 241

APPENDICES

Appendix A About the 1999 version of ITU-R recommendations 248

Appendix B Description of the orbit generator 251

Appendix C Ray-tracing software for land mobile satellite systems 258

Appendix D Equivalent currents for edge diffraction 260

Appendix E Double diffraction coefficient 265

Appendix F System-level software for estimating long-term performance from time series (COST 255 method) 267

Appendix G LEO-*N* test case: short-term performance in built-up areas (median receiving. posistion) 269

References 271

INTRODUCTION

This thesis aims at developing specific *propagation*-based *prediction* methods for personal communication networks relying on *low earth-orbit* satellite constellations. Various models and methods are proposed, starting from a physical description of tropospheric and environmental mechanisms. Furthermore, the models result in simulation tools capable of evaluating the influence of electromagnetic effects on the overall performance of systems under design.

Nowadays, demand for advanced communication capabilities spirals upward more and more steadily. Hence, telecommunication systems are now planned to operate at centimetre and millimetre waves. High-frequency bands offer broader transmission channels, thereby meeting the emergent interest for satellite high-rate and multimedia applications. However, as the wavelength shortens, interactions of radiowaves with the transmission medium increase. Especially, tropospheric constituents (rain, clouds, gas and turbulence) as well as the local environment (buildings, vegetation and obstacles) induce various mechanisms such as absorption, scattering, diffraction and reflection. These are likely to yield harmful impairments that may severely degrade system performance and availability.

Therefore, there is a need for new prediction methods of slant-path propagation effects at high-frequency bands, namely between 1 and 100 GHz. Nevertheless, a large number of

models already exist. Special attention must then be paid to new trends in propagation research. For the last decade, the latter has indeed considerably evolved from a pure modelling approach to more system-oriented methods [1], in order to fill the significant gap between the propagation community and the designers' world. That is at least one of the major conclusions of the recent COST Action 255 [2], the goal of which was the characterisation of the propagation channel for new satellite services at Ku band and above. This work is keeping with this general evolution in propagation research, the approach starting from electromagnetics and going up to predictions of coverage and error-rate.

Owing to the large variety of satellite systems, the scope of this thesis has been narrowed down to the analysis of *satellite personal communication systems* (S-PCS) based on *low earth-orbit* (LEO) constellations. For several years, a number of ambitious LEO-based projects have indeed been investigated in order to provide global coverage to individual users. Satellites in low orbit are typically 500 km to 1500 km above the earth. Obviously, low orbit systems require more satellites for continuous global coverage than geostationary systems, because of shrinking transmission footprints as orbit altitude declines. In contrast, individual satellites are smaller, lighter and less expensive. Moreover, the satellites' greater proximity to the earth greatly reduces the lengthy signal propagation delay in comparison with GEO systems [3].

The first LEO systems operating at L and S bands (land mobile satellite systems) intend to offer voice and low-rate data services. The late Iridium and the upcoming Globalstar are the main representative companies responsible for such projects. Iridium was launched in the end of 1998, but was forced in to bankruptcy around mid-2000, leaving Globalstar as the only planned voice transmission system.

Meanwhile, those who market communication services are turning to low-earth orbit satellites for applications other than phone calls. In the near future, several systems (Teledesic, Skybridge) operating as high as Ku and Ka band should be deployed in order to provide Internet access and high data rates worldwide.

Despite the commercial failure of Iridium, the propagation analysis of S-PCS's is still of interest for modelling and prediction purposes. Indeed, satellite personal communication systems combine the advantages of satellite links with a cellular concept. As a consequence, networks based on LEO constellations form *megacells* over the earth's surface [4], which consist of the footprint from clusters of multiple spotbeams moving continuously and rapidly in the sky. Quite obviously, both the size of the cells and the fast motion of the satellites require a new type of modelling approach or at least a transformation of the existing models.

Hence, these new modelling approaches, developed with LEO systems in mind, might also b applied as alternative methods in classical propagation fields, say, LAN-based or mobile terrestrial communications.

The text is divided into three chapters, dealing respectively with

- tropospheric propagation,
- propagation in built-up areas,
- performance prediction methods.

Regarding tropospheric mechanisms, Chapter 1 reviews a limited number of existing models of *attenuation* by gas and hydrometeors, as well as models of *scintillation*. In the context of low earth-orbits, these models are used in conjunction with an *orbit generator* to provide both annual availability and short-term performance. Time series modelling is introduced in order to cope with a number of *dynamic* system procedures, such as fade mitigation, satellite handover and diversity. First steps towards of a new modelling approach for long-term performance are briefly presented.

As far as propagation in *built-up areas* is concerned, two complementary models of local effects are developed in the framework of this thesis. They are widely described in Chapter 2. Both models are based on the electromagnetic description of mechanisms, so they give a further insight into the physics of environmental effects. Furthermore, because of their physical nature, the models perform well at extrapolating results to new areas where no propagation data are available.

The first model is purely deterministic, being based on a *ray-tracing* tool. It considers reflection and diffraction processes and foliage attenuation. An incremental calculation of the diffracted component is introduced. The method, which is based on edge equivalent currents, accounts for the finite length of wedges and yields more accurate results in time series simulations. Also, the deterministic model allows for characterising specific scenarios, such as a straight built-up street or a crossroad.

The second model is built on a new approach, which combines the advantages of both deterministic and statistical models while avoiding their main drawbacks, such as the poor extrapolation or the prohibitive computation time. Using this so-called *physical-statistical* modelling approach, a large number of experimental validations and applications are investigated in Chapter 2: attenuation statistics (fade distribution, level-crossing rate), multi-satellite shadowing correlation, wideband channel characterisation.

In Chapter 3, all the models described are applied in order to predict the performance of realistic systems. Starting from the models, three LEO test cases are analysed following an original formalism. It is believed that this unique general formalism constitutes an innovative endeavour to fill the gap between propagation modelling and system design. The test cases cover all types of upcoming systems and services, as well as a large frequency spectrum: L band voice transmission, S band IMT 2000 (wideband CDMA) and Ka band multimedia network.

Finally, the new approaches developed in the scope of this work are shown to be valuable alternatives in other communication areas, such as terrestrial systems. Already, personal communication system designers plan to use high-altitude platforms as very high base stations above dense metropolitan areas. Although considered as terrestrial systems, such networks fit very well with the prediction tools developed for LEO satellites. This is illustrated in the fourth test case, dealing with V band/S band stratospheric systems.

The original features of this thesis have been exemplified by several publications in international periodicals and conferences, which are listed below. A list of common variables and abbreviations, which are used throughout the text, also follows.

SCIENTIFIC PUBLICATIONS

1° Papers

[1] OESTGES, C., VANHOENACKER-JANVIER, D., A physical-statistical shadowing correlation model and its application to low earth-orbit systems, *IEEE Trans. on Veh. Techn.*, accepted for publication.

[2] OESTGES, C., VANHOENACKER-JANVIER, D., Propagation modelling and system strategies in urban mobile-satellite scenarios, *IEEE Trans. on Veh. Techn.*, accepted for publication.

[3] OESTGES, C., VANHOENACKER-JANVIER, D., Coverage analysis of a stratospheric communication system, *IEE Proc.-Microw. Antenn. Propagat.*, accepted for publication.

[4] OESTGES, C., RAYNAUD, L., CLERCKX, B., VANHOENACKER-JANVIER, D., A deterministic model for third generation mobile communication systems in urban environments, *Revue HF*, 2000, to appear.

[5] OESTGES, C., VANHOENACKER-JANVIER, D., A UTD-based physical-statistical model of the mobile-satellite channel, *Revue HF*, n° 1, pp. 17-26, 2000.

[6] OESTGES, C., VANHOENACKER-JANVIER, D., Experimental validation and system applications of a ray-tracing model in built-up areas, *Electronics Letters*, vol. 36, n° 5, pp. 461-462, 2000.

[7] OESTGES, C., VANHOENACKER-JANVIER, D., Physical-statistical prediction of performance for land mobile satellite systems, *IEE Proc.-Microw. Antenn. Propagat.*, vol. 146, n° 5, pp. 362-368, 1999.

[8] OESTGES, C., SAUNDERS, S.R., VANHOENACKER-JANVIER, D., Physical-statistical modelling of the land mobile satellite channel based on ray-tracing, *IEE Proc.-Microw. Antenn. Propagat.*, vol. 146, n° 1 , pp. 45-49, 1999.

2° Submitted papers

[1] OESTGES, C., VANHOENACKER-JANVIER, D., Impact of dynamic tropospheric mechanisms on Ka-band low earth-orbit satellite systems, *IEE Proc.-Microw. Antenn. Propagat.*, submitted for publication (November 2000).

[2] OESTGES, C., VANHOENACKER-JANVIER, D., Coverage modelling of high-altitude platforms communication systems, *Electronics Letters*, submitted for publication (October 2000).

3° Book chapters

[1] SAUNDERS, S.R., TZARAS, C., OESTGES, C., VANHOENACKER, D., Physical-statistical modelling, Part 4, Chapter 5, COST Action 255, *Radiowave propagation modelling for new satcom services at Ku band and above*, to be published.

[2] SAUNDERS, S.R., DÖTTLING, M., OESTGES, C., VÁZQUEZ-CASTRO, M.A., HABETHA, J., CERCAS, F., Test cases involving mobile links, Part 7, COST Action 255, *Radiowave propagation modelling for new satcom services at Ku band and above*, to be published.

4° International conference papers, with referees

[1] OESTGES, C., Propagation modelling for low earth-orbit satellite personal communication systems, Proc. URSI Forum 2000 (Brussels, Belgium), December 2000, accepted for communication.

[2] OESTGES, C., MAUFROID, X., VANHOENACKER-JANVIER, D., Performance simulation of a Ka band multimedia LEO satellite system, 6th Ka Band Utilization Conference (Cleveland, U.S.A.), pp. 605-612, June 2000.

[3] OESTGES, C., VANHOENACKER-JANVIER, D., Performance prediction of a 47 GHz stratospheric communication system, Millennium Conference on Antennas and Propagation, AP2000 (Davos, Switzerland), April 2000 (on CD-ROM).

[4] SAUNDERS, S.R., TZARAS, C., OESTGES, C., VANHOENACKER-JANVIER D., Physical-statistical modelling of the land mobile satellite channel, 1st International Workshop on Radiowave Propagation Modelling for SatCom Services at Ku band and above (ESTEC, Noordwijk, The Netherlands), pp.95-102, October 1998.

[5] OESTGES, C., VASSEUR, H., VANHOENACKER-JANVIER, D., Impact of edge diffraction on the performance of land mobile satellite systems in urban areas, 28th European Microwave Conference, Proc. EuMC '98 (Amsterdam, The Netherlands), pp. 357-361, October 1998.

[6] VASSEUR, H., OESTGES, C., VANDER VORST, A., Influence de la troposphère sur les liaisons sans fil aux ondes millimétriques et optiques: étude comparative, 3èmes journées d'études sur la propagation électromagnétique dans l'atmosphère: du décamétrique à l'Angström, (Rennes, France), pp. 58-63, Octobre 1997.

5° Submitted conference papers

[1] CLERCKX, B., MERTENS, D., OESTGES, C., VANHOENACKER-JANVIER, D., Application of closed-loop fade mitigation techniques to interactive satellite networks at Ka band, 19th

International Communications Satellite Systems Conference, ICSSC-19, (Toulouse, France), April 2001.

6° Other conference papers and reports

[1] OESTGES, C., Long-term performance predictions for mobile satellite communication links, Proc. URSI Forum'99 (Brussels, Belgium), 3 p., December 1999.

[2] DÖTTLING, M., OESTGES, C., VÁZQUEZ-CASTRO, M.A., Test cases involving mobile links: simulation results, COST 255 Final Workshop (Bech, Luxemburg), October 1999.

[3] OESTGES, C., System-level simulation for land mobile satellite services, Joint International Workshop COST 252/253/255 (Toulouse, France), pp. 59-63, May 1999.

[4] OESTGES, C., A new statistical model of the land mobile satellite channel based on a physical approach, Proc. URSI Forum'98 (Brussels, Belgium), p. 30, December 1998.

[5] OESTGES, C., SAUNDERS, S.R., VANHOENACKER D., Physical-statistical model for mobile-satellite fading based on a ray-tracing approach, COST255 MC5 (Vigo, Spain) CP51B04, May 1998.

[6] OESTGES, C., Physical-statistical modelling of the land mobile satellite channel based on a deterministic approach, Internal report, CCSR, University of Surrey, January 1998.

[7] OESTGES, C., Channel modelling of land mobile satellite systems, Proc. URSI Forum'97 (Gent, Belgium), p. 79, December 1997.

[8] OESTGES, C., VASSEUR, H., VANHOENACKER, D., Impact of edge diffraction on the performance of land mobile satellite systems in urban environment, COST255 MC4 (Brussels, Belgium), CP41B01, October 1997.

LIST OF COMMON VARIABLES, SYMBOLS AND ABBREVIATIONS

1° Propagation parameters

r	normalised received field amplitude
A	normalised fade level (with respect to line-of-sight/free-space conditions)
$\boldsymbol{r}$	normalised received field log-amplitude, [dB]
$\boldsymbol{A}$	normalised fade log-level, [dB]
γ_ξ	specific attenuation, due to any mechanism ξ (rain, gas, cloud, etc.), [dB/km]
σ_χ	scintillation standard deviation, [dB]

2° Link parameters

f	radiowave frequency, [Hz] or [GHz]
λ	wavelength, [m]
ω	wave angular frequency, $\omega = 2\pi f$
k	wave number, $k = 2\pi/\lambda$, [m^{-1}]
l, ψ	longitude and latitude of earth station, [deg.]
λ_{sat}, φ_{sat}	satellite longitude and latitude, [deg.]
ϑ	link elevation angle, [deg.]
ϕ_{sat}	link azimuth angle, relative to terrestrial parallel, [deg.]
ζ	polarisation tilt angle, [deg.]

3° Mathematical and statistical functions

$ln(x)$	natural logarithm of x
$log(x)$	common (base 10) logarithm of x
$\delta(x)$	delta function of x
$erfc(x)$	complementary error function of x
$T_X(x)$	probability density function (PDF) of parameter x
$P(x)$	cumulative density function (CDF) of parameter x
$E\{x\} = \hat{x}$	statistical mean of parameter x
$\Im(x)$	Fourier transform of function x

4° Electromagnetic parameters

ε	electrical permittivity, [F m^{-1}]
ε_r	relative electrical permittivity
σ	conductivity, [S m^{-1}]
$\boldsymbol{R}$	Fresnel dyadic reflection coefficient
$\boldsymbol{D}$	UTD dyadic diffraction coefficient, [$m^{1/2}$]
$\boldsymbol{C}$	UTD dyadic incremental diffraction coefficient
$\boldsymbol{D}^d$	UTD dyadic double diffraction coefficient, [m]
σ_{sca}	scattering cross section per unit area of a rough surface

5° Meteorological parameters

T	absolute temperature, [K]
w_c	cloud liquid water content, [g/m^3]
$R_{0.01}$	rainfall rate exceeded during 0.01 % of annual time, [mm/h]

6° Geometrical parameters

h_s	altitude of earth station (gateway or fixed terminal), [m] or [km]
h_m	height of mobile terminal, [m]
h_b	building height, [m]
h_v	foliage height, [m]
w	street width, [m]
d_m	transverse position of a mobile in the street, [m]
ϕ_{street}	street orientation, relative to terrestrial parallel, [deg.]
$\overline{\eta}$	vector of physical parameters (building height, street width, etc.)

7° Communication parameters and functions

$\boldsymbol{H}(\omega, t)$	time-variant passband transfer function
$\boldsymbol{H}(\Omega, t)$	time-variant baseband transfer function
$h(\tau, t)$	time-variant equivalent baseband impulse response
τ_{rms}	RMS delay spread, [s]
E_b/N_0	bit energy-to-noise spectral density ratio, [dB]
E_S/N_0	symbol energy-to-noise spectral density ratio, [dB]
C/N	signal-to-noise ratio, [dB]

8° System parameters

M_f	system clear-sky fade margin, [dB]
ΔM	handoff hysteresis margin, [dB]
ΔP_{max}	maximal fade compensation, [dB]
T_u, S_u	fade mitigation/handoff update interval, [s]

Throughout the text, vectors are always overlined, such as $\overline{a}$. Dyadic coefficients (tensors) are double-overlined, such as $\overline{\overline{A}}_m$. Averaged values are written as $\hat{x}$. Variables expressed in logarithmic scale (dB values) are usually identified by bold fonts, e.g. $\boldsymbol{A}$. Finally, functions in the Fourier domain are denoted by bold symbolic notations such as $\boldsymbol{A}$.

9° Usual frequency bands

Name	**Frequency band [GHz]**		
L	1.1	–	1.7
S	2.6	–	~ 4
C	~ 4	–	8.2
X	8.2	–	12.4
Ku	12.4	–	18.0
K	18.0	–	~ 27
Ka	~ 27	–	40.0
V	50.0	–	75.0

Table i.1 *Naming conventions for frequency bands*

10° Common abbreviations

BER	Bit Error Ratio
ECMWF	European Centre for Medium-range Weather Forecast
ETSI	European Telecommunications Standards Institute
GEO	Geostationary Earth Orbit
HAPS	High Altitude Platform System
IMT 2000	International Mobile Telecommunications 2000
ITU	International Telecommunication Union

LEO	Low Earth-Orbit
LMS(S)	Land Mobile Satellite (System)
LOS	Line-Of-Sight
MAI	Multiple Access Interference
PCS/PCN	Personal Communication System/Network
SNR	Signal-to-Noise Ratio
UTD	Uniform Theory of Diffraction

REFERENCES

[1] VANDER VORST, A., VASSEUR, H., VYNCKE, C., AMAYA, C., VANHOENACKER, D., From electromagnetics to system performance: a new method for the error rate prediction of atmospheric communications links, *IEEE J. Selected Areas Commun.*, vol. 15, n° 4, pp. 656-666, 1997.

[2] COST 255, *Radiowave propagation modelling for new SatCom services at Ku band and above*, European Commission, Brussels, to be published.

[3] MILLER, B., Satellites free the mobile phone, *IEEE Spectrum*, pp. 26-35, March 1998.

[4] SAUNDERS, S.R., Antennas and propagation for wireless communication systems, Wiley, Chichester, 1999.

CHAPTER 1 TROPOSPHERIC PROPAGATION FOR LOW EARTH-ORBIT LINKS

1.1 INTRODUCTION

This first chapter describes several existing prediction models of the various tropospheric mechanisms affecting earth-space transmissions. Ultimately, it proposes innovative answers to the specificity of low earth-orbit links. Upcoming satellite PCS's are indeed planned to operate as high as Ka band. At these frequencies, the tropospheric constituents strongly interact with the radiowave propagation, thereby severely limiting the system availability.

Phenomena such as rain, cloud and gas attenuation or scintillation have already been studied for several years. A large number of models are therefore available, each offering various advantages and drawbacks. The goal of this brief review is to select the most appropriate or accurate models in the context of multi-satellite activity, rather than listing all existing models. Since the models must fit a large range of systems, physical approaches are preferred when possible, covering the prediction of both the deterministic slant-path attenuation and the long-term statistical distribution of attenuation.

Three basic mechanisms are investigated. Section 1.2 is devoted to the gaseous attenuation and presents recent models that account for oxygen and water vapour absorption. Section 1.3 depicts the effect of hydrometeors, namely clouds and rain. Regarding rain attenuation, the ITU-R approach is presented together with a meteorologically oriented model allowing for a spatial description of rain. Models of scintillation phenomena are finally detailed in Section 1.4.

Ultimately, system performance must be predicted. However, telecommunication systems being now characterised by smaller allowed outage percentages (typically of the order of 1 %) and reduced size for the earth terminals, so rain is no longer the dominating attenuation effect. Since the statistical distributions are calculated separately for each mechanism, the problem is subsequently to combine these attenuation phenomena in order to assess the total fade level distribution. This issue is addressed in Section 1.5.

Also, a crucial question remains. All models have by now been developed for fixed earth-space links. Yet, the systems to be investigated later are based on a constellation of non-geostationary satellites and/or are scheduled to support portable terminals. Hence, Section 1.6 investigates how the classical models can be used in the context of low earth-orbit links. Moreover, besides a statistical approach, this thesis presents a simple innovative method to evaluate the short-term variation of the attenuation phenomena, in anticipation of a dynamic analysis of system procedures (see Chapter 3).

A last important remark concerns several notations that are used throughout the text. The envelope of the received signal amplitude is normally written as r while $\boldsymbol{r}$ is used when expressed in decibels [dB], thus $\boldsymbol{r} = 20 \log r$. The attenuation or fade level is defined as $A = 1/r^2$ and denoted as $\boldsymbol{A}$ when expressed in [dB]. Therefore, the basic relationship can be established: $\boldsymbol{A} = 10 \log A = -\boldsymbol{r}$.

1.2 ATTENUATION DUE TO ATMOSPHERIC GASES

1.2.1 Physical background of gaseous absorption

The presence of gaseous molecules, which absorb energy from the incoming wave, constitutes a first source of tropospheric attenuation. Absorption is caused by dielectric or magnetic resonance and depends on the molecular properties. In normal atmospheric conditions, oxygen (O_2) and water vapour (H_2O) are the principal gaseous absorbers of radiowave energy in the earth's atmosphere, particularly below 70 GHz. Nitrogen (N_2), for example, has no resonance absorption at all in the microwave region. Other gases (CO, NO_2, O_3, etc.) exhibit absorption peaks in the microwave range but their molecular density is actually very low, so their influence can be neglected [1]. The following sections present models of oxygen and water vapour absorption, dealing with both deterministic and statistical points of view.

1.2.2 Oxygen attenuation

1.2.2.1 SLANT-PATH ATTENUATION

Oxygen is a non-polar paramagnetic molecule with a permanent magnetic moment. This mechanism thereby produces several resonance peaks, related to various modes of vibration. The first peak for oxygen appears at 60 GHz. For frequencies sufficiently far away from the resonance peaks, the oxygen attenuation is however very small.

Although the oxygen attenuation is characterised by a diurnal and seasonal fluctuation, it is often assumed to be constant over the year. Several ITU-R recommendations [2] propose a simple procedure to estimate the slant-path attenuation due to oxygen. The specific attenuation γ_o [dB/km] is first estimated by ITU-R Rec. 676-2 (1997 version)[†]:

- for $f < 57$ GHz,

$$\gamma_o = \left[7.19\ 10^{-3} + \frac{6.09}{f^2+0.227} + \frac{4.81}{(f-57)^2 + 1.50} \right] f^2\ 10^{-3} \qquad (1.1)$$

[†] In late 1999, this recommendation has been modified quite substantially (ITU-R Rec. 676-4) [3]. A comparison between the new version and the version used in this thesis is discussed in Appendix A.

- for 63 GHz < f < 350 GHz,

$$\gamma_o = \left[3.79\ 10^{-7} f + \frac{0.265}{(f-63)^2 + 1.59} + \frac{0.028}{(f-118)^2 + 1.470} \right] (f-198)^2\ 10^{-3} \qquad (1.2)$$

where f is the frequency expressed in [GHz].

Expressions (1.1-2) are given at ground level (pressure equal to 1013 hPa) and at a temperature of 15 °C. They also exclude frequencies between 57 and 63 GHz, corresponding the 60 GHz peak. Expressions valid near the resonance or for other temperature and pressure conditions are detailed in [2][4].

A second model is proposed by Liebe [5]. It estimates the oxygen specific attenuation by summing spectra due to O_2-molecules. The procedure is included in the MPM software, available without charge. Figure 1.1 compares the specific attenuation obtained from both models in the same conditions (temperature: 15 °C; pressure: 1013 hPa).

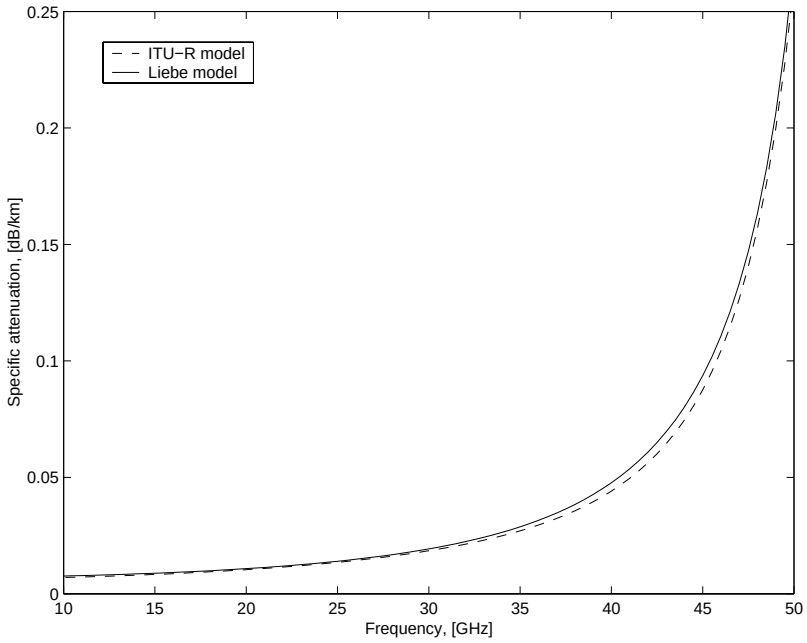

Figure 1.1 *Oxygen specific attenuation as a function of frequency*

Regardless of the model, the specific attenuation is very small up to Ka band. However, it could become significant if V band applications are considered. Because results from both models are only slightly different and because the contribution of oxygen attenuation to the

total impairment is usually the least significant one, the simple ITU-R method (1997 version) is always used later on.

The slant-path attenuation A_o [dB] is calculated following ITU-R Rec. 676-2 by:

$$A_o = \frac{\gamma_o \, h_o \, e^{-h_s/h_o}}{\sin \vartheta} \tag{1.3}$$

where

- h_S [km] is the height of the earth station,
- ϑ is the link elevation angle ($\vartheta > 10°$),
- h_o [km] is the equivalent height of oxygen,

$$h_o = \begin{cases} 6 & \text{for } f < 57 \text{ GHz} \\ 6 + \dfrac{40}{(f - 118.7)^2 + 1} & \text{for } 63 < f < 350 \text{ GHz} \end{cases} \tag{1.4}$$

Note that for $\vartheta < 10°$, the effect of the earth's curvature cannot be neglected. The denominator in (1.3) should then be replaced (ITU-R Rec. 618-5) by:

$$g(h_o, \vartheta) = 0.661 \sqrt{\sin^2 \vartheta + \frac{2 h_s}{R_e}} + 0.339 \sqrt{\sin^2 \vartheta + \frac{2 h_s + 5.5 h_o}{R_e}} \tag{1.5}$$

where R_e [km] is the effective earth radius (typically, R_e = 8500 km for $h_s < 1$ km).

The ITU-R method is quite accurate for frequencies below 30 GHz. From 50 GHz to 70 GHz, the temperature dependence must be taken into account, since the attenuation becomes significant.

1.2.2.2 STATISTICAL DISTRIBUTION

The amount of oxygen in the atmosphere is almost constant over time. Since the oxygen attenuation is limited for frequencies below 40 GHz, the small variations during the year are insignificant. The attenuation caused by oxygen is subsequently assumed to be constant and given by (1.3) for any percentage of annual time.

1.2.3 Water vapour attenuation

1.2.3.1 SLANT-PATH ATTENUATION

In contrast to oxygen, the water molecule exhibits a permanent electric dipole and absorption peaks occur at critical frequencies (22.2 and 183.3 GHz in the microwave region). The specific attenuation due to water vapour can be calculated using several approaches. Two models are considered here: the ITU-R method and the model proposed by Liebe.

Similarly to the calculation of oxygen specific attenuation, the method by Liebe [5] consists of a line-by-line summation of spectra due to water vapour molecule. It is valid up to 1000 GHz and is also included in the MPM software. The input parameters are frequency, pressure, temperature and water vapour density ρ.

The ITU-R empirical model (ITU-R Rec. 676-2[†]) proposes the following expression to calculate the specific attenuation γ_w [dB/km] in the reference conditions (temperature: 15 °C; pressure: 1013 hPa):

$$\gamma_w = \left[0.050 + 0.0021\rho + \frac{3.6}{(f-22.2)^2+8.5} + \frac{10.6}{(f-183.3)^2+9.0} + \frac{8.9}{(f-325.4)^2+26.3} \right] f^2 \rho \; 10^{-4} \tag{1.6}$$

where

- f [GHz] is the frequency,
- ρ [g/m^3] is the water vapour density.

Figure 1.2 compares the ITU-R (ITU-R Rec. 676-2) and Liebe models. The 22.2 GHz-peak is clearly visible. Meanwhile, it is worth noting that the water vapour absorption loss globally increases with frequency. The discrepancy between the methods and the relative importance of water vapour attenuation incite to use the Liebe model in all following simulations, for it is known to be more accurate [4].

[†] The updated version (ITU-R Rec. 676-4) can be found in [3]. It is similar to Liebe-Salonen model, which is used throughout this thesis.

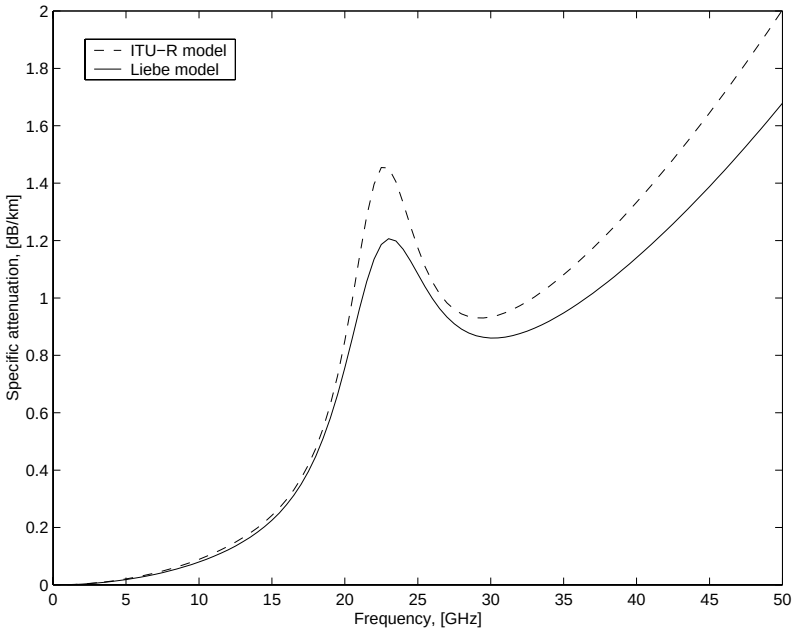

Figure 1.2 *Water vapour specific attenuation as a function of frequency*

Using ITU-R Rec. 676-2, the equivalent height of water vapour is determined by:

$$h_w = h_{w0}\left[1 + \frac{3}{(f-22.2)^2+5} + \frac{5}{(f-183.3)^2+6} + \frac{2.5}{(f-325.4)^2+4}\right] \tag{1.7}$$

where h_{w0} [km] is the equivalent height in window regions, depending on weather conditions. It is conventionally assumed that h_{w0} = 1.6 km and 2.1 km for clear and rainy weather respectively.

The water vapour slant-path attenuation in [dB] can finally be evaluated. Following the ITU-R method, an expression similar to (1.3) can be used:

$$\boldsymbol{A_w} = \frac{\gamma_w h_w}{g(h_w, \vartheta)}$$

If the model by Liebe is used, the slant-path attenuation $\boldsymbol{A_w}$ [dB] is given by:

$$\boldsymbol{A_w} = \frac{\int_{h_s}^{h_u} \gamma_{w,L}\left[f, T(z), p(z), \rho(z)\right] dz}{g(h_w, \vartheta)} \tag{1.8}$$

where

- $\gamma_{w,L}$ [dB/km] is the specific attenuation calculated by the Liebe model,
- the equivalent height h_w is given by (1.7),
- the elevation scaling function $g(h, \vartheta)$ is outlined by (1.5),
- $T(z)$, $p(z)$ and $\rho(z)$ are the temperature, pressure and water vapour content profiles from standard atmosphere,
- for the integration, the lower limit h_s [km] is the earth station altitude and the upper limit h_u [km] must be above 20 km.

1.2.3.2 STATISTICAL DISTRIBUTION

In addition to daily fluctuations, water vapour attenuation is characterised by significant seasonal differences, owing to the increase of the total water vapour content of the atmosphere during summer. The distribution of the attenuation portion due to water vapour is related to the distribution of the integrated water vapour content V, which depends on the location of the earth station and is available from worldwide ECMWF maps. For example, Figure 1.3 depicts the integrated water vapour content V exceeded during 1 % of annual time [4]. All forthcoming simulations dealing with Europe only (see Chapter 3), this map and those following, are always represented for Europe only, although data exists for the whole earth.

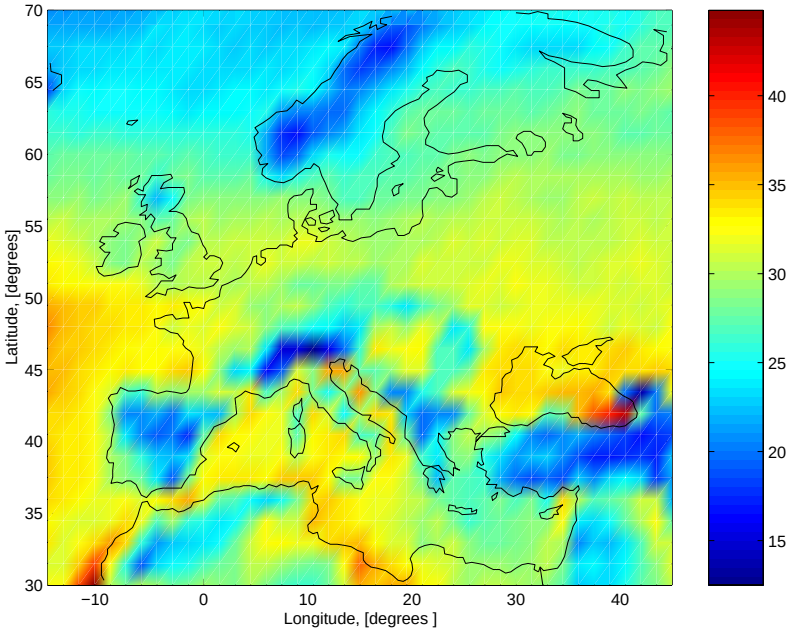

Figure 1.3 *Integrated water vapour content [kg/m^2] exceeded during 1 % of annual time in Europe*

Liebe and Salonen [5][6] propose the following formula in order to estimate the water vapour attenuation $\boldsymbol{A_{w,\tau}}$ [dB] exceeded for τ% of annual time:

$$\boldsymbol{A_{w,\tau}} = \frac{0.0173\ V(\tau)}{g(h = 2\,\text{km}, \vartheta)} \cdot \frac{\gamma_{w,L}(f, p_{ref}, \rho_{ref}, t_{ref})}{\gamma_{w,L}(f = 20.6\,\text{GHz}, p_{ref}, \rho_{ref}, t_{ref})} \tag{1.9}$$

where

- $V(\tau)$ [kg/m^2] is the integrated water vapour content exceeded during τ % of time, depending on latitude and longitude,
- $g(h, \vartheta)$ is the elevation scaling function given by (1.5),
- $\gamma_{w,L}$ [dB/km] is the water vapour specific attenuation calculated by Liebe in the reference meteorological conditions:

$$\begin{cases} p_{ref}\,[\text{hPa}] = 780 \\ \rho_{ref}\,[\text{g/m}^3] = \dfrac{V(\tau)}{4\,\text{km}} \\ t_{ref}\,[^\circ\text{C}] = 14\,ln(0.22\,\rho_{ref}) + 3 \end{cases}$$

1.3 ATTENUATION BY HYDROMETEORS

1.3.1 Scattering and absorption by particles

Rain and clouds are composed of small liquid water drops or ice particles. The propagation of radiowaves through such particles suffer from extinction induced by both absorption and scattering of the incident energy. These mechanisms depend strongly on the size, the shape and the liquid water content of particles.

Physical models [1] are usually based on the calculation of an extinction cross section $\sigma_{ext} = \sigma_{abs} + \sigma_{sca}$. The extinction (or attenuation) cross section of a single particle is defined as the area which, when multiplied by the incident intensity, gives the total power taken away from the incident wave. The Mie single-scattering theory [7] allows for calculation of σ_{ext}, as a function of the frequency, the complex refractive index of water and the shape of the particle. When the size D of the particle is small with respect to the wavelength λ, the Mie theory is well approximated by the Rayleigh scattering theory [7], for which $\sigma_{ext} \propto D^3/\lambda$. Note that, for non-spherical drops, the diameter D is defined as that of the equivolumic sphere.

The total specific attenuation through a number of particles is finally obtained as the integral of the extinction cross section over the drop size distribution function $N(D)$ [$m^{-3}mm^{-1}$]. This function is defined such that $N(D)dD$ is the number density of drops with diameters between D and $D + dD$. Subsequently, the specific attenuation by hydrometeors γ_{hydro} [dB/km] is written [1] as:

$$\gamma_{hydro} = 4.343\,10^{-3} \int_0^{\infty} \sigma_{ext}\, N(D)\, dD \qquad (1.10)$$

1.3.2 Attenuation due to clouds

1.3.2.1 SPECIFIC CLOUD ATTENUATION

1° Physics of clouds

For very small particles, such as cloud droplets, the Rayleigh approximation of the Mie theory is valid for frequencies below 300 GHz. Hence, the complex dependence (1.10) on the size distribution reduces for clouds to:

$$\gamma_c \propto \int_0^\infty D^3 N(D)\, dD$$

The specific attenuation caused by a slab of cloud at height z can therefore be expressed independently of the size distribution of cloud droplets, by means of a linear dependence on the liquid water or ice content $w_c(z)$ [g/m^3] of the slab. The latter is defined as:

$$w_c(z) = \frac{\pi \upsilon}{6} 10^6 \int_0^\infty D^3 N(D,z)\, dD \tag{1.11}$$

where υ is the specific weight of the material ($\upsilon = 1$ for liquid water, $\upsilon = 0.916$ for ice).

The cloud attenuation also varies with temperature. Usually, the cloud particles are in liquid form above 0 °C and in ice form below – 20 °C to – 40°C, depending on the cloud type. In the interim range of temperatures, the cloud droplets exist in a mixture of supercooled water and ice. The attenuation due to ice clouds can be neglected in the microwave range, although ice clouds play a significant role in signal depolarisation.

The major problems, when dealing with cloud attenuation, are the complex physical modelling of cloud structures as well as the lack of data. The liquid water content, for example, is not a standard observable quantity and cannot easily be estimated from available meteorological quantities. In view of the complexity of cloud modelling, several attempts have been made in order to classify clouds in a relationship with measurable parameters. However, these classifications sometimes lead to different characteristics for the same cloud. For instance, Table 1.1 summarises a number of characteristics such as the vertical/horizontal extent and liquid water content for several types of clouds, as given in [1] and [8].

	Brussaard & Watson			**Dissanayake, Allnut & Haidara (DAH)**			
Cloud type	**w_c [g/m^3]**	**Bottom [km]**	**Top [km]**	**w_c [g/m^3]**	**Bottom [km]**	**Top [km]**	**Horizontal extent [km]**
Cumulonimbus	-	-	-	1.0	0.4-1	5.0-10.0	4.0
Cumulus	1.0	0.7	2.7	0.6	0.8-1.5	2.0-5.0	3.0
Nimbostratus	0.6	0.7	2.7	1.0	0.1-1	4.0	10.0
Stratus	0.4-0.3	0.2-0.3	0.7-1.0	0.4	0.1-0.7	1.0	10.0
Stratocumulus	0.3	0.2	0.7	-	-	-	-

Table 1.1 *Typical characteristics of some clouds for mid-latitude conditions*

In order to relate the liquid water content to objective parameters, the Salonen-Uppala model [9] allows estimation of $w_c(z)$ [g/m^3] as a function of the temperature and height h_c [m] from the cloud base:

$$w_c = w_{c,ref}\,(1+c\,t)\left\lceil \frac{h_c}{h_{ref}} \right\rceil^a p_w(t) \tag{1.12}$$

where

- a = 1.4, h_{ref} = 1500 m, c = 0.041 °C^{-1} and $w_{c,\,ref}$ = 0.14 g/m^3
- $p_w(t)$ is the liquid water fraction, approximated by

$$p_w(t) = \begin{cases} 1 & t > 0\,°\text{C} \\ 1 + t/20 & -20\,°\text{C} < t < 0\,°\text{C} \\ 0 & t < -20\,°\text{C} \end{cases}$$

However, the method is only accurate for stratiform horizontal structures, and is thus not valid for cumulus and cumulonimbus.

2° Model by Liebe

Liebe, Manabe and Hufford [10] have tried to establish a complete description of cloud attenuation as a function of the liquid water content, based on the Rayleigh approximation of the exact Mie scattering theory. The model is known as ITU-R Rec. 840-1 [2]. The specific attenuation γ_c [dB/km] of a cloud located at height z is written in the form:

$$\gamma_c(z) = 0.182\, f\, N''_w(f,z) \tag{1.13}$$

where

- f [GHz] is the frequency,
- N''_w [ppm] is the imaginary part of the complex refractivity,

$$N''_w(f,z) = \frac{9}{2}\frac{w_c(z)}{\varepsilon''(1+\eta^2)} \tag{1.14}$$

In expression (1.14),

- $w_c(z)$ is the liquid water content defined by (1.11),
- $\eta \overset{\Delta}{=} (2+\varepsilon')/\varepsilon''$, ε' and ε'' being the real and imaginary parts of the permittivity of water.

The dependence of the permittivity of water on frequency is given [9] by the double Debye relaxation model:

$$\varepsilon'(f) = \varepsilon_2 + \frac{\varepsilon_0 - \varepsilon_1}{1 + \left(\frac{f}{f_p}\right)^2} + \frac{\varepsilon_1 - \varepsilon_2}{1 + \left(\frac{f}{f_s}\right)^2} \tag{1.15-a}$$

$$\varepsilon''(f) = \frac{f(\varepsilon_0 - \varepsilon_1)}{f_p\left[1 + \left(\frac{f}{f_p}\right)^2\right]} + \frac{f(\varepsilon_1 - \varepsilon_2)}{f_s\left[1 + \left(\frac{f}{f_s}\right)^2\right]} \tag{1.15-b}$$

where

- $\varepsilon_0 = 77.66 + 103.3(\theta - 1)$, $\varepsilon_1 = 5.48$ and $\varepsilon_2 = 3.52$
- the inverse temperature θ is given by $\theta = 300/T$, T being expressed in Kelvin
- the principal and secondary relaxation frequencies are respectively, in [GHz],

$$f_p = 20.09 - 142(\theta - 1) + 294(\theta - 1)^2$$
$$f_s = 590 - 1500(\theta - 1)$$

A temperature of 0 °C (273 K) is recommended by Rec. ITU-R 840-1.

1.3.2.2 STATISTICAL DISTRIBUTION

The specific cloud attenuation depends on frequency f, liquid water content w_c and temperature T. The temperature dependence is taken into account by defining the reduced liquid water content w_{red} so that the following holds:

$$\gamma_c(f = 43\,\text{GHz}, w_{red}, T = 273\,\text{K}) = \gamma_c(f = 43\,\text{GHz}, w_c, T) \tag{1.16}$$

Because temperature dependence of γ_c is almost similar over the frequency range from 10 to 60 GHz, the value of w_{red} and the derived statistics are also valid within this frequency range. Then, the reduced liquid water content is integrated as a function of height, resulting in the integrated reduced liquid water content W_{red} [kg/m^2]. Statistics of the latter are calculated using data from the ECMWF numerical analysis [4], so that world maps of W_{red} values exceeded during τ% of annual time are derived, as illustrated in Figure 1.4 for Europe.

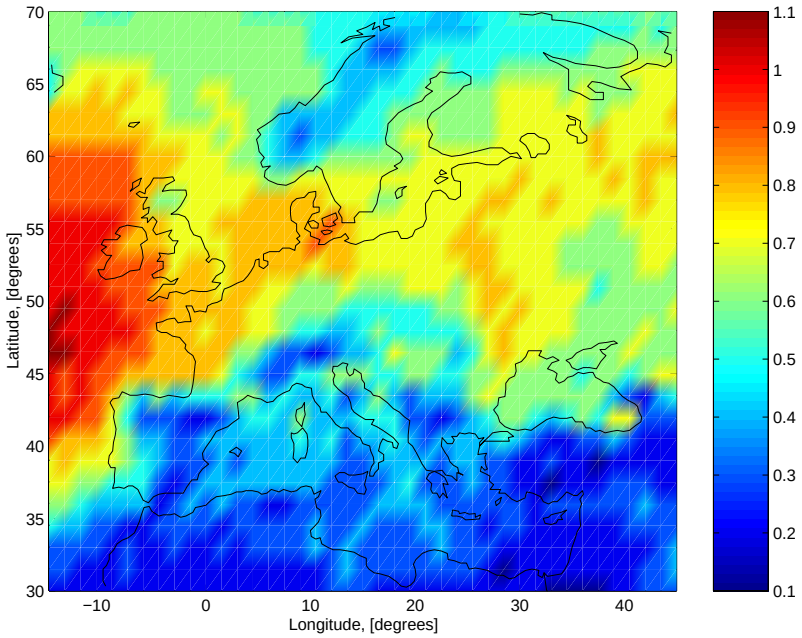

Figure 1.4 *Integrated reduced liquid water content [kg/m^2] exceeded during 1 % of time in Europe*

From (1.13-14) and (1.16), the slant-path cloud attenuation $A_{c,\tau}$ [dB] exceeded during τ % of time can finally be written [9] as:

$$A_{c,\tau} = \frac{0.819\, f\, W_{red}(\tau)}{\varepsilon''(1+\eta^2)} \frac{1}{\sin\vartheta} \tag{1.17}$$

where ϑ is the elevation angle of the link.

1.3.3 Rain attenuation

1.3.3.1 Models of rain attenuation

Attenuation caused by rain is often the dominant source of impairment for satellite links and absolutely must be considered. However, measurements of rain attenuation are scarce, since experiments have only been carried out in few places all over the world and for a limited number of frequencies. Hence, a large diversity of models can be found in the literature, with varying accuracy.

In this thesis, only two models of rain attenuation statistics are presented and investigated. The first one is the ITU-R model (1997 version, ITU-R Rec. 618-5), which is very simple and requires few input parameters. Note that this model has been replaced in late 1999 by a new recommendation (ITU-R Rec. 618-6), based on the DAH model [3][8]. A brief overview of this new recommendation can be found in Appendix A. However, only the 1997 version is considered, mainly because it has been recently reported from Olympus and Italsat experiments [4] and ACTS [11] to perform still satisfactorily in most of the cases.

A second model (EXCELL) is also described, for several reasons:

- it is based on the ITU-R specific attenuation and effective height,
- it has been tested against data within COST 255 [4] and ACTS [11] projects and has been found to be one of the best models,
- its approach is comprehensively meteorologically oriented and is thereby particularly suited for time series simulations.

1.3.3.2 ITU-R SPECIFIC ATTENUATION AND EFFECTIVE RAIN HEIGHT

Considering rain attenuation, the single-scattering theory can be applied assuming coherent scattering within a homogeneous slab of sparsely populated particles. Usually, $N(D)$ is assigned a negative exponential form:

$$N(D) = N_0 \, exp(-\Lambda D) \tag{1.18}$$

where N_0 and Λ are empirically related to the rainfall rate R [mm/h] (Marshall-Palmer or Laws-Parsons relationships). The specific attenuation is then expressed as:

$$\gamma_r [\text{dB/km}] = 4.343 \, 10^{-3} \int_0^{\infty} \sigma_{ext} \, N_0 \, exp(-\Lambda D) \, dD \tag{1.19}$$

Expression (1.19) can be rewritten so that it only depends on the rainfall rate, postulating a drop size distribution, a drop temperature and a particle shape. This yields the well-known ITU-R Rec. 838 [2] for estimating rain specific attenuation:

$$\gamma_r = K \, R^{\alpha} \tag{1.20}$$

The parameters K and α are determined for linear and circular polarisation by means of the following relationships:

$$\begin{aligned} K &= \left[k_h + k_v + (k_h - k_v)\cos^2\vartheta\cos 2\zeta\right]/2 \\ \alpha &= \left[k_h\alpha_h + k_v\alpha_v + (k_h\alpha_h - k_v\alpha_v)\cos^2\vartheta\cos 2\zeta\right]/2K \end{aligned} \tag{1.21}$$

where

- ϑ is the path elevation angle,
- ζ is the polarisation tilt angle relative to the horizontal (ζ = 45° for a circular polarisation),
- frequency-dependent coefficients k_h, k_v, α_h and α_v are tabulated in the recommendation; they are calculated using the Laws-Parsons drop size distribution, considering a temperature of 20 °C and aligned oblate spheroidal drops.

A second important parameter for the slant-path attenuation is the height of rain that determines the path length through rain. The latter is barely measurable and depends furthermore upon the type of rain, the climate and the season. Hence, its evaluation is not straightforward. In this study, the ITU-R model for effective rain height (ITU-R Rec. 839 and 618-5 [2]) is used. The rain height h_r [km] is related to the latitude ψ [deg.] of the station by:

$$h_r = \begin{cases} 5 - 0.075(\Psi - 23) & \Psi > 23° \\ 5 & -21° \le \Psi \le 23° \\ 5 + 0.1(\Psi + 21) & -71° \le \Psi < -21° \\ 0 & \Psi < -71° \end{cases} \tag{1.22}$$

1.3.3.3 ITU-R RAIN ATTENUATION STATISTICS

Once the specific rain attenuation and effective height are known, ITU-R Rec. 618-5 [2] proposes a simple method to evaluate the attenuation $A_{r,\tau}$ [dB], exceeded during a given percentage τ of annual time:

$$A_{r,\tau} = 0.12\, A_{r,0.01}\, \tau^{-(0.546 + 0.043\, \log \tau)} \tag{1.23}$$

This expression has been validated for 0.001 % ≤ τ ≤ 1 %.

In (1.23), the attenuation $A_{r,0.01}$ exceeded during 0.01 % of time is calculated by:

$$A_{r,0.01} = \gamma_{r,0.01}\ L_s\ r_{0.01} \tag{1.24}$$

where

- $\gamma_{r,0.01}$ [dB/km] is estimated by (1.20) for a point rainfall rate exceeded during 0.01 % of time, $\gamma_{r,0.01} = K\,(R_{0.01})^{\alpha}$
- L_s [km] is the slant-path length below rain height,
- $r_{0.01}$ is a reduction factor.

The rainfall rate exceeded during 0.01 % of time is available from ITU-R Rec. 837-2 [3], inferred from ECMWF maps, with 1.5° spatial resolution (see Figure 1.5). If not, it can roughly be estimated from the old ITU-R maps of rain climates (ITU-R Rec. 837-1).

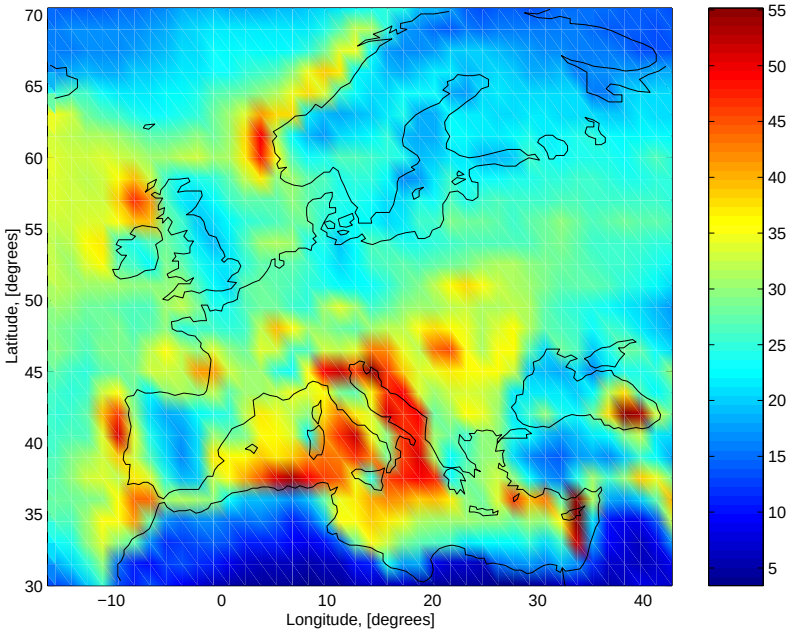

Figure 1.5 *Rainfall rate [mm/h] exceeded during 0.01 % of time in Europe*

The slant-path length L_s is given by:

$$L_s = \frac{h_r - h_s}{\sin\vartheta} \qquad \vartheta \geq 5°$$

$$L_s = \frac{2\,(h_r - h_s)}{\sqrt{\sin^2\vartheta + \dfrac{2\,(h_r - h_s)}{R_e}} + \sin\vartheta} \qquad \vartheta < 5° \tag{1.25}$$

where

- h_s [km] is the height of the earth station,
- ϑ is the link elevation angle ($\vartheta > 10°$),
- R_e [km] is the effective height of earth's radius (typically, R_e = 8500 km for $h_s < 1$ km).

The reduction factor $r_{0.01}$ accounts for the non-uniformity of the rain along the path:

$$r_{0.01} = \frac{1}{1 + L_g / L_0} \tag{1.26}$$

where

- L_g [km] is the horizontal projection of the slant-path length,

$$L_g = L_s \cos\vartheta \tag{1.27}$$

- $L_0 = 35\, exp(-0.015\, R_{0.01})$ is given in [km].

The expression of L_0 is only valid for $R_{0.01} < 100$ mm/h. For $R_{0.01} > 100$ mm/h, the use of 100 mm/h in place of $R_{0.01}$ is recommended.

The cumulative density function of rain attenuation can easily be computed by inverting equation (1.23):

$$P(A_r) = 10^{11.628(-0.546 + \sqrt{0.298 + 0.172\, log(0.12\, A_{r,0.01}/A_{r,\tau})})} \tag{1.28}$$

1.3.3.4 EXCELL MODEL

1° Introduction to the concept

The ITU-R statistical approach does not allow representation of the horizontal distribution of the rain structures. Yet, any rain event of interest for propagation of radio waves is generated by the movement of the above mentioned rain structures in the region where the terrestrial station is located (this motion is assumed to be a pure translation caused e.g. by wind, without any deformation). These structures, however, are quite similar at each site, only their probability of occurrence varies according to the location of the receiving site.

Consider a fixed receiver, together with rain structures that assume randomly all possible positions in the horizontal plane. The probability that the given value V of any propagation parameter (e.g. the point rainfall rate R) is exceeded is quite evidently proportional to the number of positions of the rain structures for which the value V is exceeded at the receiving point. This concept can be described the other way around. The position of rain structures can be frozen while the receiver is allowed to move completely randomly. All the positions in which the value V is exceeded constitute a surface, the area of which, denoted as S, is clearly proportional to the referred probability [12].

If a physical model is determined for the rain structures, these can be described by a reduced number of parameters, denoted by α, β, etc. The referred area can then be expressed [12] as a function $S(V,\alpha,\beta,...,a,b,...)$ of these parameters, the prefixed value V and the link parameters (frequency, elevation angle) a, b, etc.

The probability of exceeding the value V of the observed parameter is finally given by:

$$P(V,a,b,...) = \frac{1}{100} \quad ... \quad S(V,\alpha,\beta,...,a,b,...)\, N(\alpha,\beta,...)\, d\alpha\, d\beta ... \tag{1.29}$$

where $N(\alpha,\beta,...)$ is the spatial density of rain structures, namely the number of structures per unit area with characteristics α, β, …

2° Representation of a population of rain cells

Rain cells are defined as areas encircled by a 5-mm/h contour. Within a cell, the rain rate is modelled by an exponential profile and a rotational symmetry [13]. The rainfall rate at distance ρ from the centre is given by:

$$R(\rho) = R_M \; exp(-\rho/\rho_0) \tag{1.30}$$

where R_M is the peak intensity and ρ_0, referred to as cell radius, is the distance at which the rain rate decays by factor 1/e.

Each cell is thus characterised by these two parameters. The spatial density of the population $N\left[ln\, R_M\, , \rho_0/\hat{\rho}_0\right]$, i.e. the number of cells per square kilometre and per unit range of $ln\ R_M$ and $\rho_0/\hat{\rho}_0$, is expressed [13] by:

$$N\left[ln\, R_M\, , \rho_0/\hat{\rho}_0\right] = N_0\, (ln\, R_M)\; exp(-\rho_0/\hat{\rho}_0) \tag{1.31}$$

where

- $\hat{\rho}_0$ is the conditional average cell radius, $\hat{\rho}_0 = 1.7\left[(R_M/6)^{-10} + (R_M/6)^{-0.26}\right]$
- N_0, expressed for convenience as a function of $ln\ R_M$, is related to the local cumulative statistical distribution of the rain intensity, $P(R)$, by means of

$$N_0(ln\,R_M) = -\frac{1}{4\pi\,\hat{\rho}_0^2}\,\frac{d^3P(R)}{d(ln\,R)}\bigg|_{R=R_M} \tag{1.32}$$

3° Slant-path attenuation through a cell

In order to evaluate the attenuation through a cell, one must integrate the specific attenuation (1.20) along the path crossing the cell:

$$\boldsymbol{A_r} = \int_{path\ L_s} \gamma_r\ dl \tag{1.33}$$

Most of the time, this has to be done numerically. An equivalent rain intensity can be defined [12] by:

$$\hat{R} = \left[\frac{1}{K\,L_s}\int_{path\ L_s} \gamma_r\ dl\right]^{\frac{1}{\alpha}} \tag{1.34}$$

where K, α and L_s are defined by (1.21) and (1.25) respectively.

The total attenuation must also include a residual attenuation $\boldsymbol{A_p}$ due to the rain debris [12], which is not taken into account by the exponential cell model:

$$\boldsymbol{A_r} = K\,\hat{R}^{\alpha} L_s + \boldsymbol{A_p} \tag{1.35}$$

For simplicity, $\boldsymbol{A_p}$ [dB] is assumed to be produced by a uniform rain of 4 mm/h:

$$\boldsymbol{A_p} = K\,4^{\alpha} L_s \tag{1.36}$$

If the link is centred on the cell peak, the equivalent rain $\hat{R}$ reaches its maximum value, denoted as R_E. This parameter, which is necessary to the calculation of the attenuation distribution, is easily analytically expressed by:

$$R_E = R_M \left\{ \frac{2\rho_0}{\alpha L_g} \left[1 - exp(-\alpha L_g / 2\rho_0) \right] \right\}^{\frac{1}{\alpha}} \tag{1.37}$$

where L_g is the length of the horizontal projection of the slant-path given by (1.27).

4° Rain attenuation statistics

The calculation of area function S is demonstrated in [12]. The result is given by:

$$S = exp(-\rho_{0,min} / \hat{\rho}_0) \left[2\pi M^{*2} + L_g M^* \right] \tag{1.38}$$

where

- $M^* = \hat{\rho}_0 \, ln(R_M / R_E)$
- $\rho_{0,min} = \frac{\alpha L_g}{2} \frac{t(3-t)}{4(1-t)}$ is the minimum radius producing the amount of averaged rain, the intermediate variable t being given by $t = (R_E / R_M)^{\alpha}$.

Inserting (1.38) and (1.31) into (1.29) finally yields the following solution for the attenuation distribution:

$$P(A_r) = \frac{1}{100} \int_{ln R_E}^{\infty} exp(-\rho_{0,min} / \hat{\rho}_0) \left[2\pi M^{*2} + L_g M^* \right] N_0(ln R_M) \, d(ln R_M) \tag{1.39}$$

It is worth noting that EXCELL model requires the complete cumulative distribution of the rainfall rate (see 1.32). In contrast, the ITU-R model only requires the percentile $R_{0.01}$, what makes it easier to use.

As a conclusion, Figure 1.6 presents a comparison between EXCELL and ITU-R predictions. The link is characterised by an elevation angle of 30 degrees, a circular polarisation and a frequency of 30 GHz. The earth receiver is assumed to be located in Belgium.

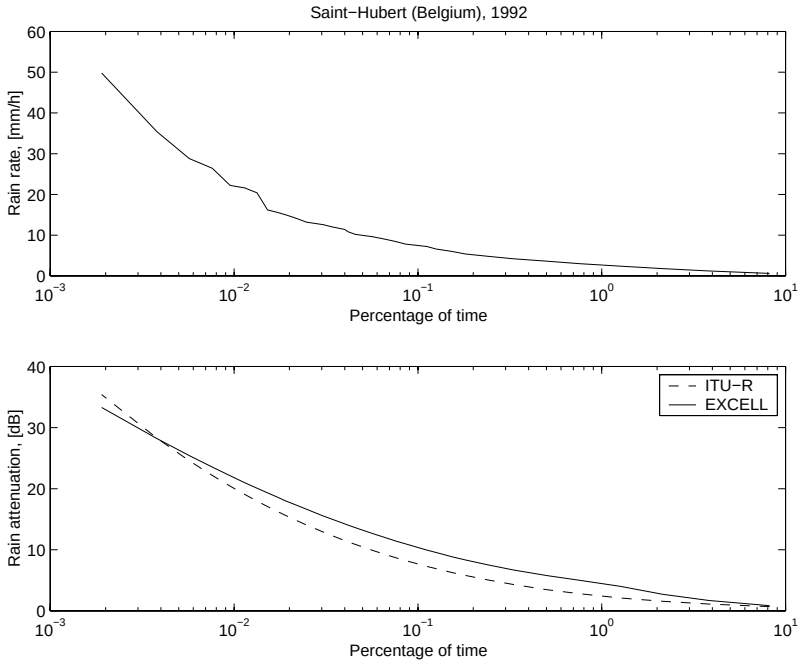

Figure 1.6 *Comparison between ITU-R and EXCELL models of rain attenuation statistics for a given distribution of rain rate*

The rainfall rate distribution measured in Saint-Hubert (Belgium) in 1992 is represented on the upper graph. The point rainfall intensity exceeded during 0.01 % of time is 21.73 mm/h (the value of $R_{0.01}$ obtained from ITU-R rain climatic zone E is 22 mm/h). On the lower graph, it is observed that both models can really differ by several decibels (3 dB for 0.1 % of time). For percentages of time less than 0.004, the ITU-R is the most pessimistic, while it is the contrary for higher percentages of time.

1.3.4 Attenuation by other hydrometeors

The attenuation by hydrometeors such as hail, sleet, snow and fog is not well known. Several relationships relating fog attenuation to liquid water content are given in [14], but there is no statistical repartition of fog particles during the year. Regarding snow events, no annual cumulative snowfall rate distributions are available. Moreover, it is shown in [15] that the size distribution of snowflakes depends strongly on the snow type.

The influence of the melting layer is also neglected, although recent studies [16] have shown that the resulting attenuation might be significant. However, this attenuation is often accounted for by the empirical models for rain attenuation. These models being built on

measurements, it is indeed difficult to model rain attenuation only, so that many models do not separate the effects of rain and of the melting layer.

For all these reasons, additional hydrometeors will not be considered in this thesis.

1.4 SCINTILLATION

1.4.1 Definition

Tropospheric scintillation consists of rapid fluctuations of the amplitude, phase and angle-of-arrival of radio waves due to small-scale variations of the refractive index. These are caused by temperature, humidity and pressure irregularities, known as tropospheric turbulence. On satellite-earth links, the strongest scintillation generally occurs during the passage of cumulus clouds through the propagation path. Scintillation effects become significant above 10 GHz and increase with higher carrier frequency, lower elevation angle and smaller receiving antenna aperture [17][18].

Note that scintillation is usually defined as a clear-sky effect. The fast fluctuations and scintillation induced during precipitation are often stronger than clear-sky scintillation [19], but they are usually not modelled as scintillation. However, they are often masked by rain attenuation.

1.4.2 Physical and empirical models

1.4.2.1 SHORT-TERM VARIATION

For a fixed link, a turbulence-induced scintillation event is characterised by a stationary period of a few minutes (up to fifteen minutes). Within this period, the scintillation log-amplitude is not symmetrically distributed [20]. However, the log-amplitude distribution is well approximated by a Gaussian distribution [18], the variance of which is the mean scintillation variance σ_χ^2 during the period. The log-amplitude of the received signal affected by scintillation is denoted as $\boldsymbol{r} = 20\,log(r)$, r being the amplitude of the signal envelope. The distribution of $\boldsymbol{r}$ conditional upon σ_χ^2 is thereby given by:

$$T_{\boldsymbol{R}|\sigma_\chi}(\boldsymbol{r}\,|\sigma_\chi) = \frac{1}{\sqrt{2\pi}\,\sigma_\chi} exp(-\frac{\boldsymbol{r}^2}{2\sigma_\chi^2}) \tag{1.40}$$

Assuming a point receiver, the short-term variance σ_χ^2 [dB^2] can be estimated using Tatarskii's theory of wave propagation in a turbulent medium, as illustrated in [17][18]:

$$\sigma_\chi^2 = 42.48\, k^{7/6} \int_{L_1}^{L_2} C_n^2(z)\, z^{5/6} dz \tag{1.41}$$

where

- k [m^{-1}] is the frequency wave number,
- L_1 and L_2 are respectively the bottom and top of the turbulent layer along the path coordinate,
- $C_n^2(z)$ [m$^{-2/3}$] is the varying structure parameter of the refractive index along the thickness of the layer.

For a thin layer, equation (1.41) can be rewritten as:

$$\sigma_\chi^2 = 42.48\, k^{7/6}\, \widehat{C}_n^2\, T\, L^{5/6} \tag{1.42}$$

where

- $\widehat{C}_n^2$ is the mean structure parameter inside the layer,
- $L\ [\mathrm{m}] = \dfrac{2h_t}{\sqrt{\sin^2\vartheta + 2h_t/R_e} + \sin\vartheta} \cong \dfrac{h_t}{\sin\vartheta}$ is the mean location of the turbulent layer according to the path coordinate, related to the mean turbulent layer height h_t and the link elevation angle ϑ,
- $T\ [\mathrm{m}] = L_2 - L_1$ is the layer thickness along the path coordinate ($T << L$ for a thin layer).

Consider now a receiving antenna of effective diameter D_e [m]. This diameter is calculated from antenna real diameter D and efficiency η, as $D_e = D\sqrt{\eta}$. The scintillation variance given by (1.41) or (1.42) must then be multiplied by an averaging factor [21]:

$$G(D_e) = 3.8637\,(x^2+1)^{11/12} \sin\left(\frac{11}{6} a\tan\frac{1}{x}\right) - 7.0835\, x^{5/6} \tag{1.43}$$

with $x = \dfrac{0.0584\, k\, D_e^{\,2}}{L}$.

The major problem in the previous equations is that the determination of the structure parameter of the layer is not straightforward, because it is not easy to relate this parameter to available meteorological elements. Nevertheless, some approaches, such as the UCL method [17][18][22], based on inversion procedures from measured data, allow the extraction of realistic turbulent structures. Anyway, the application of such models to the case of moving satellites generally remains difficult.

1.4.2.2 LONG-TERM STANDARD DEVIATION OF SCINTILLATION

Over long periods of time (at least one month), the average standard deviation of scintillation is predicted by means of several semi-empirical models. All models commonly use as an input parameter the wet part of ground refractivity N_{wet} [ppm], which is a function of relative humidity and temperature. The predicted average long-term standard deviation of the log-amplitude is usually written as [4]:

$$\hat{\sigma}_{\chi} = \sigma_{\chi,ref} \sqrt{\frac{f^{a} G(D_e)}{\sin^{b} \vartheta}} \tag{1.44}$$

where

- f [GHz] is the frequency,
- $\sigma_{\chi,ref}$, a and b depend on the model,
- $G(D_e)$ is the antenna-averaging factor.

1° ITU-R model

Following ITU-R model [2], $a = 7/6$, $b = 2.4$, $G(D_e)$ is given by (1.43), and

$$\begin{aligned} \sigma_{\chi,ref} &= 3.6\,10^{-3} + 10^{-4} N_{wet} \\ N_{wet} &= \frac{22813.78\, U\, e^{17.502 t/(t+240.97)}}{(t+273)^2} \end{aligned} \tag{1.45}$$

where t [°C] is the temperature and U [%] is the ground relative humidity, both averaged over the considered period (month or year).

2° Karasawa model

This model [23] is very similar, with $a = 0.9$, $b = 2.6$, and

$$G(D_e) = \begin{cases} 1.0 - 0.7 \dfrac{D_e}{\sqrt{\lambda L}} & 0 \le \dfrac{D_e}{\sqrt{\lambda L}} \le 1 \\ 0.5 - 0.2 \dfrac{D_e}{\sqrt{\lambda L}} & 1 < \dfrac{D_e}{\sqrt{\lambda L}} \le 2 \\ 0.1 & \dfrac{D_e}{\sqrt{\lambda L}} > 2 \end{cases} \tag{1.46}$$

$$\sigma_{\chi,ref} = 3.42\,10^{-3} + 1.186\,10^{-4}\,N_{wet}$$
$$N_{wet} = \frac{22790\,U\,e^{19.7\,t/(t+273)}}{(t+273)^2} \tag{1.47}$$

3° Ortgies models

Two recent models have been developed by Ortgies [25], yielding the monthly mean value of $ln\ \sigma_\chi^2$ as a function of the monthly mean value of either the temperature t [°C] or N_{wet}:

$$E\{ln\ \sigma_\chi^2\} = ln\left[\sigma_{\chi,ref}^2\ \frac{f^a G(D_e)}{sin^b\ \vartheta}\right] \tag{1.48-a}$$

$$\sigma_{\chi,ref}^2 = e^{0.0462\,\tilde{N}_{wet} - 13.45}$$
$$\sigma_{\chi,ref}^2 = e^{0.0865\,\tilde{t} - 12.5} \tag{1.48-b}$$

Parameters a and b equal 1.01 and 2.4 respectively while $G(D_e)$ is given by (1.43) or (1.46).

It should be added that the average value of the wet part of ground refractivity N_{wet} is normally available from worldwide ECMWF maps, with 1.5° spatial resolution, on a monthly or annual basis (see Figure 1.7, for Europe).

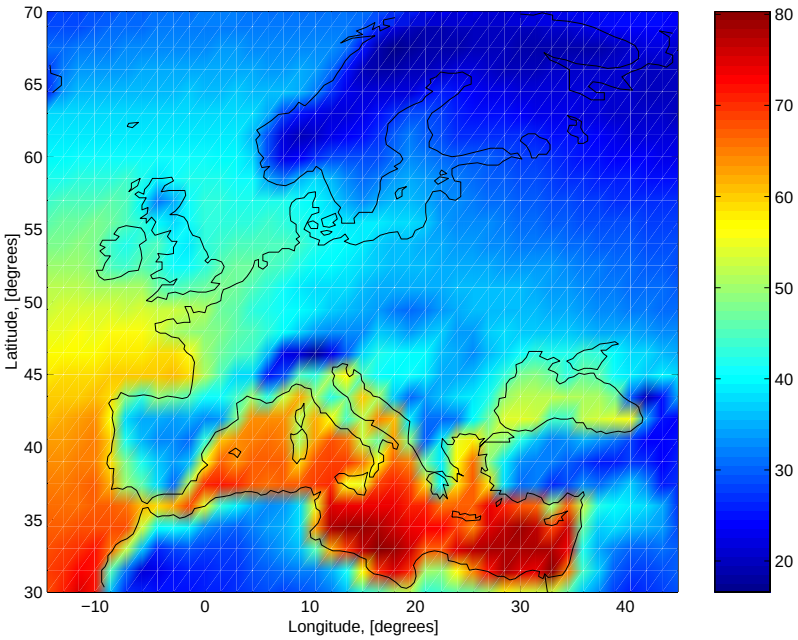

Figure 1.7 *Annual mean N_{wet} values [ppm] in Europe*

1.4.3 Time distribution of the variance of scintillation

Several models allow definition of a probability density function of the long-term standard deviation or variance, the mean values of which have been calculated in the previous section.

Karasawa [23] postulates that the distribution of the standard deviation σ_χ is closely approximated with a gamma distribution:

$$T_{\Sigma_\chi}(\sigma_\chi) = \frac{\beta^\alpha}{\Gamma(\alpha)} \sigma_\chi^{\alpha\text{-}1} \, exp(-\beta \sigma_\chi) \tag{1.49}$$

with $\alpha = 10$ and $\beta = 10/\hat{\sigma}_\chi$.

Mousley & Vilar [24] and Ortgies [25] assume that the long-term variance of scintillation follows a lognormal distribution:

$$T_{\Sigma_\chi^2}(\sigma_\chi^2) = \frac{1}{\sqrt{2\pi}\, s\, \sigma_\chi^2} exp\left[-\frac{(ln\ \sigma_\chi^2 - m)^2}{2 s^2} \right] \tag{1.50}$$

where $m = E\{ln\ \sigma_\chi^2\}$ is given by (1.48) and s = 1.01 [25].

1.4.4 Cumulative time distribution of the signal variation

It has been mentioned in Section 1.4.2.1 that the conditional distribution for short-term log-amplitude is normally taken as Gaussian. Combining this conditional distribution with the probability density function given by (1.49) or (1.50) provides an estimation of the cumulative distribution of the signal log-amplitude.

Karasawa [23] proposes some expressions for the distribution of the log-amplitude variation due to scintillation, based on (1.44), (1.46-47) and (1.49). The resulting fade or enhancement of the signal envelope exceeded during τ% of time can subsequently be calculated

- for signal fading, by:

$$A_{\chi,\tau} = \hat{\sigma}_\chi\ (-0.061\ log^3\ \tau - 0.072\ log^2\ \tau - 1.171\ log\ \tau + 3) \qquad 0.01 \le \tau \le 50 \tag{1.51-a}$$

- for signal enhancement ($\tau' = 100 - \tau$), by:

$$E_{\chi,\tau} = \hat{\sigma}_\chi\ (-0.0597\ log^3\ \tau' - 0.0835\ log^2\ \tau' - 1.258\ log\ \tau' + 2.672) \qquad 50 \le \tau \le 99.99 \tag{1.51-b}$$

where $\hat{\sigma}_\chi$ is given by (1.44-47).

In its recommendation, the ITU-R has adopted only the distribution of signal fades of the Karasawa prediction method.

1.5 COMBINATION OF ATTENUATION EFFECTS

1.5.1 Introduction

The major atmospheric effects have been characterised deterministically (specific attenuation) and statistically (cumulative distribution). At this stage, the question remains of how these attenuation/scintillation phenomena can be combined in order to assess the global attenuation.

With regard to specific meteorological scenarios, it seems quite straightforward to predict the attenuation on a deterministic basis, the occurrence of phenomena being fixed by the scenario. In contrast, the statistical annual or monthly distribution of the total attenuation depends on the correlation between the various mechanisms.

In a first part, the present section reviews the mathematical methods of combination, which serve as a basis for propagation predictions. Two propagation-oriented combination methods are described in a second part: the ITU-R method and the recent Castanet-Lemorton method.

1.5.2 Mathematical background for combination of phenomena

1.5.2.1 EQUIPROBABILITY SUMMING

When two mechanisms are fully correlated, the attenuation levels exceeded for a given percentage of time simply add together. The total attenuation $\boldsymbol{A}_\tau$ [dB] exceeded during τ% of time is thereby given by:

$$\boldsymbol{A}_\tau = \boldsymbol{A}_{1,\tau} + \boldsymbol{A}_{2,\tau} \tag{1.52}$$

In reality, mechanisms are seldom fully correlated. Equiprobability summing may therefore be looked on as a worst-case approximation of the total impairment.

1.5.2.2 CONVOLUTION METHOD

Consider now that two mechanisms are statistically independent. The cumulative distribution of the total attenuation $\boldsymbol{A} = \boldsymbol{A}_1 + \boldsymbol{A}_2$ is then described by a convolution:

$$P(\boldsymbol{A}) = \int_{-\infty}^{\boldsymbol{A}} T_{\boldsymbol{A_1}}(\boldsymbol{A_1})\, P_{\boldsymbol{A_2}}(\boldsymbol{A} - \boldsymbol{A_1})\, d\boldsymbol{A_1} \tag{1.53}$$

where

- $T_{\boldsymbol{A_1}}(\boldsymbol{A_1})$ is the probability density function of $\boldsymbol{A_1}$,
- $P_{\boldsymbol{A_2}}(\boldsymbol{A_2})$ is the cumulative distribution of $\boldsymbol{A_2}$.

This method is particularly suited when considering the combination between atmospheric effects and non-atmospheric mechanisms, such as building shadowing.

1.5.2.3 DISJOINT SUMMING

In the case of disjoint phenomena, the cumulative distributions of attenuation are combined by summing the probabilities for given attenuation levels, so that the cumulative distribution of the global attenuation is obtained by:

$$P(\boldsymbol{A} > \boldsymbol{A}^*) = P(\boldsymbol{A_1} > \boldsymbol{A}^*) + P(\boldsymbol{A_2} > \boldsymbol{A}^*) \tag{1.54}$$

Disjoint summing is for instance used when attenuation effects are estimated separately for rainy and non-rainy conditions.

1.5.2.4 SQUARE-ROOT-SUM COMBINATION

Another method for combining attenuation effects is to use the square-root-sum method:

$$\boldsymbol{A}_\tau = \sqrt{\boldsymbol{A}_{1,\tau}{}^2 + \boldsymbol{A}_{2,\tau}{}^2} \tag{1.55}$$

Quite evidently, (1.55) gives a smaller combined level than (1.52) at same percentages of time. The major drawback of this method is the absence of physical basis.

1.5.2.5 COHERENT SUMMING

When time series of attenuation values $\boldsymbol{A}_i(t)$ are calculated for N different mechanisms ($1 \le i \le N$), the total attenuation on the path is given by:

$$A(t) = \sum_{i=1}^{N} A_i(t) \tag{1.56}$$

The latter assumes naturally that all effects are coherent. The use of (1.56) is however limited to the production of time series in given meteorological scenarios. Its extension to the prediction of long-term attenuation statistics is actually quite difficult, owing to the lack of all the necessary input data.

Equation (1.56) concerns slant-path attenuation only. Scintillation should be accounted for by considering that the short-term log-amplitude of scintillation is Gaussian-distributed around the mean attenuation level.

1.5.3 Propagation methods of combination

1.5.3.1 ITU-R METHOD

Following ITU-R Rec. 618-5 [2], the attenuation exceeded during τ % time, which results from the combination of rain and cloud attenuation with scintillation, is given by:

$$A_{rc\chi,\tau} = \sqrt{\left[A_{r,\tau} + A_{c,\tau}\right]^2 + A_{\chi,\tau}^{\ 2}} \tag{1.57}$$

The equiprobability summing of rain and cloud attenuation might cause a slight overestimation, but the latter is compensated by use of the square-root-sum method to add the scintillation effect.

Even if not explicitly indicated in the recommendation, the total attenuation is obtained by considering an equiprobability combination between (1.57) and the gaseous attenuation:

$$A_{tot,\tau} = A_{rc\chi,\tau} + A_o + A_{w,\tau} \tag{1.58}$$

1.5.3.2 CASTANET-LEMORTON METHOD

The combination method proposed by Castanet-Lemorton [26] is based on the assumption that water vapour absorption, cloud attenuation and fade scintillation are correlated. The

resulting distribution is then combined with the distribution of rain attenuation using the square-root-sum method. Finally, oxygen attenuation is simply added on an equiprobable basis. The whole approach is summarised by the following equation:

$$A_{tot,\tau} = A_o + \sqrt{\left[A_{w,\tau} + A_{c,\tau} + A_{\chi,\tau}\right]^2 + A_{r,\tau}{}^2} \tag{1.59}$$

On one hand, the use of the square-root-sum method yields a slight underestimation of the total attenuation. On the other hand, the scintillation fading is added on an equiprobable basis, although scintillation also causes enhancement in the signal level. This last approximation overestimates the global attenuation and compensates for the previous underestimation.

1.6 HOW TO ACCOUNT FOR THE SPECIFICITY OF NON-GEOSTATIONARY ORBIT SYSTEMS

1.6.1 Introduction

Tropospheric models assume a fixed link between a geostationary satellite and an earth station.

The fact is that satellite personal communication systems are usually transportable, meaning that they can be installed everywhere. Meanwhile, many of them – this thesis is restricted to these – are based on a network of low earth-orbit satellites. As a consequence, the link cannot be considered as fixed anymore, but should be looked on as a multi-site multi-satellite configuration. The models must therefore be applied in such a fashion that they are able to account for this significant difference.

Two methods are presented hereafter. The first one (Section 1.6.2) is purely statistical and calculates the long-term annual or monthly distribution of attenuation. A second approach relies upon deterministic time-series simulations in realistic meteorological scenarios. The major problem, however, is finding a single source for all the necessary input data in generating the time series. Furthermore, the temporal structural variation of any atmospheric event is rarely known. Nevertheless, several assumptions can be made in view of preliminary results. These are detailed in Section 1.6.3.

1.6.2 Statistical modelling

In order to take into account the varying elevation angle ϑ when establishing attenuation statistics, the probability density function of the elevation angle must be introduced. With the aim of characterising non-geostationary orbit systems, a software package has been developed, which is detailed in Appendix B. The package, referred to as an *orbit generator*, simulates any satellite constellation motion around the earth.

The distribution $T_\Theta(\vartheta)$ of elevation angle can thereby be inferred anywhere on earth as soon as the satellite selection strategy is known. This issue is discussed in further detail in Chapter 3. In the case of the statistical long-term average, it is simply postulated that the terrestrial receiver is always connected to the satellite that is seen with the highest elevation angle.

For example, Figure 1.8 depicts the statistical distribution of maximum elevation angle for Teledesic constellation (288 satellites with worldwide coverage), as seen from several latitudes.

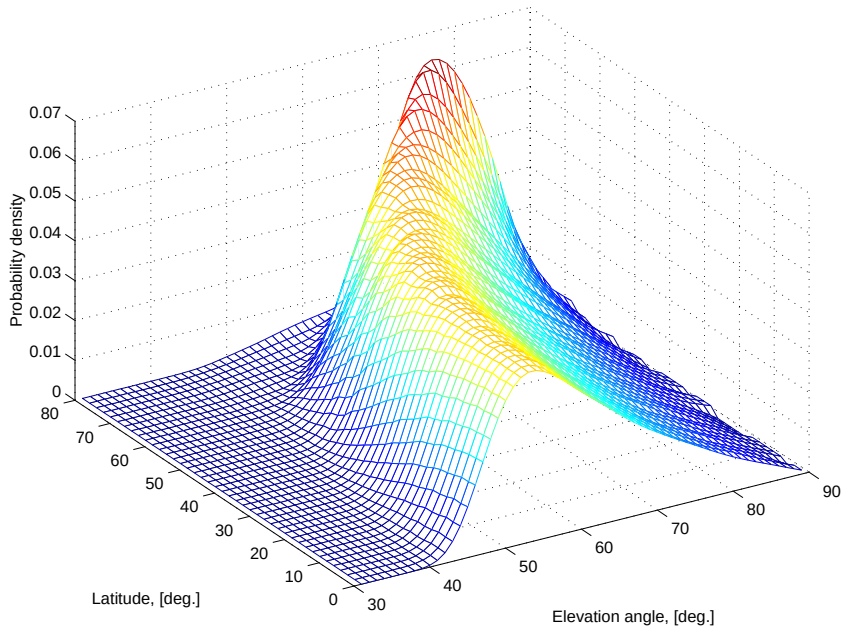

Figure 1.8 *Distribution of maximum elevation angle (Teledesic constellation) as a function of latitude*

In the case of Teledesic, it is observed that the lower limit on the elevation angle is very high, going from 40° up to 50°. On average, the elevation angle increases with higher latitude, being thus minimum at 0° latitude. At the equator, the spacing between orbital planes indeed reaches its largest value, causing the mean elevation angle to be smaller. Note that analytical expressions of $T_\Theta(\vartheta)$ will be discussed in Chapter 2 for several LEO constellations.

Assume thus that $T_\Theta(\vartheta)$ is known at any point on earth. The ultimate goal is either the estimation of availability (at a given outage percentage) over an extended region, or the calculation of the cumulative distribution of attenuation in a reduced number of terrestrial locations.

The statistical models of attenuation yield relationships for the attenuation level exceeded during a given percentage of time τ, conditional upon the elevation angle ϑ. This fade level is denoted as $\boldsymbol{A}_{\xi,\tau}(\vartheta)$, ξ standing for individual or combined mechanisms (gas, cloud, rain, scintillation or any combination). It should be observed that values of $\boldsymbol{A}_{\xi,\tau}(\vartheta)$ for all percentiles τ implicitly form the cumulative distribution of the attenuation conditional upon

the elevation angle, $P_{A_\xi|\Theta}(A_\xi \mid \vartheta)$. Hence, the long-term distribution of attenuation accounting for the varying elevation angle is easily obtained by:

$$P_{A_\xi}(A_\xi) = \int_0^{\pi/2} P_{A_\xi|\Theta}(A_\xi \mid \vartheta)\, T_\Theta(\vartheta)\, d\vartheta \tag{1.60}$$

Numerically, the following procedure can be applied [4]:

(i) determine the distribution of elevation angle at a given point on the globe,

(ii) calculate the cumulative distribution of attenuation for each elevation angle increment,

(iii) for every elevation angle, calculate the percentage of time during which each fade level is exceeded (product of the probability to have this elevation angle by the percentage of time during which this conditional fade level is exceeded),

(iv) for all fade levels, sum the percentages obtained in (iii),

(v) finally, determine from (iv) the attenuation $A_{\xi,\tau}$, exceeded during the desired outage percentage.

1.6.3 Time series model

1.6.3.1 A MODELLING PROBLEM

The classical approach, based on a statistical description of both the atmospheric effects and the variation of elevation angle, only provides the long-term attenuation with respect to a percentage of exceeded time. Although very useful in the primary design of a system, it is not the most significant indicator of the dynamic behaviour of the tropospheric channel. For instance, various system procedures, such as fade mitigation and satellite diversity, are not easily optimised by means of a pure statistical model, because they strongly depend on the dynamics of tropospheric mechanisms. Moreover, considering a LEO constellation, the satellites move continuously with respect to the earth, so an additional dynamic variation must be taken into account. Therefore, statistical prediction methods are suitably completed by deterministic predictions based on time series, which inherently consider the complex correlation between fade dynamics and satellite motion.

Ideally, measured time series of tropospheric events should be used. However, due to the lack of available data, time series must be simulated. Obviously, such simulations require modelling of the simultaneous spatial distribution of rain cells and clouds. This issue

constitutes the most difficult problem of a time series approach. The present section details the answers and assumptions that allow the problem to be tackled.

Assume first that the attenuation from all tropospheric effects is known at a given time for a given link. Then, the total attenuation is simply obtained by coherent summing, as described by (1.56).

Among the tropospheric effects, rain attenuation is certainly the dominant one, and fortunately, the best known. Moreover, some recent physical models, such as EXCELL, have introduced an objective description of rain cells based on their spatial distribution. What is the situation regarding other mechanisms? On one hand, the gaseous attenuation is almost a static effect with very slow variations (see Section 1.2). Hence, equations (1.3-8), with constant parameters, are valid during the whole duration of short periods (i.e. up to several hours). On the other hand, the impact of clouds (attenuation and scintillation) is hardly modelled in a dynamic fashion, due to the large variety of cloud types. Sections 1.3.2.1 and 1.4.2.1 presented physical models for cloud attenuation and scintillation. They are however highly dependent on the nature of the clouds. Therefore, assumptions are needed.

Finally, a basic concept must be introduced. Meteorological mechanisms and models are indeed commonly characterised by a temporal variation. If a multi-satellite scenario is considered, the spatial distribution of clouds and rain cells also matters crucially. Sometimes, meteorological information is available, so that maps defining the location of meteorological events can be produced. If not, the key point is to look on the temporal distribution of tropospheric events at one specific location as an equivalent spatial distribution around this location. That means that the spatial distribution of rain cells, clouds and turbulent zones is based on the temporal distribution of the resulting attenuation/scintillation. This is certainly appropriate for EXCELL rain cells, since the model has been built on radar measurements of the spatial distribution of cells. The application of this concept to scintillation is more questionable, but seems at least reasonable in a preliminary analysis, e.g. because of the Taylor hypothesis of frozen turbulence, that seems to work properly [18].

1.6.3.2 SHORT-TERM EFFECTS OF HYDROMETEORS

1° Rain attenuation

Time series modelling is obtained as soon as the rain events are described in shape and dimension as well as by their distribution in space and structural evolution in time.

Rain events are usually represented by cylindrical moving cells. Their characteristics are for example given by EXCELL representation. Remember that the latter allows the rain rate at distance ρ from the centre of the cell to be obtained, using:

$$R(\rho) = R_M \, exp(-\rho / \rho_0) \tag{1.30}$$

where R_M is the peak intensity and ρ_0 is referred to as the cell radius. The height of the cylindrical cells is given by the usual ITU-R rain height h_r (1.22). The structural evolution of cells with time is neglected during short-term periods, since no information is easily available.

A canonical scenario is defined by choosing a given site and peak intensity R^*. The value R^* is chosen such that it is several times greater than the maximum measured rain rate. It is constituted by placing rain cells described by $\{R_M < R^*, \rho_0\}$ within a given area, according to the spatial distribution (1.31). Note that a similar procedure, based on the Awaka cell model [27], has been recently presented in [28], in order to visualise rain rate fields.

The cells are assumed to move under the effect of a constant wind, the direction of which must be specified. However, their structure is assumed to be frozen in time.

Considering now transmission between a satellite and a receiver located inside the rainy area, the total rain attenuation (including the rain debris) is given by:

$$\boldsymbol{A_r} = \sum_{cells} \int_{path\ L_s} \left[\gamma_r + K 4^{\alpha} \right] dl \tag{1.61}$$

where γ_r is the specific ITU-R rain attenuation (1.20), K and α are the ITU-R parameters (1.21), and the rain rate of 4 mm/h is that in the rain debris (1.36).

Instead of starting from the EXCELL spatial distribution, a real meteorological map can be converted into the EXCELL formalism, and used as a canonical scenario [29]. Such a map[†] is depicted in Figure 1.9. The rain zones are clearly noticeable above Scandinavia and the Balkan states.

Once the map is converted into effective rain cells, the total rain attenuation is obviously calculated by (1.61).

[†] The author would like to thank the *Dipartemento di Elettronica e Informazione*, *Politecnico di Milano* (Italy), for providing the meteorological map and its conversion into rain cells.

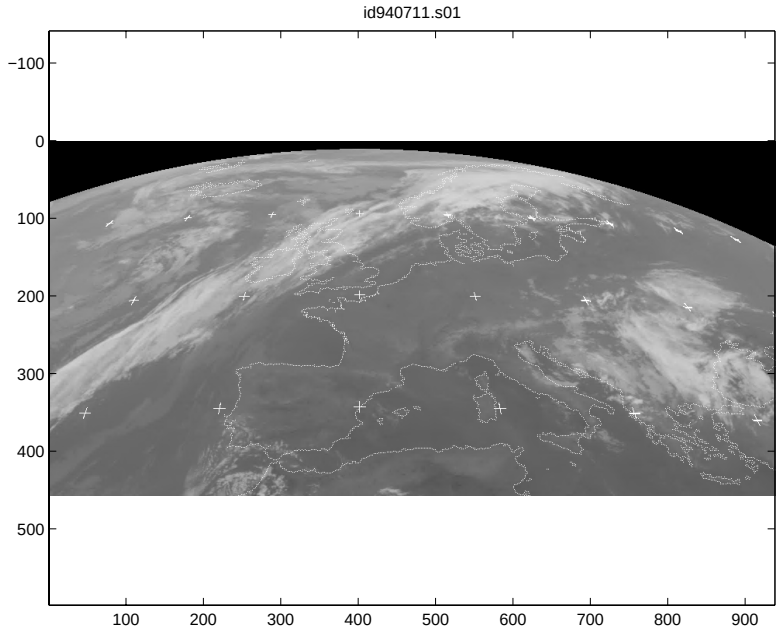

Figure 1.9 *Real meteorological map (recorded July 11th, 1994)*

2° Cloud attenuation

If the position and type of all clouds are known at a given time above a given place, the attenuation is simply calculated by using (1.13-14). As mentioned earlier, that implies at once to determine:

- the characteristics of each type of cloud
- the spatial distribution of clouds.

Regarding the characterisation of clouds, stratiform horizontal structures (horizontal extent of some 10 km) are described by the Salonen-Uppala model (1.12), which allows evaluation of the liquid water content as a function of temperature and height from cloud base. Other clouds, such as cumulus and cumulonimbus, can only be characterised by average values for the vertical/horizontal extent and liquid water content (see Table 1.1, DAH model).

As far as the spatial distribution of clouds is concerned, information is very rare. In the simulations to be carried out, it is assumed that a cumulus/cumulonimbus is placed above each rain cell (or group of rain cells). That seems to be a realistic assumption. In clear-sky conditions, the percentage of cloud coverage is used in order to simulate uniformly spread stratiform clouds in the percentage of covered sky.

1.6.3.3 SHORT-TERM SIMULATION OF SCINTILLATION

Section 1.4 has described a physical model for short-term scintillation variance [17][18]. For a thin layer, equation (1.42) could be used in order to evaluate the scintillation variance. However, it does require the knowledge of the mean structure parameter, the determination of which is not really easy. That explains why another simple procedure is proposed in the following.

Assume that each cloud represents a turbulent zone. Following the Karasawa or Ortgies models, a monthly mean value of σ_χ or $ln\,\sigma_\chi^2$ can be calculated at each time step as a function of the average temperature and/or N_{wet}, the antenna diameter and the elevation angle. Meanwhile, time distributions are also given by (1.49-50) as a function of the mentioned mean value. If this monthly time distribution is considered as a spatial distribution, each turbulent zone associated with a cloud can be assigned a random value of σ_χ according to the mentioned distribution. A zero-mean random scintillation signal is then built using the Gaussian property of the short-term scintillation during the time interval. This signal is finally superimposed on the attenuated signal.

This procedure is obviously too simplistic, notably because it relies on the first-order statistics only. Moreover, the passage from long-term statistics to short-term results might really be questionable. Anyway, it relies on observable parameters while it still integrates the impact of the elevation angle on the scintillation variance.

1.6.3.4 RETURNING FROM SHORT-TERM TO LONG-TERM PREDICTIONS

As a conclusion to this section, a few words introduce a possible new prediction method that might integrate time series simulations and long-term predictions.

Let us consider that the only dynamic effect is produced by the passage of rain cells in a multi-satellite environment. For any location on earth, it is possible [4] to know the percentage of rainy periods, denoted as μ_R [%]. During (100 – μ_R) % of annual time, the meteorological configuration is assumed to be a slowly varying clear-sky situation, so that a quasi-static analysis holds.

Regarding the μ_R % of rainy time, an iterative procedure is applied in a limited area (e.g. 5° x 5°), in the centre of which a receiver is assumed to be located.

(i) From the local rain rate distribution $P(R)$, a spatial distribution of rain cells is inferred by (1.31-32), so that a canonical map of rain cells is built according to EXCELL model.

(ii) For this scenario, a short-term simulation is run over a geosynchronous period of the orbit, using the orbit generator and considering that rain cells remain in the same place during the complete simulation period (i.e. assuming that there is no wind).

(iii) Given the simulation results, the short-term availability and any characteristic parameter, such as the satellite dwell time, can be computed.

(iv) The local rain rate is finally calculated and associated to a given percentage of time based on the rain rate distribution.

If this procedure is run a sufficient number of times, the average of all short-term availability values yields an estimation of the long-term performance during rainy periods. The latter is then suitably combined with the clear-sky performance in order to provide the global long-term performance. However, this estimated performance now accounts for all system procedures such as fade mitigation, satellite handover and diversity. The necessary number of simulations is reached when all possible values of the local rain rate are covered with the desired precision.

1.7 SUMMARY

In this chapter, useful existing models of tropospheric propagation have been reviewed. Several mechanisms have therefore been modelled from both deterministic and statistical points of view. They are listed below, together with the corresponding models.

(i) Oxygen attenuation: ITU-R Rec.672-2 or Liebe model – MPM.

(ii) Water vapour attenuation: ITU-R Rec. 672-2 or Liebe model – MPM (specific attenuation), Liebe-Salonen model (statistical distribution).

(iii) Cloud attenuation: ITU-R Rec. 840-1 (Liebe model for specific attenuation, Salonen-Uppala model for statistical distribution).

(iv) Rain attenuation: ITU-R Rec. 838 (specific attenuation), ITU-R Rec. 618-5 or EXCELL model (statistical distribution).

(v) Scintillation: UCL model (short-term standard deviation), ITU-R Rec. 618-5, Karasawa or Ortgies model (long-term standard deviation, time distribution).

A specific section has been dedicated to the combination of attenuation effects, and two methods for combining attenuation CDF's have been presented: ITU-R Rec. 618-5 and Castanet-Lemorton model.

The modelling approach has been applied to the case of non-geostationary satellites. Therefore, a statistical method and a deterministic time series approach have been discussed. The time series based modelling will allow dynamic considerations, such as the design of fade mitigation techniques (see Chapter 3).

Finally, first steps towards a new prediction method, which might use time series simulations in view of long-term statistical predictions, have been introduced.

1.8 REFERENCES

[1] BRUSSAARD, G, WATSON, P.A., *Atmospheric modelling and millimetre wave propagation*, Chapman & Hall, London, 1995.

[2] ITU-R, *ITU-R Recommendations – Propagation in non-ionized media,* PN series vol., ITU, Geneva, 1997.

[3] ITU-R, *ITU-R Recommendations – Propagation in non-ionized media,* PN series vol., ITU, Geneva, 1999.

[4] COST 255, *Radiowave propagation modelling for new SatCom services at Ku band and above*, European Commission, Brussels, to be published.

[5] LIEBE, H., MPM – An atmospheric millimetre wave propagation model, *Int. J. Infrared Millimeter Waves,* vol. 10, n° 6, pp. 631-650, 1989.

[6] SALONEN, E., Prediction models of atmospheric gases and clouds for slant path attenuation, Olympus Utilisation Conference (Sevilla, Spain), pp. 615-622, 1993.

[7] KYLE, T.G, *Atmospheric transmission, emission and scattering*, Pergamon Press, Oxford, 1991.

[8] DISSANAYAKE A., ALLNUT, J, HAIDARA, F., A prediction model that combines rain attenuation and other propagation impairments along earth-satellite paths, *IEEE Trans. Antennas Propagat.,* vol. 45, n° 10, pp. 1546-1558, 1997.

[9] SALONEN, E., UPPALA, S., New prediction method of cloud attenuation, *Electronics Letters*, vol. 27, n° 12, pp. 1106-1108, 1991.

[10] LIEBE, H., MANABE, T., HUFFORD, G.A., Millimeter-wave attenuation and delay rates due to fog/cloud conditions, *IEEE Trans. Antennas Propagat.,* vol. 37, n° 12, pp. 1617-1623, 1989.

[11] MAYER, C.E., JAEGER, B.E., Rain attenuation model comparison and validation, 6th Ka band Utilization Conference (Cleveland, U.S.A.), pp. 35-42, June 2000.

[12] CAPSONI, C., FEDI, F., PARABONI, A., A comprehensive meteorologically oriented methodology for the prediction of wave propagation parameters in telecommunication applications beyond 10 GHz, *Radio Sci.,* vol. 22, n° 3, pp. 387-393, 1987.

[13] CAPSONI, C., FEDI, F., MAGISTRONI, C., PARABONI, A., PAWLINA, A., Data and theory for a new model of the horizontal structure of rain cells for propagation applications, *Radio Sci.,* vol. 22, n° 3, pp. 395-404, 1987.

[14] VASSEUR, H, GIBBINS, C., Inference of fog characteristics from attenuation measurements art millimeter and optical wavelengths, *Radio Sci.,* vol. 31, n° 5, pp. 1089-1097, 1996.

[15] VASSEUR, H, OESTGES, C., VANDER VORST, A., Influence de la troposphère sur les liaisns sans fil aux ondes millimétriques et optiques: étude comparative, 3èmes journées

d'études sur la propagation électromagnétique dans l'atmosphère: du décamétrique à l'Angström, (Rennes, France), pp. 58-63, 1997.

[16] RAYNAUD, L. *Modélisation électromagnétique de la propagation des ondes radioélectriques dans la couche de fusion des précipitations*, PhD thesis, Université Paul Sabatier – Toulouse, 1999.

[17] VASSEUR, H., *Bandwidth limitations on millimetre-wave communications due to tropospheric clear-air phenomena*, PhD thesis, Université catholique de Louvain, 1995.

[18] VANHOENACKER, D., *Modèle radioélectrique pour la scintillation observée aux hyperfréquences sur une liaison satellite-terre*, PhD thesis, Université catholique de Louvain, 1987.

[19] MATRICCIANI, E, MAURI, M., RIVA, C., Scintillation and simultaneous rain attenuation at 12.5 GHz to satellite Olympus, *Radio Sci.,* vol. 32, n° 5, pp. 1861-1866, 1997.

[20] VAN DE KAMP, M.M.J.L., Asymmetrical signal level distribution due to tropospheric scintillation, *Electronics Letters*, vol. 34, n° 11, pp. 1145-1146, 1998.

[21] HADDON, H., VILAR, E., Scattering-induced microwave scintillation from clear air and rain on earth space paths and the influence of the antenna aperture, *IEEE Trans. Antennas Propagat.,* vol. 34, n° 5, pp. 646-657, 1986.

[22] VANHOENACKER, D., Impact of atmospheric turbulences on earth-space propagation, Olympus Utilisation Conference, ESA WPP-60 (Sevilla, Spain), pp. 509-514, 1993.

[23] KARASAWA, Y., YAMADA, M., ALLNUTT, J.E., A new prediction method for tropospheric scintillation on earth-space paths, *IEEE Trans. Antennas Propagat.,* vol. 36, n° 11, pp. 1608-1614, 1988.

[24] MOUSLEY, T.J., VILAR, E., Experimental and theoretical statistics of microwave amplitude scintillations on satellite down-links, *IEEE Trans. Antennas Propagat.,* vol. 30, n° 6, pp. 1099-1106, 1982.

[25] ORTGIES, G., Prediction of slant-path amplitude scintillation from meteorological parameters, Proc. Int. Symp. on Radio Propagation, (Beijing, China), pp. 218-221, 1993.

[26] CASTANET, L., LEMORTON, J., KONEFAL, T., SHUKLA, A.K., WATSON, P.A., WRENCH, C.L., Comparison of various methods for combining propagation effects and predicting loss in low-availability systems in the 20 GHz to 50 GHz frequency range, *Int. J. Sat. Comm.,* to be published, 2000.

[27] AWAKA, J., A three-dimensional rain cell model for the study of interference due to hydrometeor scattering, *J. Commun. Res. Lab.*, vol. 36, n° 147, pp. 13-44, 1989.

[28] GOLDHIRSH, J., Two-dimensional visualization of rain cell structures, *Radio Sci*., vol. 35, n° 3, pp. 713-729, 2000.

[29] OESTGES, C., MAUFROID, X., VANHOENACKER-JANVIER, D., Performance simulation of a Ka band multimedia LEO satellite system, 6th Ka Band Utilization Conference (Cleveland, U.S.A.), pp. 605-612, June 2000.

CHAPTER 2 NEW PROPAGATION MODELS FOR TRANSMISSION IN BUILT-UP AREAS

2.1 INTRODUCTION

Having discussed the way tropospheric mechanisms affect earth-satellite propagation, this chapter deals principally with propagation between low earth-orbit satellites and terminals located at street level and surrounded by buildings. Two new models are proposed in the following: a deterministic *ray-tracing* tool and an innovative approach based on a *physical-statistical* concept.

Within built-up areas, *shadowing* by buildings and obstacles, as well as *multipath* mechanisms resulting from the scattering environment, produce strong performance degradations. One point worth clarifying at once is that the term *built-up areas* is somewhat ambiguous, in the sense that it amalgamates a large number of different environments. Generally, in propagation studies for mobile radio, a qualitative description of the area is employed, based on terms such as *rural*, *suburban* and *urban*. *Urban* areas are defined as being dominated by high buildings, office blocks and other commercial stores while the

denomination *suburban* is related to residential houses, parks and gardens. *Rural* areas comprise open farmlands with sparse buildings, woodland and forests.

Since this qualitative description is open to different interpretations by different users, there is an obvious need for:

- describing the environments quantitatively, for example in terms of building height and density,
- developing models that allow to account for this quantitative description.

In modelling any land mobile propagation parameter, the aims are broadly similar [1][2]. The ultimate goal is the prediction of any relevant parameter with maximum accuracy, consistent with minimum cost in terms of the quantity and expense of the input data and in terms of the computational effort required to produce the prediction (Figure 2.1).

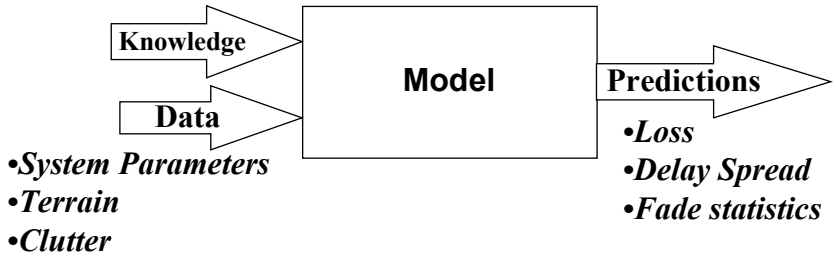

Figure 2.1 *A generic propagation model*

In empirical (Figure 2.2) and pure statistical modelling approaches (e.g. [3][4][5][6]), the input knowledge consists almost entirely of previous measurements which have been made in environments judged to be representative of common areas. An approximation to this data, usually consisting of a curve-fit to the measurements, is used as prediction model. The input data is fairly simple, consisting primarily of operating frequency, elevation angle and a qualitative description of the environment (e.g. rural, urban). Predictions are easy to compute and have good accuracy within the parameter ranges spanned by the original measurements.

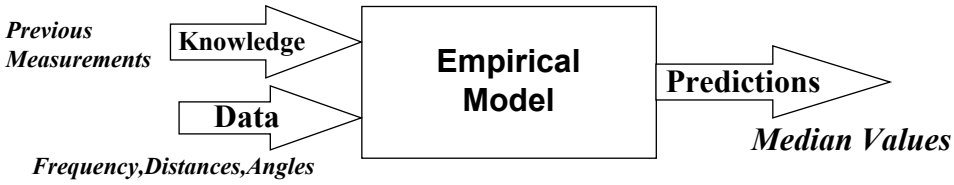

Figure 2.2 *An empirical propagation model*

However, since the models lack a physical basis, they are usually very poor at extrapolating outside these parameter ranges. As mentioned earlier, there is also a classification problem involved in describing the environment, since an environment judged to be dense urban in some countries may be little more than a small town elsewhere. Additionally, the use of a curve-fitting approach implies that the real data will generally be considerably scattered around the predicted values and this represents a lower limit on the prediction error.

The input knowledge used in deterministic physical models [7], by contrast, consists of electromagnetic theory combined with engineering expertise that allows to make reasonable assumptions about which propagation modes are significant in a given situation (Figure 2.3). Provided that the correct modes are identified, the theoretical approach is capable of making very accurate predictions of a wide range of parameters in a deterministic manner. The output is specific to particular locations rather than being an average value, so the model can apply to very wide ranges of system and environment parameters, certainly well beyond the range within which measurements have been made. These models are necessarily more time consuming, but are also more revealing concerning physical details. In order to make such predictions, however, the models may require very precise input data concerning the geometrical and electrical properties of the environment. This may be expensive or even impossible to obtain with sufficient accuracy. Also, the computations required for a full theoretical calculation are sometimes prohibitive, so extra assumptions have to be made for simplification, leading to compromised accuracy.

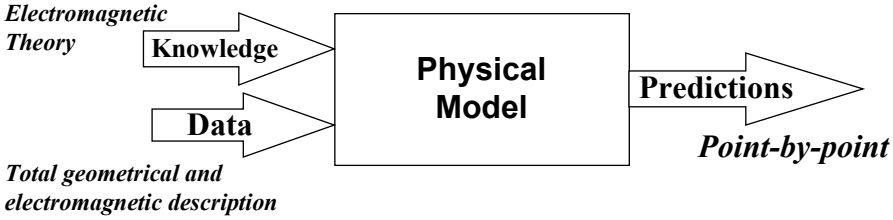

Figure 2.3 *A deterministic physical propagation model*

Chapter 2 is divided in two main sections. In Section 2.2, a deterministic physical model based on ray-tracing is established. Several physical mechanisms, such as reflection, diffraction and scattering are modelled and experimental validations are presented. Section 2.3 introduces an innovative modelling approach, referred to as physical-statistical model, which combines advantages of both statistical and physical methods at a very low computational cost. Again, the basic concept, applications and comparisons with measurements are described.

2.2 PHYSICAL MODELLING

2.2.1 Introduction

For several reasons detailed above, a propagation tool may need to be deterministic in some way. Any deterministic approach in mobile propagation should in theory:

- be three-dimensional, because several significant interactions are not included in 2-D models;
- be computationally efficient, the tool being required to make area coverage predictions,
- have a wideband capability, in order to estimate multipath effects on high-rate digital transmissions.

Deterministic predictions are always based on a precise description of the area, by means of terrain, building and/or vegetation databases. Hence, various procedures can be considered. Full-wave parabolic and integral equation models have been used for several years to model refraction and diffraction by the troposphere and terrain. An alternative solution consists of ray methods, which have been widely applied to the mobile terrestrial channel [8][9][10]. In such techniques, the electromagnetic mechanisms are described by extensions of geometrical optics. Therefore, the ray approximation holds as long as the wavelength is small compared to the size of obstacles. In the field of mobile terrestrial communications, ray-tracing relies on the determination of all ray paths connecting the base station and a receiver, taking into account all relevant propagation mechanisms. The parameters of interest (e.g. the field strength or the transfer function) are then calculated by a suitable combination of the rays. The major difficulty lies in the implementation of an efficient algorithm for finding the ray paths.

The physical model detailed in the following is built on a ray-tracing technique applied to the mobile satellite channel. Methods and algorithms are briefly described in Section 2.2.2. Several simplifications, which result directly from the fact that one point of the link is now a satellite, are pointed out. Sections 2.2.3 to 2.2.5 outline the electromagnetic parameters and models that are involved in the propagation mechanisms. Finally, a comparison with experimental results at 12.5 and 30 GHz is presented in Section 2.2.6.

2.2.2 The ray-tracing method

Consider that a satellite radiowave is incident upon a built-up area. The ray-tracing tool is based on the assumption that the built-up area is composed of parallelepipeds with plane

faces. Any block is homogeneous and represents either a building or a slab of vegetation. Lateral faces do not need to be orthogonal, but rooftop and basement as well as the ground surface are assumed to be horizontal.

The basic problem consists in the calculation of the electric field received at the mobile terminal in amplitude, phase and polarisation. This field, regarded as a complex vector, results from the combination of the direct component with several contributions due to specular reflection, diffraction and scattering as well as multiple combinations of these mechanisms. Specular reflection occurs when a propagating electromagnetic wave impinges upon a plane surface with dimensions very large compared to the wavelength. Diffraction appears when the path between the transmitter and the receiver is obstructed by a discontinuity, such as an edge, wedge or cylinder. Finally, scattering is caused by interactions of the wave with objects, the dimensions of which are on the order of the wavelength, e.g. foliage or rough obstacles. Each of these contributions endures the free-space loss but may also be attenuated owing to the penetration through buildings and/or trees.

The satellite signal is modelled as a spherical wave ray tube. However, due to the large distance from satellite to earth, this spherical wavefront is well approximated locally by a plane wave. In addition to the free-space loss, each ray is affected by the amplitude reduction and phase shift caused by the interaction. This complex vector field is then weighted by the receiver antenna gain. A scalar complex field is finally obtained along the receiving antenna polarisation. Mathematically, any single contribution at receiving point P is therefore expressed as:

$$E_m(P) = [\overline{g}_m^R]^* \cdot \overline{\overline{T}}_m \cdot \overline{E}_0 \; K(s,s') \, e^{-jks} \; K_m(s,s') \, e^{-jks'} \tag{2.1}$$

where

- $\overline{E}_0$ [V m^{-1}] is the emitted field (vector),
- k [m^{-1}] is the wave number,
- s [m] is the path length from the satellite to the obstacle,
- s' [m] is the path length from the obstacle to the receiver,
- $K(s,s')$ and $K_m(s,s')$ are respectively the free-space satellite-to-obstacle and obstacle-to-receiver spreading factors (accounting for extra attenuation as well),
- $\overline{\overline{T}}_m$ is a dyadic coefficient modelling the electromagnetic mechanism responsible for the considered contribution,

- $\overline{g}_m^R = g_m^R \ \overline{p}^R$ is a complex vector accounting for the receiving antenna polarisation $\overline{p}^R$ and the amplitude gain g_m^R in the direction of the incoming wave (the symbol {*} designates the complex conjugate) [11].

Multiple contributions are easily expressed in the same way as equation (2.1). Assume, for instance, that a double contribution is caused consecutively by interactions *m* then *n*, as shown in Figure 2.4.

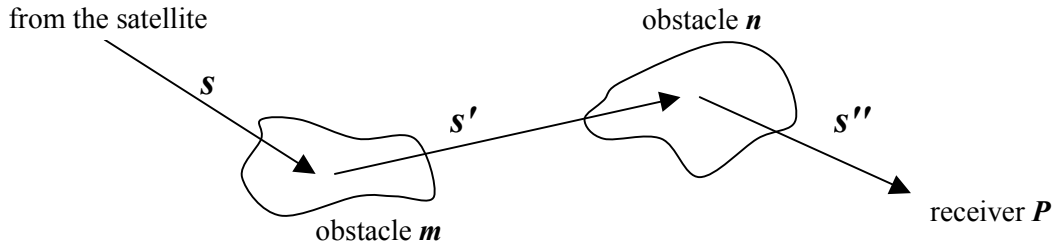

Figure 2.4 *Double interaction*

The received field at *P* is then given by:

$$E_{mn}(P) = [\overline{g}_n^R]^* \cdot \overline{\overline{T}}_n \cdot \overline{\overline{T}}_m \cdot \overline{E}_0 \ K(s,s') \, e^{-jks} \ K_m(s,s') \ e^{-jks'} \ K_n(s',s'') \, e^{-jks''} \qquad (2.2)$$

s, s′ and *s″* being respectively the satellite-to-obstacle *m*, obstacle *m*-to-obstacle *n* and obstacle *n*-to-receiver path lengths.

Given all single and multiple contributions, the total complex field is calculated by the following addition:

$$E(P) = \sum_m E_m(P) + \sum_{m,n} E_{mn}(P) + \sum_{m,n,p} E_{mnp}(P) + \ldots \qquad (2.3)$$

In equations (2.1) and (2.2), one point is worth attention. The spreading factor $K(s,s') = 1/s$ if a spherical wavefront is considered. With the plane wave approximation, $K(s,s') = 1$. Since this may look like a contradiction, consider two receiving points placed at two different heights h_1 and h_2, with a satellite located at zenith.

- For spherical waves: $K(s_1) = 1/(h_s - h_1)$ and $K(s_2) = 1/(h_s - h_2)$, h_s being the satellite altitude.
- For the plane wave assumption: $K(s_1) = K(s_2) = 1$.

If $h_s >> h_1$ and h_2, the spherical spreading factors tend towards the constant value $1/h_s$. Hence, the contradiction disappears since the relative field amplitude with respect to the line-of-sight (LOS) level is identical. It can thus be assumed that $K(s,s') = 1/s$ but that the wave is suitably represented by a theoretical plane wave if this assumption allows simplification of analytical expressions. For example, the LOS field in the absence of attenuation through building or tree is given by:

$$E_{LOS}(P) = [\overline{g}_{LOS}^{R}]^{*} \cdot \overline{E}_0 \frac{e^{-jkd}}{d} \tag{2.4}$$

where d is the distance between the satellite and the receiver.

In order to simplify equations (2.1-2), all further expressions are from now on given as a function of the incident field on the first obstacle $\overline{E}_{inc}(Q_m)$, Q_m being the location of the obstacle:

$$\overline{E}_{inc}(Q_m) = \overline{E}_0 \frac{e^{-jks}}{s} \tag{2.5}$$

Considering any single interaction, equation (2.1) is rewritten as:

$$E_m(P) = [\overline{g}_{Q_m}^{R}]^{*} \cdot \overline{\overline{T}}_m \cdot \overline{E}_{inc}(Q_m)\, K_m(s,s')\, e^{-jks'} \tag{2.6}$$

In the framework of the ray-tracing tool, only the following mechanisms are investigated:

- reflection, at any order,
- single and double edge diffraction.

Scattering by rough walls is also briefly considered. As far as transmission through blocks is concerned, the study is restricted to the absorption by vegetation. Building penetration is neglected, although this approximation might sometimes lead to errors. It is indeed often difficult to predict the effects of transmission through buildings, because the indoor structure is highly inhomogeneous and variable. The impact on the computational workload is also extremely significant, and ad hoc methods should be devised to keep the problem tractable. Consequently, all rays passing through building blocks are postulated to undergo infinite attenuation and are neglected.

2.2.3 Material characteristics

Each material defined to represent wall and ground surfaces is represented by electromagnetic parameters depending on the frequency, principally the relative permittivity ε_r and the conductivity σ [S m^{-1}]. A complex effective relative permittivity can be defined by:

$$\varepsilon_{r,eff} = \varepsilon_r - j\frac{\sigma}{\omega\varepsilon_0} \tag{2.7}$$

where ε_0 = 8.85 10^{-12} F m^{-1} is the permittivity of vacuum and ω [rad s^{-1}] is the wave angular frequency.

Unfortunately, there is a relative scarcity in finding values for ε_r and σ. For ground and brick walls, Table 2.1 [12] and Table 2.2 [7] summarize typical values that are used throughout this work.

Frequency [GHz]	Wet ground	Fairly dry ground	Dry ground
1	ε_r = 30.0 σ = 0.15	ε_r = 15.0 σ = 0.04	ε_r = 3.0 σ = 1.50 10^{-4}
5	ε_r = 20.0 σ = 1.50	ε_r = 15.0 σ = 0.50	ε_r = 3.0 σ = 0.01
10	ε_r = 12.0 σ = 3.00	ε_r = 12.0 σ = 1.70	ε_r = 3.0 σ = 0.05
30	ε_r = 5.0 σ = 10.00	ε_r = 5.0 σ = 7.00	ε_r = 3.0 σ = 0.40
40	ε_r = 4.5 σ = 12.00	ε_r = 4.5 σ = 10.00	ε_r = 3.0 σ = 0.50

Table 2.1 *Relative permittivity ε_r and conductivity σ [S m^{-1}] of typical ground surfaces as a function of frequency*

Other descriptive parameters characterize the surface roughness, namely the standard deviation Δh_0 and the correlation length ΔL_0 of the surface height. The correlation length ΔL_0 is defined as the distance for which the value of the correlation function of height variation decays by 1/*e*. Individual bricks are typically characterized by a standard deviation of surface height Δh_0 of 0.1 mm [13], while for brick walls, average values from 1 mm to 5 mm and 6.2

mm are found in [14], [15] and [16] respectively. Finally, it seems reasonable to assume an order of magnitude of some centimetres for the correlation length of usual brick walls.

Frequency [GHz]	**Relative humidity**			
	0 %	**5 %**	**10 %**	**15 %**
0.1	$\varepsilon_r = 3.3$ $\sigma = 0.0$	$\varepsilon_r = 5.3$ $\sigma = 4.4$	$\varepsilon_r = 8.7$ $\sigma = 6.6$	$\varepsilon_r = 12.9$ $\sigma = 8.9$
0.3	$\varepsilon_r = 3.3$ $\sigma = 0.0$	$\varepsilon_r = 5.3$ $\sigma = 6.6$	$\varepsilon_r = 8.7$ $\sigma = 11.7$	$\varepsilon_r = 12.9$ $\sigma = 16.7$
1	$\varepsilon_r = 3.3$ $\sigma = 0.0$	$\varepsilon_r = 5.3$ $\sigma = 16.7$	$\varepsilon_r = 8.7$ $\sigma = 33.4$	$\varepsilon_r = 12.9$ $\sigma = 46.2$
3	$\varepsilon_r = 3.3$ $\sigma = 0.0$	$\varepsilon_r = 5.3$ $\sigma = 83.4$	$\varepsilon_r = 8.7$ $\sigma = 156.9$	$\varepsilon_r = 12.9$ $\sigma = 267.0$
10	$\varepsilon_r = 3.3$ $\sigma = 0.0$	$\varepsilon_r = 4.9$ $\sigma = 389.4$	$\varepsilon_r = 7.5$ $\sigma = 1001.4$	$\varepsilon_r = 11.6$ $\sigma = 1780.2$
30	$\varepsilon_r = 3.3$ $\sigma = 0.0$	$\varepsilon_r = 4.4$ $\sigma = 1168.3$	$\varepsilon_r = 5.8$ $\sigma = 3004.1$	$\varepsilon_r = 7.6$ $\sigma = 5507.0$

Table 2.2 *Relative permittivity ε_r and conductivity σ [mS m^{-1}] of brick as a function of frequency and humidity*

2.2.4 Propagation mechanisms

2.2.4.1 Reflection

The theory of reflection is based on geometrical optics. When a smooth object is placed in the path of an electromagnetic wave, scattered fields are reradiated in all directions. If the object is an infinite plane surface, the contribution of all scattered fields interfere destructively, except for those coming from one particular point, called the *point of reflection* and denoted as Q_{ref}. However, real surfaces like buildings faces are neither infinite nor plane. Nevertheless, as long as the dimensions of the surface are much larger than the wavelength and the roughness is small compared to the wavelength, the geometrical optics assumption holds.

Consider a plane surface with unit normal vector $\bar{n}$. The incident wave is denoted by a unit vector $\bar{s}_{inc}$ in its direction of propagation. The plane containing $\bar{n}$ and $\bar{s}_{inc}$ is called the plane of incidence of the ray at point Q_{ref}. The angle of incidence measured in this plane is given by:

$$\vartheta_{inc} = -\arccos(\bar{n} \cdot \bar{s}_{inc}) \tag{2.8}$$

The unit vector $\bar{s}_{ref}$ indicates the direction of propagation of the reflected field. The pair $(\bar{n}, \bar{s}_{ref})$ defines the plane of reflection as well as the angle of reflection:

$$\vartheta_{ref} = \arccos(\bar{n} \cdot \bar{s}_{ref}) \tag{2.9}$$

The incident electric field $\bar{E}_{inc}(Q_{ref})$ can be resolved into components parallel (along unit vector $\bar{e}_{inc,||}$) and perpendicular (along unit vector $\bar{e}_{inc,\perp}$) to the plane of incidence. The reflected field at Q_{ref} can similarly be resolved into components parallel and perpendicular to the plane of reflection along unit vectors $\bar{e}_{ref,||}$ and $\bar{e}_{ref,\perp}$.

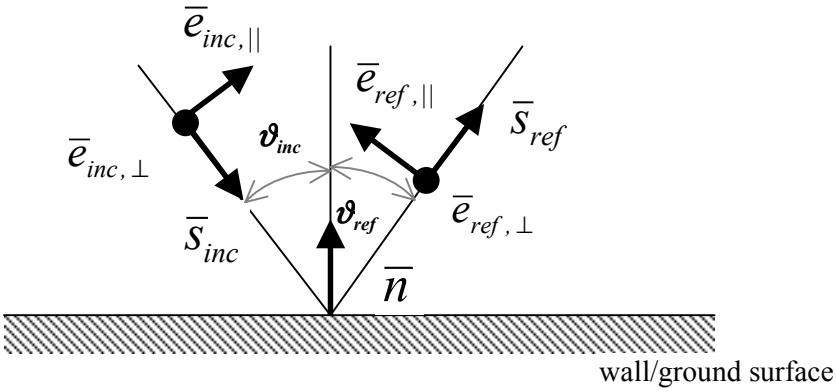

Figure 2.5 *Planes of incidence and reflection with ray-fixed coordinate systems*

Vectors $(\bar{s}_{inc}, \bar{e}_{inc,||}, \bar{e}_{inc,\perp})$ and $(\bar{s}_{ref}, \bar{e}_{ref,||}, \bar{e}_{ref,\perp})$ define a ray-fixed coordinate system, as depicted in Figure 2.5.

Snell's law of reflection [17] states that the angle of incidence ϑ_{inc} equals the angle of reflection ϑ_{ref}. This implies at once that:

- $\bar{n} \cdot \bar{s}_{inc} = -\bar{n} \cdot \bar{s}_{ref}$ according to (2.8-9),
- the planes of incidence and reflection coincide, so that $\bar{e}_{inc,\perp} = e_{ref,\perp} \stackrel{\Delta}{=} e_{\perp}$
- the direction of the reflected field can be expressed as:

$$\bar{s}_{ref} = \bar{s}_{inc} - 2\,(\bar{n} \cdot \bar{s}_{inc})\,\bar{n} \tag{2.10}$$

Relationship (2.10) allows determination of the location of the reflection point. For a given incident wave and reflection surface, the vector $\bar{s}_{inc}$ (known from the link elevation and azimuth angles), the receiving location and the normal vector $\bar{n}$ are fully specified, so the only unknown quantity in (2.10) is the vector $\bar{s}_{ref}$, and thus the location of Q_{ref}.

If the reflection point belongs to the finite dimension of the surface, the reflected field is evaluated at the receiving point P by:

$$E_{ref}(P) = [\bar{g}^{R}_{Q_{ref}}]^{*} \cdot \overline{\overline{\boldsymbol{R}}} \cdot \bar{E}_{inc}(Q_{ref})\ \frac{s}{s+s'}\, e^{-jks'} \tag{2.11}$$

where

- s is the path length from the satellite to the reflection point,
- s' is the path length from the reflection point to the receiver,
- $\overline{\overline{\boldsymbol{R}}}$ is the Fresnel dyadic coefficient.

With the plane wave assumption, $s >> s'$, and the spreading factor reduces to unity. In general, the dyadic coefficient $\boldsymbol{R}$ is a 3 x 3 matrix featured by the following expressions [18]:

$$\overline{\overline{\boldsymbol{R}}} = R_h\ \bar{e}_{inc,||}\,\bar{e}_{ref,||} + R_s\ \bar{e}_{\perp}\,\bar{e}_{\perp} \tag{2.12}$$

$$R_h = \frac{\varepsilon_{r,eff}\cos\vartheta_{inc} - \sqrt{\varepsilon_{r,eff} - \sin^2\vartheta_{inc}}}{\varepsilon_{r,eff}\cos\vartheta_{inc} + \sqrt{\varepsilon_{r,eff} - \sin^2\vartheta_{inc}}} \tag{2.13}$$

$$R_s = \frac{\cos\vartheta_{inc} - \sqrt{\varepsilon_{r,eff} - \sin^2\vartheta_{inc}}}{\cos\vartheta_{inc} + \sqrt{\varepsilon_{r,eff} - \sin^2\vartheta_{inc}}} \tag{2.14}$$

Furthermore, if the standard deviation of surface height is significantly smaller than the wavelength ($\Delta h_0 < \lambda$), the effect of surface roughness can be taken into account in the calculation of the specular component. The Fresnel coefficients R_h and R_s are then multiplied by an additional empirical attenuation factor [15]:

$$\chi = exp(-2k^2\Delta h_0^2\cos^2\vartheta_{inc}) \tag{2.15}$$

where Δh_0 is the standard deviation of the surface height.

2.2.4.2 EDGE DIFFRACTION

1° Single edge diffraction

Consider a propagating wave impinging upon a infinite straight wedge of interior angle denoted as α. A parameter $n = 2 - \alpha/\pi$ is defined, so that $n\pi$ represents the exterior angle of the wedge. According to geometrical optics, three regions should be considered:

- the reflected lit region I, where direct and reflected fields exist,
- the lit region II, where there is only a direct field,
- the shadow region III, where no field would exist.

Two shadow boundaries subsequently appear: the RSB (reflection shadow boundary) and the ISB (incident shadow boundary). They are depicted in Figure 2.6.

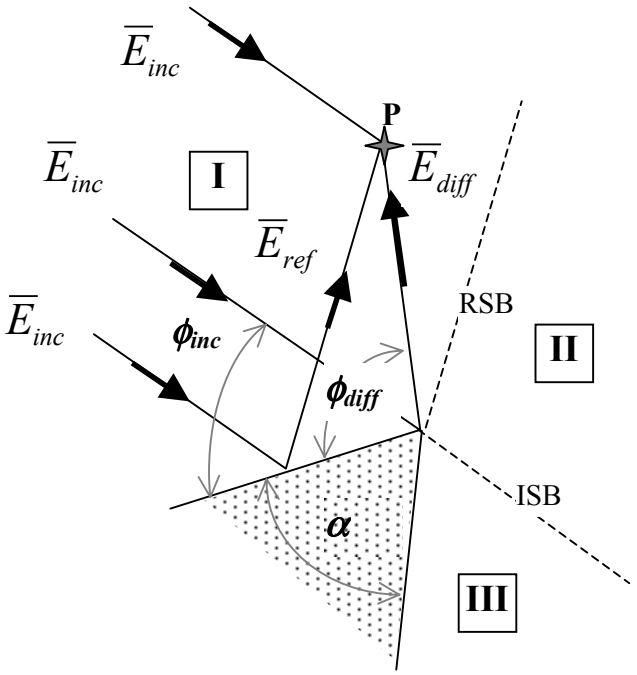

Figure 2.6 *Geometry for diffraction from a wedge*

However, due to Huygens' principle, secondary waves are formed even behind the obstructing wedge, leading to the existence of a diffracted field in all regions. Similarly to what is done for reflection, diffraction can be ray-modelled by means of the *Uniform Theory of Diffraction* (UTD). The UTD solution for the total field is then given by:

$$\overline{E}_t = \begin{cases} \overline{E}_{inc} + \overline{E}_{ref} + \overline{E}_{diff}, & 0 \le \phi < \pi - \phi_{inc} \quad \text{(Region I)} \\ \overline{E}_{inc} + \overline{E}_{diff}, & \pi - \phi_{inc} < \phi < \pi + \phi_{inc} \quad \text{(Region II)} \\ \overline{E}_{diff}, & \pi + \phi_{inc} < \phi < 2\pi - \alpha \quad \text{(Region III)} \end{cases} \tag{2.16}$$

The faces of the wedge are labelled 0-face and n-face. Although the designation of which face is called the 0-face is arbitrary, it is conventional to consider the angles ϕ_{inc} and ϕ_{diff} between the incident/diffracted ray and one of the faces to be measured from the 0-face. The 0-face is thus located at $\phi = 0$ while the n-face is located at an angle $\phi = n\pi$.

The *law of diffraction* has been formulated as follows by Keller [19]. "A diffracted ray and the corresponding incident ray make equal angles with the edge at the point of diffraction; they lie on opposite sides of the plane normal to the edge at the point of diffraction."

Thus assume that a ray is incident to an edge with angle $\beta_{0,inc}$. The various diffracted rays form a cone with half-angle $\beta_{0,diff}$ as shown in Figure 2.7. Following the law of diffraction, $\beta_{0,diff} = \beta_{0,inc} \overset{\Delta}{=} \beta_0$.

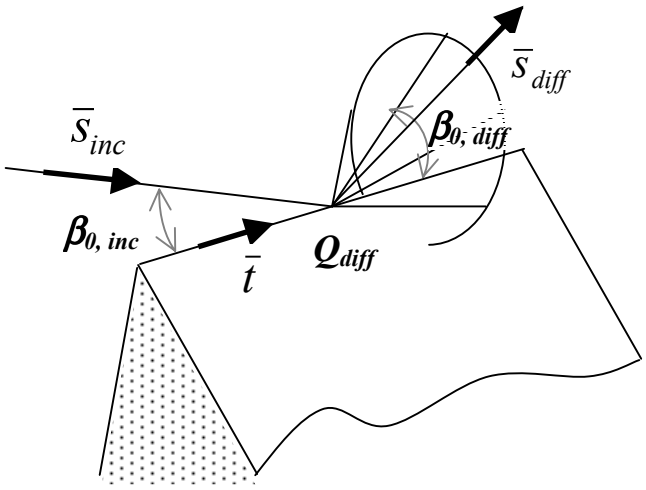

Figure 2.7 *Cone of diffracted rays*

The location of the diffraction point Q_{diff} can subsequently be determined using:

$$sin\ \beta_0 = \left| \overline{s}_{inc} \times \overline{t} \right| = \left| \overline{s}_{diff} \times \overline{t} \right| \tag{2.17}$$

where $\overline{s}_{inc}$ and $\overline{s}_{diff}$ are unit vectors in the direction of propagation of the incident and diffracted waves respectively and $\overline{t}$ is a vector tangential to the edge.

Because $\bar{s}_{inc}$ (given by the link elevation and azimuth angles), the receiving location and $\bar{t}$ are known, the only unknown quantity in (2.17) is $\bar{s}_{diff}$, and thereby, the location of Q_{diff}.

In order to evaluate the diffracted field, edge-fixed coordinate systems ($\bar{s}_{inc}$, $\bar{\beta}_{0,inc}$, $\bar{\phi}_{inc}$) and ($\bar{s}_{diff}$, $\bar{\beta}_{0,diff}$, $\bar{\phi}_{diff}$) are defined:

$$\bar{\phi}_{inc} = \frac{\bar{s}_{inc} \times \bar{t}}{\left| \bar{s}_{inc} \times \bar{t} \right|} \qquad \bar{\beta}_{0,inc} = \bar{\phi}_{inc} \times \bar{s}_{inc}$$

$$\bar{\phi}_{diff} = \frac{\bar{t} \times \bar{s}_{diff}}{\left| \bar{t} \times \bar{s}_{diff} \right|} \qquad \bar{\beta}_{0,diff} = \bar{\phi}_{diff} \times \bar{s}_{diff} \tag{2.18}$$

Following the UTD, the three-dimensional first-order edge-diffracted field is expressed in a dyadic form as:

$$E_{diff}(P) = [\bar{g}^{R}_{Q_{diff}}]^{*} \cdot \overline{\overline{\boldsymbol{D}}} \cdot \bar{E}_{inc}(Q_{diff}) \sqrt{\frac{s}{s'(s'+s)}}\, e^{-jks'} \tag{2.19}$$

where

- s is the path length from the satellite to the diffraction point,
- s' is the path length from the diffraction point to the receiver,
- $\overline{\overline{\boldsymbol{D}}}$ is the UTD dyadic coefficient.

With the plane wave assumption, $s >> s'$, and the spreading factor reduces to $1/\sqrt{s'}$. The dyadic coefficient $\overline{\overline{\boldsymbol{D}}}$ is a 3 x 3 matrix [20][21] defined by:

$$\overline{\overline{\boldsymbol{D}}} = -D_s\, \bar{\beta}_{0,inc} \bar{\beta}_{0,diff} - D_h\, \bar{\phi}_{inc} \bar{\phi}_{diff} \tag{2.20}$$

$$D_{s,h} = D_1 + D_2 + R_{s,h}(D_3 + D_4) \tag{2.21}$$

The components of the diffraction coefficients are outlined by:

$$D_1 = \frac{-e^{-j\pi/4}}{2n\sqrt{2\pi k}\, \sin\beta_0} \cot\left[\frac{\pi + (\phi_{diff} - \phi_{inc})}{2n}\right] F\left[kL\, a^{+}(\phi_{diff} - \phi_{inc})\right] \tag{2.22-a}$$

$$D_2 = \frac{-e^{-j\pi/4}}{2n\sqrt{2\pi k}\, \sin\beta_0} \cot\left[\frac{\pi - (\phi_{diff} - \phi_{inc})}{2n}\right] F\left[kL\, a^{-}(\phi_{diff} - \phi_{inc})\right] \tag{2.22-b}$$

$$D_3 = \frac{-e^{-j\pi/4}}{2n\sqrt{2\pi k}\,\sin\beta_0}\cot\left[\frac{\pi+(\phi_{diff}+\phi_{inc})}{2n}\right]F\left[kL\,a^{+}(\phi_{diff}+\phi_{inc})\right] \qquad (2.22\text{-c})$$

$$D_4 = \frac{-e^{-j\pi/4}}{2n\sqrt{2\pi k}\,\sin\beta_0}\cot\left[\frac{\pi-(\phi_{diff}+\phi_{inc})}{2n}\right]F\left[kL\,a^{-}(\phi_{diff}+\phi_{inc})\right] \qquad (2.22\text{-d})$$

where

- $F(x)$ is the transition function, $F(x) = 2j\sqrt{x}\,e^{jx}\int_{\sqrt{x}}^{\infty} e^{-ju^2}\,du$
- $a^{\pm}(\xi) = 2\cos^2\left(\frac{2n\pi N^{\pm}-\xi}{2}\right)$ with $N^{\pm}$ being integers that most nearly satisfy $2n\pi N^{\pm}-\xi = \pm\pi$
- $L = \frac{s\,s'}{s+s'}\sin^2\beta_0$ for a spherical wavefront, reducing to $L = s'\sin^2\beta_0$ for plane wave incidence.

Figure 2.8 depicts the field diffracted by the rooftop wedge of a single building as a function of its height, for several frequency bands. The satellite signal is assumed to come from behind the building with normal incidence to the edge and an elevation angle of 60 degrees. Building and ground electromagnetic parameters are found in Table 2.1 and Table 2.2 (a relative humidity of 5 % is assumed for the walls, while the ground is taken as fairly dry).

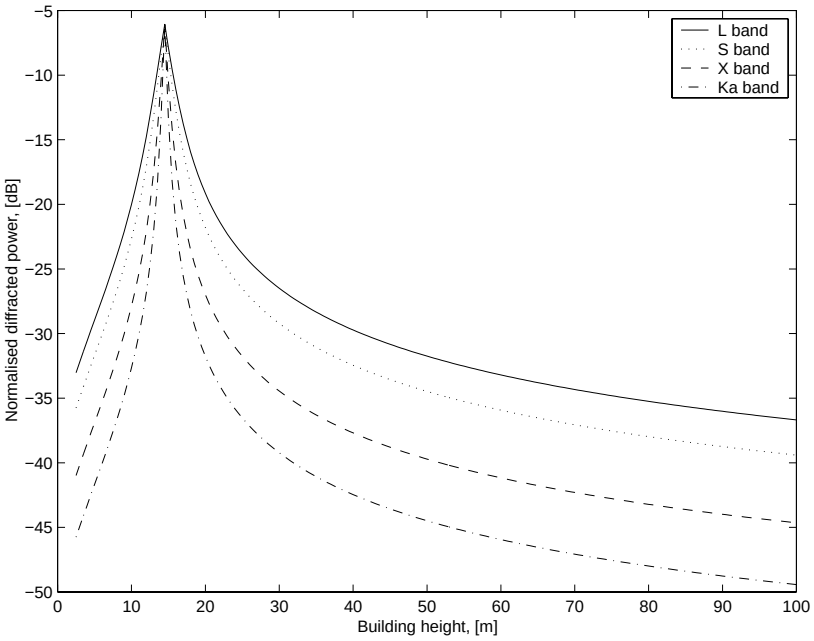

Figure 2.8 *Rooftop single diffracted power versus building height and frequency*

The receiver is located at a height of 2 metres and 7.5 metres away from the building. The receiving antenna is omnidirectional. It can be observed that the magnitude of the diffracted power decreases as frequency increases, except for the peak value. This maximum value is reached when the height is around 15 metres. For this particular value, the incident and diffracted rays are aligned, which corresponds to the incident shadow boundary defined in Figure 2.6.

The classical diffraction theory (UTD) assumes however that edges are of infinite length. This assumption is valid for edges of finite length as long as the diffraction point is sufficiently far away from the corners of the wedge. If the Keller's diffraction point lies near the corners,

- it can be located inside the edge: the UTD-diffracted field calculated by (2.19) completely ignores corner effects,
- it can be located outside the edge: the UTD-diffracted field would then be zero, which does not make much physical sense.

It seems obvious that the application of the classical UTD to wedges of finite length causes the field to be discontinuous when the diffraction point lies on a corner. As far as the UTD is concerned, these discontinuities can be treated by using corner diffraction or an alternative method based on equivalent currents. The latter is detailed in the following section.

2° Single diffraction by an edge of finite length: equivalent currents

This section describes an incremental model based on equivalent currents [22] that deals with corner effects. It should be noticed that the proposed method is only valid for plane wave incidence.

The derivation of equivalent currents starts with the calculation of the UTD-diffracted field from an infinite edge, which can be artificially expressed as resulting from the integration of a line source of current along the infinite length of the edge. The equivalent current is then integrated over the actual length of the edge only. Finally, the diffracted field can be expressed by the simple integral:

$$E_{diff}(P) = \int_0^l [\overline{g}^R_{Q_{diff}}]^* \cdot \overline{\overline{C}} \cdot \overline{E}_{inc}(r') \frac{e^{-jkr''}}{4\pi r''} dr' \tag{2.23}$$

where

- r' is the position of any point of the wedge ($0 \le r' \le l$),

- r'' *is* the path length between this point and the observation point (receiver),
- $\overline{\overline{C}}$ is a dyadic diffraction coefficient, given by:

$$\overline{\overline{C}} = -C_s\,\bar{\beta}_{0,inc}\left[\bar{t}-(\bar{t}\cdot\bar{s}_{diff})\bar{s}_{diff}\right]-C_h\,\bar{\phi}_{inc}\left[\bar{t}\times\bar{s}_{diff}\right] \tag{2.24}$$

$$C_s = -j\sqrt{8\pi k}\;e^{-j\pi/4}\,D_s(r') \tag{2.25}$$

$$C_h = j\sqrt{8\pi k}\;e^{-j\pi/4}\,D_h(r') \tag{2.26}$$

In (2.25-26), the diffraction coefficients $D_{s,h}$ must be evaluated at any point lying on the edge, even though these points violate the Keller cone concept. Therefore, $\beta_{0,diff}(r') \neq \beta_{0,inc}(r')$, and the angle β_0 appearing in equations (2.21-24) as well as in the expression of L should be replaced as suggested in [23] by: $sin\,\beta_0 = \sqrt{sin\,\beta_{0,inc}\;sin\,\beta_{0,diff}}$. The derivation of equations (2.23) to (2.26) is detailed in Appendix D.

A comparison between the classical UTD and edge equivalent currents is presented hereafter [24], considering the case of a single building described in Figure 2.9. The L band satellite signal is assumed to come from behind the building with a normal incidence to the edge and a elevation angle of 30 degrees. Building and ground electromagnetic parameters are still estimated by considering a relative brick humidity of 5 % and a fairly dry ground. The receiver is located at a height of 2 metres and its antenna pattern is omnidirectional. It moves along a direction perpendicular to the incident wave, as indicated in Figure 2.9.

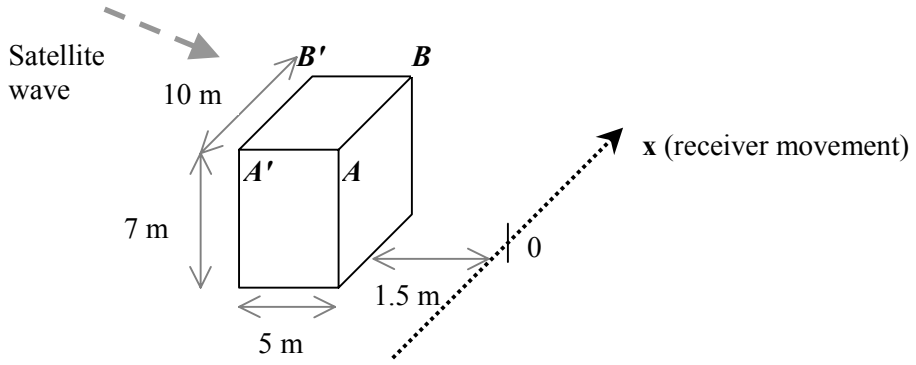

Figure 2.9 *Single building scenario*

Results are depicted in Figure 2.10.

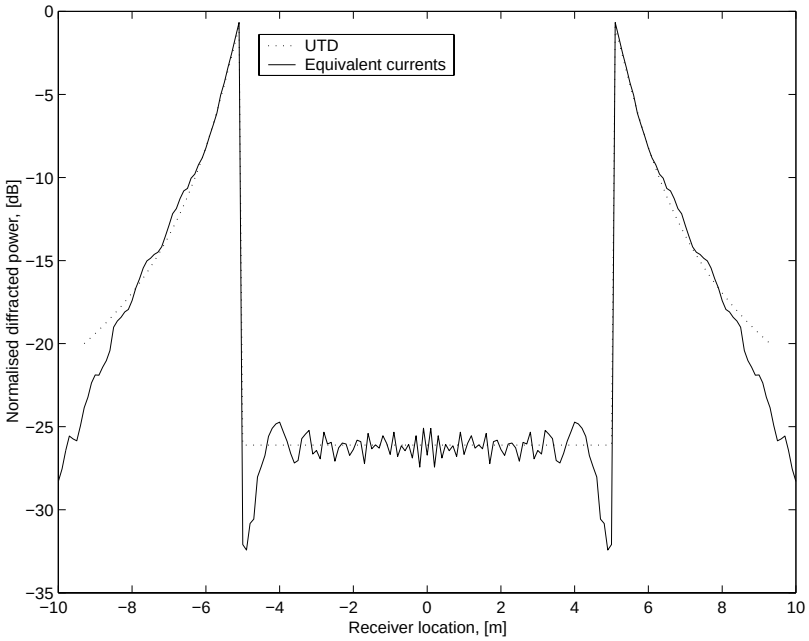

Figure 2.10 *Comparison between classical UTD and edge equivalent currents (only the diffracted power is represented)*

Corner effects from rooftop wedge ***AB*** are clearly observed, even at a quite long distance from the corners. Also, for receiver locations $|x| \geq 9\,\mathrm{m}$, the UTD abruptly predicts a null diffracted field, while equivalent currents provide a continuous solution for the field diffracted by ***AB*** and ***AA'*** or ***BB'***.

The edge equivalent current method offers consequently several advantages that are summarized here:

- the diffracted field can be calculated while the Keller's diffraction point does not belong to the edge,
- the approach takes into account every visible edge with respect to its length,
- it also allows for a more physical description of the diffraction process than the so-called corner diffraction method.

It will be shown later that equivalent currents also perform very well when realistic time series are needed, in contrast to the classical UTD. The main drawback of equivalent currents, in comparison with the classical UTD and corner diffraction method, is the computation time, since the calculation is based on the integration of an incremental diffracted field. In order to limit the computational load, a mixed method is implemented in the ray-tracing tool. If the Keller's diffraction point is sufficiently far away from the corners of the wedge with regard to

the wavelength (practically, farther than 30λ), the classical UTD calculation (2.19) is used. If not, equation (2.23) is applied.

Finally, it is interesting to add that surface equivalent currents could be used to derive the field reflected from finite dimension bodies, although it is not considered in this study.

3° Double diffraction

Concerning second order diffraction effects, a high-frequency UTD-based analytical solution for the field doubly diffracted in the far zone from a pair of parallel lossy wedges is implemented [25][26]. It is given by:

$$E_{diff-diff}(P) = [\overline{g}^{R}_{Q''_{diff}}]^{*} \cdot \overline{\overline{\boldsymbol{D}}}^{d} \cdot \overline{E}_{inc}(Q'_{diff}) \sqrt{\frac{s}{s's''(s''+s'+s)}}\, e^{-jk(s''+s')} \tag{2.27}$$

where

- s is the path length from the satellite to the first diffraction point Q'_{diff};
- s' is the path length from Q'_{diff} to the second diffraction point Q''_{diff};
- s'' is the path length from Q''_{diff} to the receiver;
- $\overline{\overline{\boldsymbol{D}}}^{d}$ is the dyadic double diffraction coefficient, the expression of which is given in Appendix E.

For plane wave incidence, the spreading factor reduces to $1/\sqrt{s's''}$.

Figure 2.11 compares the single diffracted field by a rooftop edge with the double-diffracted field by two adjacent wedges (belonging to the same building). The L band satellite signal is assumed to come from behind the building with normal incidence to both wedges and an elevation angle of 60 degrees. The building is 7 metres in height and 5 metres in width. The receiver is located 2 metres above ground and moves away from the building. The antenna pattern is omnidirectional. As before, ε_r = 5.3, σ = 16 mS m^{-1} for walls and ε_r = 15, σ = 0.04 S m^{-1} for ground.

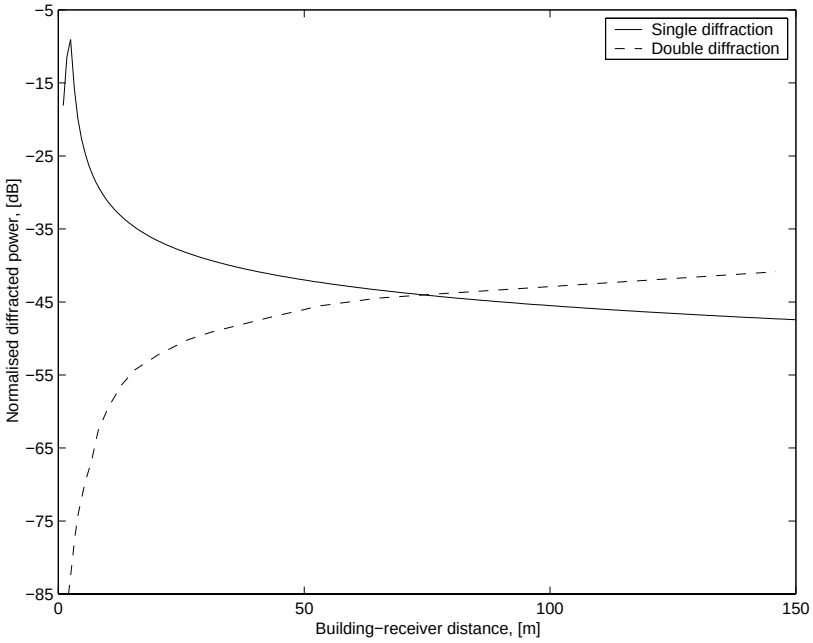

Figure 2.11 *Comparison between single-diffracted and double-diffracted contributions from joined wedges as a function of the distance from the building*

Double-diffracted contribution from adjacent wedges does not seem to be much significant. It exceeds the single diffraction contribution only for large building-receiver distances, for which other contributions (LOS, reflection) are likely to be dominant.

2.2.4.3 DIFFUSE SCATTERING BY ROUGH SURFACES

For a smooth surface, the reflected wave is coherent with the incident wave and is calculated by means of the reflection coefficient. If the surface gets slightly rough, this specular component is attenuated due to scattering in all directions. That effect is accounted for by the reduction factor χ in equation (2.15). Combining (2.11-15), the specular power, for incident and received polarisation parallel to the interface, can be expressed as:

$$P_{ref} = P_T \left(\frac{\lambda}{4\pi} \right)^2 \frac{G_T G_R}{(s+s')^2} R^2 \chi^2 \tag{2.28}$$

where

- P_T is the transmitted power,

- s is the path length between the transmitter and reflection point,
- s' *is* the path length between the reflection point and the receiver,
- R is the reflection coefficient (i.e. R_s for a polarisation parallel to the interface),
- χ is defined by (2.15),
- G_T and G_R are the transmitter/receiver gain functions.

The scattered power is called the *diffuse* component. Given the roughness of typical walls, this contribution is often negligible compared to the specular one. There is one major exception at high frequencies (above X band): when the receiving antenna is characterized by a narrow beam, the specular component can be strongly attenuated if falling outside the beamwidth. For these cases, the diffuse contribution might become significant. This section presents two simple methods among others to evaluate the diffuse contribution scattered by walls in the case of narrow-beam antennas.

Consider an incident wave defined by a incident angle ϑ_{inc}, the power is scattered in all directions ϑ_s. The angle ϕ_s is defined as the angle between the planes of incidence and scattering.

The scattered power is calculated using the bistatic radar equation:

$$P_{sca} = P_T \left(\frac{\lambda}{4\pi} \right)^2 \int_S \frac{\sigma_{sca} G_T G_R}{4\pi r^2 r'^2} ds \tag{2.29}$$

where

- r is the path length between transmitter and surface ds,
- r' *is* the path length between surface ds and receiver,
- σ_{sca} is the scattering cross section per unit area of rough surface, which is still to be estimated.

Before describing models of scattering cross section, a new parameter must be introduced to characterize the slope of the surface height. The roughness slope ρ_0 of the surface is defined by:

$$\rho_0 = \frac{\Delta h_0}{\Delta L_0} \tag{2.30}$$

where Δh_0 and ΔL_0 are the standard deviation and correlation length of surface height respectively.

1° Rough surface scattering model: Kirchhoff approximation

The Kirchhoff model is valid under the condition that the correlation length of the surface height ΔL_0 is larger than the wavelength: $\Delta L_0 > \lambda$ [13]. For a typical brick wall, this is equivalent to a frequency larger than several GHz (3 to 30 GHz, depending on the correlation length).

For *slightly rough* surfaces, the scalar approximation of the Kirchhoff model requires additionally that $\sqrt{2}\rho_0 < 0.25$ [13]. The scattering cross section per unit area of rough surface is then given by [27]:

$$\sigma_{sca} = \pi k^4 R^2 \left[1 + \cos\vartheta_{inc}\cos\vartheta_s - \sin\vartheta_{inc}\sin\vartheta_s\cos\phi_s\right]^2 W(p,q) \tag{2.31}$$

where

- R is the Fresnel reflection coefficient for the incident polarisation,
- $p = k(\sin\vartheta_s\cos\phi_s - \sin\vartheta_{inc})$ (2.32)
- $q = k\sin\vartheta_s\sin\phi_s$ (2.33)
- $W(p, q)$ is the bidimensional spectral density of the rough surface and is a Fourier transform of the surface height correlation function; it can be quite easily calculated if the surface height is normally distributed.

If the surface is *very rough*, i.e. when $\left|2\rho_0(\cos\vartheta_{inc} + \cos\vartheta_s)\right| > 1$, the approximation of expression (2.31) in the case of normally distributed surface height is outlined by:

$$\sigma_{sca} = R^2 \frac{\cos^2\vartheta_{inc}}{(\cos\vartheta_{inc} + \cos\vartheta_s)^2}\left(\frac{1 + \cos\vartheta_{inc}\cos\vartheta_s - \sin\vartheta_{inc}\sin\vartheta_s\cos\phi_s}{\rho_0\cos\vartheta_{inc}(\cos\vartheta_{inc} + \cos\vartheta_s)}\right)^2 \cdot exp\left[-\frac{p^2 + q^2}{4k^2\rho_0{}^2(\cos\vartheta_{inc} + \cos\vartheta_s)^2}\right] \tag{2.34}$$

For the following typical values: Δh_0 = 6.2 mm, ΔL_0 = 3 cm (see Section 2.2.3), a roughness slope $\rho_0 \cong 0.2$ is obtained. At 30 GHz, this constitutes an intermediate case, between slightly rough and very rough surfaces. However, the use of expression (2.34) is very straightforward and can be considered as a first approximation.

Figure 2.12 depicts the scattering cross section at 30 GHz as a function of the scattering angle and the angle ϕ_s. The incidence angle ϑ_{inc} is assumed to be equal to 10 degrees, while the

slope is assigned the value $\rho_0 = 0.3$ ($\Delta L_0 = 2$ cm, $\Delta h_0 = 6$ mm). These values fulfil the validity condition of expression (2.34) for observation angles $\vartheta_s \leq 50°$.

In Figure 2.12, it is observed that the diffuse power is scattered in all directions, with no preference for the specular direction ($\phi_s = 0°, \vartheta_s = \vartheta_{inc} = 10°$). Scattering is maximum in the direction perpendicular to the surface ($\vartheta_s = 0°$) and decreases while both ϑ_s and ϕ_s increase.

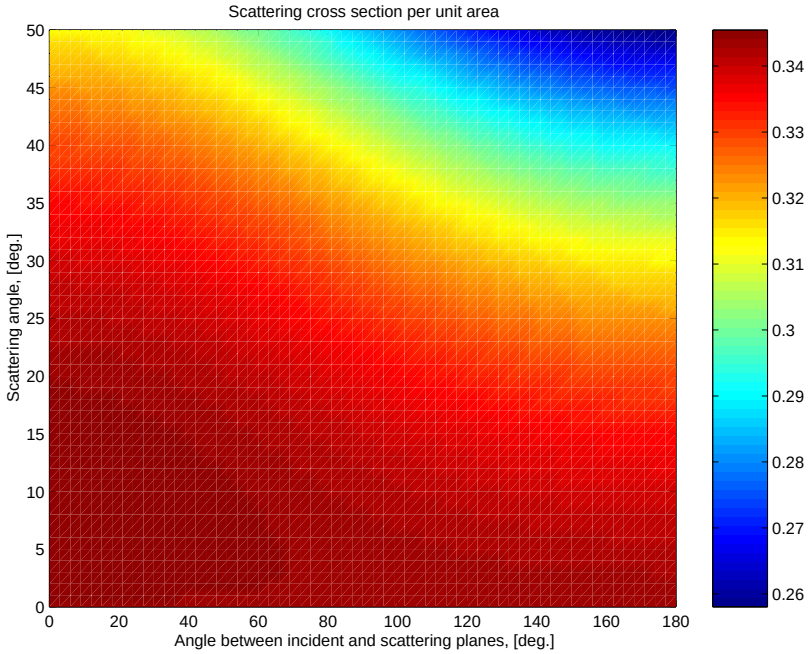

Figure 2.12 *Scattering cross section per unit area as a function of the scattering angle and the angle between incident and scattering planes*

The major drawback of the Kirchhoff approximation is that the method is based on the Fresnel reflection coefficient valid for plane surfaces. Hence, it does not include the complete polarisation effect.

2° First order perturbation solution

This method yields better polarisation effects than the Kirchhoff model because it is based on the correct boundary condition on the surface. It is bounded in validity by: $k\,\Delta h_0 < 0.3$ and $\sqrt{2}\rho_0 < 0.25$ [13]. For a typical brick wall ($\Delta h_0 = 6.2$ mm), the frequency must consequently be higher than 2.3 GHz. The first order perturbation solution for the scattering cross section per unit area is detailed in [27].

2.2.4.4 ATTENUATION BY FOLIAGE

The tree foliage is modelled by means of parallelepipedic blocks representing the leaves. Every ray passing through a block is then attenuated, following the ITU-R Recommendation 236-6 [28]:

$$L\,[\mathrm{dB}] = A\, f^{\beta}\, d_f^{\nu} \tag{2.35}$$

where the frequency f is given in MHz and the vegetation depth d_f, in metre.

The various constants in (2.35) have been investigated in the literature, as summarized in Table 2.3.

Model	A	β	ν
ITU-R [28]	0.187	0.284	0.588
Barts & Stutzmann, $0 < d < 14$ m [29]	0.063	0.284	1.000
Seville et al. [30]	0.370	0.284	0.380
COST 235 [10]	15.600	-0.009	0.260

Table 2.3 *Vegetation attenuation model: empirical constants*

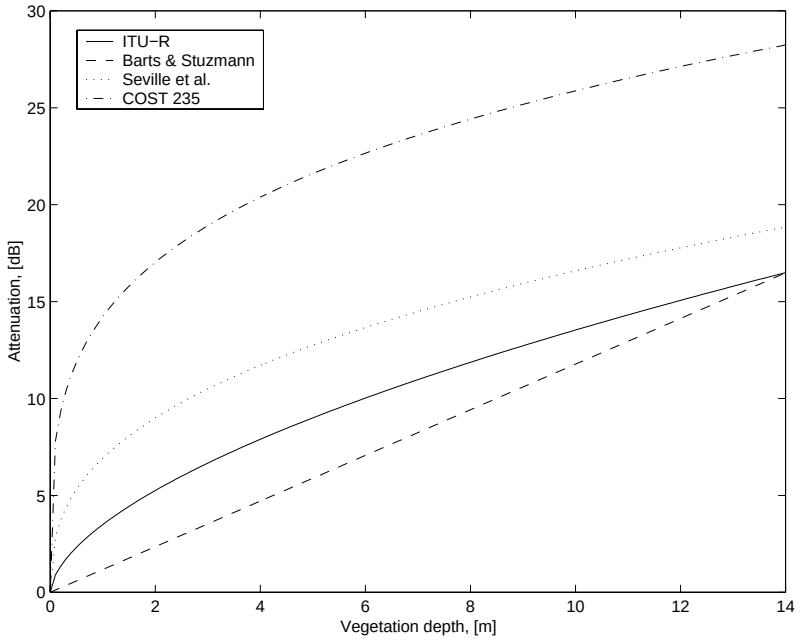

Figure 2.13 *Vegetation attenuation models: attenuation at 30 GHz*

The predicted attenuation is depicted in Figure 2.13 for all models at a frequency of 30 GHz. Results differ greatly from one model to another. This is the obvious consequence of the empirical nature of the models, the parameters given in Table 2.3 being fitted from measurements. In the absence of decisive information, the ray-tracing tool is based on the ITU-R parameters.

2.2.4.5 SIMULATION RESULTS

The present section is dedicated to several L band simulations. They compare, in a specific built-up scenario, reflection and diffraction contributions, with respect to the calculation method.

The built-up scenario consists of a long straight street represented by means of four building, as described in Figure 2.14 (view from above). The characteristic parameters of the area are:

- the building heights $H_1 = H_2 = H_3 = 7$ m
- the street width $w = 15$ m
- the receiving location relative to building 1, $d_m = 7.5$ m.

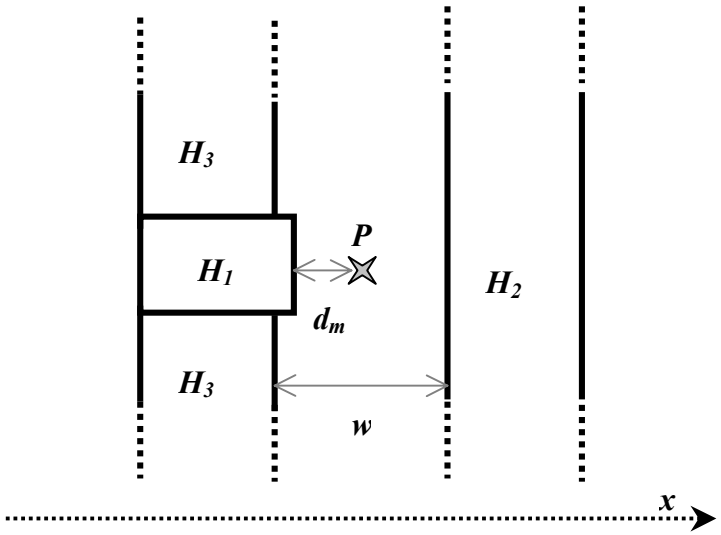

Figure 2.14 *Long straight street scenario*

The building of height H_1 is represented by a slightly larger width. Hence, diffraction by vertical wedges can be accounted for. Electromagnetic parameters are chosen as: $\varepsilon_r = 5.3$, $\sigma = 16$ mS m^{-1} for walls and $\varepsilon_r = 15$, $\sigma = 0.04$ S m^{-1} for ground. The L band receiver is a quadrifilar helix, quasi omnidirectional in the upper half-space [31], whose co-polar pattern is

depicted in Figure 2.15. The contra-polar radiation pattern is always neglected in the following.

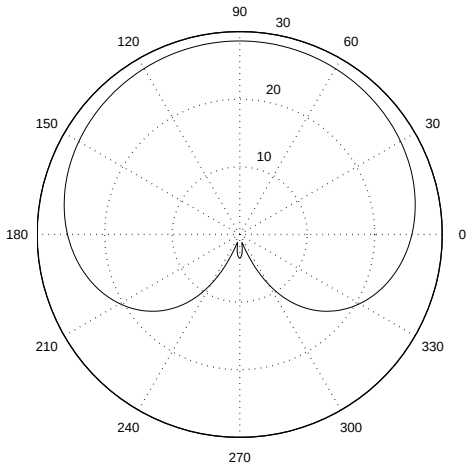

Figure 2.15 *Radiation pattern in* [dB] *of a L band quadrifilar helix antenna (the zenith is given by an angle of 90 degrees)*

The first simulation concerns a moving terminal crossing the street from building 1 to building 2. The path-loss calculation includes contributions from LOS, single diffraction (UTD) as well as single and double reflection. The satellite is assumed to be fixed with an elevation angle of 60 degrees and an azimuth angle relative to x-axis equal to 180 degrees (in other words, the satellite is located behind building 1).

Figure 2.16 depicts the power of all contributions as a function of the mobile location.

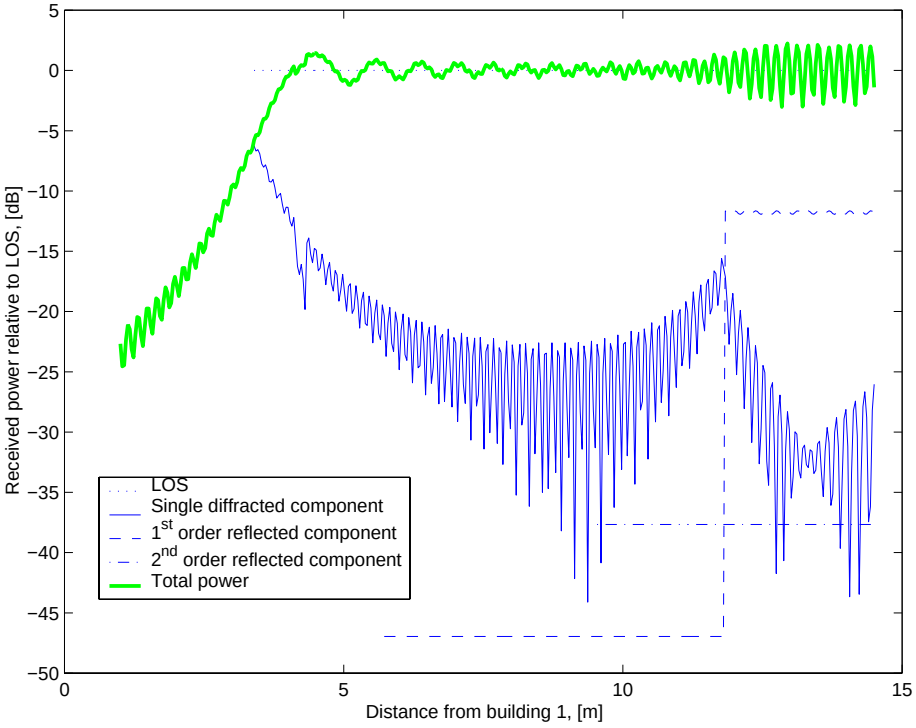

Figure 2.16 *Impact of several contributions for a moving terminal (fixed satellite)*

The LOS component exists for $d_m > 4$ m. For $d_m < 4$ m, the only contribution comes from diffraction by at least both rooftop edges (buildings 1 and 2). The diffracted field presents two local maxima related to the shadow boundaries of Figure 2.6 (ISB from building 1 and RSB from building 2). Between these two shadow boundaries, a field is reflected by the ground, and is negligible compared to double building reflection. This is mainly due to the co-polar radiation pattern of the antenna, which dramatically cuts down the ground-reflected contribution. When a single building-reflected contribution exits, it becomes the dominant contribution below the LOS field.

The second simulation deals with a fixed terminal ($d_m = w_0/2 = 7.5$ m) but takes into account the satellite constellation. An orbit generator (see Appendix A) is used to simulate the motion of the satellites around the earth. The street (Figure 2.14) is assumed to be located in London and oriented along the direction of a terrestrial parallel. It is also postulated that the mobile terminal always communicates with the nearest satellite (i.e. seen under the highest elevation angle). A random period of 600 seconds is simulated. During this period, the elevation angle varies for the considered constellation (Iridium) between 10 and 63 degrees.

Several path-loss calculations are carried out. The LOS component is successively combined with:

- the reflected contribution (single and double interactions) plus the equivalent current single diffracted contribution,
- the single reflected contribution plus the equivalent current single diffracted contribution,
- the reflected contribution (single and double interactions) plus the UTD single diffracted contribution.

Results are presented in Figure 2.17.

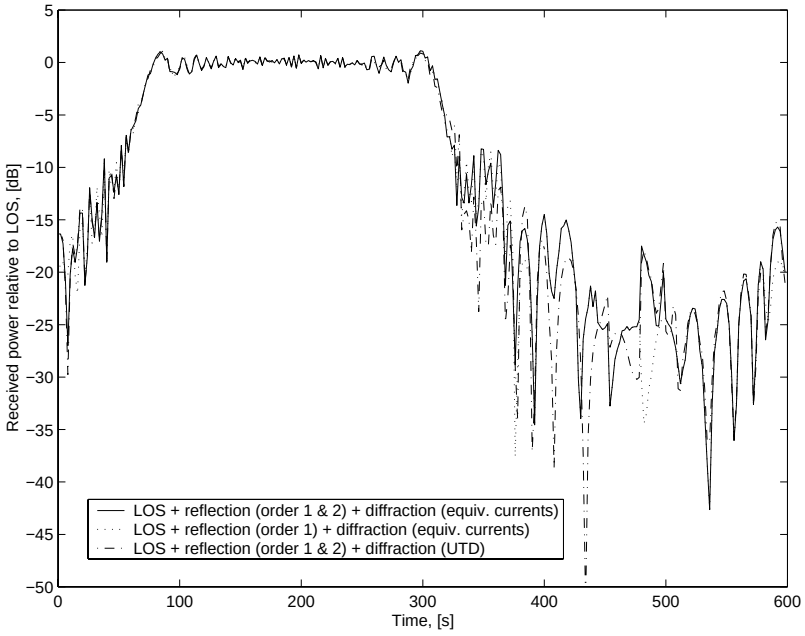

Figure 2.17 *Impact of second order reflection and of edge equivalent currents on path-loss calculation for moving satellites*

Regarding the global path-loss, the terminal receives the LOS signal only between $t = 100$ s and 300 s. Outside this time interval, the signal is blocked by lateral buildings. Double reflection is usually not very significant, yet it can have a certain impact in deep shadowing periods (around $t = 480$ s). With regard to the comparison between classical UTD and edge equivalent currents, the classical UTD can strongly deviate from the equivalent current method (see e.g. the path-loss between $t = 300$ s and 500 s). This deviation should be even more critical when a large number of narrow buildings (and thus short wedges) are involved.

2.2.5 Wideband characterization

The ray method is inherently a wideband approach, provided that all significant mechanisms are properly accounted for. Equation (2.3) can indeed be rewritten as:

$$\begin{aligned} E(\omega, P) = & \sum_m \left| E_m(\omega, P) \right| e^{-j\varphi_m(\omega, P)} \; e^{-j\frac{\omega}{c}(s+s')} \; e^{j\frac{r_P}{|\bar{v}|}\Delta\omega_m} \\ & + \sum_{m,n} \left| E_{mn}(\omega, P) \right| e^{-j\varphi_{mn}(\omega, P)} \; e^{-j\frac{\omega}{c}(s+s'+s'')} \; e^{j\frac{r_P}{|\bar{v}|}\Delta\omega_{mn}} + \ldots \end{aligned} \tag{2.36}$$

with $$\left| E_m(\omega, P) \right| e^{-j\varphi_m(P, \omega)} = [\bar{g}_m^R(\omega)]^* \cdot \overline{\overline{T}}_m \cdot \bar{E}_0 \; K(s,s') \; K_m(s,s') \tag{2.37}$$

In (2.36), r_P and $\bar{v}$ are the receiver position and relative speed respectively, and $\Delta\omega_m$ is the Doppler shift associated with ray m:

$$\Delta\omega_m = k \; \bar{v} \cdot \bar{s}_m \tag{2.38}$$

$\bar{s}_m$ being a unit vector indicating the direction of ray m at the receiver.

Expression (2.37) represents the complex received field in amplitude and phase associated with each ray. Note that the phase shift due to the delay and the Doppler effect is expressly not included in the phase $\varphi_m(\omega, P)$.

Expression (2.36) can be considered as a passband transfer function $E(\omega, t = r_P / |\bar{v}|)$ [32] since it results from the ray-tracing simulation, all parameters being kept constant, except the frequency. When centred on the carrier frequency ω_0, this transfer function can be translated into the baseband, yielding the function $\boldsymbol{H}(\Omega, t) = \boldsymbol{E}(\omega - \omega_0, t)$. The inverse Fourier transform of $\boldsymbol{H}(\Omega, t)$ is the equivalent baseband impulse response:

$$\begin{aligned} h(\tau, t) &= \Im^{-1}\{\boldsymbol{H}(\Omega, t)\} \\ &= \sum_m \alpha_m(t) \; \delta[\tau - \tau_m(t)] \; exp[-j\omega_0\tau_m(t) + j\Delta\omega_m t] + \ldots \end{aligned} \tag{2.39}$$

where

- the complex tap α_m is given by (2.37),
- $\tau_m = (s + s')/c$ is the delay of the m^{th} ray-contribution.

Since the ray-tracing includes a limited number of rays, solutions for $h(\tau, t)$ only model the near echoes, caused by a restricted number of interactions. Multipaths due to terrain effects are, for example, completely ignored simply because terrain modelling is not included in the ray-tracing tool. The size of the studied area also matters quite significantly, for the same reason.

For simulating system behaviour, the calculation of $\boldsymbol{H}(\Omega, t)$ is only needed over the system bandwidth of the radio link. The transfer function is consequently filtered by the transmission and reception filters, for example square-root raised cosine filters. The inverse Fourier transform of this band-limited transfer function yields a filtered version of $h(\tau, t)$: the different taps in (2.39) are spread by the filtering. When the relative speed $\bar{v}$ is equal to zero, the static transfer functions $\boldsymbol{E}(\omega)$ and $\boldsymbol{H}(\Omega)$ as well as the static equivalent baseband impulse response $h(\tau)$ are obtained.

Using the scenario described by Figure 2.14 and Figure 2.16 (fixed satellite, L band receiver crossing the street), the transfer function is calculated over a bandwidth of 1 GHz, so that the resolution, in the time domain, is 1 ns. Figure 2.18 represents the equivalent baseband impulse response as a function of the mobile terminal location.

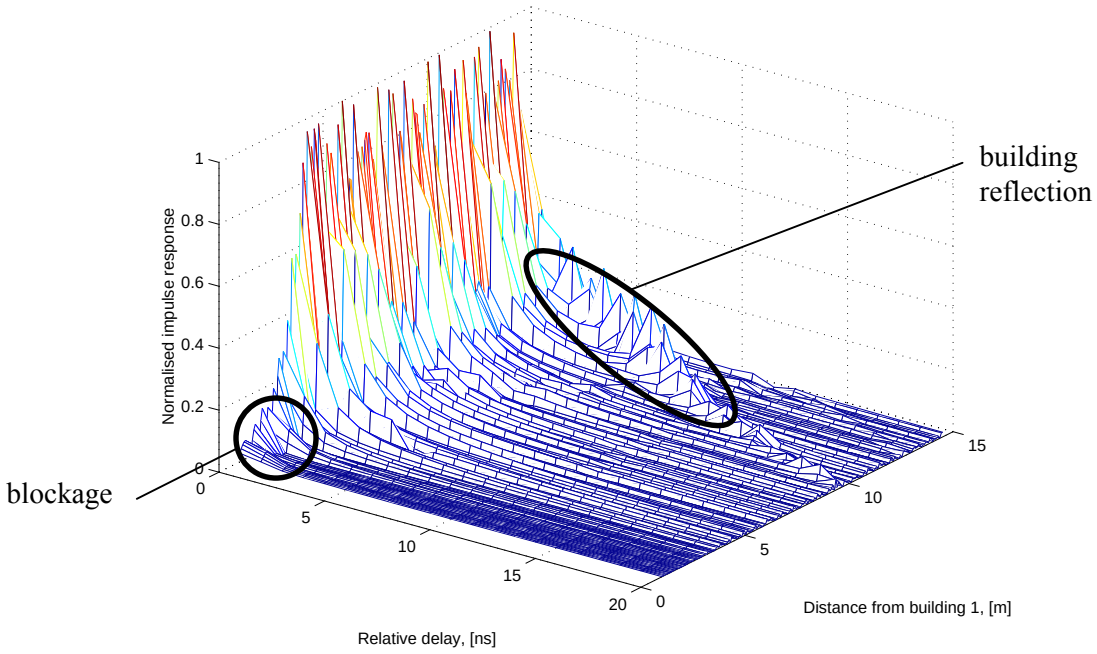

Figure 2.18 *Static equivalent baseband impulse responses (normalized to unity), for successive mobile locations, at L band*

The blockage effect (d_m < 4 m), as well the building-reflected component (d_m > 12 m) are highlighted on the graph.

A well-known wideband parameter is the RMS delay spread, which characterizes the spread of the equivalent baseband impulse response. It is given by:

$$\tau_{rms}(t) = \sqrt{\frac{\int_0^\infty (\tau - \bar{\tau}(t))^2 \left| h(\tau,t) \right|^2 d\tau}{\int_0^\infty \left| h(\tau,t) \right|^2 d\tau}} \tag{2.40}$$

where the average delay $\bar{\tau}(t) \triangleq \frac{\int_0^\infty \tau \left| h(\tau,t) \right|^2 d\tau}{\int_0^\infty \left| h(\tau,t) \right|^2 d\tau}$, assuming the first path arrives at delay $\tau = 0$.

It is important to notice that the RMS delay spread is very sensitive to the number of paths that are accounted for in the ray-tracing, and therefore, to the size of the considered area and the number of buildings.

2.2.6 Experimental validation

Experiments were carried out in a street of Louvain-la-Neuve, in October 1998 and February 1999 [33], along a distance of about 60 metres. The experimental antennas were two corrugated horns, one being fixed and placed on the roof of a high building (Maxwell building), the other one being mounted on a transportable equipment. A positioner allows movements in both azimuth and elevation. Antennas operate concurrently at 12.5 and 30 GHz with vertical polarisation. The street is lined on both sides by buildings as represented in Figure 2.19. The transmission was made on the axis of the street, and antenna orientations were continuously aligned. In October, the link was obstructed by deciduous trees in leaves (schematically represented in Figure 2.19) from the half of the experimental path. However, in February, trees had no leaves and all branches had been cut before winter.

Simulations include reflection at the first two orders as well as UTD single diffraction. Ground and walls are given the following electromagnetic parameters: ε_r = 3.3, σ = 0 S m^{-1} for walls at both frequencies, ε_r = 12 and 5, σ = 1.7 and 7.0 S m^{-1} for the ground at 12.5 and

30 GHz respectively. All buildings are modelled as accurately as possible by juxtaposing parallelepipeds. With regard to the tree, only leaves are modelled, the ITU-R parameters being used to estimate the foliage attenuation.

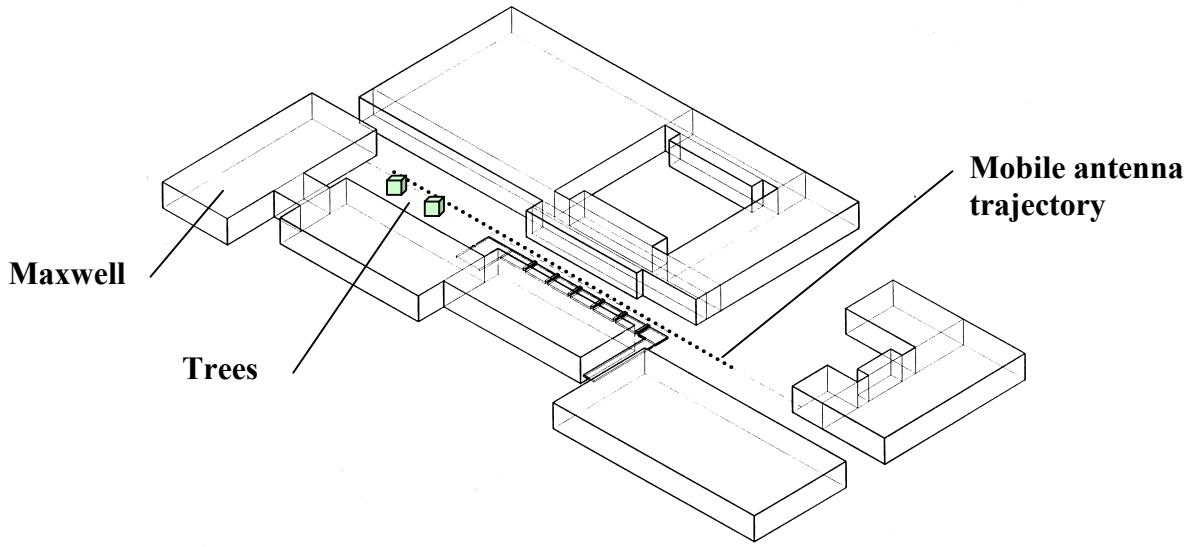

Figure 2.19 *Experimental configuration (Levant street)*

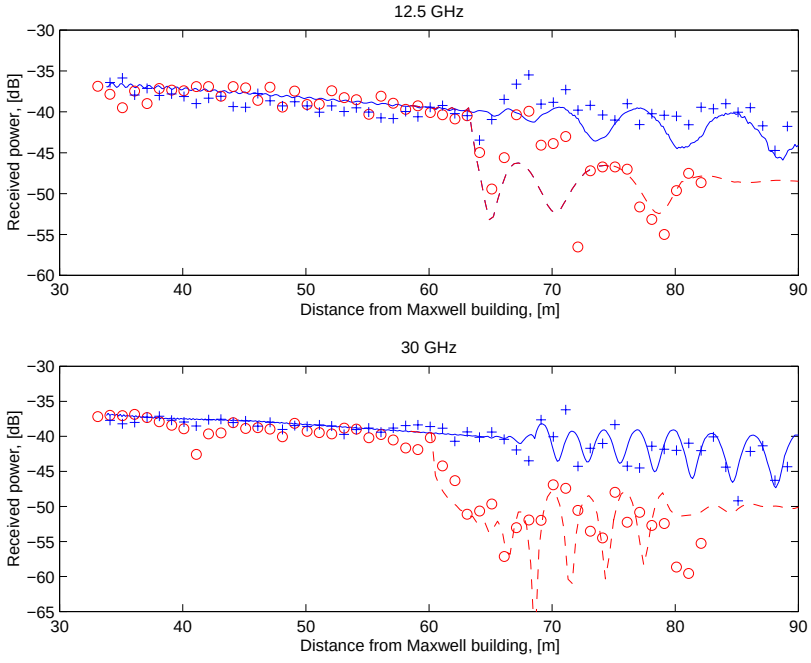

Figure 2.20 *Comparison between simulations and measurements at 12.5 GHz (upper graph) and 30 GHz (lower graph): meas. February {+} versus simulation without trees {solid lines}, meas. October {circles} versus simulation including trees {dashed lines}*

Figure 2.20 compares simulations and experimental results. In every case, a good agreement is found on average. Since the received power was measured every metre, it is impossible for the experimental curves to reproduce every variation of the simulated signal. However, the amplitude of oscillations as well as the attenuation effect of foliage are clearly well reproduced at both frequency bands. Note that, because every single ray separately undergoes the attenuation through foliage, the resulting path-loss is not obtained by applying a global loss to the no-tree case.

The models used in the simulations are very simple. For instance, surface roughness is not taken into account. Mechanisms of scattering by rough walls and various unmodelled obstacles could explain for the observed discrepancies.

2.3 PHYSICAL-STATISTICAL MODELLING

2.3.1 The physical-statistical approach

As already mentioned, two classes of models are widely used to characterize the built-up channel: empirical/statistical models and deterministic physical models. The use of empirical/statistical models is quite straightforward and requires low computational effort since the model parameters have been pre-determined by fitting to measured data. However, due to this lack of physical background, such models only apply with good results in environments that are very close to the one they have been inferred from.

On the other hand, deterministic physical models, such as those described in [7] and Section 2.2, provide high accuracy together with a strong link to the real parameters. Unfortunately, they require a precise description of the environment and time-consuming computations. Therefore, they are particularly suited to short-term analysis and dynamic modelling in typical reduced configurations.

As far as average predictions are concerned, an element of statistics has to be introduced. One approach is to devise physical models, in order to examine typical signal variations in environments of various descriptive categories, and then use them to generalise over wider areas. A more appropriate approach is to use *physical-statistical models* [29][34][35], which derive fading distributions directly from distributions of physical parameters using simple electromagnetic theory.

Physical-statistical modelling (Figure 2.21) is a hybrid approach, which builds on the advantages of both empirical and physical models, while avoiding many of their disadvantages. As in physical models, the input knowledge consists of electromagnetic theory and sound physical understanding. However, this knowledge is then properly combined with a *statistical* input data set, yielding a *distribution* of the output predictions. The outputs can still effectively be point by point, although the predictions are no longer linked to specific locations. For example, a physical-statistical model can predict the distribution of shadowing, avoiding the errors inherent in the empirical approach, although it does not predict what the shadowing value will be at a particular location. This information is usually adequate for the system designer.

Physical-statistical models therefore require only simple input data, such as input distribution parameters (e.g. mean building height, building height variance). The environment description is entirely objective, avoiding problems of subjective classification, and capable of high

statistical accuracy. The models are based on physical principles, so they are applicable over very wide parameter ranges. Finally, by pre-calculating the effect of specific input distributions, the required computational effort can be very small.

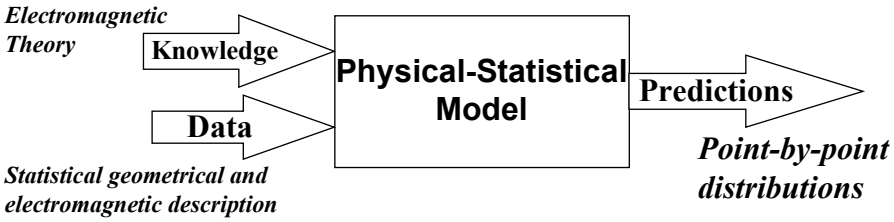

Figure 2.21 *A physical-statistical propagation model*

In a number of cases, the analytical formulation of a physical-statistical prediction is outlined by the following relationship [36][37]:

$$F(x) = \int_{\Xi} f(x \mid \overline{\eta})\, T_{\overline{N}}(\overline{\eta})\, d\overline{\eta} \tag{2.41}$$

where

- $F(x)$ is any parameter or function featuring the channel behaviour,
- $\overline{\eta} \subseteq \Xi$ is the vector of physical parameters, Ξ representing the whole set of possible parameters (building height and spacing, street width, elevation and azimuth angles of the link, etc.),
- $T_{\overline{N}}(\overline{\eta})$ is the measured joint probability density function of the physical parameters in the area considered,
- $f(x \mid \overline{\eta})$ expresses the conditional relationship between the channel parameter/function to be predicted and the set of physical parameters (this relationship need be evaluated only once, regardless of the environment).

In this thesis, the conditional relationship $f(x \mid \overline{\eta})$ is estimated by means of a physical ray-tracing technique. The incident satellite signal is assumed to be a plane wave, with linear or circular polarisation. The ray-tracer evaluates the fields that are received by the mobile terminal through various mechanisms (detailed in Section 2.2) and weighted by the receiving antenna far-field pattern. The direct field exists in line-of-sight conditions. The fields reflected at first and second order from ground and wall surfaces as well as the fields diffracted by single building wedges are also accounted for.

The vector of physical parameters serves as input for generating a simulation area, described in Figure 2.22. The latter represents a straight section of any vehicle trajectory through a built-up area.

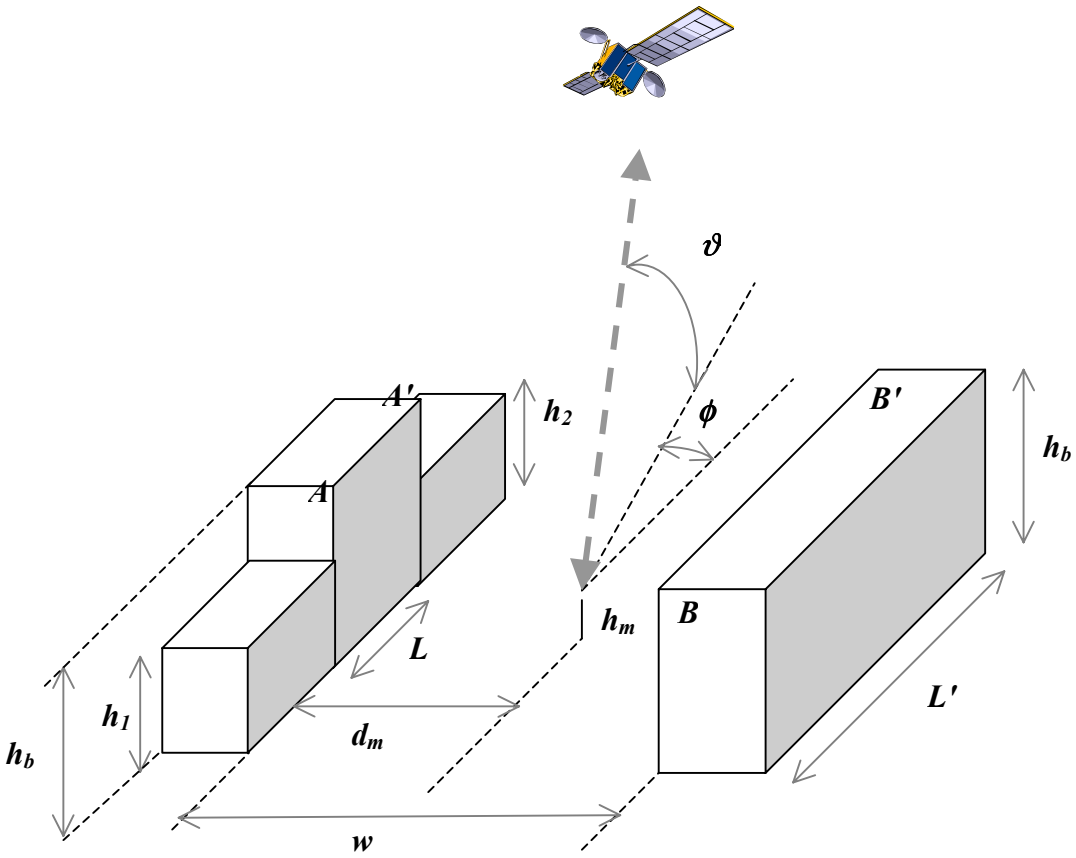

Figure 2.22 *Generic scenario in built-up areas*

The geometrical parameters are defined as follows:

- ϕ – azimuth angle of the satellite from the mobile relative to the axis of the street
- ϑ – elevation angle of the satellite link
- w [m] – street width
- d_m [m] – perpendicular distance from the mobile to the building face
- h_b [m] – height of the building immediately below the direct ray and height of the opposite building, relative to local ground level
- h_1, h_2 [m] – heights of the buildings next to the previous one, relative to local ground level
- h_m [m] – height of the phase centre of the mobile antenna relative to local ground level
- L [m] – building length on the left side of the street (the same value for every building)

- L' [m] – length of the fourth building (right side of the street in Figure 2.22), taken as much larger than L.

This list is obviously non-exhaustive. Nevertheless, the parameters listed above seem to be the most relevant ones. Their distribution can be easily measured and then described by known analytical distributions.

The number of buildings in the canonical configuration is limited. The study is indeed focused on the influence of the nearest buildings only. The restriction to four buildings is justified by the following observations.

(i) In urban areas, streets are not very long while in suburban areas, they are not straight. This reduces canyon effects and allows restriction to the local environment.

(ii) A small number of buildings eliminates artificial enhancing of far reflected or diffracted components, which are actually strongly attenuated along their way to the receiver due to roughness effects or multiple diffraction and absorption by obstacles.

It is worth noting that an analytical formulation such as (2.41) is sometimes inappropriate. That is mainly the case when second-order statistics or fade dynamics are considered. Assuming that the statistical variation of the conditional channel is equivalently described by a spatial movement of the receiver within the canonical area, the integration over Ξ is then realised by time series simulations. These are based on a random database generator whose inputs are precisely the measured distributions of the physical parameters. The random environments that are created do not represent any real area, but they share the same statistical properties as real areas. Hence, ray-tracing is used with a series of roadside buildings, randomly generated according to known statistical distributions for building height and spacing, street width, etc. For example, Figure 2.23 represents a typical suburban skyline (upper graph) together with the received power relative to LOS along the street at 2.1 GHz, with $\phi = 90\ °$, $\vartheta = 35°$, $w = 15$ m, $d_m = 5$ m.

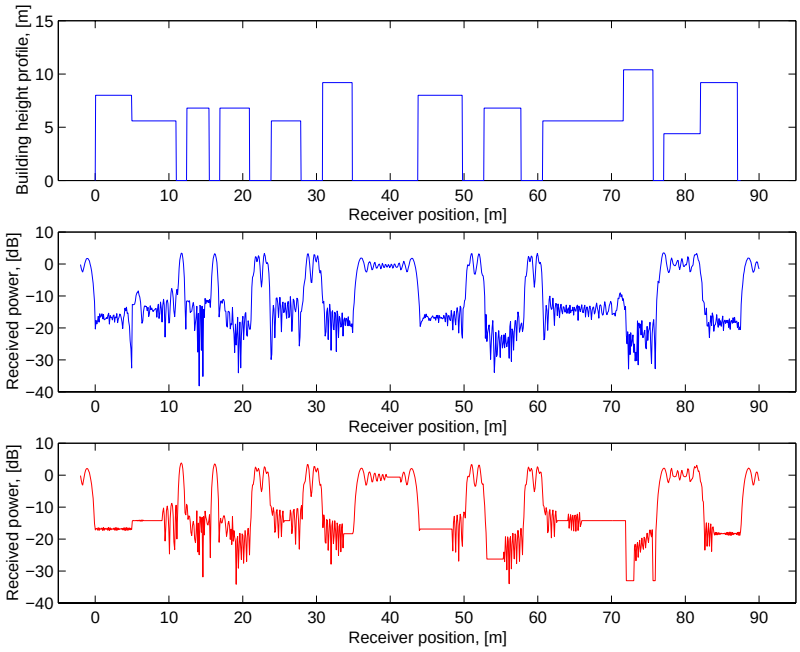

Figure 2.23 *Random building height profile and theoretical simulation outputs*

Meanwhile, two diffraction methods are compared. On the mid graph, equivalent currents (2.23) are used, while the last graph is based on classical UTD (2.19). Qualitatively, the characteristics of the signal resulting from the use of equivalent currents look fairly realistic. This is not the case with the UTD-based ray-tracing, which predicts a constant value for the received power in some locations.

As a conclusion, the classical UTD can be used as far as average results are expected. If finer descriptions of fade are needed, such as time series, then the use of equivalent currents (or any other method dealing with corner effects) is highly recommended.

2.3.2 Distribution of physical parameters

2.3.2.1 Building height

Regarding the distribution of building height in typical built-up areas, a suitable form is sought by comparing analytical distributions with geographical data measured in London (Westminster [38], Soho [39]) and in a typical suburban site (Guildford, Surrey [40]). Height measurements in Guildford (December 1997) were carried out on a road along which radio

data were measured in Spring 1992 [41]. Around 200 building heights were recorded along a distance of 5 km.

Figure 2.24 and Figure 2.25 depict measured building height histograms in Westminster and Guildford. They are best-fitted by a log-normal distribution:

$$T_{H_b}(h_b) = \frac{1}{h_b\sqrt{2\pi\sigma^2}} exp\left[-\frac{ln^2(h_b/\mu)}{2\sigma^2}\right] \tag{2.42}$$

where $ln(\mu)$ is the mean value of $ln(h_b)$ and σ is the standard deviation of $ln(h_b/\mu)$.

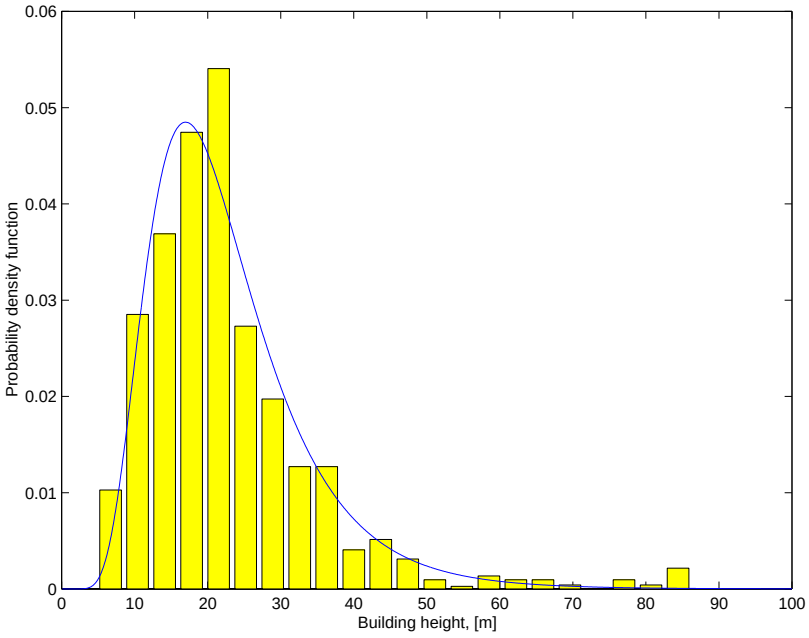

Figure 2.24 *Building height distribution measured in Westminster compared with a lognormal distribution*

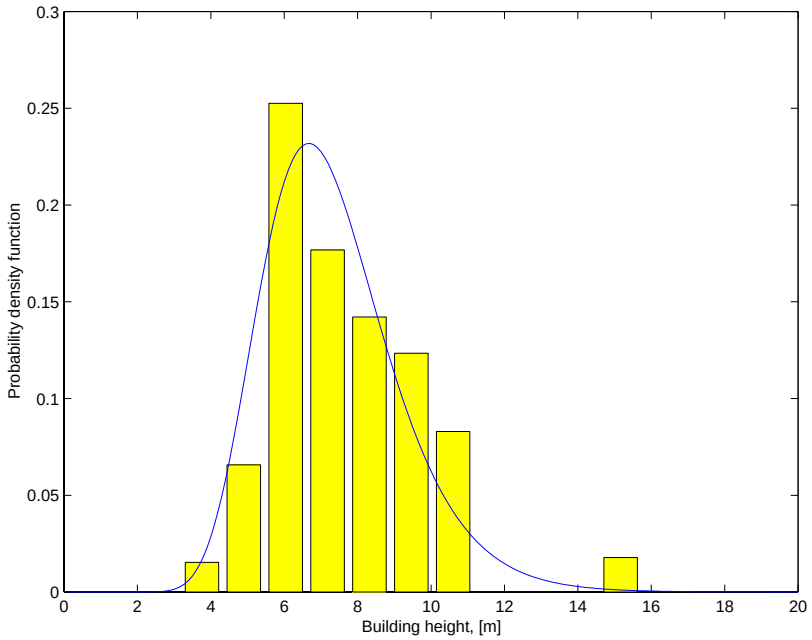

Figure 2.25 *Building height distribution measured in Guildford compared with a lognormal distribution*

A chi-square goodness-of-fit test has been performed on the data and the log-normal assumption is accepted with a good level of significance. Beyond its simplicity, the main advantage of the log-normal distribution is that the height probability density can be very small for small heights, which seems somewhat realistic. Estimated parameters μ and σ for all data sets are listed in Table 2.4.

Type of area	**Building height parameters**	
	μ **[m]**	σ
Westminster	20.6	0.44
Soho (London)	17.6	0.31
Guildford	7.1	0.25

Table 2.4 *Statistical parameters of the log-normal distributions*

When no geometrical information is known about the building height distribution in the area, typical values for classified environments can be found in the literature. For example, the following classification is proposed in [39], with sub-classes as appropriate:

- class 1 (rural)
  - A – flat
  - B – hilly
  - C – mountainous
- class 2 (suburban)
  - A – residential with some open spaces
  - B – residential with little or no open space
  - C – high-rise residential
- class 3 (urban and dense urban)
  - A – shopping area
  - B – commercial area
  - C – industrial area

Based on observed statistics of data, values for the building height parameters (in terms of number of storeys) are listed in Table 2.5 with regard to the sub-classes in class 2 and 3 environments. The number of storeys N_S is then easily converted into building height, using for example the simple rule given in [38]:

$$h_b\ [\mathrm{m}] = 3 + 3.7\, N_S \tag{2.43}$$

Class	Building height parameters [no. of storeys]	
	Mean	Standard deviation
2A	1	1
2B	1-2	1
2C	≥ 3	1
3A	≥ 3	1
3B	2	1
3C	1-2	1

Table 2.5 *Building height parameters for class 2 and 3 environments*

2.3.2.2 STREET WIDTH

Street width can be highly variable, especially in suburban areas. During this work, the street width is defined as the actual distance between buildings placed on opposite sides of the road,

including gardens and alleys. Measurements were recorded in Guildford in December 1997 [40] along the same road as discussed in the previous section. Again, the log-normal distribution appears to be the most reasonable choice. The limitation of the street width by a minimum value (about 9.5 m in Guildford suburbs) can indeed be well approximated by a lognormal probability density function. Figure 2.26 shows the measured histogram and the lognormal approximation. The parameters μ and σ estimated from the measurements are 14.9 and 0.65 respectively.

In dense urban areas, the street width tends to be more constant. The distribution can be validly approximated by a delta-function.

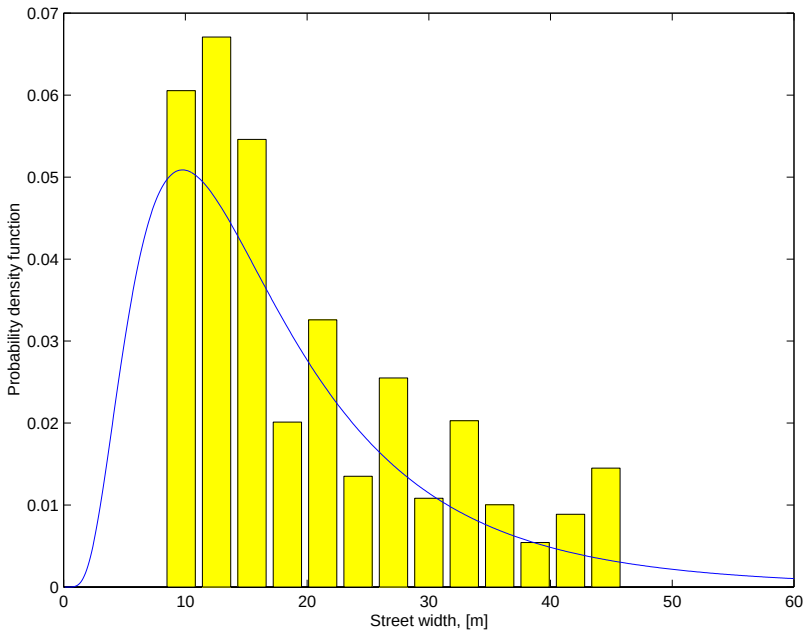

Figure 2.26 *Street width distribution measured in Guildford compared with a lognormal distribution*

2.3.2.3 Elevation angle

As far as non-geostationary satellites are concerned, the elevation angle varies continuously over time, even for static terminals. Using the orbit generator described in Appendix A, the distribution of elevation angle as seen from any point on the earth can be inferred from time series simulations, depending on the satellite selection strategy (see Section 1.6.3). Since the physical-statistical model deals with average results, it is again assumed that the system always chooses the satellite that is seen with the highest elevation angle.

In the simulations, four constellations are considered: Iridium (LEO-66), Globalstar (LEO-48), Teledesic (LEO-288) and Deligo (LEO-64). Whether possible, suitable analytical forms must be found to express the elevation angle probability density function.

Figure 2.27 illustrates the histogram of elevation angle for Iridium at the London latitude (51.5° N).

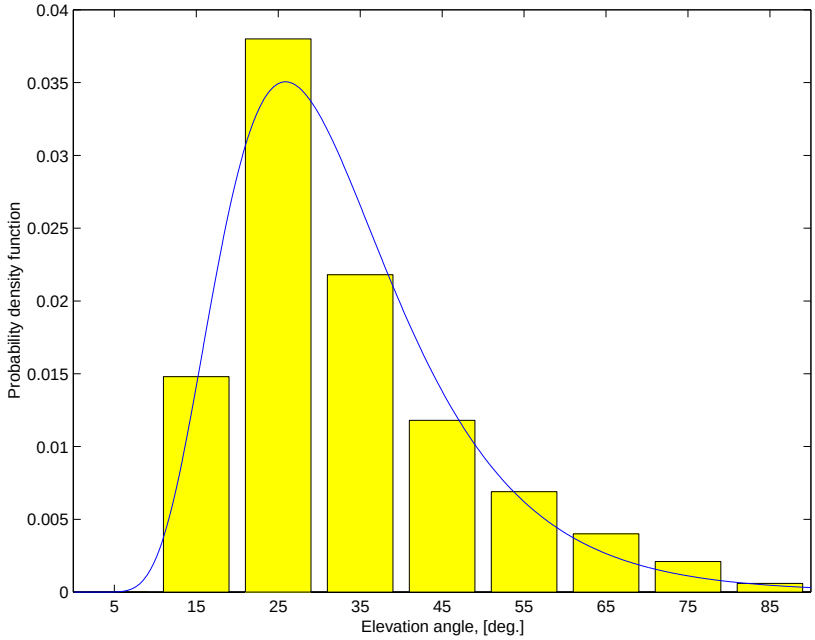

Figure 2.27 *Maximum elevation angle distribution for Iridium constellation at London compared with a lognormal distribution*

A lognormal distribution is actually the best fit:

$$T_{\Theta}(\vartheta) = \frac{1}{\vartheta\sqrt{2\pi\sigma^2}} exp\left[-\frac{ln^2(\vartheta/\mu)}{2\sigma^2} \right] \tag{2.44}$$

where the parameters μ and σ, depending on latitude, are assigned the following values for London and Rome latitudes respectively: (μ, σ) = (30.5°, 0.405) and (μ, σ) = (28.0°, 0.420).

For the two other constellations, no easy analytical formulation seems appropriate. Therefore the numerical distribution is used in the computations. Figure 2.28 illustrates for example the distribution of maximum elevation angle for Deligo system, at London and Rome.

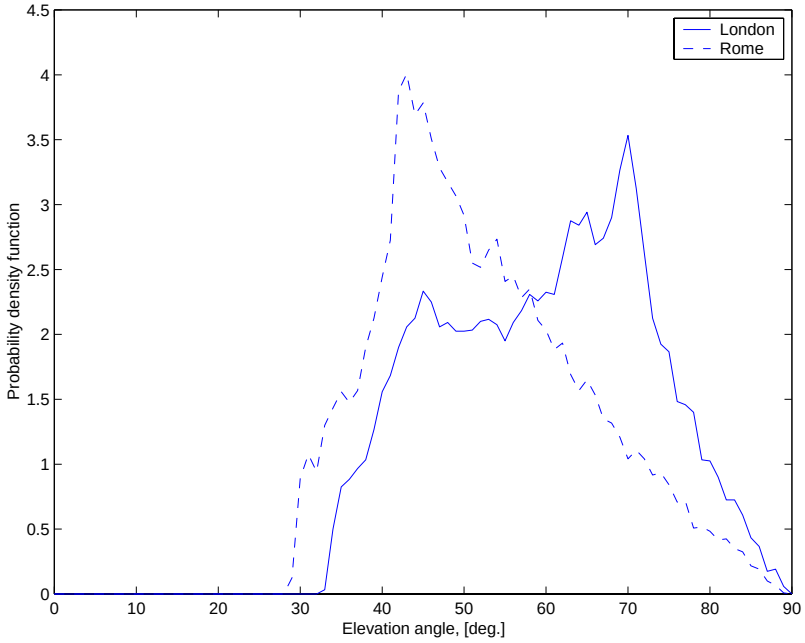

Figure 2.28 *Maximum elevation angle distribution for Deligo constellation at London and Rome*

For non-satellite systems, such as stratospheric platforms or experimental configurations (e.g. a helicopter), the distribution of elevation angle is easily featured by analytical expressions. For instance, when a helicopter is used as a transmitter platform, the elevation angle is usually kept at a constant value ϑ_0, so that the distribution is simply given by:

$$T_{\Theta}(\vartheta) = \delta(\vartheta - \vartheta_0) \tag{2.45}$$

2.3.2.4 AZIMUTH ANGLE

In particular situations, such as in experimental configurations, the value of the azimuth angle is precisely known. The distribution $T_{\Phi}(\phi)$ is then expressed as:

$$T_{\Phi}(\phi) = \delta(\phi - \phi_0) \tag{2.46}$$

where ϕ_0 is the known value for the azimuth angle relative to the street axis.

For mobile-satellite links, the azimuth angle relative to the street axis is the difference between the orientation of the street ϕ_{street} and the azimuth of the satellite link ϕ_{sat}, both

measured relative to the same reference direction, e.g. a terrestrial parallel. Therefore, the resulting azimuth angle, $\phi = \phi_{street} - \phi_{sat}$, is highly variable. The receiver can indeed be located in various streets that are randomly oriented with regard to the satellite link, while the latter continuously moves over time. In European cities, the orientation of the streets is assumed to be uniformly distributed over 360 degrees:

$$T_{\Phi_{street}}(\phi_{street}) = \frac{1}{2\pi} \tag{2.47}$$

In Northern American cities, the probability density would rather be a two-value discrete distribution along two perpendicular orientations.

The distribution of ϕ_{sat} depends on the system being considered. Figure 2.29 depicts for instance the probability density of ϕ_{sat} for the Iridium constellation. The distribution is not uniform and presents two maxima at 0 and π.

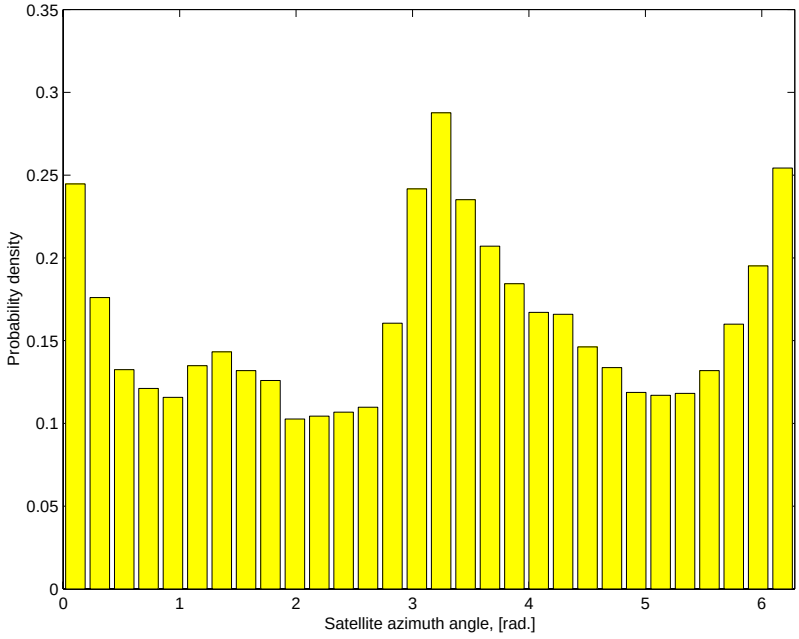

Figure 2.29 *Distribution of the nearest satellite azimuth angle (relative to terrestrial parallel) for Iridium constellation at London latitude*

Both azimuth angles being non correlated, the global distribution of ϕ results from the following convolution:

$$T_{\Phi}(\phi) = \int_0^{2\pi} T_{\Phi_{street}}(\phi + \upsilon)\, T_{\Phi_{sat}}(\upsilon)\, d\upsilon \tag{2.48}$$

If ϕ_{street} is assumed to be uniformly distributed, then the distribution of ϕ tends to be uniform too, as demonstrated in Figure 2.30. The distribution of ϕ is obtained by combination of a uniform distribution for ϕ_{street} with the distribution of Figure 2.29 for ϕ_{sat}. A uniform distribution is superimposed.

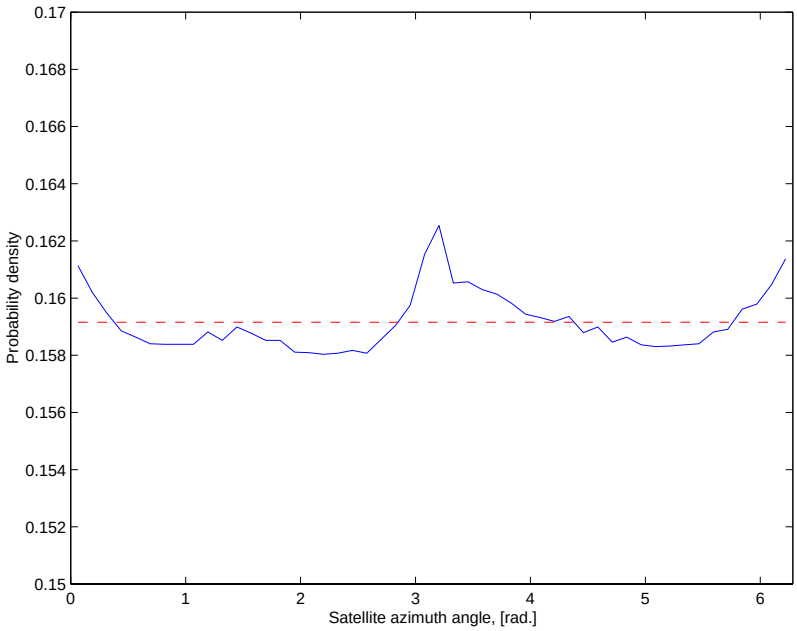

Figure 2.30 *Distribution of the global azimuth angle (relative to street axis) for Iridium constellation at London latitude compared with a uniform distribution*

The distribution of ϕ is considerably more uniform than that of ϕ_{sat}. Consequently, for mobile-satellite links, the distribution of azimuth angle relative to street axis can generally be approximated by:

$$T_{\Phi}(\phi) = \frac{1}{2\pi} \tag{2.49}$$

However, it is always possible to estimate the real distribution of ϕ_{sat} by means of the orbit generator, and then calculate from (2.48) a numerical distribution of relative azimuth angle.

2.3.2.5 OTHER PARAMETERS

Building heights h_1 and h_2 are fixed and equal to the average height in the area. The building length L is chosen sufficiently high so that the generic scenario is a good representation of a

significant street section, i.e. at least 10 metres, while L' should be of about tens of metres. Concerning receiver height and position, these can be assigned constant values, eventually relative to the street width *w*.

The following values or distributions have often been used throughout the simulations: h_m = 1.5 m to 2 m. The transverse position is for instance characterized by:

$$T_{D_m}(d_m) = \delta(d_m - w/2) \tag{2.50}$$

2.3.3 Narrowband channel characterization

2.3.3.1 BUILT-UP AND OPEN AREAS

In terrestrial microcellular applications, short and long scale variations are usually modelled on a separate basis [39], leading to the well-known concepts of fast and slow fading. In contrast, megacell propagation models must combine multipath and shadowing effects since they occur on similar distance scales [2]. In the proposed approach [36][40], the variation of the mean signal level is therefore modelled simultaneously with the fast fading fluctuations, both being directly related to the variation of the surrounding physical parameters.

Any urban or suburban area is described by the combination of road sections of two kinds, along which the envelope of the received field is not identically distributed: a distinction is made between open-area sections and built-up sections. Hence, the global distribution of the received amplitude is suitably represented by:

$$T_R(r) = p\, T_{R_O}(r) + (1-p)\, T_{R_b}(r) \tag{2.51}$$

where *p* is the percentage of open area, $T_{R_O}(r)$ is the probability density function of amplitude in open areas, and $T_{R_b}(r)$ is the probability density function of amplitude in built-up areas.

The percentage *p* must be estimated from inspection of the area.

1° Built-up areas

In built-up areas, the complex field amplitude is postulated to be given by the sum of a coherent main component plus a random contribution arising from multipath. The amplitude,

which is normalized with respect to that of the field received in the line-of-sight, is thus modelled as:

$$r_b = c + s \tag{2.52}$$

where c is the dominant component affected by shadowing and s is a complex quantity with zero mean and independent quadrature components, accounting for the multipath random contribution.

The field amplitude r_b in built-up areas is therefore Ricean distributed, as defined by:

$$T_{R_b}(r) = \frac{r}{\sigma^2} exp\left[-\frac{r^2 + c^2}{2\sigma^2} \right] I_0\left[\frac{rc}{\sigma^2} \right] \tag{2.53}$$

where σ^2 is the power of the multipath contribution s.

The combined physical-statistical approach allows the statistical parameters to vary with the physical parameters, depending on both the satellite and receiver position (azimuth and elevation angles, building height, street width, etc.). The Ricean parameters c and σ^2 must thereby be evaluated for every combination of the varying physical parameters, so that a distribution conditional on these parameters is obtain. This conditional probability density function is given by:

$$T_{R_b|\overline{N}}(r \mid \overline{\eta}) = \frac{r}{\sigma^2(\overline{\eta})} exp\left[-\frac{r^2 + c^2(\overline{\eta})}{2\sigma^2(\overline{\eta})} \right] I_0\left[\frac{rc(\overline{\eta})}{\sigma^2(\overline{\eta})} \right] \tag{2.54}$$

The relationships between the physical parameters and the Ricean parameters c and σ^2 are established in Section 2.3.3.2.

2° Open areas

In open areas, the ratio of the power in the main signal to that in the multipath components is a very large value. Subsequently, the Ricean distribution is expected to become a Gaussian distribution of unit mean and of variance depending on the physical parameters. Meanwhile, open areas are characterized by the absence of building, so the parameters (h_b, w, ϕ) are no relevant parameters anymore. The conditional distribution only depends on the elevation angle:

$$T_{R_O|\Theta}(r|\vartheta) = \frac{1}{\alpha_O(\vartheta)\sqrt{2\pi}} exp\left[-\frac{(r-1)^2}{2[\alpha_O(\vartheta)]^2}\right] \tag{2.55}$$

Experimental fade distributions, measured in open areas and reported in [41], show that (2.55) is actually a good representation of the open-area behaviour and that the variance α_O^2 of the Gaussian distribution decreases while both the elevation angle and the frequency increase.

Once both conditional distributions are known, the global conditional distribution is computed by (2.51). The global distribution of the received amplitude is finally determined by applying (2.41):

$$T_R(r) = \int_{\Xi} T_{R|\overline{N}}(r\,|\,\overline{\eta})\; T_{\overline{N}}(\overline{\eta})\; d\overline{\eta} \tag{2.56}$$

2.3.3.2 RELATIONSHIPS BETWEEN PHYSICAL AND STATISTICAL PARAMETERS

In built-up areas, the conditional relationships between the physical parameters and the Ricean parameters *c* and σ^2 are estimated by means of a ray-tracing technique applied to the canonical configuration of Figure 2.22. The amplitude *c* of the dominant component is taken to be that of the direct component in line-of-sight conditions, and for non-line-of-sight cases, that of the field diffracted by the wedge ***XX'*** immediately above the obstructed direct ray (***AA'*** or ***BB'*** depending of the link azimuth). In order to estimate the multipath contribution σ^2, all elementary contributions due to reflection and diffraction are power-added, except the one constituting the main component in non-LOS cases. Table 2.6 summarizes the calculation of the Ricean parameters.

Ricean parameters	**LOS**	**Non-LOS**
c	$\left\|E_{LOS}\right\|$	$\left\|E_{diff,XX'}\right\|$ ***XX'*** ≡ ***AA'*** or ***BB'***
σ^2	$\sum_n \frac{1}{2}\left\|E_{diff,n}\right\|^2 + \sum_m \frac{1}{2}\left\|E_{ref,m}\right\|^2$	$\sum_{n\neq XX'} \frac{1}{2}\left\|E_{diff,n}\right\|^2 + \sum_m \frac{1}{2}\left\|E_{ref,m}\right\|^2$

Table 2.6 *Relationships between the Ricean parameters and the ray-tracing outputs [36]*

In open areas, values of the variance α_O^2 extracted from measurements [41] are listed in Table 2.7 for three frequency bands and two elevation angles.

Elevation angle [degrees]	Frequency band		
	L band	S band	X band
60	– 16	– 15	– 11
70	– 18	– 17	– 16

Table 2.7 *Variance of fade* [dB] *in open areas*

2.3.4 Shadowing correlation model for satellite diversity

Satellite diversity is occasionally used in order to improve the availability of satellite communication services. However, the achieved gain is somewhat significant only if the combined path links behave differently. In this sense, useful information is provided by the shadowing correlation coefficient between two satellite links as a function of their angular separation [42]. Hence, the combined path links will behave differently if the correlation coefficient is negative (anti-correlation). If the correlation coefficient equals zero, then the path links are said to be statistically independent. This section illustrates that the physical-statistical approach inherently contains a shadowing correlation model for satellite diversity. This is a major advantage of the model, since most models in the literature do require some extra assumptions to account for correlation modelling.

For the sake of simplicity, assume that the vector of physical parameters is constituted by three components: building height h_b as well as azimuth and elevation angles ϕ and ϑ (the parameters w and d_m are assigned constant values). Considering two satellite links separated in azimuth by $\Delta\phi$, the shadowing variables are defined by:

$$\begin{aligned} c_1 &\stackrel{\Delta}{=} c(h_b, \phi, \vartheta_1) \\ c_2 &\stackrel{\Delta}{=} c(h_b, \phi + \Delta\phi, \vartheta_2) \end{aligned} \tag{2.57}$$

where c is the Ricean main component defined in Table 2.6.

The shadowing correlation coefficient is then expressed as:

$$\rho(\vartheta_1, \vartheta_2, \Delta\phi) = \frac{E\{(c_1 - \hat{c}_1)(c_2 - \hat{c}_2)\}}{\sqrt{E\{(c_1 - \hat{c}_1)^2\} E\{(c_2 - \hat{c}_2)^2\}}} \tag{2.58}$$

where the expectation is taken over all azimuth angles and building heights, assuming a uniform distribution for ϕ and a particular building height distribution, hence:

$$E\{x\} \stackrel{\Delta}{=} \hat{x} = \int_0^{2\pi} \int_0^{\infty} x(h_b, \phi)\, T_{H_b}(h_b)\, \frac{1}{2\pi}\, dh_b\, d\phi \tag{2.59}$$

The shadowing variables can also be expressed in dB, and expressions (2.57-58) become:

$$\begin{aligned} \boldsymbol{c_1} &= 20\, log\left[c(h_b, \phi, \vartheta_1)\right] \\ \boldsymbol{c_2} &= 20\, log\left[c(h_b, \phi + \Delta\phi, \vartheta_2)\right] \\ \rho_{dB}(\vartheta_1, \vartheta_2, \Delta\phi) &= \frac{E\left\{(\boldsymbol{c_1} - \hat{\boldsymbol{c}}_1)(\boldsymbol{c_2} - \hat{\boldsymbol{c}}_2)\right\}}{\sqrt{E\left\{(\boldsymbol{c_1} - \hat{\boldsymbol{c}}_1)^2\right\} E\left\{(\boldsymbol{c_2} - \hat{\boldsymbol{c}}_2)^2\right\}}} \end{aligned} \tag{2.60}$$

Various simulation results based on the correlation coefficient model are presented in Figure 2.31 (same elevations) and Figure 2.32 (different elevations) for various pairs of satellites in urban environment, at L band (1.6 GHz). The physical parameters are defined as follows:

- w_0 = 12 m, $d_m = w/2$
- h_m = 2 m (quadrifilar helix antenna),
- lognormal distribution for building height, with (μ, σ) = (20.6, 0.44).

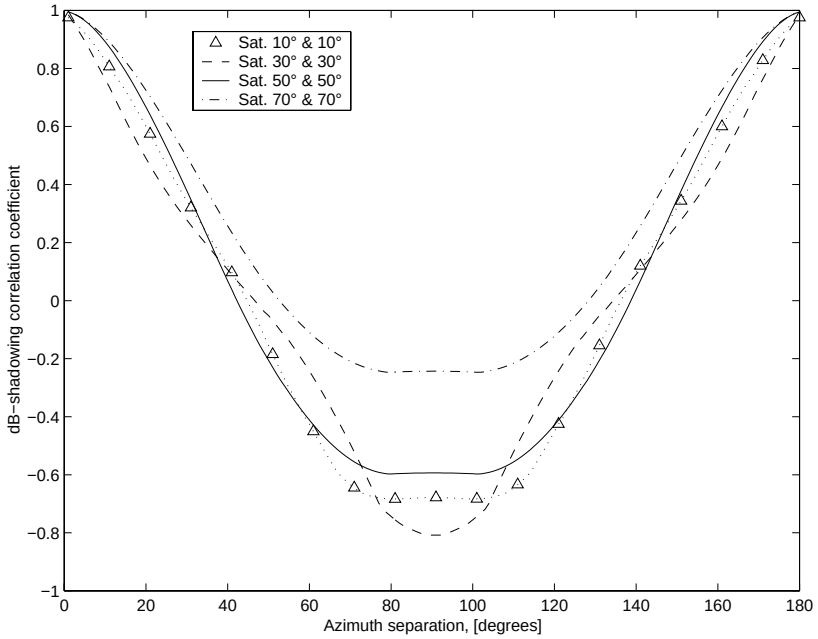

Figure 2.31 *Correlation coefficient of log-shadowing for several pairs of satellites with equal elevation angles ($d_m = w_0/2$)*

Several noteworthy points, in agreement with [43], are listed below.

(i) For azimuth separations less than around 30 to 40 degrees (depending on the elevation angle), a significant positive correlation is observed. For such separations, both satellite paths traverse the same building or are roughly aligned with the street axis for most azimuth angles.

(ii) For azimuth separations between around 40 and 140 degrees, the correlation is found to be negative, peaking for a separation of 90 degrees. The latter corresponds to the situation where a building often obstructs one path while the other is roughly aligned with the direction of the street canyon. This is particularly true at intermediate elevation angles (around 30 degrees), as seen on the graph. At lower (10 degrees) and higher (50 degrees and more) elevations, the probability for both signals to be simultaneously in the same state (i.e. blocked or unshadowed) is much higher than at intermediate angles.

(iii) For separations larger than around 140 or 150 degrees, a positive correlation is again observed, corresponding to the case where the paths cross buildings on opposite sides of the street or are both essentially in the line-of-sight due to alignment with the street. The symmetry of the curve with respect to 90 degrees results mainly from assumptions regarding both the mobile position ($d_m = w_0/2$) and the perfect correlation between building heights on opposite sides of the street.

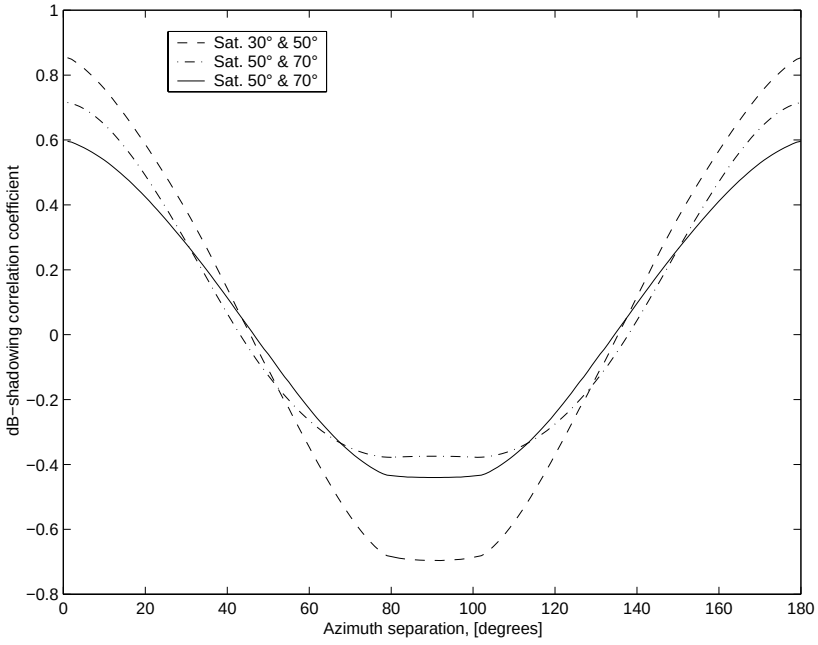

Figure 2.32 *Correlation coefficient of log-shadowing for several pairs of satellites with different elevation angles ($d_m = w_0/2$)*

(iv) If the two elevation angles are different, the positive correlation coefficient is reduced. However, the level of this correlation does not only depend on the difference between the elevation angles, but also on the average value of the elevation angles. Anyway, for larger differences and larger average elevations, the positive correlation tends to be smaller.

The case of very large elevation angles (> 80°) is not shown on the graph, the correlation being highly positive for any separation (both signals are always in LOS conditions).

Regarding the influence of the geometrical parameters, Figure 2.33 and Figure 2.34 present several shadowing correlation results in a suburban area as a function of the azimuth separation and one elevation angle. The area is described by a street width w_0 = 12 m and a building height distribution with parameters (μ [m], σ) = (7.1, 0.25). In Figure 2.33, elevation angles are taken as equal ($\vartheta_1 = \vartheta_2 = \vartheta$). In Figure 2.34, $\vartheta_1 = 45°$ is fixed and $\vartheta_2 = \vartheta$ is variable.

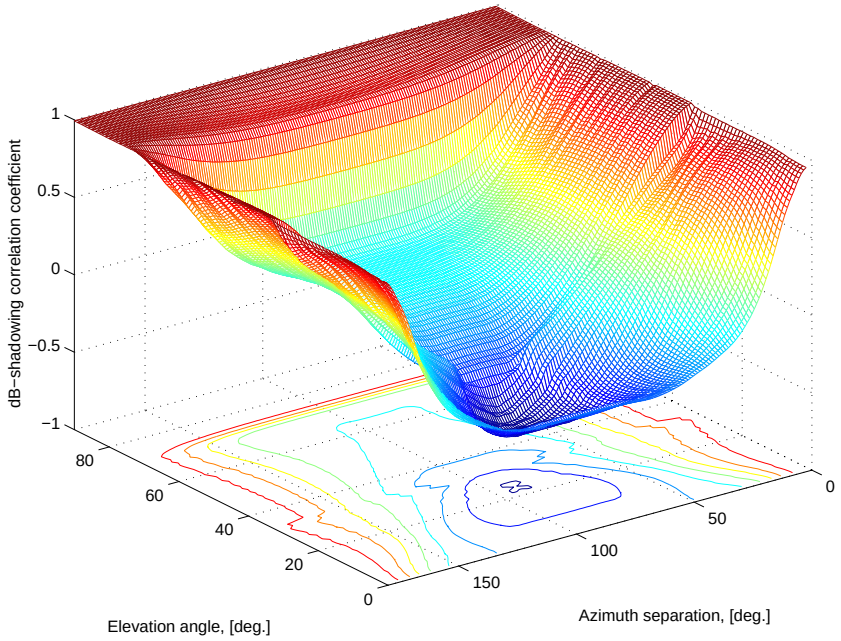

Figure 2.33 *Correlation coefficient of log-shadowing for all pairs of satellites with equal elevation angles in suburban area ($d_m = w_0/2$)*

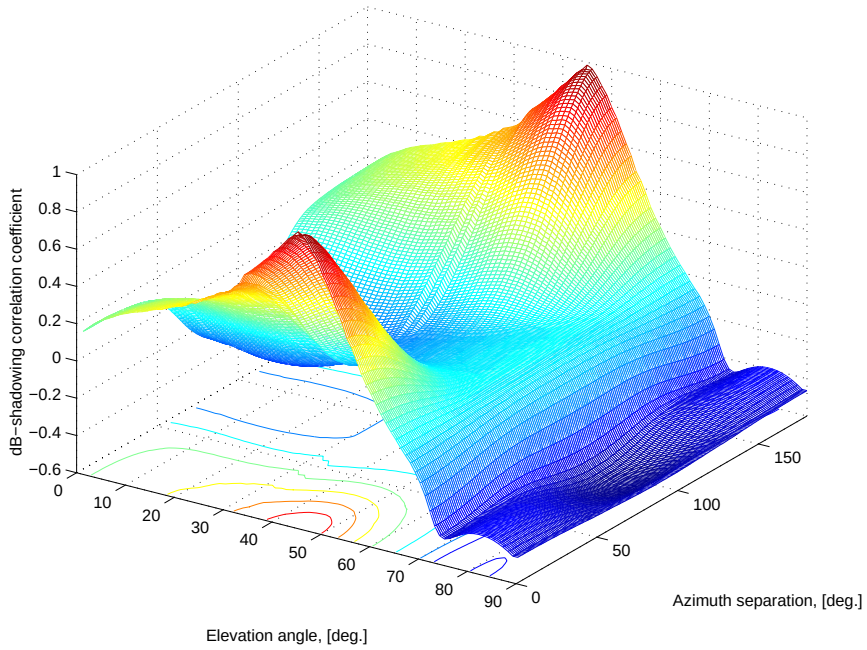

Figure 2.34 *Correlation coefficient of log-shadowing for all pairs of satellites with different elevation angles ($\vartheta_1 = 45°$) in suburban area ($d_m = w_0/2$)*

The absolute value of the negative correlation in Figure 2.33 is again maximum for an elevation angle of about 25 degrees. The elevation angle for which the negative correlation peaks is highly related to the average values of building height and street width. From additional simulations (w_0 = 20 m, with suburban/urban building height distributions), it seems that the larger the street width, the smaller this elevation angle. The same tendency is observed with respect to the building height, although the concerned elevation angle only slightly diminishes when the average building height increases. This completes remark (ii).

Figure 2.35 depicts the correlation coefficient of linear shadowing in a number of urban cases (w_0 = 12 m, (μ, σ) = (20.6, 0.44) and $d_m = w_0/2$). Quite naturally, the curves are less smooth than in the previous graphs. The linear shadowing variable c is indeed a quasi-discrete variable, with $c = 1$ in LOS cases and $c \cong 0$ in non-LOS situations. Nevertheless, remarks (i) to (iv) are still valid.

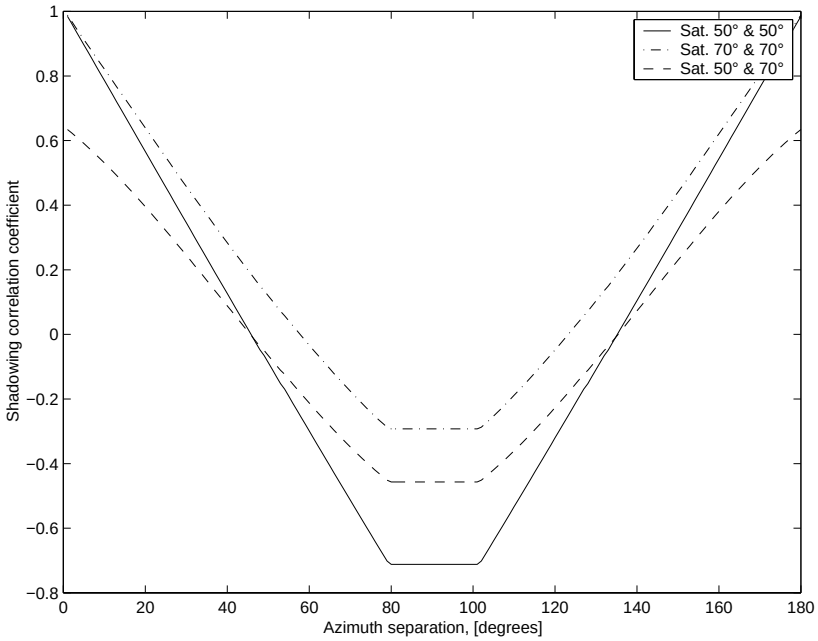

Figure 2.35 *Correlation coefficient of linear shadowing for several pairs of satellites with different elevation angles (urban area, $d_m = w_0/2$)*

Finally, Figure 2.36 illustrates the correlation achieved in the case of $d_m << w_0/2$ in the simulated urban area.

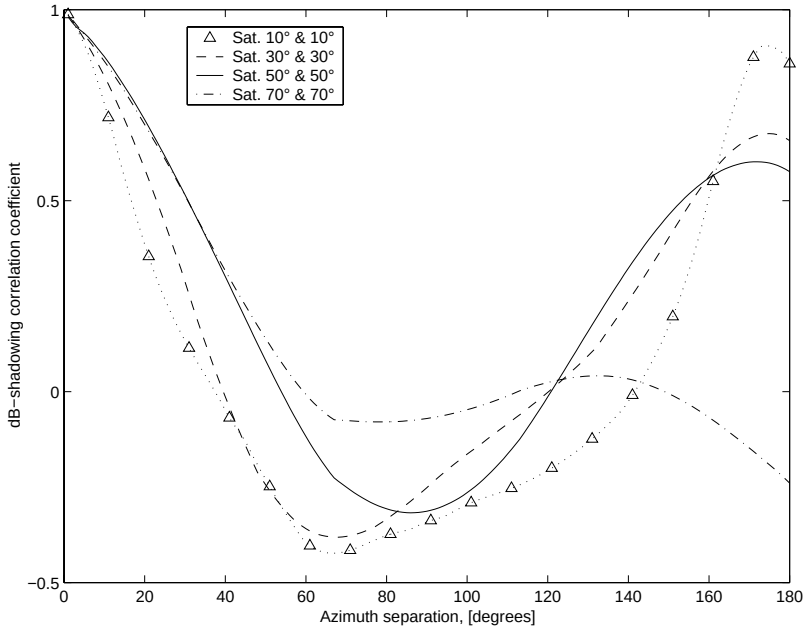

Figure 2.36 *Correlation coefficient of log-shadowing for several pairs of satellites with equal elevation angles ($d_m = 1$ m $<< w_0/2$)*

In this situation, the curves are no longer symmetrical. For very low elevation angles (< 10°), the correlation is still positive for $\Delta\phi < 40°$ and $\Delta\phi > 140°$ and the negative correlation peaks around 70°. When the elevation angle increases up to around 75° (for higher elevation angles, both signals would always be in the line-of-sight), the correlation remains positive for low azimuth separations (i.e. when both signals originate from the same side). However, it decreases as the separation increases and even becomes negative at 70° of elevation for separation higher than 140°. That can easily be explained. At such elevation angles, one path is often blocked while the other is in the line-of-sight, due to the non-central receiving position.

In order to obtain the global correlation coefficient for a given satellite constellation, one has to compute the following integration:

$$\hat{\rho}_{dB} = \int_0^{\pi/2}\int_0^{\pi/2}\int_0^{\pi} \rho_{dB}(\vartheta_1, \vartheta_2, \Delta\phi)\, T_{\Theta_1\Theta_2\Delta\Phi}(\vartheta_1, \vartheta_2, \Delta\phi)\, d\Delta\phi\, d\vartheta_2\, d\vartheta_1 \tag{2.61}$$

In order to evaluate (2.61), the joint distribution of the two highest elevation angles and the azimuth separation must be determined. However, these three parameters are highly correlated. Therefore, statistical independence between these variables cannot be assumed, so that $T_{\Theta_1\Theta_2\Delta\Phi}(\vartheta_1, \vartheta_2, \Delta\phi) \neq T_{\Theta_1}(\vartheta_1)\, T_{\Theta_2}(\vartheta_2)\, T_{\Delta\Phi}(\Delta\phi)$. This apparent problem can be solved by means of the orbit generator, which is able to provide simultaneous time series of ϑ_1, ϑ_2 and $\Delta\phi$. Hence, the integration is performed by computing the mean correlation coefficient from time series over a geosynchronous period of the orbit.

Nevertheless, it must be pointed out that the average shadowing correlation coefficient (2.61) is not as meaningful as it would be expected. Indeed, a small average correlation could result from a balance between high positive and negative correlation values as well. Subsequently, the distribution of the shadowing correlation coefficient appears to be a more significant output. Since all computations deal with time series, the evaluation of this distribution is quite straightforward.

2.3.5 Wideband channel characterization

The wideband channel characterization in built-up areas is based on the calculation of a conditional transfer function in the generic scenario of Figure 2.22. Within this reduced area, the ray-tracing tool allows for obtaining the channel baseband transfer function $\boldsymbol{H}(\Omega, t\,|\,\overline{\eta})$ or

the equivalent baseband impulse response $h(\tau, t\,|\overline{\eta})$ conditionally upon the vector of physical parameters. Considering the remarks of Section 2.2.5, simulations take into account reflection at the first two orders and UTD single diffraction. Figure 2.37 represents the transfer function amplitude versus building height over a bandwidth of 1 GHz around 1.6 GHz. Other physical parameters are given the following values:

- $w_0 = 15$ m
- $d_m = w_0/2$
- $\phi_0 = 90°$
- $\vartheta_0 = 60°$.

The receiver is a quadrifilar helix antenna (see Figure 2.15).

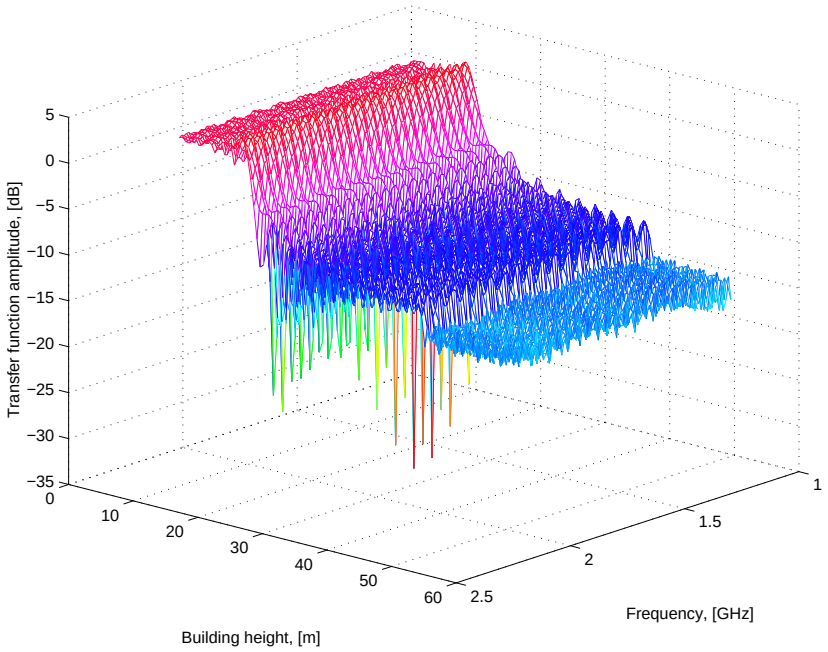

Figure 2.37 *Conditional static transfer function as a function of building height*

Every wideband parameter or function depending upon $\boldsymbol{H}(\Omega, t\,|\overline{\eta})$ or $h(\tau, t\,|\overline{\eta})$ (e.g. the RMS delay spread, etc.) can then be conditionally estimated and finally averaged over the set of physical parameters Ξ, as outlined by (2.41).

2.3.6 Validation and applications

2.3.6.1 FADE STATISTICS

1° First order distribution

The fade level resulting from building shadowing and multipath is denoted as $A_B = 1/r^2$. The fade distribution being easily related to the distribution of the amplitude, applying equation (2.41) yields:

$$T_{A_B}(A_B) = \int_0^{\pi/2}\int_0^{2\pi}\int_0^{\infty}\int_0^{w}\int_0^{\infty} T_{A_B|H_b D_m W \Phi \Theta}(A_B \mid h_b, d_m, w, \phi, \vartheta)\, T_{H_b}(h_b)\, T_{D_m}(d_m)\, T_W(w) \cdot \cdot T_{\Phi}(\phi)\, T_{\Theta}(\vartheta)\, dh_b\, dd_m\, dw\, d\phi\, d\vartheta \qquad (2.62)$$

with $T_{A_B|\overline{N}}(A_B \mid \overline{\eta}) = \frac{1}{2\, A_B^{3/2}} T_{R|\overline{N}}\left(\frac{1}{\sqrt{A_B}} \mid \overline{\eta}\right)$

Note that the above equation illustrates a major advantage of the method. It is clear from (2.62) that the influence of each physical parameter can be isolated and analyzed separately.

2° Second order statistics: level-crossing rate

First order statistics do not depend on the precise time (or location). Indeed, the fade distribution gives information such as the overall percentage of time, or the overall percentage of locations, for which the fade lies below a specified level. There is no indication of how this time/area percentage is made up. Yet, system engineers are interested in a quantitative description of the rate at which fades of any depth occur as well as of the average duration of a fade below a certain depth.

The level-crossing rate (LCR) at any specified level is defined as the expected rate at which the envelope crosses that level in a positive-going (or negative-going) direction [39]. A normalized LCR is often expressed as the average number of level crossings per wavelength.

The prediction of second-order statistics, however, does not stand any analytical simulation. Equation (2.41) is thus applied using time-series simulations as previously explained.

Obviously, time series also allow for estimating the average fade duration at any level of attenuation.

3° Comparison with experimental data

The physical-statistical model is applied to the case of a suburban road in Guildford, at 3 frequency bands and two elevation angles. Results are compared with fade statistics measured in Guildford in spring 1992 [41]. The experiment consisted of transmission between a vehicle moving along a suburban road, and a helicopter, used as a satellite simulation platform, moving parallel to the road at the same speed as the vehicle. This scenario was executed for several elevation angles. Given this configuration, expression (2.46) is used for the azimuth angle distribution: a value of 90 degrees relative to the street axis is assigned to the azimuth angle ϕ_0. In addition, it is assumed that the vehicle was situated in the middle of the street, so that expression (2.50) is used. The experimental receiving horn antenna far-field patterns for each frequency band (1.3 GHz, 2.4 GHz and 10 GHz) are included in the modelling and are shown in Figure 2.38.

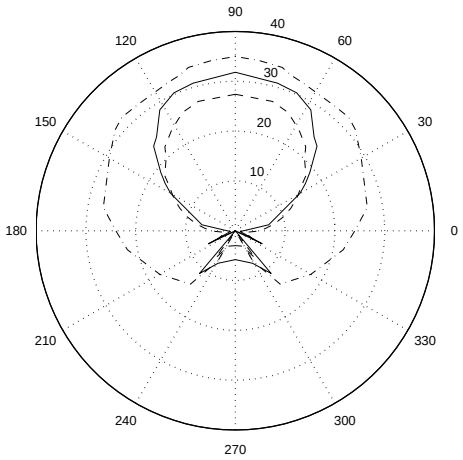

Figure 2.38 *Radiation patterns for the experimental antennas at L (dashed line), S (solid line) and X (dot-dashed line) bands*

The antennas were placed at a height h_m = 1.5 m. The percentage of open area is estimated, from inspection of the experimental area, as 20 %. In open areas, the measured values of the variance α_O^2 listed in Table 2.7 are used. The comparison between simulated and experimental fade distributions is shown in Figure 2.39 [40].

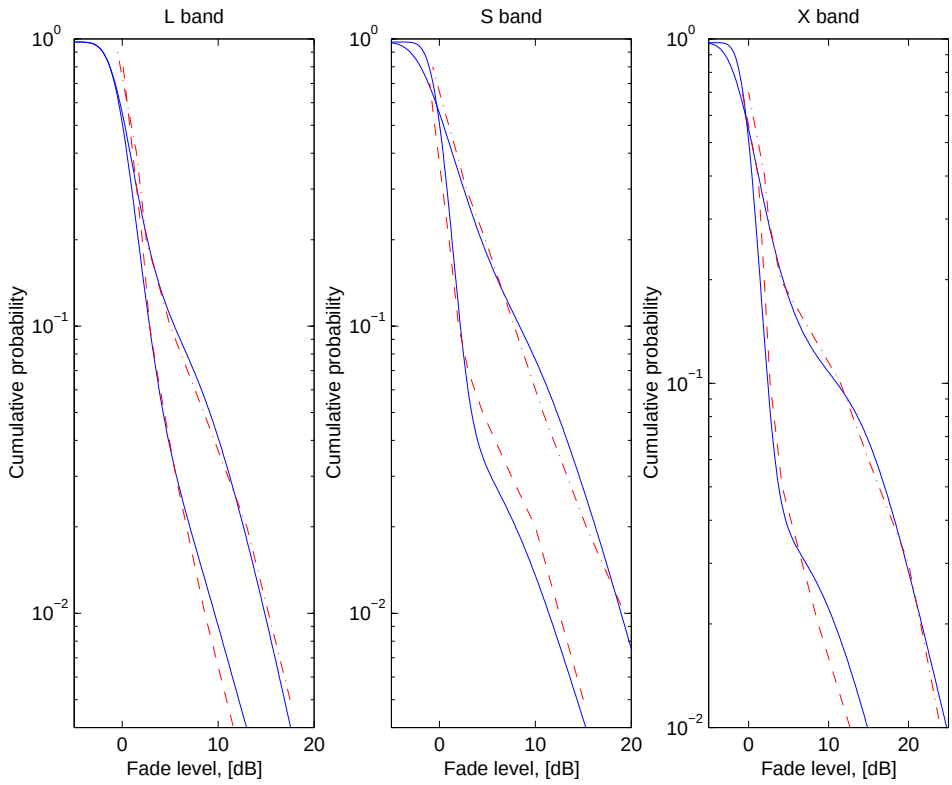

Figure 2.39 *Measured fade statistics at L (1.3 GHz), S (2.4 GHz) and X (10 GHz) bands for two elevation angles: 60° {dashed-dot lines} - 70° {dashed lines} together with simulation results {solid lines}*

Considering firstly simulated curves only, the fade levels exceeded during 1 % of time are summarized in Table 2.8.

Elevation angle [degrees]	Frequency band		
	L band	S band	X band
60	15	19	25
70	10	12	14.8

Table 2.8 *Attenuation [dB] exceeded during 1 % of time for various frequency bands and elevation angles*

Comparing now simulation results and measured data, a good agreement is found, especially at L band. Both experimental and simulated distributions are characterized by a knee. The position of this knee is related to the ratio of line-of-sight to non-line-of-sight conditions. For low probabilities and high frequencies, a small discrepancy is sometimes visible. At these

frequencies, radio propagation is very sensitive to effects that are not taken into account by the model (building shape, surface roughness, and foliage).

Results provided by the model have also been compared to fade distribution and LCR measurements recorded at L band in Athens City centre [44]. These data were also collected at various elevation angles by means of a helicopter used as satellite platform, flying parallel to the mobile terminal.

The street width was around 12 metres and the building height mainly varied between 15 and 21 metres. This physical information is used to infer a rough approximation of $T_{\overline{N}}(\overline{\eta})$. Building height is estimated by a lognormal distribution with (μ, σ) = (15 m, 0.30). Other parameters are given constant values:

- w_0 = 12 m
- $d_m = w_0/2$
- $\phi_0 = 90°$
- ϑ_0 depends on the experiment.

The L band receiving antenna is assumed to be a quadrifilar helix antenna (see Figure 2.15). Figure 2.40, Figure 2.41 and Figure 2.42 illustrate the comparison for elevation angles of 60, 70 and 80 degrees respectively [45].

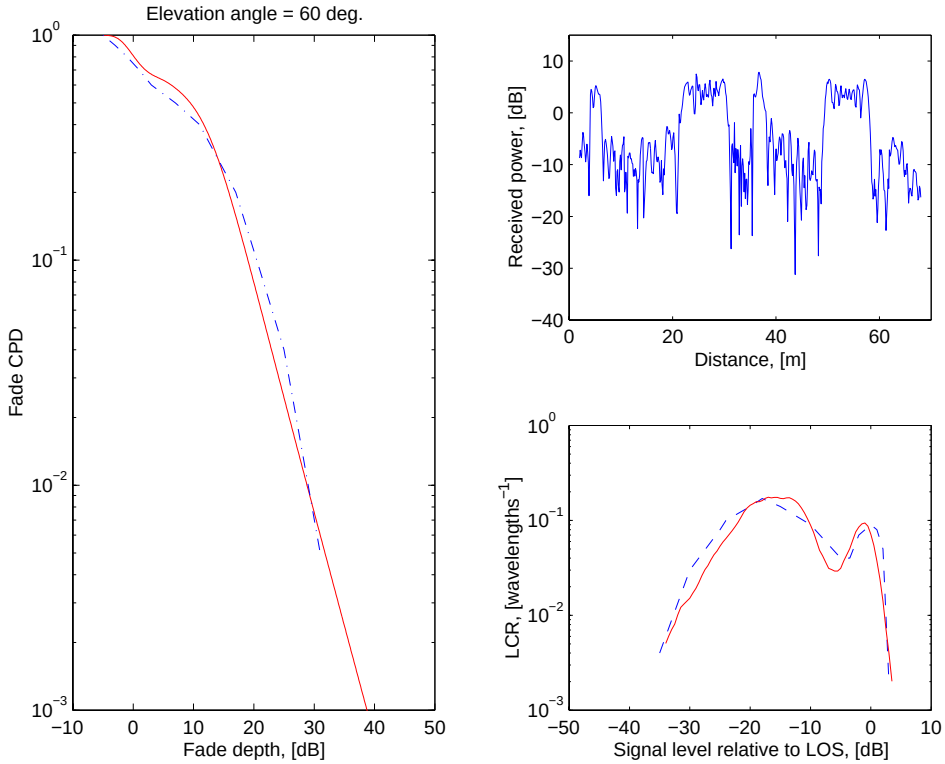

Figure 2.40 *Comparison between the model {solid lines} and measurements {dashed line} for an elevation of 60 degrees:*

- *cumulative fade distribution*
- *simulated path-loss (measurements are not represented)*
- *normalized level-crossing rate*

Again, a good agreement is found, while the simulated path-loss provided by time series looks clearly realistic if compared to measured path-losses presented in [44]. It can be noticed that the LCR at 60 degrees presents two peaks, which means that the channel is equivalent to a two-state Markov process. However, in comparison with Markov models, the physical-statistical modelling approach is physically derived from the environment and contains no empirical assumption.

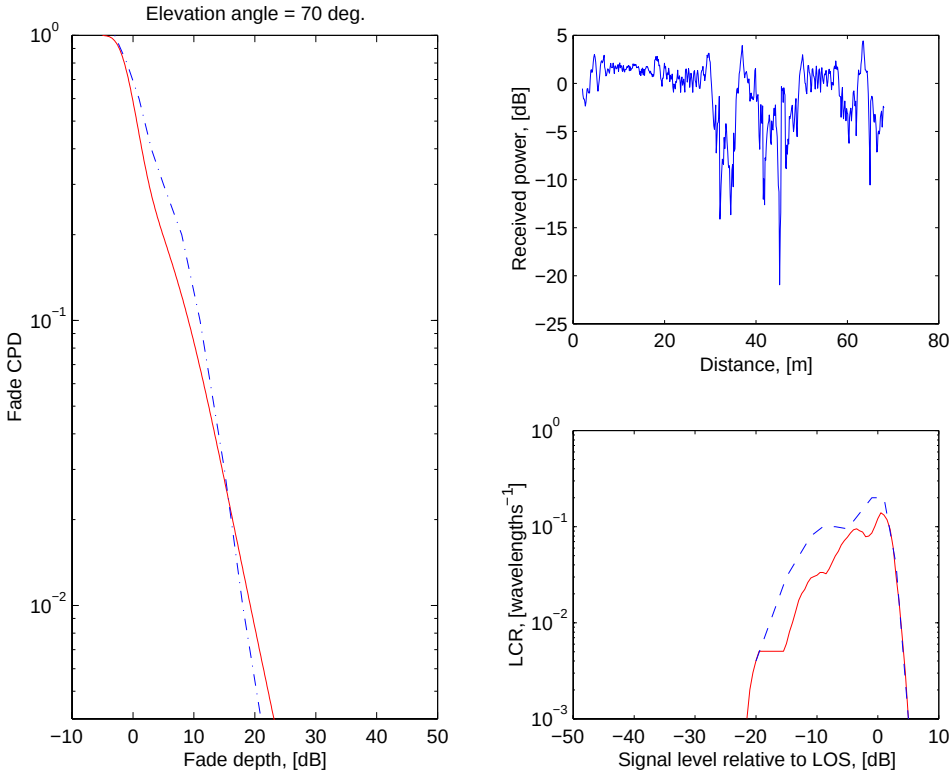

Figure 2.41 *Comparison between the model {solid lines} and measurements {dashed line} for an elevation of 70 degrees:*

- *cumulative fade distribution*
- *simulated path-loss (measurements are not represented)*
- *normalized level-crossing rate*

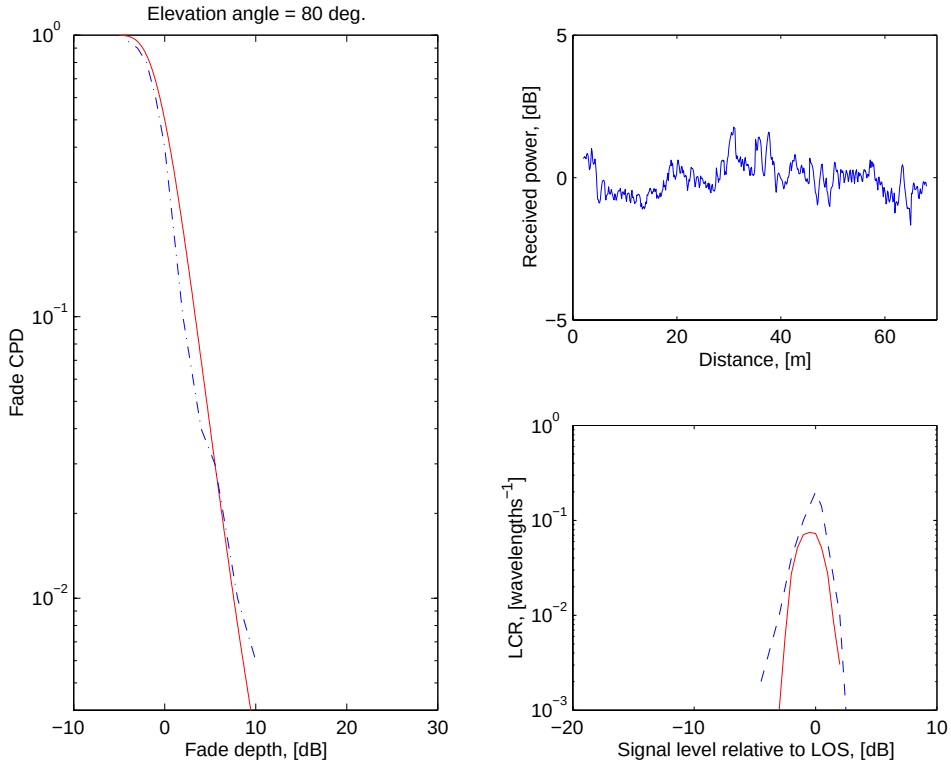

Figure 2.42 *Comparison between the model {solid lines} and measurements {dashed line} for an elevation of 80 degrees:*

- *cumulative fade distribution*
- *simulated path-loss (measurements are not represented)*
- *normalized level-crossing rate*

A comparison between fade statistics provided by the model and measurements from an airborne campaign carried out by the European Space Agency [46] is finally described. The environment is featured as a "residential area with detached two-three storeys houses (10-20 metres distant from the road)". Therefore, the distributions of physical parameters are approximately inferred as follows:

- a lognormal distribution for building height, with (μ, σ) = (7.1 m, 0.25) as in Guildford,
- w_0 = 35 m
- $d_m = w_0/2$
- $\phi_0 = 90°$
- ϑ_0 depends on the experiment.

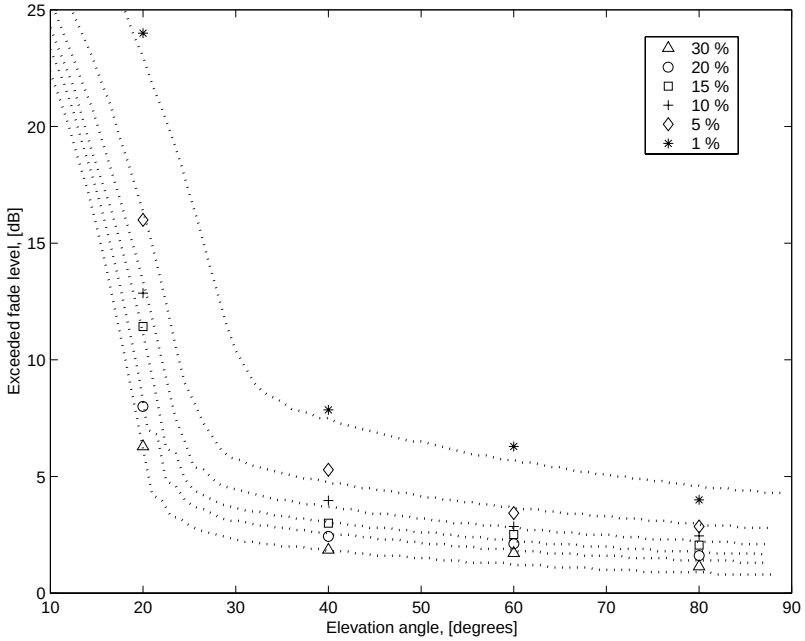

Figure 2.43 *Fade depth versus elevation angle (L band): comparison between simulations {dot lines} and measurements {various symbols}, for the following outage figures (from up to down): 1, 5, 10, 15, 20 and 30 %*

In Figure 2.43, fade depths are plotted versus elevation angle for six different values of the related percentage of time, i.e. link outage from a system point of view. The measured results are only given for four elevation angles from 20 up to 80 degrees. In general, the tendencies and orders of magnitude that are observed in the measured statistics are quite well reproduced by the model. There are some discrepancies, especially for elevation angles around 60 degrees. This could possibly be explained by interactions with trees or man-made objects that are closer to the actual road than the buildings (remember the definition of the street width) and that are not considered in the modelling approach. However, one should not forget that there is only one measurement point at 60 degrees within this interval.

Since trees might have a certain influence on fade statistics, the next section investigates how to include foliage attenuation in the physical-statistical approach.

2.3.6.2 EFFECT OF FOLIAGE

In suburban areas, roads are sometimes lined by trees. These are integrated in the model by including slabs of vegetation on both sides of the road, as illustrated in Figure 2.44.

The slabs of vegetation are assumed to be disposed symmetrically with respect to the middle of the street. They are characterized by three parameters:

- h_v – height of vegetation [m]
- w_v – width of the vegetation slab [m]
- w_{eff} – road width [m].

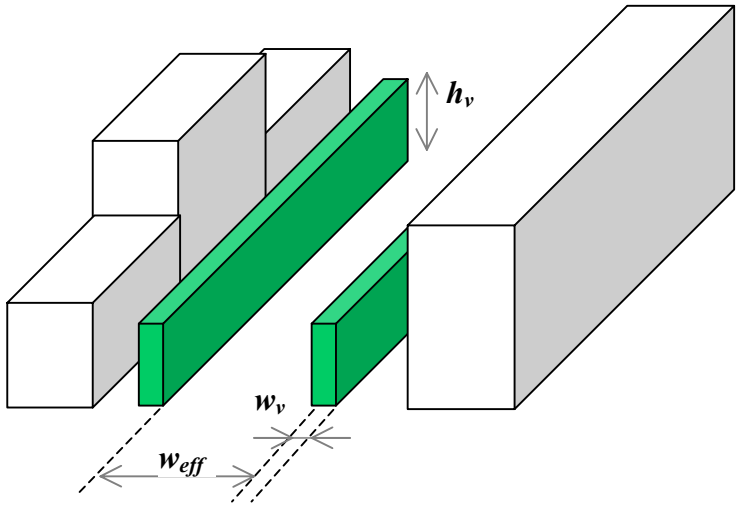

Figure 2.44 *Generic scenario accounting for roadside trees*

It is somewhat difficult to obtain objective description of tree statistics. In the following example, the physical parameters defining roadside trees are given constant values:

- $h_v = 3$ m
- $w_v = 1$ m
- $w_{eff} = 9$ m.

The ITU-R model (see Table 2.3) is used to calculate the attenuation due to the foliage slabs. Figure 2.45 depicts the effect of roadside trees at L band and X band in the same experimental configuration as the one used in Figure 2.39.

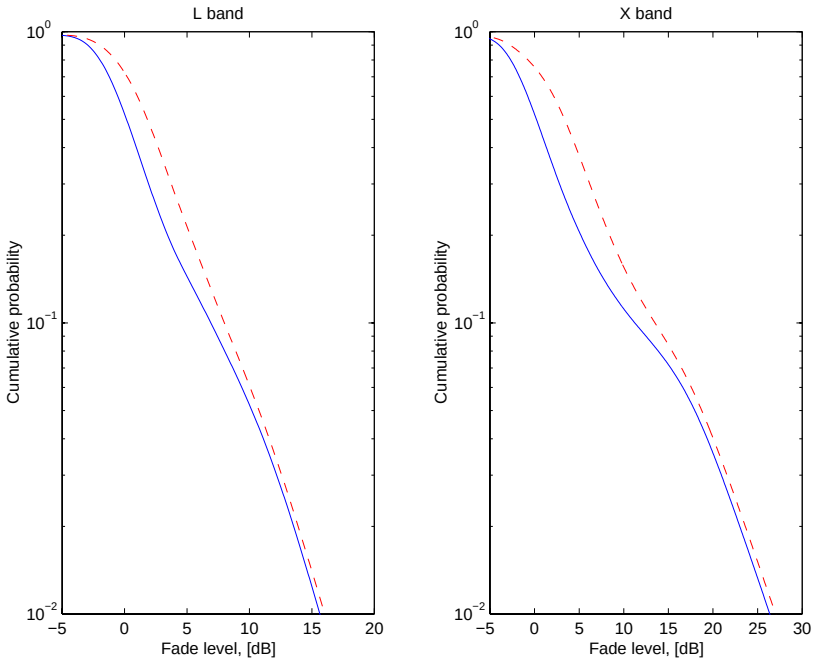

Figure 2.45 *Fade cumulative probability at L and X bands, elevation of 60°: no tree {solid lines} and roadside trees {dashed lines}*

It is observed on the graphs that the presence of roadside trees increases fade depths. This is quite expected since fade level is normalized relative to the LOS level. The latter by definition does not undergo any foliage attenuation. The effect of tree attenuation is quite reduced at L band but is somewhat more significant at 10 GHz.

2.3.6.3 WIDEBAND PARAMETERS

As already outlined, the distribution of any wideband parameter is easily estimated by means of the physical-statistical approach. For example, the average RMS delay spread is given by:

$$\hat{\tau}_{rms} = \int_{\Xi} \tau_{rms}(\overline{\eta}) T(\overline{\eta}) d\overline{\eta} \tag{2.63}$$

where $\tau_{rms}(\overline{\eta}) = \sqrt{\dfrac{\int_0^{\infty} [\tau - \hat{\tau}(\overline{\eta})]^2 \left| h(\tau|\overline{\eta}) \right|^2 d\tau}{\int_0^{\infty} \left| h(\tau|\overline{\eta}) \right|^2 d\tau}}$

A comparison between L band simulation results and measurements from [47] is shown in Figure 2.46. The average RMS delay spread is estimated in a suburban area as a function of the elevation angle. The ray-tracing includes single and double reflection as well as UTD single diffraction. The physical parameters are fixed as follows:

- a lognormal distribution of building height with several values for the parameters: (μ, σ) = (7.1 m, 0.25) and (12 m, 0.30) for simulations 1 and 2 respectively,
- w_0 = 15 m
- $d_m = w_0/2$
- ϕ_0 = 90° (similar to experimental configuration).

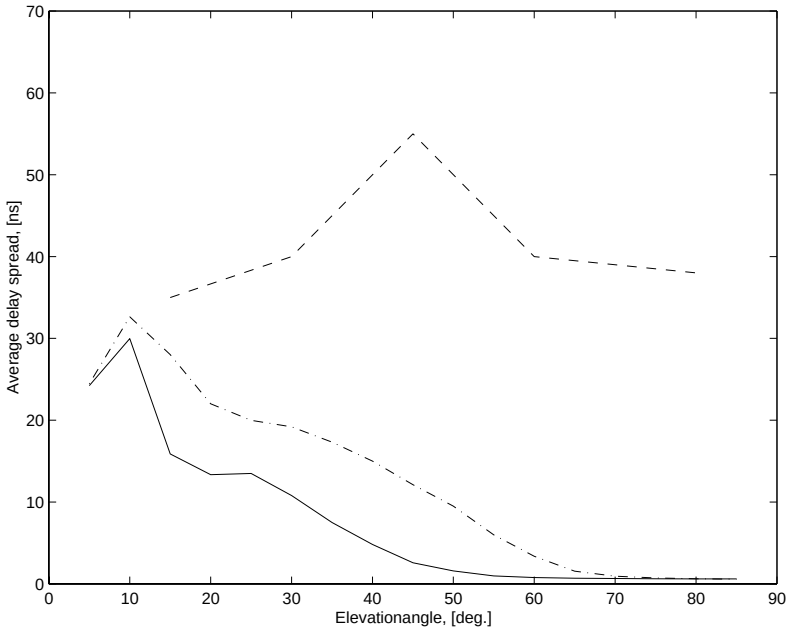

Figure 2.46 *Average RMS delay spread as a function of the elevation angle in suburban areas: measured data {dashed line}, simulations 1 {solid line} and 2 {dot-dashed line}*

It seems clear that simulations actually underestimate the average measured RMS delay spread, especially at high elevation angles. Although measured results might always be questionable, several reasons could explain for the discrepancies:

- the ray-tracing based prediction of RMS delay spread is very sensitive to the number of rays that are considered; for example, double diffraction is neglected here, though it might be significant in a wideband analysis,
- scattering from random man-made objects and obstacles such as trees is not taken into account; these interactions could really increase the value of the RMS delay spread.

2.3.7 Bit error probability

2.3.7.1 PREDICTION OF THE AVERAGE BER

For narrowband mobile phone systems, the channel is essentially non-selective. Hence, the variation of BER is only caused by the fluctuations of the received signal level. Considering multimedia applications, the system bandwidth may be larger than the coherence bandwidth of the channel (defined as the inverse of the total delay spread). In these situations, the channel is frequency-selective and the BER results from both attenuation and distortion. Note that the distortion level however depends on the receiver structure.

In each case, the average BER can be written as:

$$\widehat{P}_E(E_b/N_0) = \int_{\Xi} P_E(E_b/N_0 \,|\, \overline{\eta})\, T_{\overline{N}}(\overline{\eta})\, d\overline{\eta} \tag{2.64}$$

where E_b/N_0 designates the mean received bit-energy-to noise spectral density ratio.

Note that the integration in (2.64) can also be performed by means of time-series simulations, as explained in Section 2.3.1.

The forthcoming sections deal with methods for evaluating the conditional BER $P_E(E_b/N_0 \,|\, \overline{\eta})$ in both narrow- and wideband transmissions.

2.3.7.2 NON-SELECTIVE CHANNEL

From this point of view, the average BER as a function of average E_b/N_0 is obtained [48] by integration of the AWGN-channel bit error probability over the distribution of the received signal level, i.e.:

$$P_E(E_b/N_0 \,|\, \overline{\eta}) = \int_0^{\infty} p\left[\frac{E_b}{N_0}\frac{r^2}{E\{r^2\}}\right] T_{R|\overline{N}}(r \,|\, \overline{\eta})\, dr \tag{2.65}$$

where

- $p(E_b/N_0)$ is the probability of a bit error in the AWGN channel, the calculation of which is detailed hereafter,

- $T_{R|\overline{N}}(r\,|\,\overline{\eta})$ is the Ricean distribution (2.54-55) of the received amplitude relative to LOS level, conditional upon the set of physical parameters
- $E\{r^2\} = \int_0^\infty r^2\, T_{R|\overline{N}}(r\,|\,\overline{\eta})\, d\overline{\eta}$ is the average received power, relative to LOS level.

Therefore, the average received bit-energy (denoted as E_b/N_0) can be expressed, for a QPSK modulation in the absence of error-correcting code, as:

$$E_b = \frac{T_S}{2}\, P_{LOS}\, E\{r^2\} \tag{2.66}$$

where

- $P_{LOS} = P_T\, G_T\, G_R (\lambda/4\pi d)^2$ is the power of the line-of-sight contribution (P_T is the transmitted power, G_T and G_R and the transmitter and receiver antenna gains, and d is the distance satellite-to-receiver),
- T_S is the symbol rate.

In a QPSK modulation scheme without error-correcting code, the *raw* (uncoded) BER in the AWGN channel is given by:

$$p(E_b/N_0) = \frac{1}{2}\, erfc\,(\sqrt{E_b/N_0}) \tag{2.67}$$

Many satellite personal communication systems use convolutional codes (R_c, K). For such error correcting codes, a tight upper bound on the *coded* BER for soft Viterbi decoding is given [48] as a function of the effective E_b/N_0 by:

$$p(E_b/N_0) < \frac{1}{2k} \sum_{d=d_{free}}^{\infty} \beta(d)\, erfc\left[\sqrt{R_c\, d\, \frac{E_b}{N_0}}\right] \tag{2.68-a}$$

where

- $\beta(d)$ is the code weight distribution (derived from the code transfer function),
- d_{free} is the code free distance,
- $R_c = k/n$ is the code rate,
- K is the constraint length.

For large E_b/N_0 values, the asymptotic performance is obtained by taking the first term in (2.68-a):

$$p(E_b/N_0) < \frac{\beta(d_{free})}{2k} erfc\left[\sqrt{R_c\, d_{free}\, \frac{E_b}{N_0}}\right] \qquad (2.68\text{-b})$$

Note that in equation (2.68), the bit energy-to-noise density ratio E_b/N_0 must be an effective value, based on the information rate. For coded QPSK modulation, that means:

$$\frac{E_b}{N_0} = \frac{1}{2R_c}\frac{E_S}{N_0} \qquad (2.69)$$

where E_S is the received energy per symbol.

Figure 2.47 compares the BER achieved by two convolutional codes that are used by real systems. They are defined by:

- $R_c = 3/4$, $K = 7$
- $R_c = 1/3$, $K = 9$.

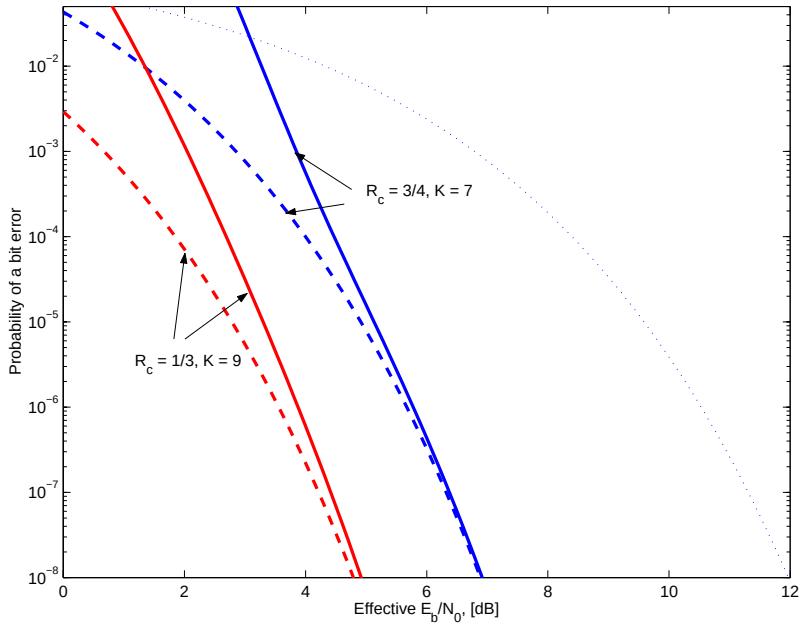

Figure 2.47 *Probability of a bit error for several convolutional codes: no code {dot line}, tight upper bound (2.68-a) {solid lines} and asymptotic bound (2.68-b) {dashed lines}*

Quite naturally, the second code performs better than the first, since both R_c and K are better. For instance, the required effective E_b/N_0 for a BER of 10^{-2} are about 3.5 dB for the R_c = 3/4 code and 1.5 dB for the R_c = 1/3 code. Considering a target BER of 10^{-3}, the required effective E_b/N_0 values are respectively 4 dB and 2dB.

2.3.7.3 SELECTIVE CHANNEL

A first method for estimation of the BER in selective channels is to use the previous relationships, but to consider that the noise spectral density N_0 integrates now all effects including system noise, inter-symbol (ISI) and multiple access interference (MAI). This assumes that ISI and MAI can be modelled by Gaussian processes, although it is only a rough approximation.

An alternative to estimate the conditional BER in selective channels postulates that a transfer function can be calculated in the generic scenario, all physical parameters being fixed [32]. This calculation is carried out using the ray-tracing method, as detailed in Sections 2.3.5.3 and 2.3.4. Having determined the transfer function, the conditional BER is estimated from noise-free scatter diagrams by means of a quasi-analytical method [32][49][50].

The transmission link is thus modelled as shown in Figure 2.48. The noise source of spectral density N_0 [W/Hz] is not indicated in the schema, since its effect is added analytically at the output of the receiver. In the following simulations, the receiver does not compensate at all for the channel distortion, being therefore suboptimal. Thereby, the BER only illustrates the maximal degradation to be encountered. Performance could be significantly improved by the use of adaptive equalizer.

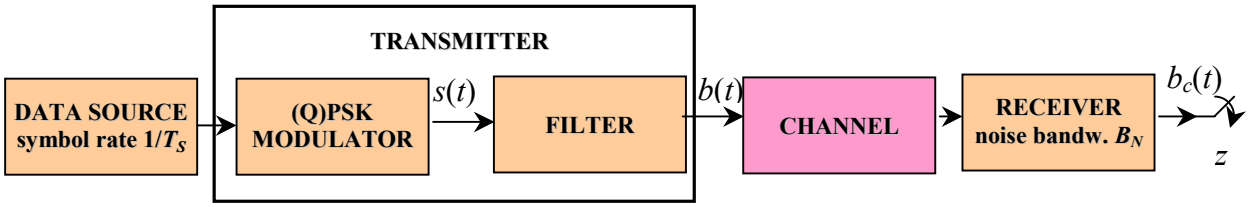

Figure 2.48 *Baseband communication system*

A sequence of N independent successive symbols, at a rate $1/T_s$, is considered at the input of the modulator. In a general PSK modulation scheme, the modulated baseband signal $s(t)$ can be written as:

$$s(t) = \sum_{k=1}^{N} (a_k + jb_k)\,\delta(t - kT_s) \tag{2.70}$$

In the case of a QPSK modulation, the pairs of values $[a_k, b_k]$ belong to $\{[(-1)^m, (-1)^n]\}$, with $m, n \in \{0, 1\}$. The signal is then filtered and passed through the channel. Transmitter and receiver filters are usually assumed to be identical square-root raised-cosine filters, denoted as $\boldsymbol{K}(\Omega)$ and $\boldsymbol{K}^*(\Omega)$ respectively. For the sake of simplicity, both transmission and reception filtering operations can actually be realised by a single raised-cosine filter.

The channel is easily accounted for in the Fourier domain. If the Fourier transform of the baseband filtered signal $b(t)$ is written as $\boldsymbol{B}(\Omega) = \Im\{b(t)\} = \Im\{s(t)\}\,\boldsymbol{K}(\Omega)$, the channel produces at the output of the receiver a signal

$$b_c(t) = \Im^{-1}\{\boldsymbol{B}(\Omega)\,\boldsymbol{H}(\Omega)\,\boldsymbol{K}^*(\Omega)\} \tag{2.71}$$

where $\boldsymbol{H}(\Omega)$ is the baseband transfer function of the physical channel.

The k^{th} noise-free sample at the output of the receiver is denoted as $z_k = x_k + jy_k = b_c(k\,T_s + \tilde{\tau}_d)$, $\tilde{\tau}_d$ being the estimated global transmission delay. The estimation of τ_d is carried out by maximizing the correlation between $[a_k, b_k]$ and $[x_k, y_k]$. Assuming perfect coherent demodulation, the average probability of a bit error is approximated [49] by:

$$P_E(E_b/N_0 \mid \overline{\eta}) = \frac{1}{N} \sum_{k=1}^{N} p_\varepsilon(E_b/N_0 \mid \overline{\eta} \parallel x_k, y_k)) \tag{2.72}$$

where $p_\varepsilon(E_b/N_0 \mid \overline{\eta} \parallel x_k, y_k)$ is the conditional bit error probability on the pair $[x_k, y_k]$.

Because the values $[x_k, y_k]$ are scaled quantities, they must be calibrated by the average power factor $\hat{P}$. For linear channels such as those defined in Sections 2.2.5 and 2.3.5, this calibration factor is well represented by the mean square value of the detected samples, i.e. $\hat{P} = \frac{1}{N} \sum_{k=1}^{N} (x_k^2 + y_k^2)$. In non-linear channels, different conventions are detailed in [49].

Using a quasi-analytical method, the conditional error probability for the pair $[x_k, y_k]$ is finally obtained in a QPSK modulation scheme by averaging (2.67) over all symbols $[x_k, y_k]$, as detailed in [49]:

$$p_\varepsilon(E_b/N_0 \mid \overline{\eta} \parallel x_k, y_k) = \frac{1}{4}\left\{ erfc\left[\frac{|x_k|}{\sqrt{N_0 B_N T_S}}\sqrt{\frac{E_S}{\hat{P}}}\right] + erfc\left[\frac{|y_k|}{\sqrt{N_0 B_N T_S}}\sqrt{\frac{E_S}{\hat{P}}}\right]\right\} \quad (2.73)$$

where

- N_0 is the system noise spectral density,
- E_S is the average energy per received symbol ($E_S = 2\ E_b$ for a QPSK modulation scheme), given by:

$$E_S = T_S\ P_{LOS}\ \frac{|\boldsymbol{B}(\Omega)\ \boldsymbol{H}(\Omega)|^2\ d\Omega}{|\boldsymbol{B}(\Omega)|^2\ d\Omega} \quad (2.74)$$

where the free-space loss and antennas gains are removed from the expressions of the channel transfer function $\boldsymbol{H}(\Omega)$.

Note that for ideal Nyquist filtering ($B_N T_S = 1$) and in the absence of channel ($x_k = y_k = \pm 1$), (2.73) reduces to the well-known theoretical result (2.67).

2.3.7.4 SIMULATION RESULTS

Several simulations are performed in a typical suburban area. Its characteristics are given by:

- a lognormal distribution for building height, with (μ, σ) = (7.1 m, 0.25),
- w_0 = 10 m
- $d_m = w_0/2$
- ϕ_0 = 90° (which constitutes the worst situation)
- ϑ_0 = 60°.

The satellite signal is defined by a frequency of 1.6 GHz and by circular polarisation. For non-selective channels, a comparison is made between the model (2.64-66) and simple statistical fading models such as Rayleigh or Nakagami.

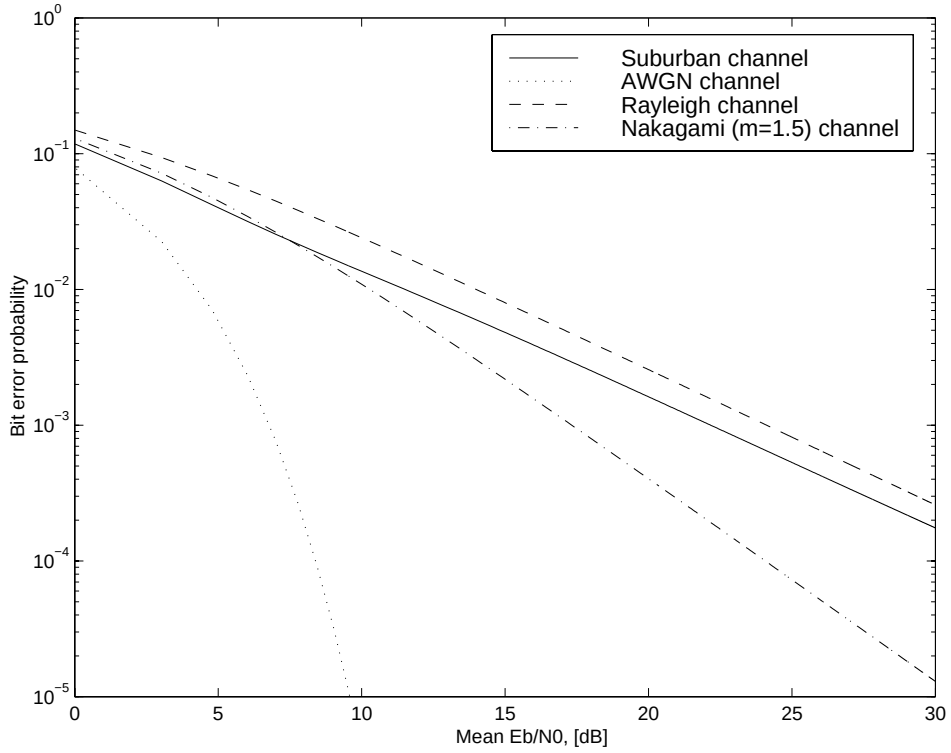

Figure 2.49 *Comparison between suburban narrowband channel and Nakagami channels (m = 1 being equivalent to a Rayleigh channel)*

Figure 2.49 shows that the suburban channel with an elevation angle of 60 degrees can be compared to a Nakagami channel with *m*-factor between 1 (Rayleigh) and 1.5. This means that suburban propagation conditions will severely degrade the narrowband system performance if a sufficient margin is not implemented. Enhanced fade margins are therefore required in built-up areas. For example, an 11-dB margin is recommended in [51] for a typical L band mobile-satellite system under mixed shadowed/unshadowed conditions. However, this fade margin is geared towards low elevation angles. At higher elevation angles, shadowing is less likely and thus less margin should be necessary. It is therefore interesting, as suggested in [51], to implement a margin requirement that drops linearly moving from low to high angles.

Figure 2.50 compares for a weakly-selective channel (2 MHz bandwidth) predictions (2.71-74) of BER resulting from analytical integration (2.64) and time-series approaches. Remember that, in the time-series simulations, the integration (2.64) is performed by moving the receiver in a randomly generated area, featured by the same statistical characteristics as those used in the analytical estimation. Agreement is good, meaning that the reduced number of buildings in the canonical case of Figure 2.22 is a good representation of a real street.

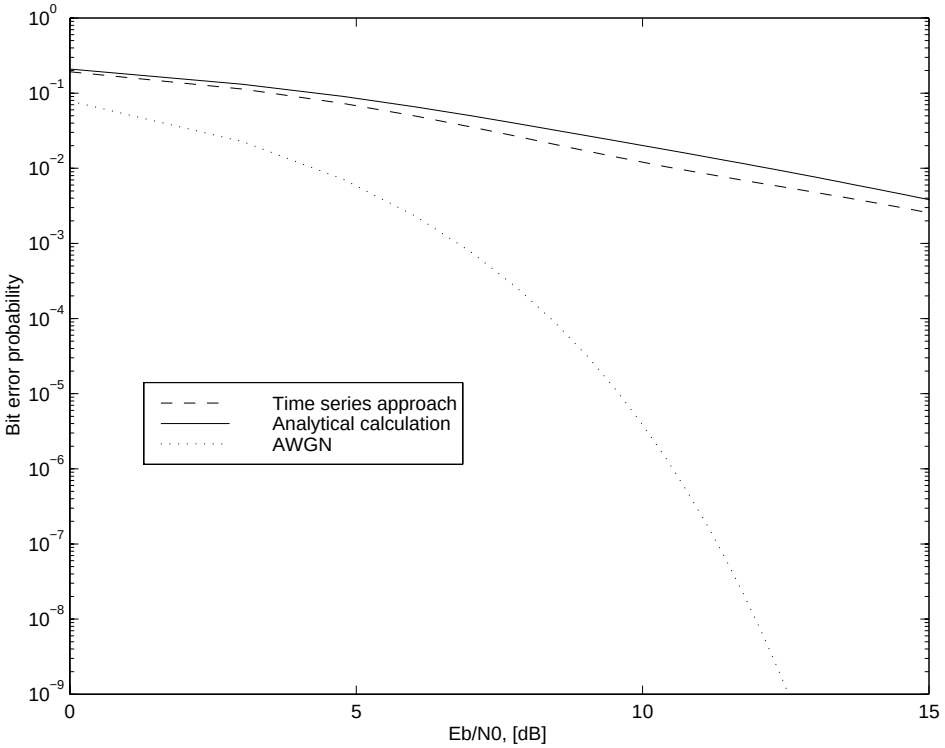

Figure 2.50 *Comparison between wideband analytical and time series estimations of BER*

Finally, methods of BER estimation for selective and non-selective channels (eqns. (2.71-74) versus (2.65)) are compared in a narrowband case (bandwidth of 200 kHz). In Figure 2.51, both methods actually give analogous results. This indicates at least that both methods converge in the case of narrowband transmissions.

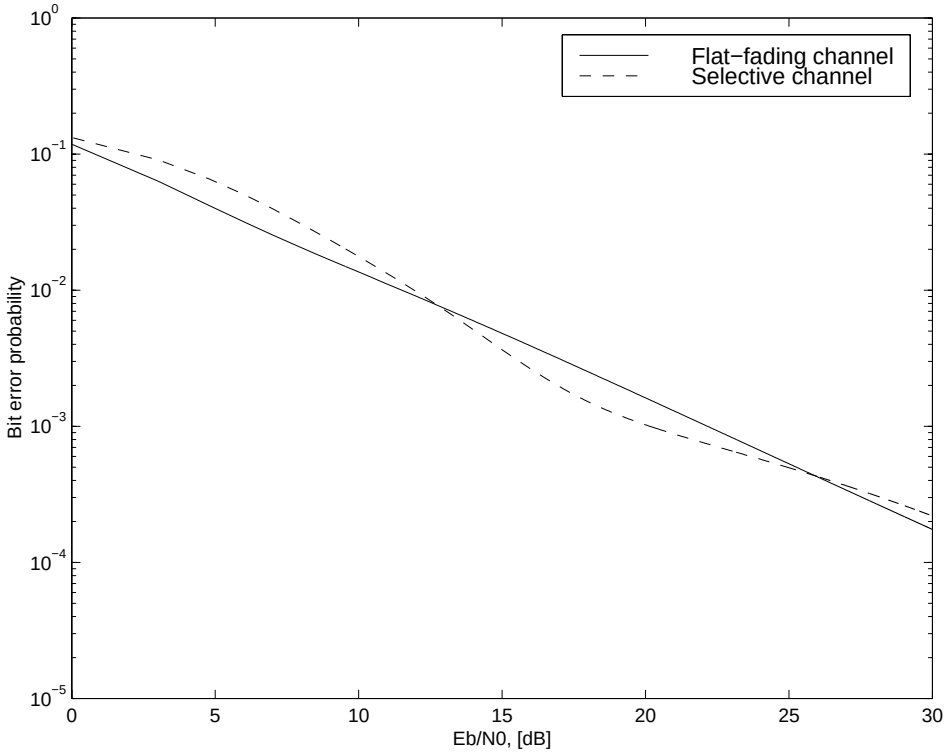

Figure 2.51 *Comparison between BER estimation for selectivity and non-selectivity assumptions in a narrowband case*

2.4 SUMMARY

Physical and physical-statistical models have been developed to account for the propagation mechanisms in built-up areas, which are responsible for shadowing and multipath effects.

The physical modelling is based on a ray-tracing approach. The latter includes several physical interactions, such as reflection by ground and wall surfaces, diffraction by building wedges, scattering by rough surfaces and attenuation through foliage. Reflection is modelled by the use of the complex Fresnel coefficient depending upon frequency-varying material electromagnetic properties. Regarding single edge diffraction, the Uniform Theory of Diffraction is completed by the use of equivalent currents that allow taking into account the finite length of the wedge and corner effects.

Scattering by rough walls is briefly introduced. It is also explained why this contribution might become significant with respect to specular reflection. Finally, several empirical models accounting for the attenuation through foliage and trees are presented.

As far as wideband applications are involved, the ray-tracing technique is extended, in order to yield predictions of channel transfer function and related parameters, such as the RMS delay spread and the BER.

The physical model has been quite successfully compared from a narrowband point of view with experimental data recorded in a street of Louvain-la-Neuve at 12.5 and 30 GHz.

A combination of physical and statistical approaches has also been developed which integrates the statistical ease-of-use and low computational requirements of empirical or statistical models with the physical insight and wide parameter range of deterministic models. This approach is referred to as physical-statistical modelling. The general method relates any channel simulation to the statistical distribution of physical parameters, such as building height, width and spacing, street width or elevation and azimuth angles of the satellite link. Relationships between physical and statistical results are estimated by means of the developed ray-tracing tool. The variation of several physical parameters has been measured or simulated and analytical statistical distributions have been proposed within the text. The physical-statistical modelling has then been widely applied: prediction of fade statistics, delay spread and BER, shadowing correlation model. Several experimental results at L, S and X bands have finally been compared with the model and a very good agreement is generally found, especially for fade statistics (probability density and level crossing rate).

2.5 REFERENCES

[1] SAUNDERS, S.R., TZARAS, C., OESTGES, C., VANHOENACKER D., Physical-statistical modelling of the land mobile-satellite channel, 1st International Workshop on Radiowave Propagation Modelling for SatCom Services at Ku band and above (ESTEC, Noordwijk, The Netherlands), pp.95-102, October 1998.

[2] SAUNDERS, S.R., *Antennas and propagation for wireless communication systems,* Wiley, Chichester, 1999.

[3] ITU-R, *ITU-R Recommendations – Propagation in non-ionized media,* PN series vol., ITU, Geneva, 1994.

[4] GOLDHIRSH, J., VOGEL, W.J., Propagation effects for land mobile-satellite systems: overview of experimental and modelling results, *NASA Reference Publication*, n° 1274, February 1992.

[5] LOO, C., A statistical model for a land mobile-satellite link, *IEEE Trans. Veh. Tech.*, vol. 34, n° 3, pp. 122–127, 1985.

[6] LUTZ, E., CYGAN, D., DIPPOLD, M., DOLAINSKY, F., PAPKE, W., The land mobile-satellite communication channel-recording, statistics and channel model, *IEEE Trans. Veh. Tech.*, vol. 40, n° 2, pp. 375–385, 1991.

[7] VAN DOOREN, G.A.J., *A deterministic approach to the modelling of electromagnetic wave propagation in urban environments*, PhD thesis, Technische Universiteit Eindhoven, 1994.

[8] CHARRIÈRE, P., CRAIG, K.H., A ray based propagation tool for digital systems, 4th Symposium of the AGARD Sensor and Propagat. Panel on Digital Communications Systems: propagation effects, technical solutions, system design (Athens, Greece), September 1995.

[9] VYNCKE, C., *Diffraction by obstacles in communication systems: modelling and validation*, PhD thesis, Université catholique de Louvain, 1995.

[10] COST 235, *Radiowave propagation effects on next generation fixed-services terrestrial telecommunications systems*, European Commission, Brussels, 1996.

[11] BALANIS, C.A., *Antenna theory: analysis and design*, Harper & Row, New York, 1982.

[12] BOITHIAS, L., *Propagation des ondes radioélectriques dans l'environnement terrestre*, Dunod, Paris, 1983.

[13] COST 255, *Radiowave propagation modelling for new SatCom services at Ku band and above*, European Commission, Brussels, to be published.

[14] LAYER, F., FRÜCHTING, H., Modeling time-variant wideband indoor radio channels with rough scattering surfaces: a comparison, European Wireless '99 (Munich, Germany), pp. 279-284, October 1999.

[15] LANDRON, O., FEUERSTEIN, M.J., RAPPAPORT, T.S., A comparison of theoretical and empirical reflection coefficients for typical exterior wall surfaces in a mobile radio environment, *IEEE Trans. Antenn. Propagat.*, vol. 44, n°3, pp. 341-351, 1996.

[16] HAMMOUDEH, A.M., SANCHEZ, M.G, GRINDROD, E., Experimental analysis of propagation at 62 GHz in suburban mobile radio microcells, *IEEE Trans. Veh. Tech.*, vol. 48, n° 2, pp. 576-587, 1999.

[17] MCNAMARA, D. A., PISTORIUS, C.W.I., MALHERBE, J.A.G., *Introduction to the Uniform Geometrical Theory of Diffraction*, Artech House, London, 1990.

[18] VANDER VORST, A., *Transmission, propagation et rayonnement*, De Boeck-Université, Bruxelles, 1995.

[19] KELLER, J.B., Geometrical Theory of diffraction, *J. Opt. Soc. Of America*, vol. 52, n° 2, pp. 116-130, 1962.

[20] KOUYOUMJIAN, R.G., PATHAK, P.H., A uniform geometrical theory of diffraction for an edge in a perfectly conducting surface, *Proc. IEEE,* vol. 62, n° 11, pp. 1448-1461, 1974.

[21] LUEBBERS, R.J., Finite conductivity uniform GTD versus knife edge diffraction in prediction of propagation path-loss, *IEEE Trans. Antennas Propagat.,* vol. 32, n° 1, pp. 70-76, 1984.

[22] MICHAELI, A., Equivalent currents for arbitrary aspects of observation, *IEEE Trans. Antennas Propagat.,* vol. 32, n° 3, pp. 252-258, 1984.

[23] KNOTT, E.F., SENIOR, T.B.A., Comparison of three high-frequency diffraction techniques, *Proc. IEEE,* vol. 62, n° 11, pp. 1468-1474, 1974.

[24] OESTGES, C., VASSEUR, H., VANHOENACKER, D., Impact of edge diffraction on the performance of land mobile satellite systems in urban areas, 28th European Microwave Conference, Proc. EuMC '98 (Amsterdam, The Netherlands), pp. 357-361, October 1998.

[25] TIBERIO, R., MANARA, G., PELOSI, G., KOUYOUMJIAN, R.G., High-frequency electromagnetic scattering of plane waves from double wedges, *IEEE Trans. Antenn. Propagat.*, vol. 37, n°9, pp. 1172-1180, 1989.

[26] SCHNEIDER, M., LUEBBERS, R.J., A general, uniform double wedge diffraction coefficient, *IEEE Trans. Antenn. Propagat*., vol. 39, n°1, pp. 8-14, 1991.

[27] ISHIMARU, A., *Wave propagation and scattering in random media (vol. 2)*, Academic Press, New York, 1978.

[28] CCIR, *CCIR Recommendations and Reports - Propagation in non-ionized media*, vol. 5, ITU, Geneva, 1986.

[29] BARTS, R.M., STUTZMAN, W.L., Modeling and simulation of mobile-satellite propagation, *IEEE Trans. Antenn. Propagat.*, vol. 40, n°4, pp. 375-382, 1992.

[30] SEVILLE, A., YILMAZ, U., CHARRIERE, P.G.V, POWELL, N., CRAIG, K.H., Building scatter and vegetation attenuation measurements at 38 GHz, 9th Int. Conf. on Ant. and

Prop., ICAP '95 (Eindhoven, The Netherlands), IEE Conf. Publication 407, pp. 2.46-2.50, April 1995.

[31] AGIUS, A.A., SAUNDERS, S.R., EVANS, B.G., Antenna design for the ICO handheld terminal, 10th Int. Conf. on Ant. and Prop., ICAP '97 (Edinburgh, UK), IEE Conf. Publication 436, pp. 1.385-1.389, April 1997.

[32] VANDER VORST, A., VASSEUR, H., VYNCKE, C., AMAYA, C., VANHOENACKER, D., From electromagnetics to system performance: a new method for the error rate prediction of atmospheric communications links, *IEEE J. Selected Areas Commun.*, vol. 15, n° 4, pp. 656-666, 1997.

[33] OESTGES, C., VANHOENACKER-JANVIER, D., Experimental validation and system applications of a ray-tracing model in built-up areas, *Electronics Letters*, vol. 36, n° 5, pp. 461-462, 2000.

[34] SAUNDERS, S.R., EVANS, B.G., A physical model of shadowing probability for land mobile-satellite propagation, *Electron. Lett.*, vol. 32, n° 17, pp. 1548-1549, 1996.

[35] SAUNDERS, S.R., EVANS, B.G., A physical-statistical model for land mobile-satellite propagation in built-up areas, 10th Int. Conf. on Ant. and Prop., ICAP '97 (Edinburgh, UK), IEE Conf. Publication 436, pp. 2.44-2.47, April 1997.

[36] OESTGES, C., VANHOENACKER-JANVIER, D., A UTD-based physical-statistical model of the mobile-satellite channel, *Revue HF*, n° 1, pp. 17-26, 2000.

[37] SAUNDERS, S.R., TZARAS, C., OESTGES, C., VANHOENACKER D., Physical-statistical modelling of the land mobile satellite channel, 1st International Workshop on Radiowave Propagation Modelling for SatCom Services at Ku band and above (ESTEC, Noordwijk, The Netherlands), pp.95-102, October 1998.

[38] SAUNDERS, S.R., *Diffraction modelling of mobile radio wave propagation in built-up areas*, PhD thesis, Brunel University, 1991.

[39] PARSONS, D., *The mobile radio propagation channel*, Pentech Press, London, 1992.

[40] OESTGES, C., SAUNDERS, S.R., VANHOENACKER-JANVIER, D., Physical-statistical modelling of the land mobile satellite channel based on ray-tracing, *IEE Proc.-Microw. Antenn. Propagat.*, vol. 146, n° 1 , pp. 45-49, 1999.

[41] BUTT, G., *Narrowband characterization of high elevation angle land mobile-satellite channel*, PhD thesis, University of Surrey, 1992.

[42] VÁZQUEZ-CASTRO, M., TZARAS, C., SAUNDERS, S.R., PÉREZ-FONTÁN, F., Shadowing correlation for mobile-satellite diversity, Joint International Workshop COST 252 – 253 – 255 (Toulouse, France), pp. 37-48, May 1999.

[43] TZARAS, C., SAUNDERS, S.R.,EVANS, B.G., A physical-statistical propagation model for diversity in mobile-satellite PCN, Proc. IEEE International Vehicular Technology Conference (Ottawa, Canada), pp. 525-529, May 1998.

[44] KANATAS, A.G., CONSTANTINOU, P., City center high-elevation angle propagation measurements at L band for land mobile-satellite systems, *IEEE Trans. Veh. Technol.*, vol. 47, n° 3, pp. 1002-1011, 1998.

[45] OESTGES, C., VANHOENACKER-JANVIER, D., Physical-statistical prediction of performance for land mobile satellite systems, *IEE Proc.-Microw. Antenn. Propagat.*, vol. 146, n° 5, pp. 362-368, 1999.

[46] SFORZA, M., BUONOMO, S., Characterization of the LMS propagation channel at L and S bands: narrowband experimental data and channel modelling, Proc. NAPEX XVII (Pasadena, USA), JPL Publication 93-21, pp. 183-192, June 1993.

[47] PARKS, M.A.N., SAUNDERS, S.R., EVANS, B.G., Wideband characterization and modelling of the mobile-satellite propagation channel at L and S bands, 10th Int. Conf. on Ant. and Prop., ICAP '97 (Edinburgh, UK), IEE Conf. Publication 436, pp. 2.39-2.43, April 1997.

[48] PROAKIS, J.G., *Digital communications*, 3d edn., McGraw-Hill, New-York, 1995.

[49] PALMER, L.C., Computer modelling and simulation of communication satellite channels, *IEEE J. Selected Areas Commun.*, vol. 2, n° 1, pp. 89-101, 1984.

[50] JERUCHIM, M.C., Techniques for estimating the bit error rate in the simulations of digital communications systems, *IEEE J. Selected Areas Commun.*, vol. 2, n° 1, pp. 153-170, 1984.

[51] HESS, G.C., *Land-mobile radio system engineering*, Artech House, Boston-London, 1993.

CHAPTER 3 EVALUATION OF SYSTEM IMPAIRMENTS AND PERFORMANCE PREDICTION

3.1 INTRODUCTION

Chapter 3 describes and exemplifies performance prediction methods, which are based on the developed propagation models.

Performance prediction is by far the dominant activity of multi-satellite radio system design. Coverage or availability are usually addressed in terms of a given parameter that is not exceeded over a given percentage of area or during a given percentage of time. For example, Iridium's performance for voice transmission is defined by an admissible BER of 10^{-2} with a global availability of 95 % whereas Teledesic is guaranteed to achieve the desired quality of service during 99.9 % of time. This availability is usually predicted on a long-term basis. For high-frequency fixed services, the long-term availability only depends upon atmospheric effects. In contrast, mobile satellite links mainly undergo the influence of the surrounding area, but the latter can eventually be combined with the impact of tropospheric mechanisms.

Long-term performance, however, does not reflect the short-term performance to be experienced by any specific user at specific place and time. Furthermore, statistical predictions do not usually consider the complex interaction and correlation between different propagation factors, like azimuth correlation of shadowing in diversity schemes, imperfect system procedure (SNR estimation, delays) and satellite motion. Global predictions have therefore to be completed with deterministic analysis, which inherently accounts for all mentioned effects simultaneously. Meanwhile, deterministic simulations allow investigating several dynamic system strategies, which cannot easily be included within a pure statistical context.

Subsequently, the first sections of Chapter 3 are dedicated to methods for estimation of long- and short-term performance respectively. As a preliminary, Table 3.1 summarizes the main differences between both approaches.

Long-term prediction	**Short-term prediction**
Long periods of time (from 1 day to 1 year)	Short periods of time (length of a typical communication)
Large areas (city, country)	Reduced areas (street, single site)
(Physical-)Statistical models	Deterministic models
Analytical or time series simulations	Time series simulations
Generic area (urban, rural) or annual data	Specific scenarios (crossroad/meteosat map)
Static analysis (or quasi-static)	Integration of system dynamic behaviour

Table 3.1 *Comparison between long- and short-term predictions*

With regard to long-term performance, a method has been described in Section 1.6.2 in order to integrate the variation of elevation angle in the prediction of tropospheric attenuation statistics. The approach underlined in Section 1.6.2 is actually generalised in Section 3.2 to the most general case of mobile or transportable links, in the view of

- including the impact of local effects in the predicted attenuation,
- accounting for the eventual mobility of the receiver.

Section 3.3 presents the implementation of a number of system strategies, such as dynamic fade compensation, satellite handover and diversity. They constitute the required tools for a short-term analysis.

As mentioned, the prediction methods are often developed during the chapter with land mobile satellite links in mind, so the largest number of eventual effects is covered. The general methodology can therefore be particularised to all kinds of systems, namely

- a fixed (single-site) single satellite system, e.g. a multimedia system based on geostationary satellites, for which atmospheric conditions vary, elevation angle and surrounding area are constant (this case is not treated in this thesis, for only LEO satellites are investigated),
- a fixed (single-site or transportable) multi-satellite system, e.g. a multimedia system using a LEO constellation or any gateway link of LEO satellite systems; in this case, the elevation angle and climatic conditions vary, but the surrounding area remains unchanged,
- a mobile multi-satellite system, e.g. a voice transmission LEO satellite system, for which the elevation angle, the environment as well as the atmospheric conditions are variable.

Once the methods are established, a number of typical systems are investigated:

- a L band LEO satellite voice transmission system, in Section 3.4,
- a S band satellite-IMT2000 (wideband CDMA), in Section 3.5,
- a Ka band multimedia LEO satellite system (Teledesic-like), in Section 3.6,
- a V band/S band stratospheric communication system (multimedia and wideband fixed/mobile applications), in Section 3.7.

In the above list, the last system uses high-altitude platforms in place of satellites. Nevertheless, it is shown that this type of system can be analyzed in a very similar way to LEO systems, indicating that the general developed approach might also be suitable for purely terrestrial mobile applications.

Finally, it should be noticed that the simulated systems cover a large frequency range as well as different technologies and applications. Each one also allows highlighting of a particular aspect of the developed prediction methods. While mobile links at L and S band are only impaired by local effects, multimedia systems operating at Ka band and above are also and quite exclusively concerned with atmospheric propagation. It is important to note that the test cases to be presented are only exemplary. Hence, the goal is certainly not to execute the complete design of a particular system. More expressly, the test cases aim at emphasizing the capability of theoretical models to yield useful system-oriented simulation results in a number of very different communication systems.

3.2 PREDICTION OF LONG-TERM PERFORMANCE FOR LOW EARTH-ORBIT SATELLITE LINKS

3.2.1 Outline

As mentioned in the introduction, the most general study case is constituted by a mobile multi-satellite system: the elevation angle and all propagation conditions (local and tropospheric effects) vary with time and receiver location. In order to account for this dual source of variation, Section 3.2 introduces a distinction between the temporal availability (denoted as *availability*) and the spatial *coverage*. As ultimate goal, it is desired to define the performance of any satellite personal communication system over a specific area, such as a city, by a performance criterion expressed as a given value of parameter *x*, exceeded during τ % of the time and over β % of the outdoor area (i.e. outside buildings). Subsequently, Section 3.2.2 describes a general analytical approach with *x* being the *fade level*. Section 3.2.3 applies the same method to the prediction of raw (uncoded) or coded *BER*. Finally, Section 3.2.4 briefly presents another similar methodology that has been proposed within the framework of COST 255 Action and that is based on *time series* simulations.

3.2.2 Fade distribution over time and area

Assume that a receiving terminal is fixed to a random location in a given area, the physical characteristics of which are statistically known. Using a physical-statistical formalism, the random characteristics of the mobile satellite link are therefore featured by a given set of physical parameters $\overline{\eta}$, which is related to a probability of occurrence $T_{\overline{N}}(\overline{\eta})$.

The vector of physical parameters can be divided into two parts, covering area and time variations respectively . On one hand, some parameters only depend on the *receiver location*: the nearest building height h_b, the street width w, the transverse position d_m of the mobile in the street and the orientation of the street ϕ_{street}. On the other hand, the *time*-varying satellite position determines the elevation and azimuth angles of the satellite vehicle, ϑ and ϕ_{sat}.

The azimuth angle relative to street axis ($\phi \overset{\Delta}{=} \phi_{street} - \phi_{sat}$) depends on the location of both the satellite and the receiver. In order to simplify the calculations, it is assumed in the following that the distribution of the satellite azimuth can be approximated by:

$$T_{\Phi_{sat}}(\phi_{sat}) = \frac{1}{2}\delta(\phi_{sat}) + \frac{1}{2}\delta(\phi_{sat} - \pi) \tag{3.1}$$

Regarding a LEO-66 constellation, it has been shown in Chapter 2 (Figure 2.29) that the distribution of ϕ_{sat} at London latitude actually presents two maxima at 0 and π, so equation (3.1) is partly justified. In fact, in a symmetric scenario like the generic configuration of Figure 2.22, the approximation of (3.1) is equivalent to assuming that the link azimuth angle ϕ (relative to street axis) only depends on the street orientation. Hence, the azimuth angle ϕ is associated with the mobile position, although the approach is still valid if both azimuth angles ϕ_{street} and ϕ_{sat} are separately associated respectively with area and time.

The above distinction between *area* and *time* can be analytically formulated. The distribution $T_{\bar{N}}(\bar{\eta})$ is divided into two independent distributions, $T_{\bar{\Gamma}}(\bar{\gamma})$ and $T_X(\chi)$, given by:

$$T_{\bar{\Gamma}}(\bar{\gamma})\, d\bar{\gamma} = T_{H_b}(h_b)\, T_{D_m}(d_m)\, T_W(w)\, T_{\Phi}(\phi)\, dh_b\, dd_m\, dw\, d\phi \tag{3.2-a}$$

and $$T_X(\chi)\, d\chi = T_{\Theta}(\vartheta)\, d\vartheta \tag{3.2-b}$$

The distributions of all physical parameters appearing in (3.2) have already been examined in Chapter 2.

Equation (2.62) is then rewritten as:

$$\begin{aligned} T_{A_B}(A_B) = &\quad T_{A_B|\bar{\Gamma}X}(A_B \mid \bar{\gamma}, \chi)\, T_X(\chi)\, d\chi\, T_{\bar{\Gamma}}(\bar{\gamma})\, d\bar{\gamma} \\ = &\quad T_{A_B|\bar{\Gamma}\Theta}(A_B \mid \bar{\gamma}, \vartheta)\, T_{\Theta}(\vartheta)\, d\vartheta\, T_{\bar{\Gamma}}(\bar{\gamma})\, d\bar{\gamma} \\ = &\quad T_{A_B|\bar{\Gamma}}(A_B \mid \bar{\gamma})\, T_{\bar{\Gamma}}(\bar{\gamma})\, d\bar{\gamma} \end{aligned} \tag{3.3}$$

where

$$T_{A_B|\bar{\Gamma}}(A_B \mid \bar{\gamma}) = \quad T_{A_B|\bar{\Gamma}\Theta}(A_B \mid \bar{\gamma}, \vartheta)\, T_{\Theta}(\vartheta)\, d\vartheta \tag{3.4}$$

Expression (3.4) can be looked on as the fade distribution over time for a given receiver location defined by $\bar{\gamma}$. This distribution is the combination of the distribution of elevation angle with the conditional distribution of the attenuation (related to the Ricean distribution of the received envelope). The location $\bar{\gamma}$ is characterized by a given probability of occurrence $T_{\bar{\Gamma}}(\bar{\gamma})\, d\bar{\gamma}$, which is also a percentage of the open-air area. The whole approach is schematically summarized in Figure 3.1.

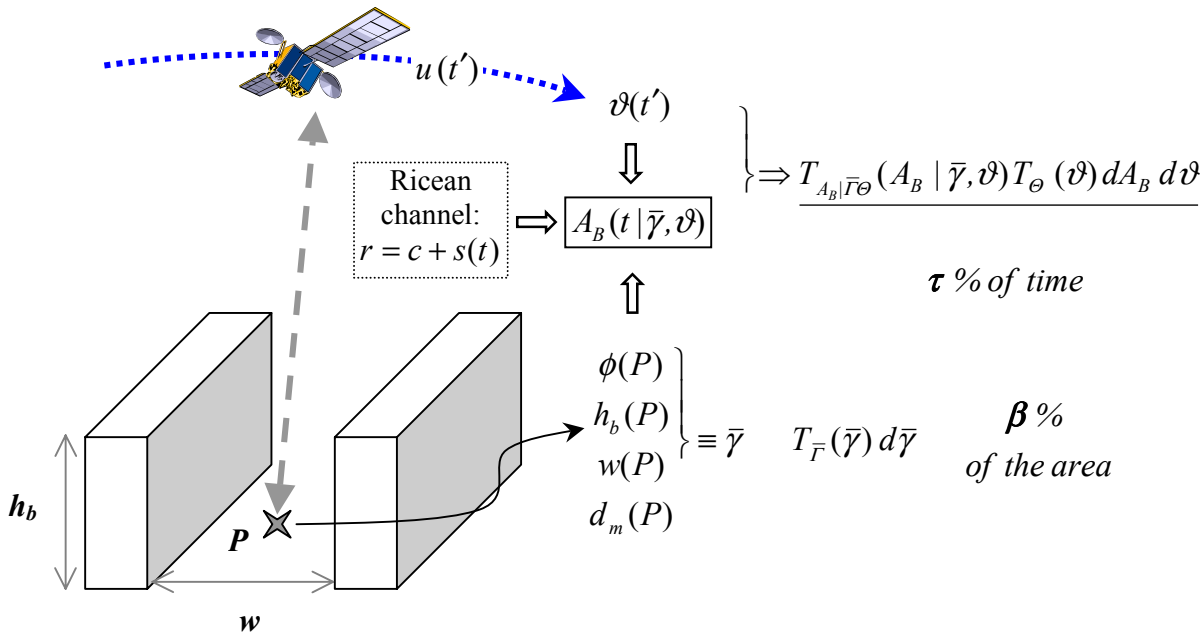

Figure 3.1 *A general approach for prediction of fade distribution over time and area*

Note that in Figure 3.1, the time variation of the elevation angle $\vartheta(t')$ is caused by the satellite motion $u(t')$. Regarding the conditional fade level (at fixed $\bar{\gamma}$ and ϑ), the temporal variation $A_B(t\,|\,\bar{\gamma},\vartheta)$ is featured by the Ricean distribution of the received envelope $r = 1/\sqrt{A_B}$ (c is the dominant component affected by shadowing and s is the multipath random contribution of power σ^2, see Chapter 2).

Given the fade distribution conditional upon the area, any conditional percentile $A_{B,\tau}\,|\,\bar{\gamma}$, related to a cumulated percentage of time τ, can be calculated as outlined by the following relationship:

$$\int_{A_{B,\tau}|\bar{\gamma}}^{\infty} T_{A_B|\bar{\Gamma}}(A_B\,|\,\bar{\gamma})\,dA_B = \frac{\tau}{100} \tag{3.5}$$

If the conditional percentile is a monotonic function of $\bar{\gamma}$, it is then easy to demonstrate that cumulative fade distributions over the area can be calculated for any percentage of time τ. The distribution over the area of the fade level exceeded during τ% of time is given by:

$$T_{A_{B,\tau}|\bar{\Gamma}}(A_{B,\tau} \mid \bar{\gamma}) = T_{\bar{\Gamma}}\left[F^{-1}(A_{B,\tau} \mid \bar{\gamma})\right]\left|\frac{\partial F^{-1}(A_{B,\tau} \mid \bar{\gamma})}{\partial A_{B,\tau} \mid \bar{\gamma}}\right| \tag{3.6}$$

where $A_{B,\tau} \mid \bar{\gamma} \equiv F(\bar{\gamma})$.

It is worth noting that the conditional percentile defined by (3.5) must be distinguished from the percentile (at the same percentage) of the average fade distribution denoted as $A_{B,\tau}$. The latter is indeed given by:

$$\int_{A_{B,\tau}}^{\infty} T_{A_B}(A_B)\, dA_B = \frac{\tau}{100} \tag{3.7}$$

It corresponds to the classical definition of availability. In contrast to the proposed approach, it does not make any distinction between time and area. Of course, for a specific single gateway, the performance depends only upon temporal variations (e.g. atmospheric effects) and both definitions yield the same results. As soon as spatial coverage is considered, namely for personal communication networks, the new method outlined by (3.3) to (3.6) provides a more refined analysis.

Finally, it should be added that the method could be slightly transformed in order to provide an original prediction of performance for portable links with high elevation angle, for instance high-altitude platforms (see Section 3.7).

3.2.3 BER prediction

The approach used in Section 3.2.2 to infer average fade distributions over time and area can be applied to any parameter describing the system performance, namely the raw (without error-correcting code) and coded BER.

The fade level exceeded during τ% of time can indeed be converted into a BER exceeded for the same percentage of time. Various relationships have been detailed in Section 2.3.6 for estimating both raw and coded BER in the case of convolutional codes.

The conditional BER achieved for a given nominal E_b/N_0 value and exceeded during τ% of time is denoted as $P_{E,\tau}(E_b/N_0) \mid \bar{\gamma} \equiv G(\bar{\gamma})$. The distribution over the area of any percentile of distribution of BER is then given in the same way as (3.6) by:

$$T_{P_{E,\tau}|\bar{\Gamma}}(P_{E,\tau} \mid \bar{\gamma}) = T_{\bar{\Gamma}}\left[G^{-1}(P_{E,\tau} \mid \bar{\gamma})\right]\left|\frac{\partial G^{-1}(P_{E,\tau} \mid \bar{\gamma})}{\partial P_{E,\tau} \mid \bar{\gamma}}\right| \tag{3.8}$$

Again, relationship (3.8) is valid as long as $G(\bar{\gamma})$ is a monotonous function of $\bar{\gamma}$. Note that this is usually the case. Intuitively, the performance is improved when w/h_b increases and ϕ decreases from 180° to 0°.

3.2.4 Time series simulations for long-term predictions

3.2.4.1 The COST 255 methodology

A very similar simulation method has been developed in the framework of COST 255 [1] for estimating the performance of LMS systems. The two-level modelling approach is described in Figure 3.2.

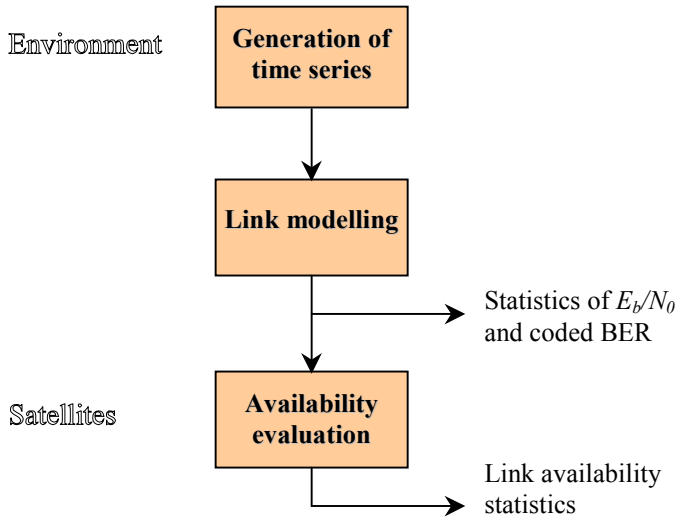

Figure 3.2 *Two-level modelling approach proposed by COST 255*

The global simulation is split into:

- a *link-level simulation*, to determine the dependence of coded BER on environment and system parameters, via analytical expression for the relationship between instantaneous signal-to-interference-plus-noise ratio (SINR) and BER,
- a *system-level simulation*, used with constellation parameters and appropriate criteria for availability to determine overall system availability results.

The key reason for this split approach is to adopt the simplest method that would yield meaningful outputs. Conventional Monte-Carlo bit by bit simulation is avoided as being too time-consuming. Note that the proposed simulation approach (and probably any other method capable of yielding the same level of information) requires channel models capable of generating representative time series. Thus purely statistical models that are only capable of predicting cumulative attenuation statistics, such as those currently recommended by ITU-R, are inappropriate. This is particularly the case when considering coded modulation schemes and dynamic system procedures, such as power-control.

3.2.4.2 LINK-LEVEL: CODED BER CALCULATION

The link-level simulation [2] is based on a time series of effective E_b/N_0 values, in addition to various system parameters, e.g. the modulation scheme and the error-correcting code characteristics. The effective E_b/N_0 values must include all effects of system noise, multi-user interference (MAI) and inter-symbol interference (ISI), as described in Chapter 2.

For TDMA/FDMA, system noise is the limiting factor, while CDMA systems are limited by MAI. Inter-symbol interference is negligible in almost all existing systems. The downlink MAI is function of the received power from each visible satellite and of a number of equivalent channels per satellite. It can easily be calculated as explained in [4]. From the effective E_b/N_0 values, the raw and coded BER are then estimated as detailed in the previous chapter (Section 2.3.6).

Figure 3.3 and Figure 3.4 depict exemplary link-level simulation outputs. The time series depicted in Figure 2.23 are used assuming a nominal E_b/N_0 of 19 dB and a pedestrian speed of 1 m/s, yielding the received E_b/N_0 time series of Figure 3.3. The derived time series of raw BER for a QPSK modulation is also presented on the lower graph.

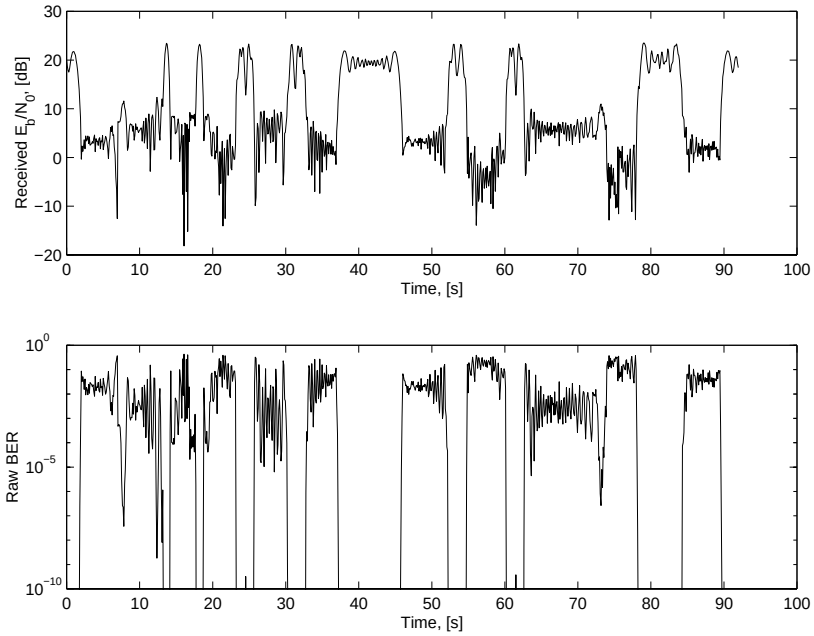

Figure 3.3 *Time series of E_b/N_0 (upper graph) and raw BER (lower graph) along a straight street (pedestrian speed)*

The link-level simulation produces cumulative distributions of the received E_b/N_0 as well as of raw and coded BER, which are depicted in Figure 3.4.

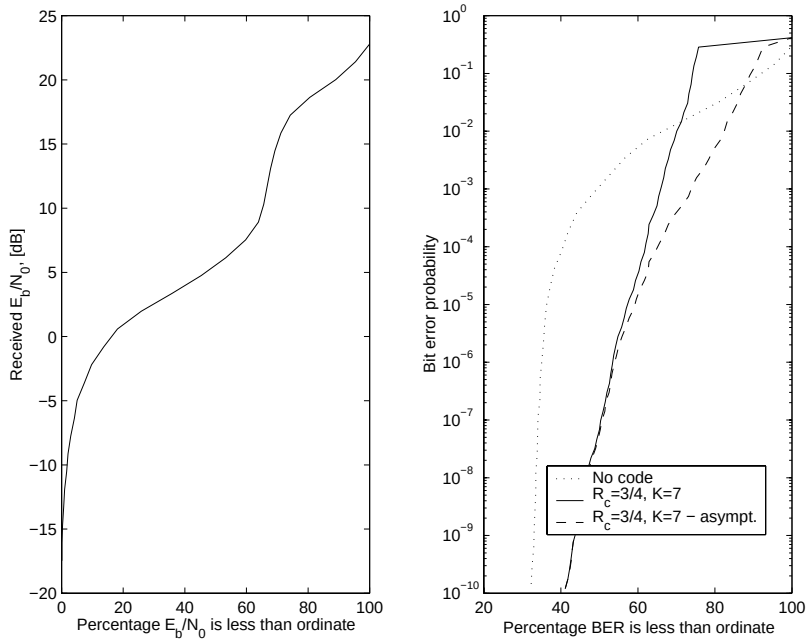

Figure 3.4 *Link-level simulation: cumulative distributions of E_b/N_0 (left) and BER (right) for convolutional code R_c = 3/4, K = 7 (tight upper bound and asymptotic bound)*

The tight upper bound and the asymptotic formula give similar results for low BER. However, for high BER, the tight upper bound takes into account the degradation of performance introduced by the decoder when the received E_b/N_0 becomes too low.

3.2.4.3 SYSTEM-LEVEL: EVALUATION OF PERFORMANCE

The system-level simulations are based on *"spatial" series* of fade level at constant elevation angle [3]. These can be generated by any appropriate propagation model, e.g. the ray-tracing model applied in a randomly generated area. Fade spatial series are then easily converted into effective E_b/N_0 time series according to the system link budget and the mobile speed. Introducing the resulting E_b/N_0 time series into the link model as previously described, statistics of coded BER are obtained for this particular elevation angle. At this stage, the term *spatial series* may be somewhat confusing. The problem is that time series is the common denomination of series, even when the series are calculated over the area. Moreover, time and area are linked by the mobile speed, so that there is a additional source of confusion. Consider in the following that *time* is associated with the satellite, while *area* (or space) is related to the mobile receiver.

This statistical distribution of any parameter x (x = coded BER or effective E_b/N_0) conditional upon the elevation angle is denoted as $T_{X|\Theta}(x \mid \vartheta)$. Obviously, fade series have to include all effects inducing a *spatial* variation of the mobile channel. The surrounding area and the azimuth angle continuously change as the receiver moves through the environment. As already explained, the azimuth angle relative to the street axis depends on both the random street orientation and the time-varying satellite position. In this method, the distribution of azimuth angle is postulated to be related only to the mobile position (i.e. the street orientation) and taken as uniform.

When the elevation angle is kept constant ($\vartheta = \vartheta_0$), the conditional distribution of x is equivalent to a distribution over the *area* for this particular value of ϑ. The probability density function of x is indeed calculated on the basis of *spatial* series, which are governed by the random characteristics of both the built-up area and the terminal motion. Meanwhile, the varying elevation angle is related to the satellite motion (depending on the constellation) and thus, to *time*. From the previous considerations, the conditional distribution $T_{X|\Theta}(x \mid \vartheta = \vartheta_0)$ can be looked to as a spatial distribution (i.e. over the *area*) of x at a fixed time given by ϑ_0.

Since the criterion x is usually a monotonous function of the elevation angle, knowing $T_{X|\Theta}(x \mid \vartheta = \vartheta_0)$ allows obtaining a spatial distribution of x achieved during a certain cumulated percentage of time τ. It is given by:

$$\begin{cases} T_{X_\tau}(x_\tau) = T_{X|\Theta}(x \mid \vartheta > \vartheta_0) \\ \tau = P[\vartheta > \vartheta_0] = \int_{\vartheta_0}^{\pi/2} T_\Theta(\vartheta)\, d\vartheta \end{cases} \tag{3.9}$$

where $T_{X_\tau}(x_\tau)$ defines the spatial distribution of performance parameter x, achieved during a cumulated percentage of time τ. The statistical distribution of elevation angle ϑ is easily calculated from an orbit generator at any latitude on the globe (see Chapter 2 and Appendix B).

It is worth noting that the COST 255 approach is actually different from the analytical method described in Sections 3.2.2 and 3.2.3.

In the analytical approach, the statistical variation of the conditional channel (for given $\bar{\gamma}$ and χ) is firstly explicitly calculated as a conditional distribution $T_{A_B|\bar{\Gamma}X}(A_B \mid \bar{\gamma}, \chi)$. This distribution is then assumed to be included in the time segment, as outlined by equation (3.4):

$$T_{A_B|\bar{\Gamma}}(A_B \mid \bar{\gamma}) = \int T_{A_B|\bar{\Gamma}\Theta}(A_B \mid \bar{\gamma}, \vartheta)\, T_\Theta(\vartheta)\, d\vartheta$$

Hence, the fade distribution over time results from the combination of the Ricean channel statistics with $T_X(\chi) = T_\Theta(\vartheta)$.

In contrast, the statistical behaviour of the conditional channel is inherently part of the area segment in the COST 255 methodology. In other words, the COST 255 method mixes the two distributions $T_{A_B|\bar{\Gamma}X}(A_B \mid \bar{\gamma}, \chi)$ and $T_{\bar{\Gamma}}(\bar{\gamma})$ into a single spatial series simulation.

Indeed, channel statistics corresponding to $T_{A_B|\bar{\Gamma}X}(A_B \mid \bar{\gamma}, \chi)$ are outlined by the signal variation when the receiver moves along each particular building[†]. Meanwhile, the succession of different buildings accounts for the statistical variation of the environment, described by $T_{\bar{\Gamma}}(\bar{\gamma})$. The unique output of the method is the fade distribution conditional upon χ, (i.e. the elevation angle ϑ), namely

[†] It should be pointed out that the equivalent current method for diffraction appears to be really more appropriate than the classical UTD in channel statistics.

$$T_{A_B|X}(A_B \mid \chi) = \quad T_{A_B|\bar{\Gamma}X}(A_B \mid \bar{\gamma}, \chi) T_{\bar{\Gamma}}(\bar{\gamma}) d\bar{\gamma} \tag{3.10}$$

where the integration procedure is performed within the time series calculation.

Comparing equations (3.10) and (3.4) really illustrates the difference between the COST 255 and the analytical approaches. The channel Ricean variation is respectively associated with area in (3.10) but with time in (3.4). Furthermore, in the analytical method, this combination is performed *a posteriori*, while the COST 255 approach performs it *a priori*, meaning that $T_{A_B|\bar{\Gamma}X}(A_B \mid \bar{\gamma}, \chi)$ cannot be isolated.

Finally, one should mention that a third similar method, which completely separates the conditional channel statistics from temporal and spatial variations, is described in [5].

A system-level simulation software package (see Appendix F) has been developed to implement the COST 255 outlined formalism. Its inputs are:

- the time series of E_b/N_0, for a range of elevation angles,
- the corresponding vector of elevation angles,
- the satellite system to be simulated,
- the latitude of the simulated area,
- the parameter x to be represented ($x \stackrel{\Delta}{=}$ coded BER or E_b/N_0).

3.3 SHORT-TERM PERFORMANCE AND SYSTEM STRATEGIES

3.3.1 Preamble

Statistical models combined with some physical background finally yield fast but nevertheless precise channel estimation and prediction of coverage. However, these models generally produce rough results, especially regarding the dynamic effects caused by the motion of LEO satellites. Since the satellite orbit is non-geostationary, the elevation angle varies quickly over time, even if the mobile terminal is static. Therefore, a number of propagation mechanisms and system procedures are inextricably mixed in a very complex way. In statistical models, this complexity is dealt with by means of strong assumptions (for example, regarding the satellite selection strategy). These are sometimes not representative of a real system. Hence, the statistical long-term prediction must be completed with some deterministic short-term analysis, which takes into account the complex correlation between simultaneous effects.

The following sections describe the system tools needed by a short-term analysis, namely several system dynamic procedures that can be implemented to mitigate shadowing: fade compensation algorithm, handoff and multi-satellite diversity.

3.3.2 Fade compensation

3.3.2.1 STATIC COMPENSATION OF FREE-SPACE LOSS

Satellite constellations usually generate clusters of cells on the earth's surface formed by parallel antenna arrays [6]. Variable antenna gains are then used to compensate for the different path losses from innermost to outermost cells.

This inherent static compensation causes the strength of a signal arriving at the receiver in the line-of-sight to be roughly independent on the elevation angle, at least for angles between, say, 10 and 65 degrees (Iridium bound values). If the elevation angle falls outside this range, the system compensates at least for the bound angle. All following calculations always postulate that this kind of compensation is implemented.

3.3.2.2 DYNAMIC FADE MITIGATION

Theoretical models show that the received signal sometimes undergoes deep fades, especially in shadowed areas or during rain events. These fade events can be corrected by means of closed-loop fade mitigation (FM) techniques, such as power-control. In this study, a dynamic fade compensation algorithm [4][7] is described: the system estimates the received effective E_b/N_0 and computes a power correction to be applied. Since the key-factor is the bit energy-to-noise spectral density ratio, one should be aware of the fact that the power correction may be implemented using several techniques:

- hardware power-control,
- data rate reduction,
- adaptive signal processing,
- a combination of various techniques.

In the simulations, no distinction is made between all these techniques. Hence, the global correction should eventually be split into a number of individual corrections related to different techniques. Also, a constant noise level is always assumed.

Two margins are distinguished. The first margin, called *fixed* or *clear-sky fade margin* and denoted as M_f , is the classical margin. For a target E_b/N_0 equalling κ_0, this fixed margin M_f is defined as the difference between κ_0 and the minimum required E_b/N_0. Subsequently, an outage is defined by a period for which the received E_b/N_0 is less than $\kappa_0 - M_f$. The second margin, named as the *detection margin* δ ($< M_f$), commands the fade compensation algorithm. The latter is switched on when the estimated E_b/N_0 falls below the quantity ($\kappa_0 - M_f$) + δ.

Additional parameters have to be defined:

- the signalling delay τ_p (including propagation and processing times),
- the power updating interval T_u ($> \tau_p$),
- the E_b/N_0 estimator window length W ($< T_u$),
- the maximum power correction ΔP_{max},
- the power increment α ($|\alpha| < 1$), which is function of the error signal and divides the dynamic range $\pm \Delta P_{max}$ into N discrete intervals.

With k being an integer and using the denomination κ for E_b/N_0, the error signal is written as:

$$\Delta\kappa(k\,T_u) = \left\langle \kappa(k\,T_u) \right\rangle_W - \kappa_0 \tag{3.11}$$

where all E_b/N_0 values are expressed in decibels and the E_b/N_0 estimation $\langle \kappa(k T_u) \rangle_W$ is carried out at time kT_u and is based on the previous E_b/N_0 values over a window of temporal length W.

The function α is outlined by

$$\alpha = \begin{cases} 0 & |\Delta\kappa_i| < M_f - \delta \\ \dfrac{\Delta\kappa_i}{\Delta P_{max}},\ 0 \le i \le N & M_f - \delta \le |\Delta\kappa_i| \le \Delta P_{max} \\ \pm 1 & |\Delta\kappa_i| > \Delta P_{max} \end{cases} \tag{3.12}$$

where $\Delta\kappa_i$ results from the quantification of the error signal, the quantification step depending on the number N of intervals. Thereby,

$$\Delta\kappa_i = (2\,i - N)\,\Delta P_{max} / N \tag{3.13}$$

while $\Delta\kappa(k T_u)$ is quantified as $\Delta\kappa_i$ if

$$\Delta\kappa_i - \Delta P_{max} / N < \Delta\kappa(k T_u) < \Delta\kappa_i + \Delta P_{max} / N \tag{3.14}$$

For $k T_u + \tau_p < t < (k+1) T_u + \tau_p$, the fade mitigation algorithm is finally described by the following relationship:

$$\kappa_{FM}(t) = \kappa(t) + \Delta P_{max}\ \alpha\{\Delta\kappa(k T_u)\} \tag{3.15}$$

where $\kappa(t)$ and $\kappa_{FM}(t)$ are respectively the initial and compensated E_b/N_0.

The E_b/N_0 estimator is for instance the filtered average of the received E_b/N_0 over the last W seconds. The estimation procedure could also account for the fade slope measured during the last W seconds.

A third approach is based on error counting. However, for low BER, this would result in long estimation sequences and computation delays. Since usual systems use error-correcting codes in order to achieve low BER, the received E_b/N_0 is then calculated from the higher BER on the coded signal. The BER on the coded signal has however to be estimated. This can be achieved using the error counter depicted in Figure 3.5 [8]. The coded signal is compared

with a re-encoded version of the (quasi-)errorless decoded signal. This estimation is valid as long as the BER on the decoded signal stays much smaller than the BER on the coded signal.

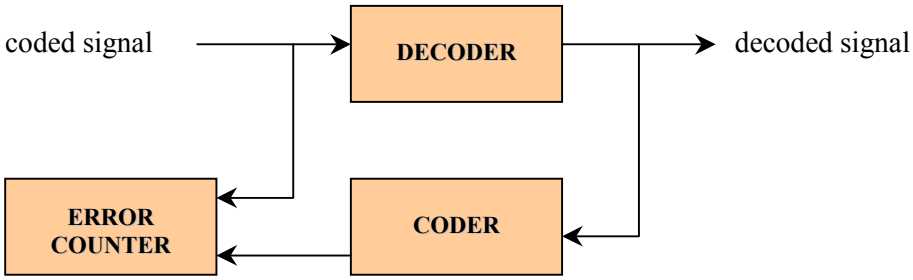

Figure 3.5 *Estimation of the raw BER on the coded signal*

Examples of fade mitigation applications are now detailed. The fade compensation algorithm described by (3.15) is used to mitigate two very different fade events. The first one is caused by rain and taken from Olympus measurements carried out in Belgium (fixed receiver). The frequency is 20 GHz. The algorithm is applied with two sets of parameters:

- $T_u = 1$ s, $W = \tau_p = 400$ ms, $\pm \Delta P_{max} = \pm 3$ dB, $2\Delta P_{max}/N = 0.5$ dB, $\delta - M_f = 0.5$ dB
- $T_u = 1$ s, $W = \tau_p = 400$ ms, $\pm \Delta P_{max} = \pm 6$ dB, $2\Delta P_{max}/N = 1$ dB, $\delta - M_f = 0.5$ dB.

Results are depicted in Figure 3.6.

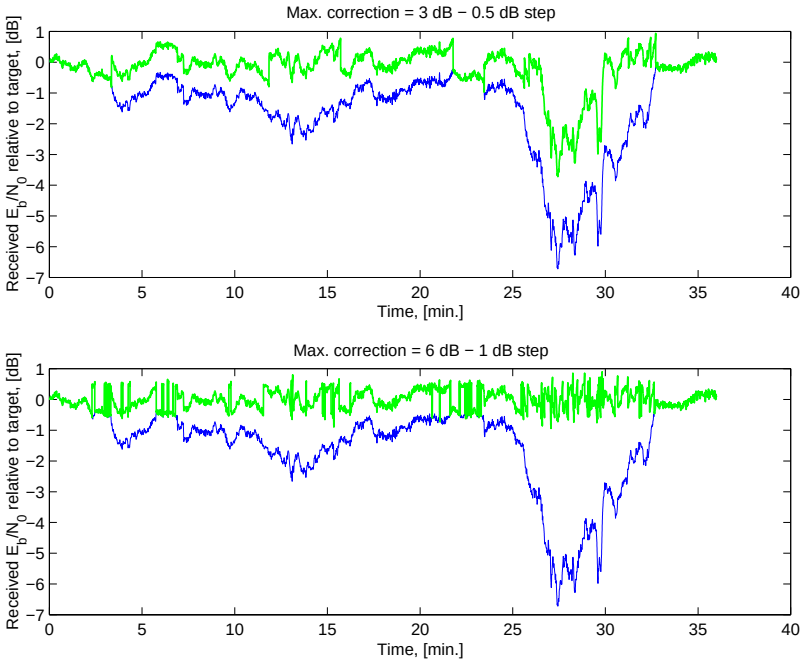

Figure 3.6 *Measured {dark lines} and compensated {bold grey lines} signals for both parameter sets*

On the upper graph, the effects of signalling delays and estimation errors are sometimes clearly visible (e.g. around t = 12 min.). The small correction step is appropriate, but the reduced maximal correction is sometimes not sufficient. On the lower graph, all fade depths are corrected but ping-pong effects are observed. They are caused by the larger correction step $\Delta P_{max}/N$.

The second fade event originates from building shadowing at S band. The simulated fade series described in Figure 2.23 (p. 96) is taken as study case (2.1 GHz, $\phi = 90$ °, $\vartheta = 35$°, w = 15 m, d_m = 5 m). However, since the received power is given as a function of the receiver location, the latter must be turned into time based on the receiver speed. A pedestrian speed of 1 m/s is first assumed. The fade compensation algorithm is applied with the following values:

- T_u = 1 s, $W = \tau_p$ = 400 ms, $\pm \Delta P_{max} = \pm$ 10 dB, $2\Delta P_{max}/N = 1$ dB, $\delta - M_f$ = 0.5 dB
- T_u = 400 ms, $W = \tau_p$ = 400 ms, $\pm \Delta P_{max} = \pm$ 10 dB, $2\Delta P_{max}/N = 1$ dB, $\delta - M_f$ = 0.5 dB
- T_u = 40 ms, $W = \tau_p$ = 40 ms, $\pm \Delta P_{max} = \pm$ 10 dB, $2\Delta P_{max}/N = 1$ dB, $\delta - M_f$ = 0.5 dB.

Results of the three simulations are represented in Figure 3.7.

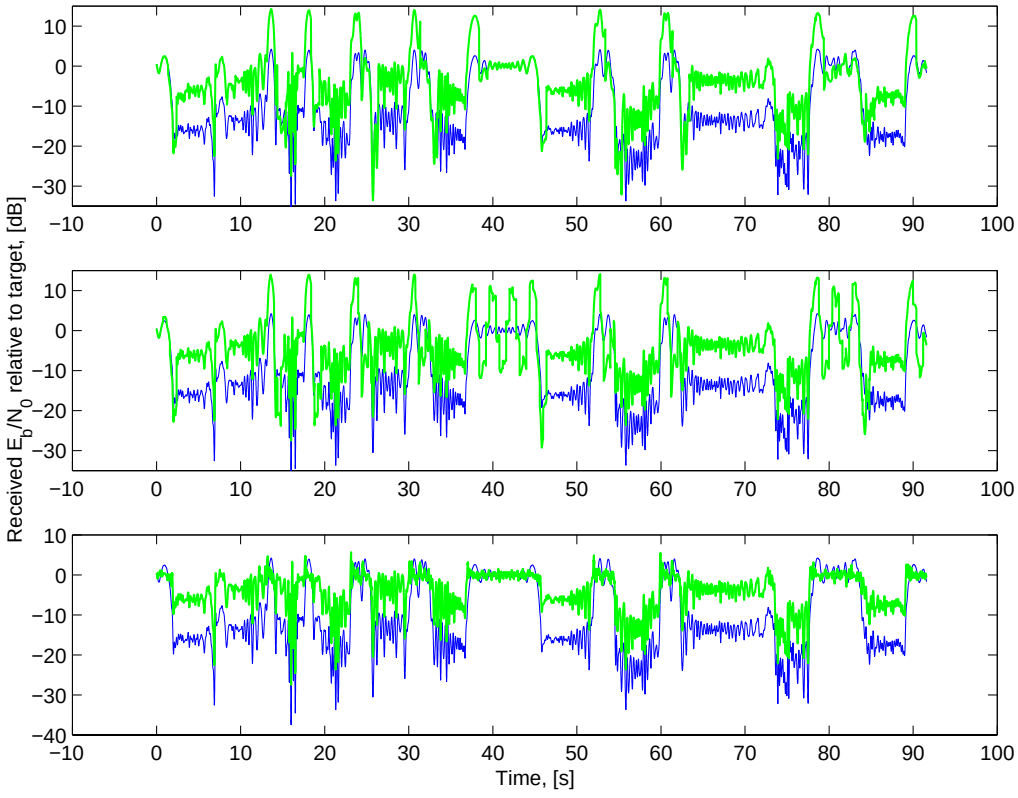

Figure 3.7 *Initial {dark lines} and compensated {bold grey lines} signals for each parameter set*

In the first graph, the large update interval causes the compensated signal to overestimate the needed E_b/N_0, especially after a period of shadowing. That leads to a power waste, as well as to a risk of saturation of the receiver. The situation gets worse in the mid graph, although the update interval is reduced down to 400 ms. Moreover, ping-pong effects are really significant in this case (see for 35 min. < t < 45 min.), due to the fact that T_u and W are also equal. The fast fade mitigation implemented in the last simulation allows for minimising the power consumption, but to the prejudice of smaller update interval and computation delay. Nevertheless, the high required update rate seems quite prohibitive. Then, the first set of parameters (with high T_u, but low W and τ_p) can be looked to as a compromise. However, a good design of the fade mitigation algorithm should also account for the satellite motion, that certainly affects the shadowing dynamics (see Section 3.4.4).

Finally, high-speed mobile cases are considered. Figure 3.8 illustrates the power-control behaviour for two mobile speeds (10 and 20 m/s). The fade mitigation is implemented with the same set of parameters as the one used for the third graph of Figure 3.7 (T_u = 40 ms, W = τ_p = 40 ms, ± ΔP_{max} = ± 10 dB, $2\Delta P_{max}/N = 1$ dB, $\delta - M_f$ = 0.5 dB). In Figure 3.8, the compensation is clearly less efficient despite the high update rate. Using an update interval of 400 ms would actually be completely inefficient.

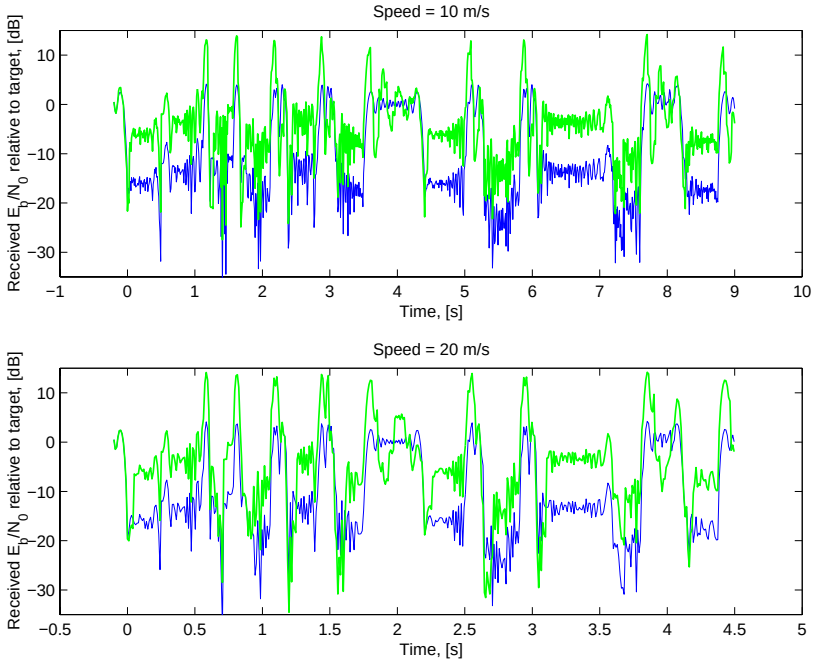

Figure 3.8 *Initial {dark lines} and compensated {bold grey lines} signals for high-speed scenarios*

3.3.3 Satellite handoff diversity

Extra-satellite handoffs rely upon various strategies. The first natural criterion is to always choose the satellite that is seen with the highest elevation angle. This type of handover has been used up to now when satellite constellations have been considered on a statistical basis. The procedure might not be very efficient, since the path to the nearest satellite is likely to be blocked or strongly attenuated, while other visible satellites, though lower, might offer a clear line-of-sight. Because free-space losses are compensated, the effect of distance is not relevant.

To mitigate shadowing, handoff diversity could subsequently be useful. Hence, the following procedure is implemented [7]. The E_b/N_0 values of all visible satellites are compared every S_u seconds. A handoff is initiated when the E_b/N_0 of the active satellite has been measured during the last V seconds below a margin ΔM with respect to the best satellite.

If more than one satellite performs better than the active one, the handover is executed in favour of

- either the best satellite,
- either the satellite among the best ones which is expected to remain for the longest time above a threshold elevation angle: the system chooses e.g. a lower satellite, but that is characterized by an increasing elevation angle (*a posteriori* determination).

The latter is particularly useful for a large number of visible satellites. For such cases, an alternative strategy could additionally include an *a priori* knowledge of the elevation angle. A handover is thereby forced if the elevation angle is expected to fall below a given value in the next S_u seconds. Finally, one should mention that the handoff procedure can be applied with or without combined dynamic fade mitigation.

The margin and the detection time V are necessary in order to avoid ping-pong effects. The detection time V can also be considered as the needed time to prepare the handover. As for fade mitigation, the handoff takes place after a delay τ_p.

The handoff efficiency is measured by the satellite dwell time t_{HO}, i.e. the average time between handoffs. Also, the percentage of time $\Delta\xi$, during which the received signal is not provided by the best satellite, is an important parameter. In the simulations, the relative accuracy regarding the dwell time is approximately given by t_{HO}/(observation length). For instance, considering an observation length of 60 minutes and a dwell time $t_{HO} \cong 270$ s, it comes that the relative accuracy is of 7.5 %.

3.3.4 Multi-satellite diversity

In order to further increase the performance, a multi-satellite diversity scheme can be examined. Such combination diversity is used for example by the Globalstar system. The proposed procedure is simply the extension of the handover scheme to more than one satellite. Considering for example a two-branch diversity, the handoff strategy described above is applied simultaneously to two satellites. Hysteresis margin ΔM, detection time V and update time S_u characterize the procedure in the same way as seen before.

Several combination techniques are commonly used. Let us postulate that the receiver is provided with two signals, with envelopes r_1 and r_2. Also, assume that the received noise processes in the two branches are statistically independent and have equal mean power.

Three techniques are compared in the following [9][10].

- Signal selection (SEL). The corresponding received envelope is given by:

$$r_{SEL} = select\{r_1, r_2\} \tag{3.16}$$

  This technique is not a real combination of signals and is equivalent to the so-called handoff diversity. This explains why the denomination SEL is sometimes used in the following sections in place of handoff diversity. The strategy consisting in choosing the best satellite at any update interval is a particular case of signal selection, where

$$r_{SEL,max} = max\{r_1, r_2\} \tag{3.17}$$

- Equal gain combining (EGC). In this technique, signals are simply summed in the combiner. Thereby, the equivalent envelope can be written as:

$$r_{EGC} = \frac{r_1 + r_2}{\sqrt{2}} \tag{3.18}$$

- Maximal ratio combining (MRC). This method implies the multiplication of each signal by a non-dimensional coefficient proportional to the received envelope (assuming equal noise levels). Taking the effect of non-coherent noise combination into account, it becomes:

$$r_{MRC} = \sqrt{r_1^2 + r_2^2} \tag{3.19-a}$$

This is equivalent to the well-known relationship for MRC:

$$SNR_{MRC} = SNR_1 + SNR_2 \tag{3.19-b}$$

Inherently, maximal ratio combining provides a minimum gain of 3 dB above signal selection. However, MRC is also much more demanding in terms of network management.

3.4 L BAND LEO-*N* VOICE TRANSMISSION SYSTEM

3.4.1 Land mobile satellite systems

The system that is considered as a first test case is a voice transmission network based on a LEO satellite constellation. Two systems are taken as examples: Iridium and Globalstar [11]. The first constellation ensures a global coverage (including poles) thanks to 66 satellites located in circular orbits at a 780-km altitude. The commercial exploitation began in 1998 but ended due bankruptcy in early 2000. The second system counts 48 satellites, distributed in orbits at a 1414-km altitude, and covers some 80 % of the earth's surface. Its arrival on market is scheduled around 2001. Both systems operate at L band regarding the mobile user link, while connections to gateways take place at K/Ka bands for Iridium and at C band for Globalstar.

The main difference, however, lies in the location of the complexity. For Iridium system, calls are processed and routed by onboard processors. This means that a call placed by an Iridium subscriber to another subscriber is transmitted directly by satellites to its destination worldwide. The number of terrestrial gateways is therefore reduced (about 11 stations worldwide). Intersatellite links are established at Ka band. If the call is to a conventional mobile or fixed phone, it is upconverted and transmitted by a feeder link from the last satellite to a gateway. The whole system is illustrated in Figure 3.9.

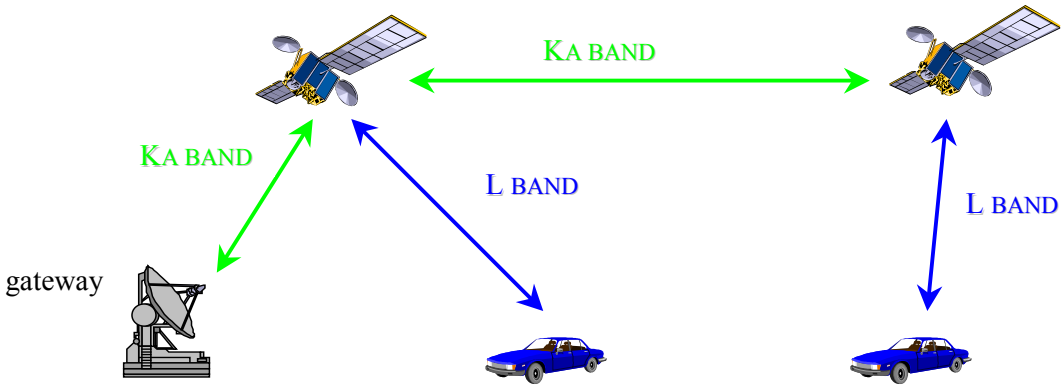

Figure 3.9 *Iridium system overview*

In contrast to Iridium, Globalstar has neither onboard processing nor intersatellite links. Instead, as many functions as possible, including call processing and switching, are located in the ground segment. Rather than directly connecting one caller to another by satellites only, Globalstar downlinks L band calls received by a satellite over feeder links to a gateway.

There, they are processed and routed through the terrestrial infrastructure. If the called party is another subscriber, the call is uplinked from the same or another gateway to a satellite for transmission to the destination. Fewer satellites and reduced space complexity mean more gateways on the ground in comparison to Iridium. As many as 240 Globalstar gateways are scheduled around the globe [12].

Since network management is beyond the scope of this thesis, the study case is restricted to a fixed feeder link and to mobile up- and downlinks. By default, it is mainly based on Iridium constellation, but the methods could easily be applied to Globalstar's parameters. That is why the case is referred as LEO-N (N = 48, 66) and not specifically as Iridium.

Both C and K/Ka bands are investigated regarding atmospheric effects on the feeder link. As far as the mobile link is concerned, long- and short-term prediction methods are applied using the developed formalism.

3.4.2 System specifications

As already mentioned, the Iridium system [6] is constituted by a constellation of 66 satellites, equally distributed on six orbital planes, while Globalstar relies on 48 satellites only. Both systems provide phone and paging services, with net (uncoded) data rates up to 2.4 kbps.

Each satellite generates a cluster of cells (48 for Iridium) on the earth's surface, formed by parallel array antennas. Variable antenna gains and automatic power-control are used to compensate for the different path losses from innermost to outermost cells, as well as for varying transmission conditions, e.g. attenuation due to vegetation and building shadowing.

Table 3.2 and Table 3.3 summarize the specifications that are chosen for the simulations. Regarding the feeder link, the fade margin is divided in two parts for clear-sky and rain attenuation respectively, the rainy part varying according to fade mitigation algorithms.

Considering the mobile link, the quadrifilar helix is the usual antenna in land mobile satellite systems [13]. Its pattern has already been presented in Section 2.2.4.5 (p. 84). The convolutional coding is taken into account using the upper bound given by (2.67-a). The fade margin is large, but a similar value is also recommended in [10] for urban use of LMS systems.

LEO-66 characteristics (feeder link)	
Orbit type (altitude)	Circular (780 km)
Gateway antenna type	Parabolic (3.5 m diameter)
Downlink frequency	19.4-19.6 GHz
Uplink frequency	29.1-29.3 GHz
Modulation scheme	QPSK
Polarisation	Right circular
Error protection	Convolutional $R_c = 1/2$, $K = 7$
Required effective E_b/N_0	6.7 dB for BER 10^{-6}
Data rate	12.5 Mbps
Availability	99.8 %
Downlink fade margin	3.3 dB (fixed) + 13 dB (variable)
Uplink fade margin	3.3 dB (fixed) + 26 dB (variable)

Table 3.2 *LEO-66 feeder link main specifications*

LEO-*N* characteristics (mobile link)	
Mobile antenna	Quadrifilar helix
Frequency	Around 1.6 GHz
Modulation scheme	QPSK
Polarisation	Right circular
Error protection	Convolutional $R_c = 3/4$, $K = 7$
Required effective E_b/N_0	3.1 dB for BER 10^{-2}
Channel symbol rate	50 ksps
Channel bandwidth	31.5 kHz
Fade margin	16 dB

Table 3.3 *LEO-N mobile link main specifications*

Whenever possible, simulations compare Iridium (LEO-66) with the Globalstar system (LEO-48). The mobile link specifications are assumed to be the same as Iridium, while Globalstar's specific characteristics are given in Table 3.4.

LEO-48 characteristics (Globalstar feeder link)	
Orbit type (altitude)	Circular (1414 km)
Gateway antenna type	Parabolic (3.5 m diameter)
Downlink frequency	6.875-7.075 GHz
Uplink frequency	5.025-5.225 GHz

Table 3.4 *Main specifications of LEO-48 feeder link*

3.4.3 Feeder link

3.4.3.1 MODELLING APPROACH

For specified elevation angle, the various fade impairments are calculated using:

- Liebe-Salonen model for water vapour attenuation,
- ITU-R model for oxygen attenuation (ITU-R Rec. PN.676-2),
- ITU-R model for rain attenuation (ITU-R Rec. PN.618-5),
- Salonen-Uppala model for cloud attenuation statistics (ITU-R Rec. PN.840-1),
- ITU-R model for scintillation (ITU-R Rec. PN.618-5),
- Castanet-Lemorton combination model for the total attenuation.

As outlined in Chapter 1, radiometeorological parameters (integrated water vapour content, integrated liquid water content of heavy clouds, $R_{0.01}$, etc.) are obtained from ECMWF maps.

Finally, the variation of the elevation angle is accounted for by combining the conditional fade cumulative distribution with the distribution of elevation angle, as described in Section 1.6.1.

3.4.3.2 SIMULATION RESULTS

In a first part, the true Iridium and Globalstar systems are simulated. The following frequencies are chosen in the simulations:

- 19.6 GHz (uplink) and 29.3 GHz (downlink) for Iridium,
- 7.075 GHz for Globalstar (downlink).

Simulations are performed considering a single receiving site located near Rome (Fucino, 41.9° N lat., 12.5° E long.). For this location, Figure 3.10 presents the distributions of maximum elevation angle as simulated by the orbit generator, together with the best-fitted lognormal approximations. The lognormal parameters μ and σ are indicated on the graphs. It must be added that the simulated distributions agree very well with those presented in [14] at the same latitude.

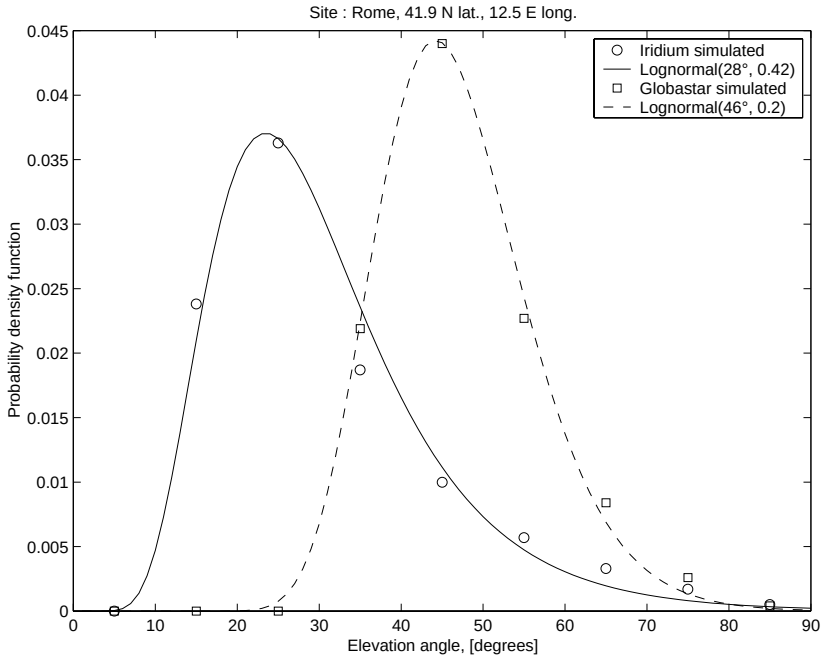

Figure 3.10 *Distribution of elevation angle for Iridium and Globalstar (Rome)*

Globalstar generally provides higher elevation angles in Rome than Iridium, despite a smaller number of satellites. However, Iridium has global coverage, while Globalstar only covers 80 % of the earth.

Several simulation results are displayed in Figure 3.11 to Figure 3.13.

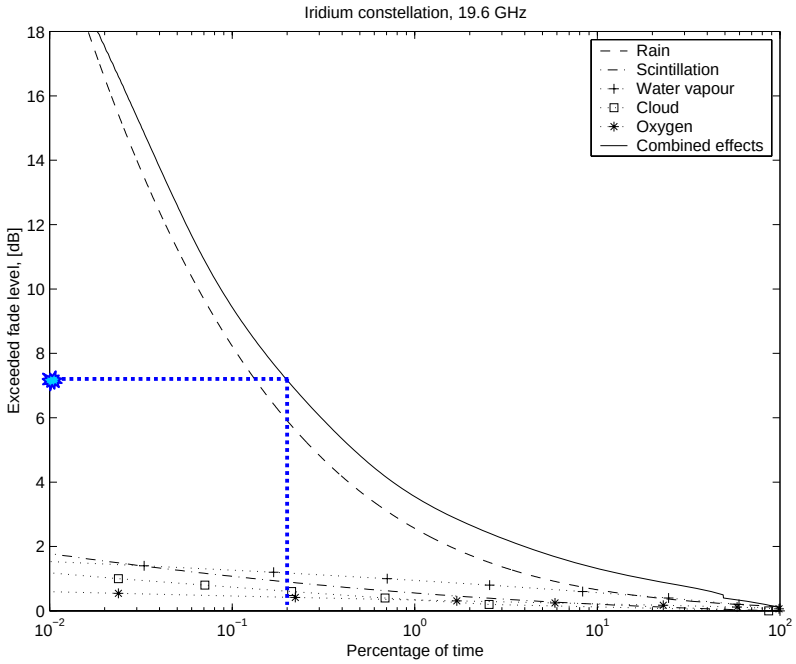

Figure 3.11 *Cumulative distribution of attenuation due to various atmospheric mechanisms, for the Iridium downlink (Rome)*

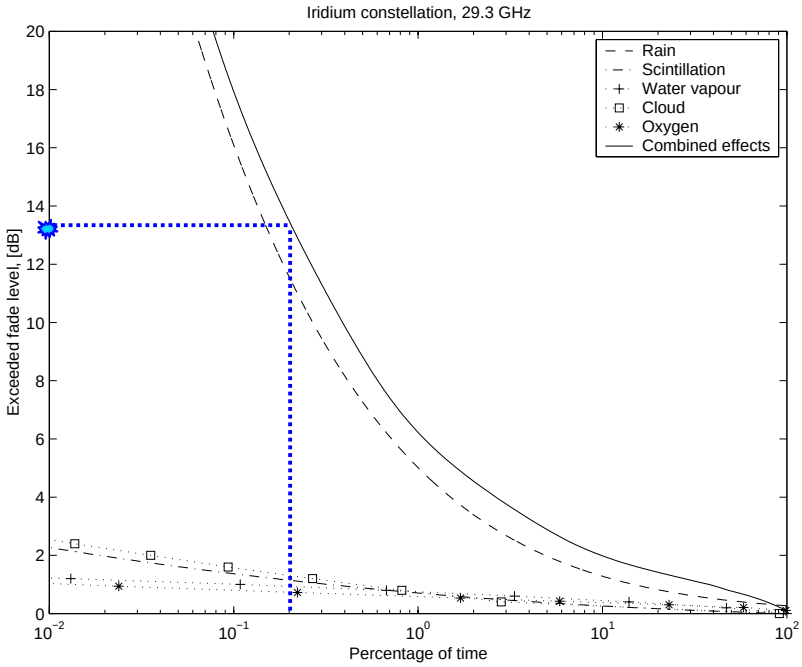

Figure 3.12 *Cumulative distribution of attenuation due to various atmospheric mechanisms, for the Iridium uplink (Rome)*

Regarding the Iridium feeder link, rain is, as expected, the main source of impairment. Among clear-sky mechanisms, water vapour attenuation dominates at 19.6 GHz, while clouds provide the highest attenuation at 29.3 GHz. This results from the 22.3-GHz peak of water vapour absorption. At both bands, the attenuation due to scintillation may not be neglected, being of the very same order of magnitude as cloud (19.6 GHz) or water vapour (29.3 GHz) attenuation. However, it should be kept in mind that the ITU-R model for the distribution of scintillation-induced variations only accounts for fading. Yet, scintillation causes both fading and enhancement (this overestimation is compensated in the estimation of total impairment, see Section 1.5.3.2).

The minimum required fade margins at 99.8 % availability (0.2 % of outage) can be easily inferred from the graphs. The clear-sky attenuation is calculated by equiprobability summing of attenuation due to gas, cloud and scintillation, while the total attenuation is simply read, as indicated by dashed lines. Values are summarized in Table 3.5.

	Clear-sky only	**Clear-sky + rain**
Downlink (19.6 GHz)	3.1 dB	7.26 dB
Uplink (29.3 GHz)	4.1 dB	13.23 dB

Table 3.5 *Required fade margins for Iridium feeder link (Rome)*

At 29.3 GHz, the clear-sky fixed margin of 3.3 dB given in Table 3.2 is exceeded by the simulated margin. However, one should not forget that:

- the clear-sky fade margin is calculated by equiprobability summing of attenuation due to gas, cloud and scintillation, what constitutes a kind of worst case,
- the ITU-R model for scintillation overestimates the attenuation.

Nevertheless, the total available margins displayed in Table 3.2 (16.3 dB and 29.3 dB for down/up links respectively) seem sufficiently large enough. Such margins would yield, following the simulations, availability of up to 99.97 % on both links.

At C band and for Globalstar constellation (Figure 3.13), the relative dominance of rain is actually less significant if compared to clear-sky effects. Meanwhile, scintillation appears to be the predominant clear-sky effect.

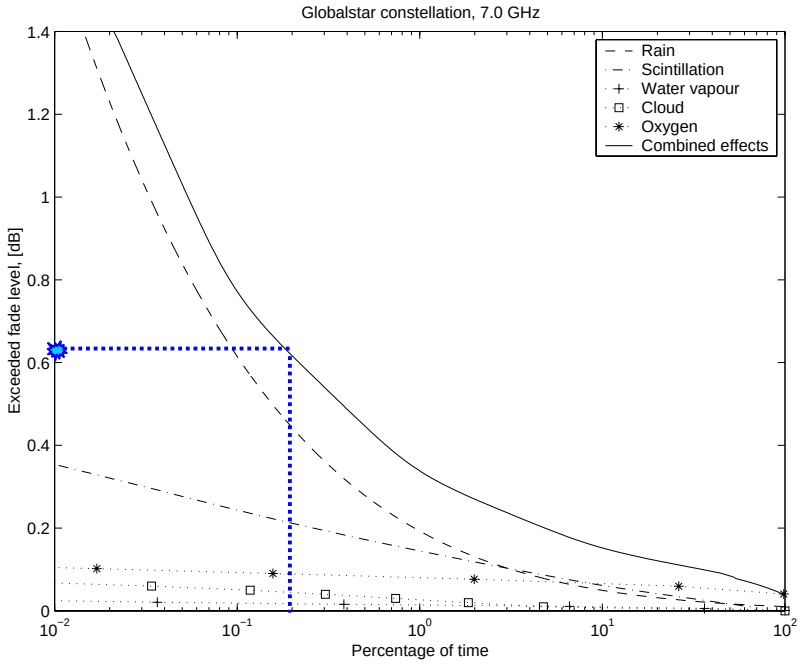

Figure 3.13 *Cumulative distribution of attenuation due to various atmospheric mechanisms, for the Globalstar downlink (Rome)*

The required fade margin to achieve 99.8 % availability is 0.36 dB and 0.63 dB for clear-sky and rain conditions respectively.

In a second stage, simulations have been performed considering hypothetical systems, based on Iridium or Globalstar constellations and operating at various frequencies: 7.075 GHz, 19.6 GHz and 29.3 GHz. The cumulative distributions of the total impairment are depicted in Figure 3.14 for the six combinations of constellation and frequency.

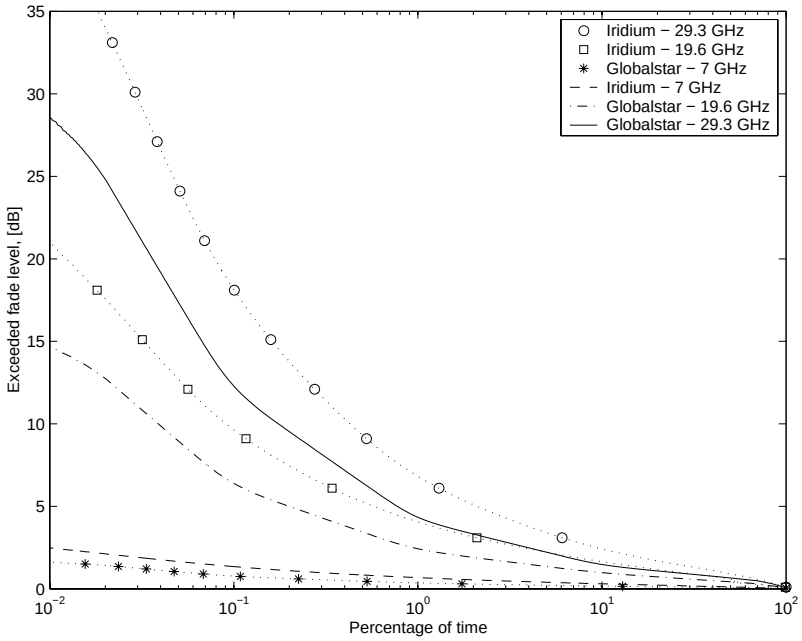

Figure 3.14 *Fade cumulative distributions considering two constellations (Iridium and Globalstar) and three frequency bands (C, K, Ka)*

It seems that Globalstar constellation, with 48 satellites, allows for a smaller fade margin than Iridium-66. That difference can really be significant at K and Ka bands. The design of the Iridium constellation might therefore be questionable, although one should not forget that Globalstar does not provide worldwide coverage.

3.4.4 Mobile user link: long-term performance

3.4.4.1 PHYSICAL-STATISTICAL ANALYSIS IN BUILT-UP AREAS

1° Distributions of physical parameters

In order to apply the physical-statistical approach, the physical parameters are assigned the following distributions:

- for the elevation angle, a lognormal distribution, whose parameters μ and σ, depending on the constellation and the latitude, are inferred by means of an orbit generator (see Table 3.6),
- for the azimuth angle, a distribution combining both open-area and built-up sections [5],

$$T_{\Phi}(\phi) = p\,\delta(\phi) + (1-p)\frac{1}{2\pi} \tag{3.20}$$

where p is defined as the percentage of open area and is represented by a LOS situation[†],

- for the building height, a lognormal distribution with parameters given in Table 3.6 for several environments (see Section 2.3.2.1),
- for the street width, a constant value w_0,
- for the mobile position in the street, a constant value relative to street width, $d_m = w_0/2$.

Table 3.6 summarizes the values of several parameters appearing in the above distributions. Three types of areas are considered: Westminster (London, urban), Guildford (Surrey, suburban) and Rome (urban, based on Athens area's parameters inferred from [17], see Section 2.3.5).

Type of area	Elevation angle		% open area p	Building height		Street width
	μ [deg.]	σ		μ [m]	σ	w_0 [m]
Urban (West.), Iridium	30.5	0.405	≈ 0	20.6	0.44	35
Suburban (Guildford), Irid.	30.5	0.405	20	7.1	0.25	15
Urban (Rome), Iridium	28	0.42	≈ 0	15	0.3	12
Urban (Rome), Globalstar	46	0.20	≈ 0	15	0.3	12

Table 3.6 *Statistical parameters describing the physical environments*

2° Simulation results

Since every physical parameter is now represented by an analytical distribution, the methods defined in Section 3.2 can be applied to LEO-66 system. The performance is predicted by means of the distribution over time and area of the fade level as well as of the coded BER. The coverage, at specified percentages of time, is defined as the percentage of area over which the achieved fade level or BER is less than a target value.

Regarding the fade level distribution, the simulation results for Rome, Westminster and Guildford are depicted in Figure 3.15, Figure 3.17 and Figure 3.16 respectively.

[†] Note that the percentage of open areas include not only actual open-area sections, but also crossroads and spaces between buildings. At this stage, they are all assumed to be suitably represented by the situation $\phi = 0°$. A more accurate analysis (see Section 3.4.6.4) will moderate the validity of this assumption.

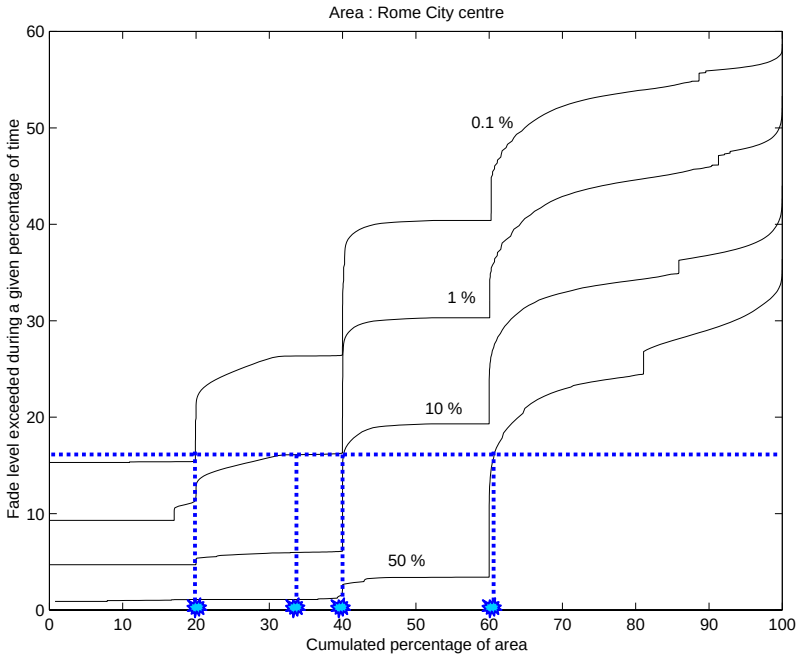

Figure 3.15 *Cumulative distribution over the area (Rome) of the exceeded fade level for 50, 10, 1 and 0.1 % of outage (Iridium constellation)*

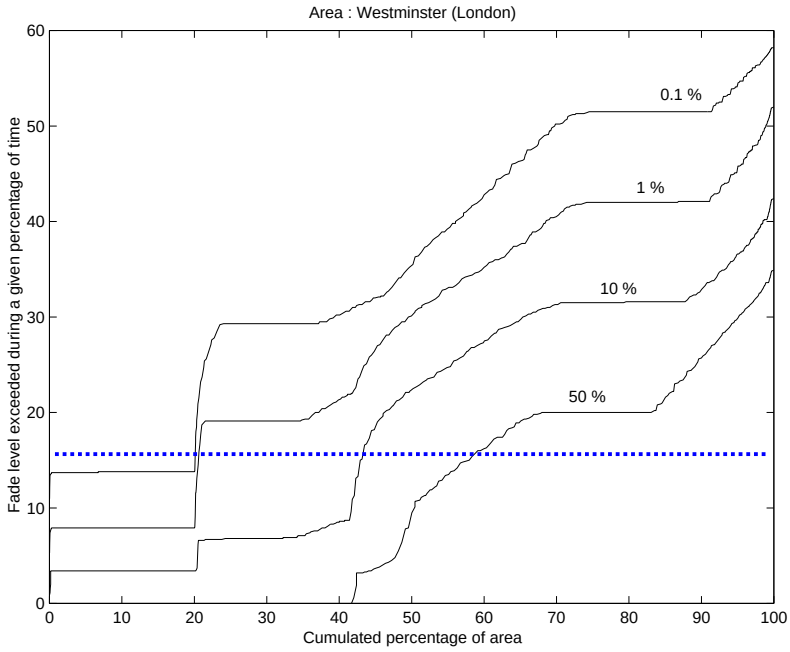

Figure 3.16 *Cumulative distribution over the area (Westminster, London) of the exceeded fade level for 50, 10, 1 and 0.1 % of outage (Iridium constellation)*

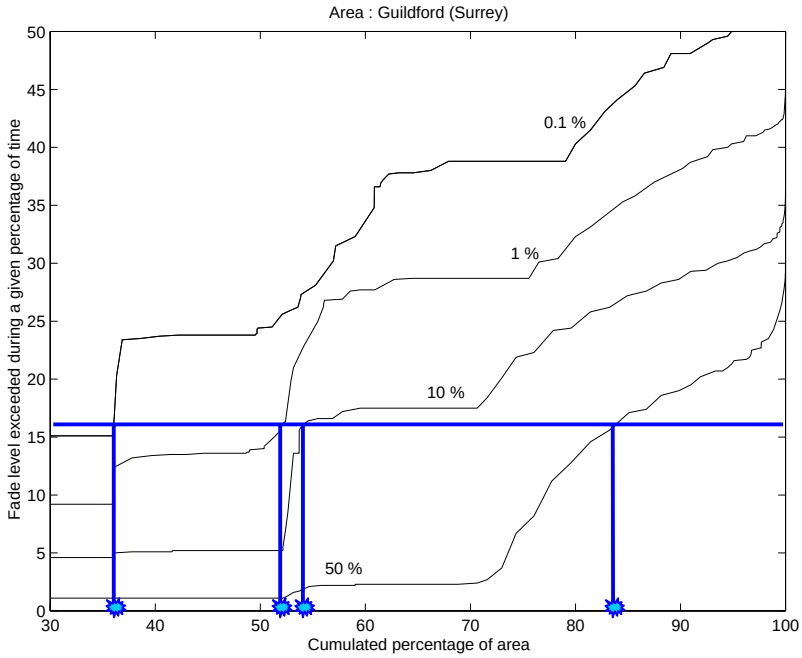

Figure 3.17 *Cumulative distribution over the area (Guildford, Surrey) of the exceeded fade level for 50, 10, 1 and 0.1 % of outage (Iridium constellation)*

These graphs can be interpreted as follows. For example, in Figure 3.17, a fade level of 16 dB is exceeded during:

50 % of time on 83.7 %
10 % of time on 54.0 %
1 % of time on 52.0 %
} of the considered area (as illustrated by the stars).
0.1 % of time on 36.0 %

In other words, the attenuation is less than 16 dB during

the availability for a margin of 16 dB is

50 % of time on 83.7 %
90 % of time on 54.0 %
99 % of time on 52.0 %
} of the considered area.
99.9 % of time on 36.0 %

The effect of the quantification of the azimuth angle clearly appears. Simulations have indeed been run every 22.5 degrees in azimuth. That causes steps to be observed on several curves (especially in Figure 3.15).

The performance is much better in the suburban area (Guildford) than in urban areas. Because the average street widths are quite similar in Rome and Guildford, the comparison points out that the difference of performance results mainly from the different open-area percentages and from the highly different mean building height values. In general, the distribution over the area is very sensitive to the percentage of line-of-sight. This percentage results from the addition of the percentage of open area *p* with the line-of-sight ratio in built-up area. For a given value of street width, the latter is directly related to the building height and azimuth angle distributions.

Being based on Globalstar's parameters in Rome, Figure 3.18 highlights the influence of the constellation design on the coverage. If this graph is compared with Figure 3.15, it can be noticed that the performance is significantly improved with Globalstar satellites.

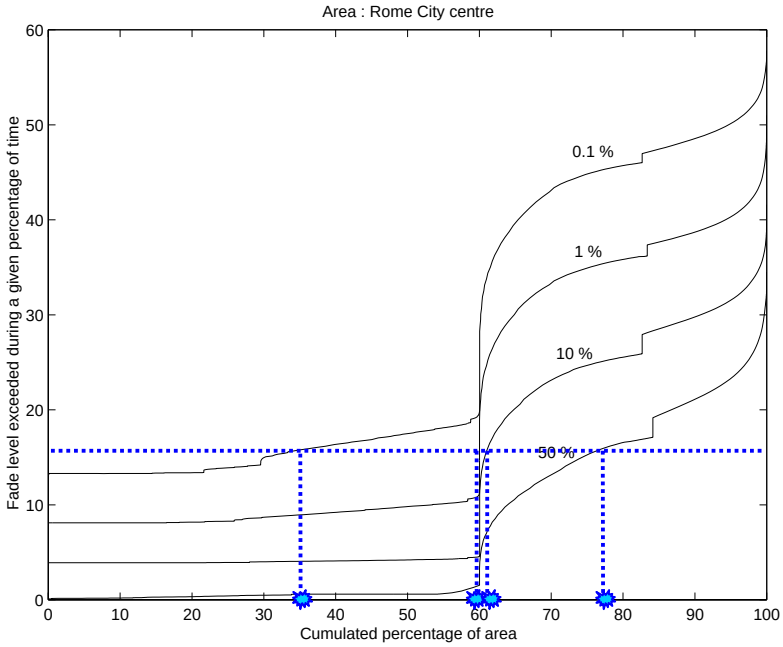

Figure 3.18 *Cumulative distribution over the area (Rome) of the exceeded fade level for 50, 10, 1 and 0.1 % of outage (Globalstar constellation)*

Considering a given fade level, a more synthetic presentation of the results is for example illustrated in Figure 3.19. The graph compares the achieved coverage in Rome, as a function of the availability (percentage of time), for Iridium and Globalstar. A difference of some 21.5 % of area is observed given any percentage of area.

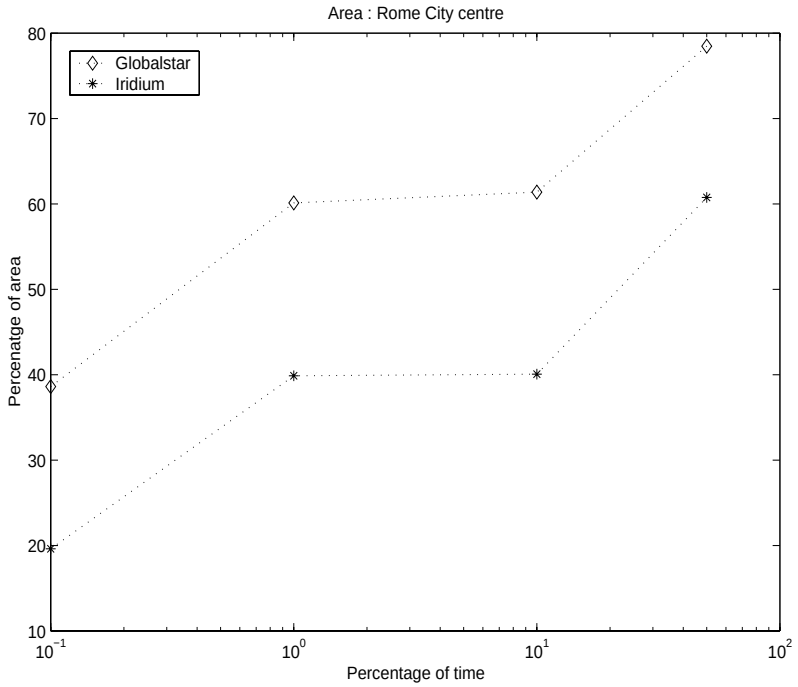

Figure 3.19 *Coverage (at 16 dB fade level) for two constellations in Rome*

The coverage can also be predicted on the basis of the BER, as soon as the system margin is known. As far as BER predictions are concerned, Figure 3.20 shows, for several percentages of time, the impact of the system margin on the coverage. The latter is defined as the percentage of area over which the BER is less than 10^{-2}. The system margin is the difference between the used SNR and the minimum SNR required to achieve a BER of 10^{-2}.

As already noticed for the fade level, the coverage is far better in suburbs. Except for 0.1 % of outage, the performance is not considerably degraded when the margin is reduced from 16 dB down to 10 dB.

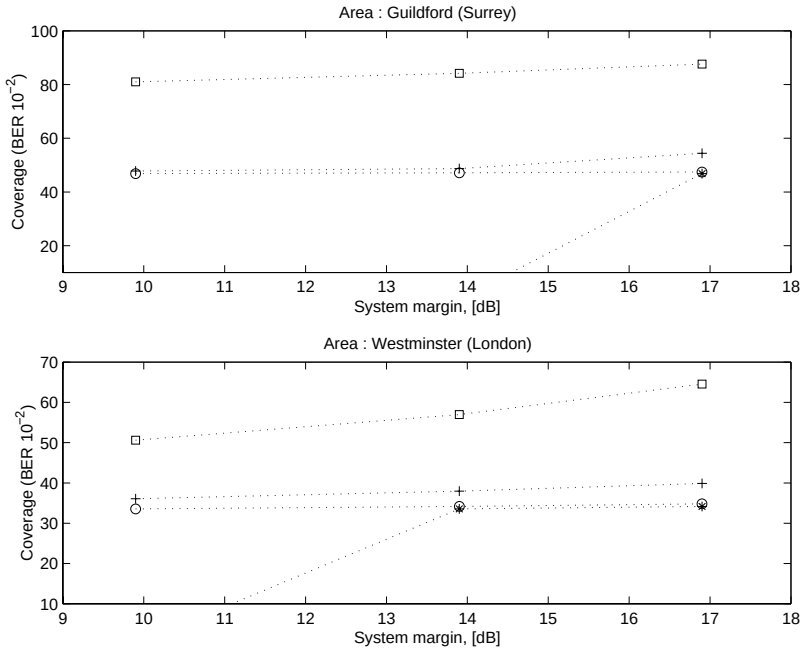

Figure 3.20 *Coverage achieved for BER 10^{-2} as a function of the system margin for several percentages of outage: 0.1 % {*}, 1 % {o}, 10 % {+} and 50 % {squares}*

3.4.4.2 TIME SERIES ANALYSIS IN BUILT-UP AREAS

1° Physical inputs

With LEO-66 system in mind, several simulations are performed using the COST 255 methodology. Typical urban and suburban areas are defined on the basis of a lognormal distribution (median μ, standard deviation σ) for the building height, and a constant value w_0 for the street width. Table 3.7 summarizes the parameters featuring each environment.

Type of area	**Building height**		**Street width w_0 [m]**
	μ [m]	**σ**	
Urban	20.6	0.44	15
Suburban	7.1	0.25	15

Table 3.7 *Physical parameters for urban and suburban types of area*

In accordance with the method, spatial series of the received signal are generated for given elevation angles. The mobile terminal is assumed to move down long straight streets, lined on both sides with buildings. Streets are consecutively oriented following various azimuth angles relative to the satellite link, assessing a uniform distribution of azimuth [15].

2° Simulations results

Figure 3.21 presents a comparison between the distributions of E_b/N_0 as a function of the spatial coverage in the two areas and for two latitudes (London and Rome). The various curves should be related with the following percentages of time (from left to right):

- 1.06, 1.61, 2.47, 3.79, 5.83, 8.93, 13.51, 20.51 (indicated by a star), 30.35, 43.63, 60.04, 77.50, 91.81, 98.88, 99.99 and 100.00 % of time if considering the London latitude,
- 0.75, 1.16, 1.79, 2.77, 4.29, 6.66, 10.33, 15.90 (indicated by a star), 24.18, 35.96, 51.58, 69.90, 87.13, 97.63, 99.98 and 100.00 % of time if considering the Rome latitude.

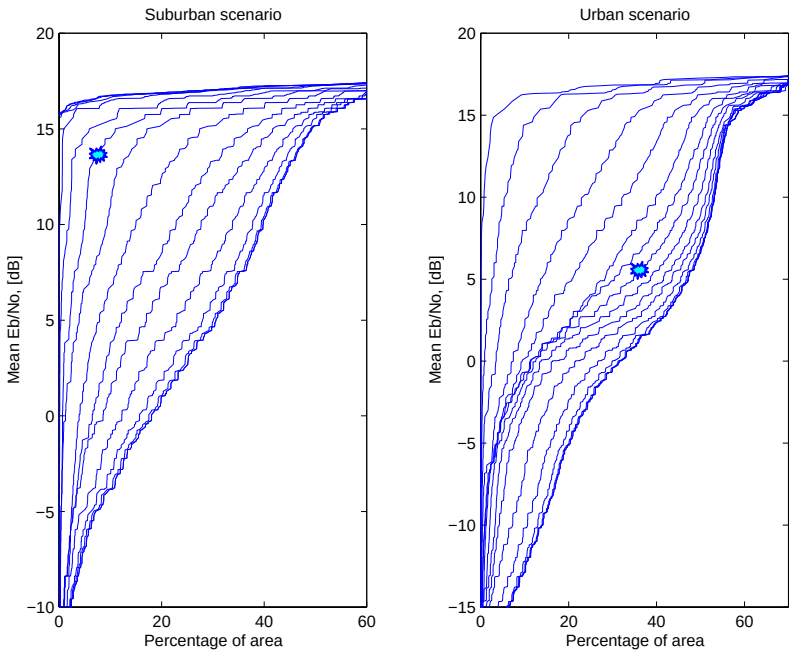

Figure 3.21 *Percentage of area over which E_b/N_0 is less than ordinate, in suburban (left) and urban (right) areas for several percentages of time*

For the suburban scenario, the five first curves (on the left) as well as the two last curves are quasi-superimposed. The same remark is valid for the three last curves with regard to the urban case. It is clear that the curves remain the same at both latitudes; only the percentage of

time related to each curve differs. The graphs of Figure 3.21 should be interpreted as follows. For example, in the urban case at the Rome latitude, the mean E_b/N_0 is less than 5 dB during:

1.16 % of time on 2.61 %
2.77 % of time on 13.58 %
6.66 % of time on 28.21 % } of the considered area.
15.90 % of time on 35.00 %
35.96 % of time on 41.79 %

Figure 3.22 allows to compare the performance at both latitudes (upper figure) as well as in both environments (lower figure). The upper figure shows what is gained in terms of absolute availability at the Rome latitude relative to the London latitude as a function of the percentage of area over which E_b/N_0 is less than 5 dB. For both types of areas, the availability can be increased by some 8 % in Rome latitude with regard to London latitude. The urban curve is naturally right-shifted, since the coverage is worse in urban environment.

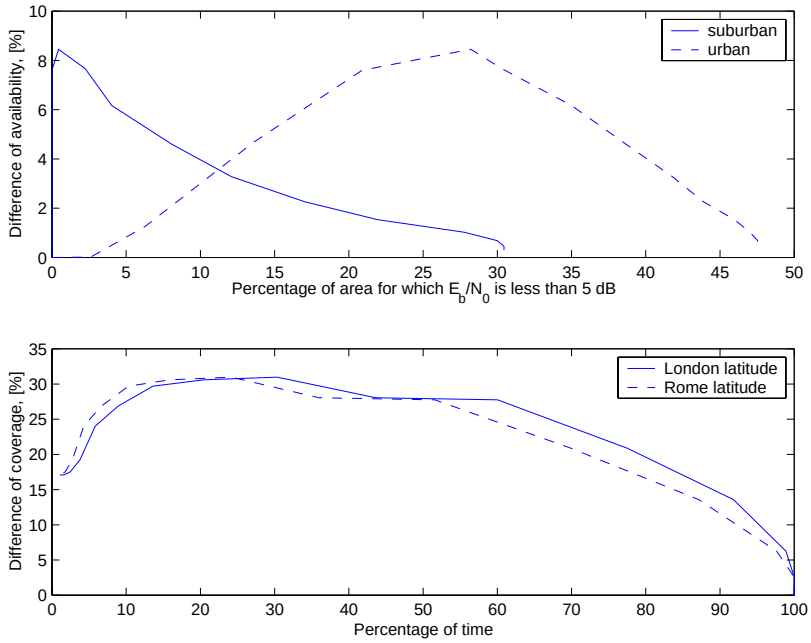

Figure 3.22 *Comparison between availability at both latitudes as a function of coverage (upper graph) and between coverage for both areas as a function of availability (lower graph)*

Concerning the improvement of performance in terms of coverage (lower graph), the results are similar at both latitudes. The absolute gain varies between 5 % and 30 %. This comparison highlights a major advantage of the approach. Thanks to the physical background, statistical

results are produced in terms of availability/coverage and are directly related to objective parameters, such as building height and street width.

3.4.5 Mobile user link: shadowing correlation analysis

3.4.5.1 STATISTICS OF ELEVATION ANGLES AND AZIMUTH SEPARATION

In order to calculate the global shadowing correlation coefficient for a given constellation, time series of first and second elevation angles as well as of azimuth separation must be computed from the orbit generator. Although they are not explicitly used on a separate basis in the following, it can be interesting to compare the statistical distributions of these three angles. For Iridium and Globalstar constellations, Figure 3.23 and Figure 3.24 describe the probability density of the two highest elevation angles and azimuth separation, at the London latitude, over a complete geosynchronous period.

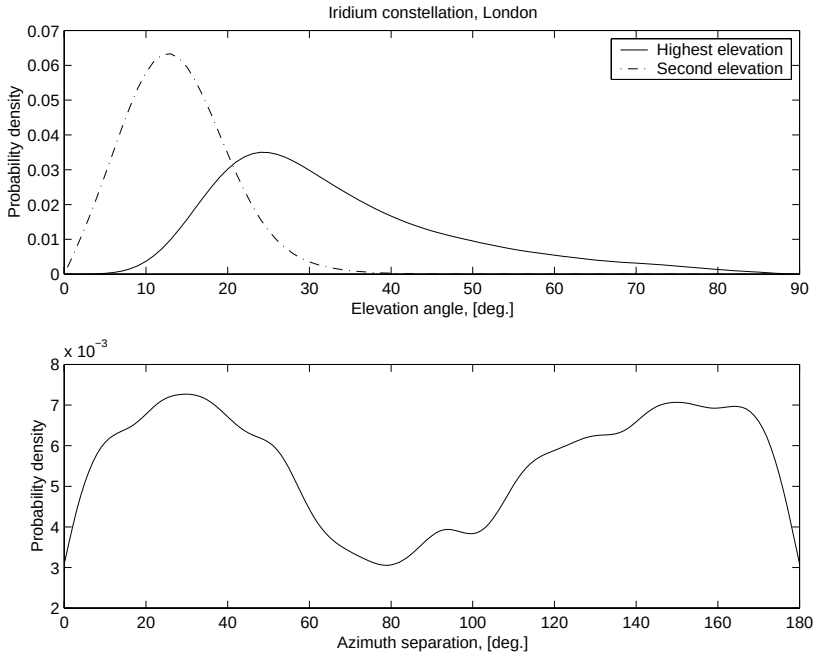

Figure 3.23 *Statistical distributions of elevation angles and azimuth separation for the two nearest satellites (Iridium constellation, London)*

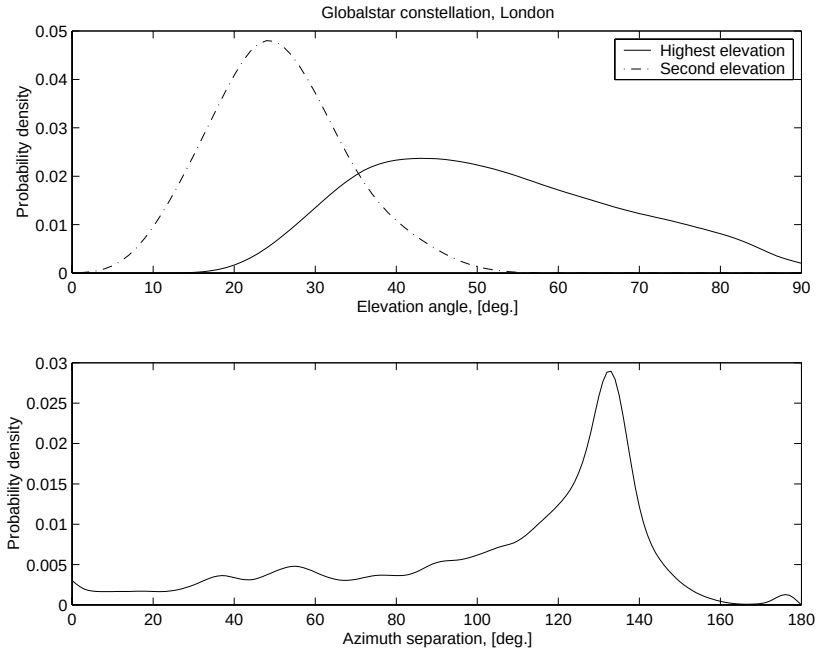

Figure 3.24 *Statistical distributions of elevation angles and azimuth separation for the two nearest satellites (Globalstar constellation, London)*

The elevation angles are in average higher for Globalstar. Also, the azimuth separation is symmetrically distributed for Iridium, while it peaks around 135 degrees for Globalstar. For such azimuth separations, the correlation coefficient is often near zero, as deduced from Figure 2.31 to 2.35. Hence, a small correlation coefficient must be expected in a large number of Globalstar-based scenarios.

3.4.5.2 SIMULATION RESULTS

As already outlined, the joint distribution of the two highest elevation angles and azimuth separation cannot be easily obtained in an analytical form, so that the integration (2.61) as well as the estimation of the distribution are performed by using concurrent time series of the mentioned angles.

Four environments, described in Table 3.8, are used in the simulations.

		E_1	E_2	E_3	E_4
Building height lognormal	μ [m]	7.1	7.1	20.6	20.6
parameters	σ	0.25	0.25	0.44	0.44
Street width w_0 [m]		12	20	12	20

Table 3.8 *Geometrical characteristics of simulated areas*

Considering first a median receiving position ($d_m = w_0/2$), the average (log-)shadowing correlation coefficients are given in Table 3.9 for both investigated constellations (at London).

		E_1	E_2	E_3	E_4
$\hat{\rho}$	Iridium	0.0567	0.0456	0.0865	0.1012
	Globalstar	– 0.0601	– 0.0098	– 0.1755	– 0.1856
$\hat{\rho}_{dB}$	Iridium	0.1212	0.0702	0.1251	0.0850
	Globalstar	– 0.0638	– 0.0495	– 0.2031	– 0.1871

Table 3.9 *Average linear and log- shadowing correlation coefficient ($d_m = w_0/2$)*

In all cases, the mean correlation coefficient is found to be positive for Iridium and negative for Globalstar. Moreover, the strong negative shadowing correlation observed in the two urban cases for Globalstar is very promising in terms of handoff diversity.

Nevertheless, when the average correlation is very low, its value is not a very significant parameter because the shadowing correlation might vary considerably around this value. Therefore, Figure 3.25 and Figure 3.26 illustrate respectively the distributions of shadowing and log-shadowing correlation coefficients considering Iridium and Globalstar constellations in the four simulated areas.

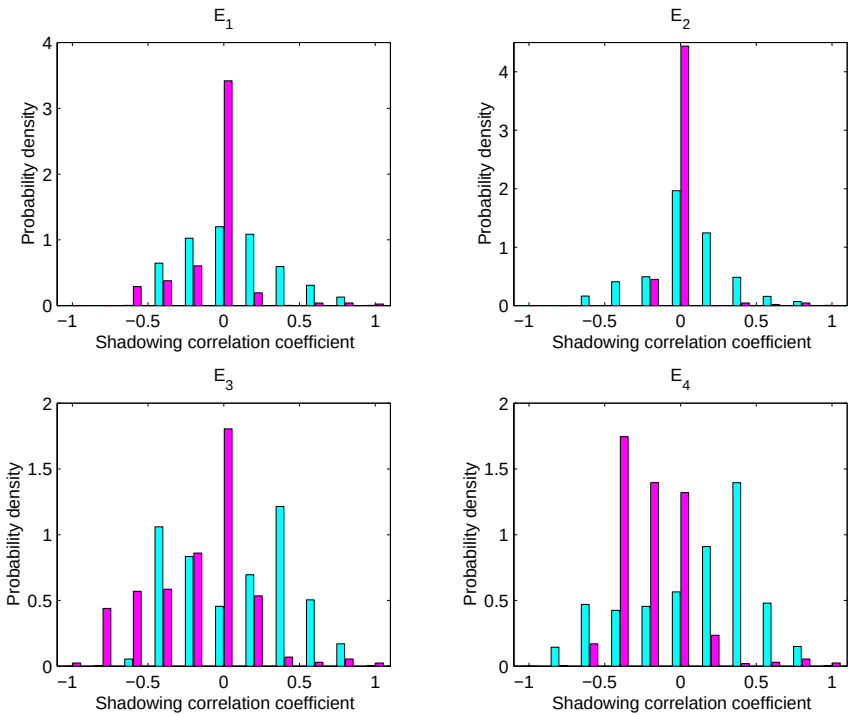

Figure 3.25 *Distribution of linear shadowing correlation coefficient for Iridium {light grey} and Globalstar {dark grey} constellations*

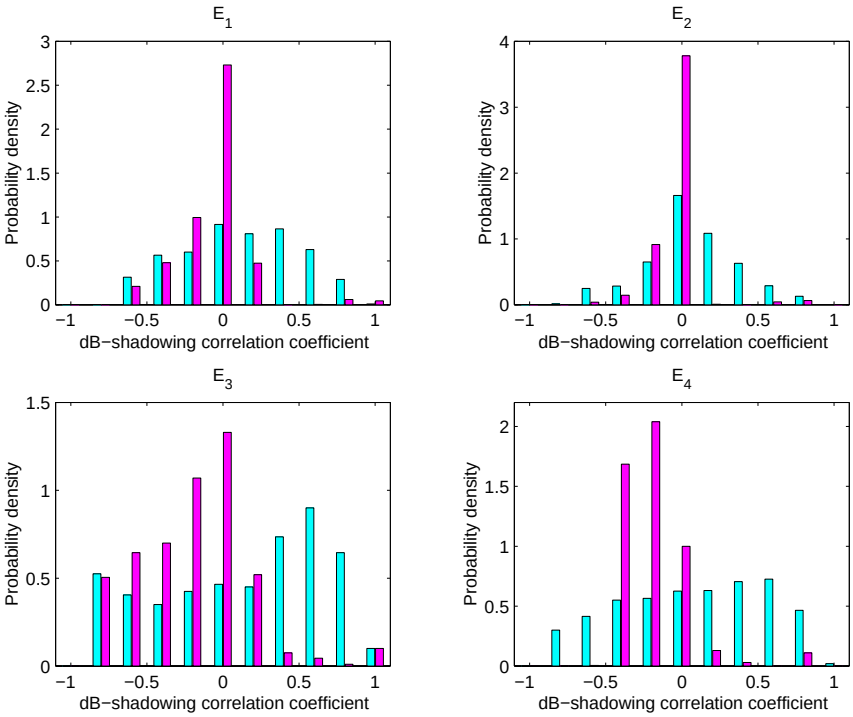

Figure 3.26 *Distribution of log-shadowing correlation coefficient for Iridium {light grey} and Globalstar {dark grey} constellations*

The distributions of ρ and ρ_{dB} are globally similar, although a few significant differences can be noticed (see for instance in area E_3, for Iridium constellation). As far as Iridium system is concerned, the (log-)shadowing correlation coefficient is more or less symmetrically spread around 0 between -1 and 1. Moreover, when the distribution is asymmetrical, the probability of positive correlation is higher than that of negative correlation (see in areas E_3 and E_4). That demonstrates that Iridium constellation does not seem to be optimised towards dual diversity, at least at London latitude.

In contrast, for Globalstar, the correlation is negative most of the time, especially in urban areas. In suburban areas, diversity paths tend to be mainly uncorrelated. As a consequence, dual diversity should significantly improve Globalstar performance.

The case of a non-median receiving position (d_m = 1 m) is also investigated in the four simulated areas. In Table 3.10, the best results (in view of dual-diversity) are again achieved by Globalstar, especially in areas E_2 and E_4.

		E_1	E_2	E_3	E_4
$\hat{\rho}_{dB}$	Iridium	0.1910	– 0.0638	0.1486	0.0246
	Globalstar	0.0327	– 0.3814	0.0728	– 0.3648

Table 3.10 *Average log-shadowing correlation coefficient (d_m = 1 m)*

In order to compare the achievable diversity gain in both receiving positions, Table 3.11 displays, for each case, the percentage of time for which the correlation is negative (≤ 0).

		E_1	E_2	E_3	E_4
$d_m = w_0/2$	Iridium	38.8	40.6	38.9	42.2
	Globalstar	61.7	92.1	72.8	89.9
$d_m = 1$ m	Iridium	28.3	53.3	40.6	47.4
	Globalstar	45.2	77.3	37.2	76.2

Table 3.11 *Percentage of time for which the correlation is negative, in the four areas*

Clearly, the diversity gain should be higher for Globalstar than for Iridium. Globalstar's diversity gain usually increases in the case of $d_m = w_0/2$ (with respect to a non-median position) as well as for large streets. This is less clear for Iridium. Also, for both

constellations, the impact of the average building height on the diversity gain is not straightforward. A more direct link could possibly be established between the diversity gain and a particular percentile of the building height distribution, rather than using the average height.

3.4.6 Mobile user link: short-term performance in canonical scenarios

3.4.6.1 DEFINITION OF CANONICAL SCENARIOS

Before applying simulation tools, typical or *canonical* scenarios must be defined. Usually, predictions deal with a generic area, such as roadside trees in ITU-R Rec. 681-1 [16]. As another example, remember that the physical-statistical model described in Chapter 2 is based on a part of a straight street combined with open-area sections.

In order to complete the developed physical-statistical model, two frequent built-up configurations are investigated in the following: a straight street and a crossroad. The latter should indeed deserve a particular attention, since crossroads might actually not be considered as simple open-area sections of a street.

Meanwhile, a multi-satellite constellation moves continuously over time. Hence, the choice of a simulation period (e.g. ten minutes) is possibly significant.

1° Canonical time periods

The orbit generator (see Appendix B) simulates the satellite constellation motion around the earth. It has been shown in Chapter 2 that the distribution of elevation angle over time strongly depends on the latitude. In the exemplary simulations to be presented, the receiver is assumed to be located in London (51.5° N) and the chosen LEO-*N* constellation is Iridium, although any other could have been used. Figure 3.27 depicts the variation of maximum elevation angle ϑ_M (related to the nearest satellite) over 240 minutes for Iridium constellation.

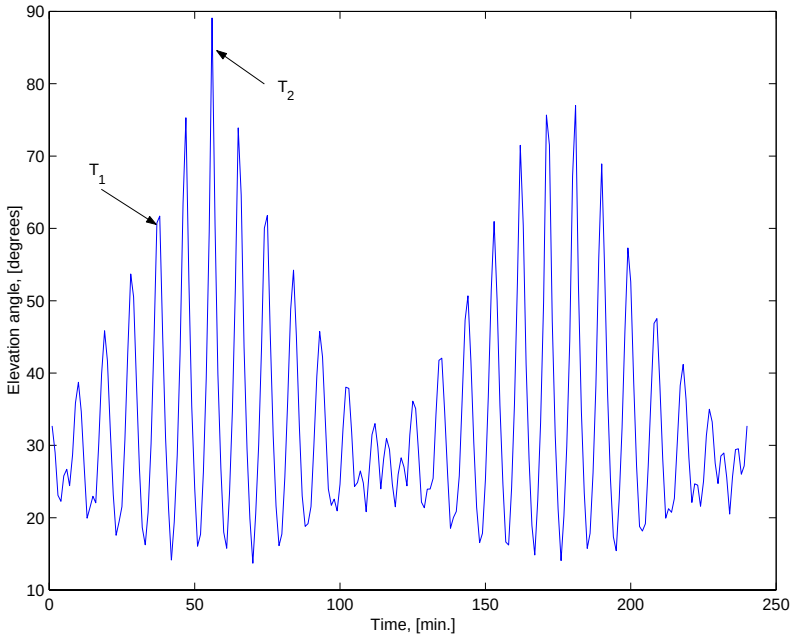

Figure 3.27 *Maximum elevation angle as a function of time (London, Iridium constellation)*

During a typical communication of ten minutes, the elevation angle is lower-bounded by a constant value (≅ 15° for the Iridium constellation), and the upper bound depends on the time the communication takes place. Subsequently, two different simulation periods are considered, as indicated in Figure 3.27: the first period (denoted hereafter as $\boldsymbol{T_1}$) is taken between the periods with maximum and minimum upper bounds. It is characterized by a local upper bound of about 63 degrees. The second period ($\boldsymbol{T_2}$) is taken to be around the global maximal value for ϑ_M, i.e. about 88 degrees. The case of low local upper bounds (e.g. around t = 120 minutes) is not analyzed, since the elevation angle does not significantly vary during such time periods, so that a quasi-static analysis may be sufficient.

As far as these two periods are concerned, Figure 3.28 describes the motion of the nearest satellites above London during the ten considered minutes. The satellites' successive positions are joined by a solid line when the considered satellite is active. It can be observed that orbits are nearly polar and that a handover occurs when the active satellite moves toward the pole.

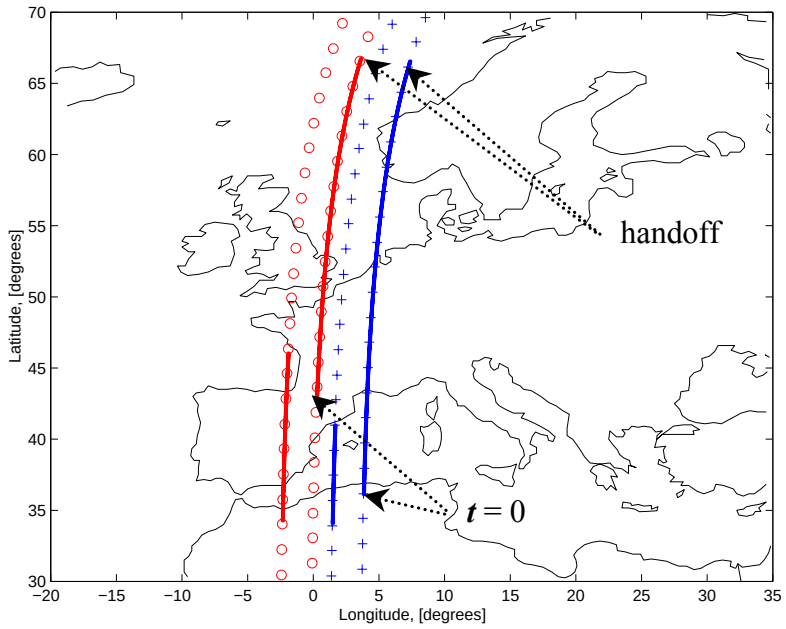

Figure 3.28 *Tracks of the active satellites during the two canonical time periods: T_1 {+} and T_2 {o}*

Figure 3.29 illustrates the variation of elevation and azimuth angles for both scenarios T_1 and T_2.

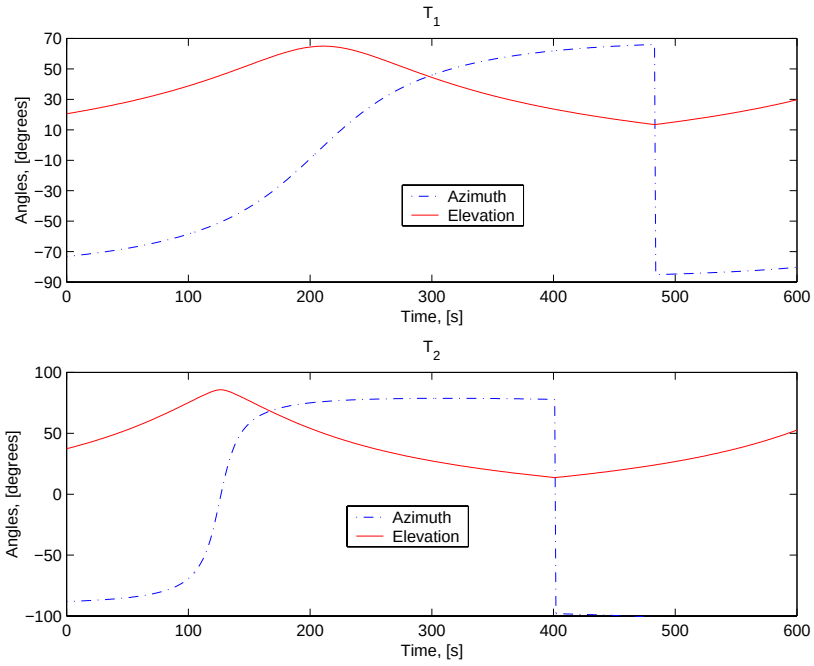

Figure 3.29 *Variation of azimuth (relative to terrestrial parallel) and elevation angles, during the two simulation periods*

The maximum elevation is not reached for a null azimuth since the trajectory of the satellites does not exactly follow meridians. When the elevation angle reaches its minimum value, a new satellite comes in the line-of-sight, causing a handoff to be achieved and the azimuth angle to change abruptly. If tracking the nearest satellite, a handoff occurs approximately every ten minutes, which appears to be of the very same length as a (not too short) communication including ring alert times, etc.

2° Typical area configurations

Two *canonical* area configurations are analyzed: a long built-up *straight street* and a *crossroad*.

The long street is represented by four buildings, as described in Figure 3.30-a.

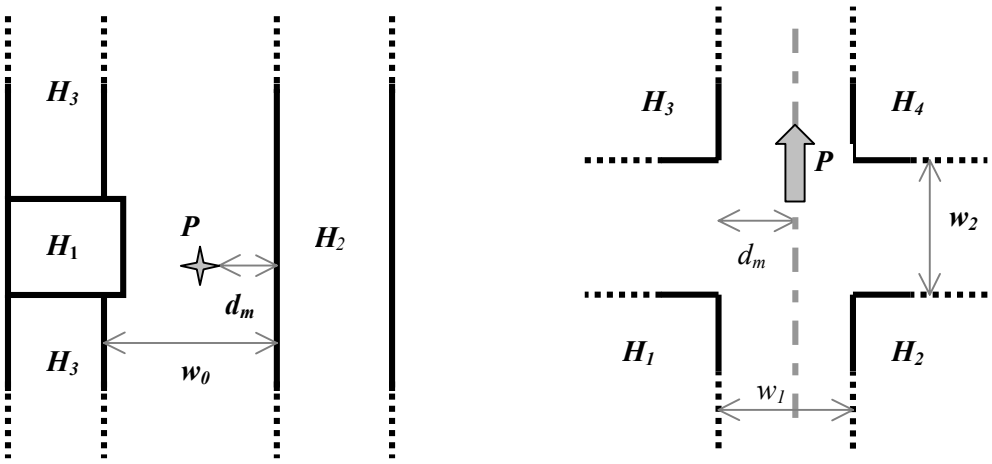

Figure 3.30 (a) *Long straight street* **(b)** *Crossroad*

The characteristic parameters are:

- the building heights H_1, H_2, H_3
- the street width w_0
- the receiving location d_m.

The building of height H_1 is represented with a larger width. This allows to take into account diffraction by vertical wedges. The street axis is given two different orientations, running either along a meridian (ϕ_{street} = 90°), either along a parallel (ϕ_{street} = 0°). Since satellites follow quite approximately meridians, the climax of elevation is respectively related to more orthogonal or more axial directions with respect to the street axis.

The crossroad is represented by means of four buildings (see Figure 3.30-b). It is characterized by the following geometrical parameters:

- the building heights H_1, H_2, H_3, H_4
- the street widths w_1 and w_2
- the receiving location d_m.

Again, the main street (width w_1) may be given the two orthogonal orientations that have been mentioned in the description of the street scenario.

Two types of environment are considered. The *suburban* or *low-urban* type of area is featured by the following set of parameters: 7 meters for all building heights, 15 metres for the street width, and d_m = 1 or 7.5 metres. A *(high-)urban* area is defined using all same values, except that buildings are taken to be 17 metres in height. The street width is not changed, since simulations are only exemplary and because it is desired to highlight the effect of building height.

3.4.6.2 IMPACT OF SYSTEM PARAMETERS

1° Fade compensation performance versus parameters

The performance of fade mitigation is examined in this section with regard to several system parameters. Handoff diversity is not applied at this stage. The following parameters are fixed:

- κ_0 = 6.5 dB
- τ_p = 400 ms
- $2\,\Delta P_{max}/N = 1\,\text{dB}$
- δ = 2 dB
- M_f = 3 dB
- W = 400 ms
- ΔP_{max} = 13 dB.

Note that the sum $M_f + \Delta P_{max}$ = 16 dB, which is also Iridium's total fade margin. The impact of the update interval on the short-term availability is analyzed, over the ten simulated minutes, in a number of low-urban scenarios. Results are reported in Figure 3.31.

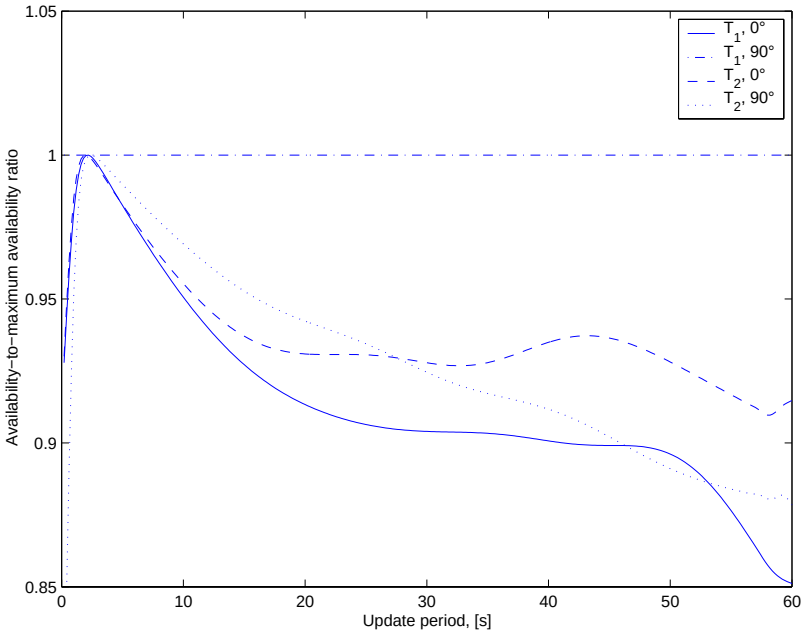

Figure 3.31 *Impact of the update interval on the short-term availability for both street orientations*

Except in one case, the availability peaks for T_u = 2 s and rapidly decreases for T_u > 10 s. Consequently, the value T_u = 2 s is chosen for all following simulations.

For instance, Figure 3.32 presents the original received E_b/N_0 together with the compensated E_b/N_0 in scenario ***T2*** – low-urban area. For both street orientations, the effects of signalling delay and estimation errors are scarcely observed (except in the upper graph, around t = 50 s). The limited power correction of 13 dB is, however, clearly noticeable.

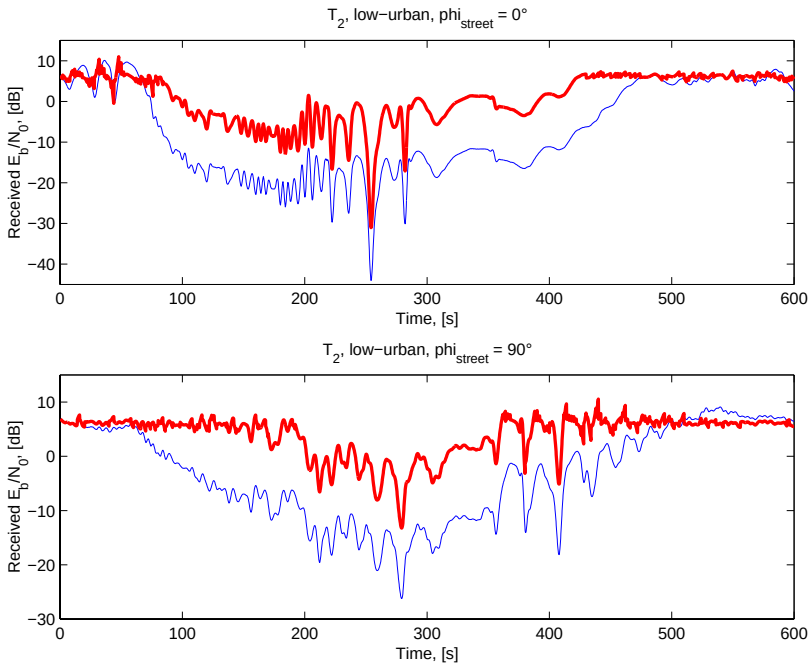

Figure 3.32 *Received E_b/N_0 in low-urban area for both street orientations: no FM {light lines} and FM {bold lines} signals*

2° *Handoff performance versus parameters*

Regarding the LEO-*N* study case, it is postulated that a handoff is initiated in favour of the best satellite, as soon as the SNR of the active satellite has been measured during the last V seconds below a margin ΔM with respect to that of the best satellite. Hence, the procedure is outlined by (3.17), no condition on the elevation angle being considered. Meanwhile, the handover algorithm is eventually combined with fade mitigation. In order to harmonise both mechanisms, the following parameters are chosen (even when there is no mitigation).

- For fade mitigation: $(E_b/N_0)_0 = 6.5$ dB; $\tau_p = 400$ ms; $T_u = 2$ s; $W = 400$ ms; $\Delta P_{max} = 13$ dB; $2\,\Delta P_{max}/N = 1$ dB; $\delta = 2$ dB; $M_f = 3$ dB.
- For handoff diversity: $\tau_p = 400$ ms; $S_u = 2$ s; $V = 400$ ms; ΔM varying between 1 dB and 7 dB.

Figure 3.33 represents a part of the globe with the satellites' initial position for period $\boldsymbol{T_1}$. Assuming that the receiver is located in London, the handoff strategy concerns, during the ten next minutes, the six satellites marked with an arrow, which indicates the direction of motion.

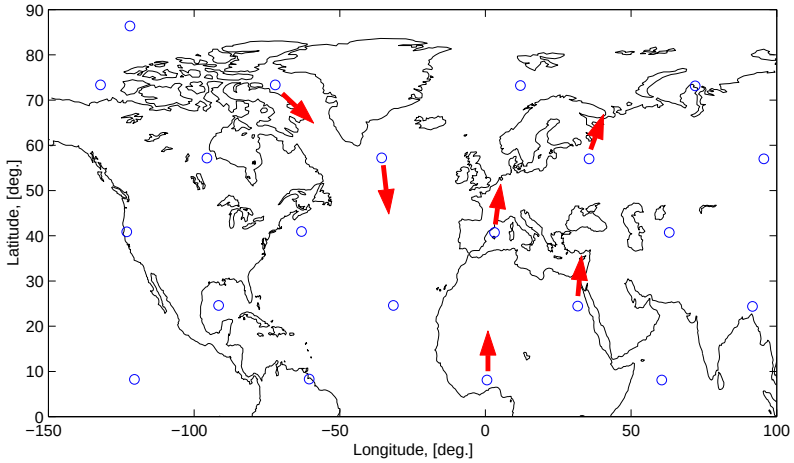

Figure 3.33 *Iridium constellation around London at time T_1 (satellites are marked by circles)*

Preliminarily, Figure 3.34 shows the final E_b/N_0 (κ_0 = 6.5 dB) in the context of scenario T_1, urban area, ϕ_{street} = 0°. The E_b/N_0 curves are obtained after various post-processing of signals received from the six visible satellites, the location of which is illustrated in Figure 3.33. The hysteresis margin ΔM is primarily fixed to 4 dB.

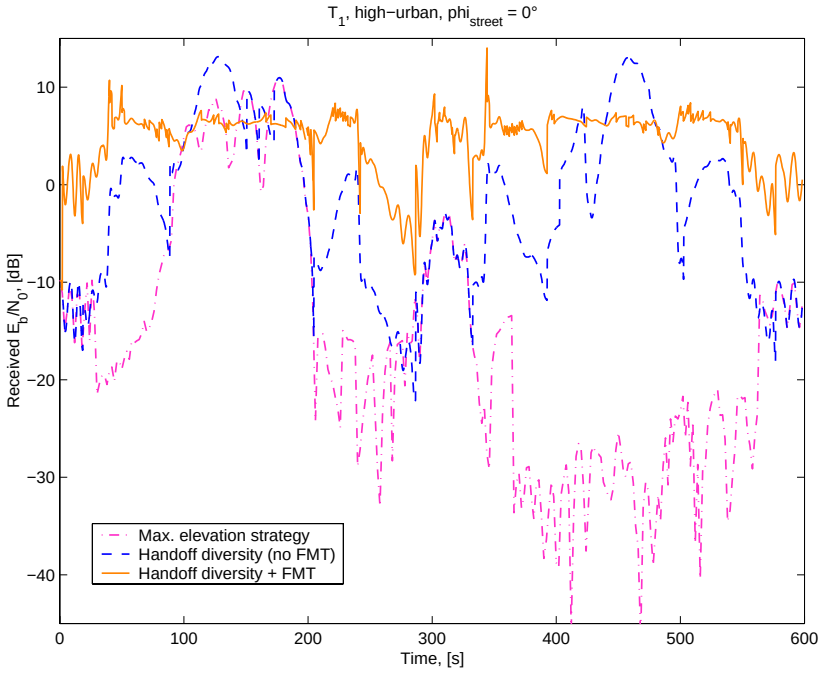

Figure 3.34 *Final E_b/N_0 resulting from three different handover strategies*

The comparison between the dot-dashed curve and the dashed curve illustrates quite well the gain obtained by handoff diversity (3.17) with respect to a simple strategy based on the

maximum elevation angle. Especially, for $t > 350$ s, the nearest satellite is blocked by a building, while another satellite is in the line-of-sight. Also, the gain from fade mitigation is important. The effect of imperfect fade compensation is sometimes clearly visible ($t = 344$ s). The choice of the hysteresis margin appears to be crucial, if one wants to avoid a too large number of handoffs. This is particularly the case when fade mitigation is applied, since all signals are then very similar to each other and near the target E_b/N_0.

Handoff performance versus hysteresis margin is finally analyzed with regard to a large number of different scenarios. All parameters are kept constant, except the handoff margin ΔM. The efficiency is measured in terms of handoff rate $\rho_{HO} = 1/t_{HO}$ (i.e. the number of handoffs per second) and of $\Delta\xi$, standing for the percentage of time during which the received signal is not provided by the best satellite. Results are shown in Figure 3.35.

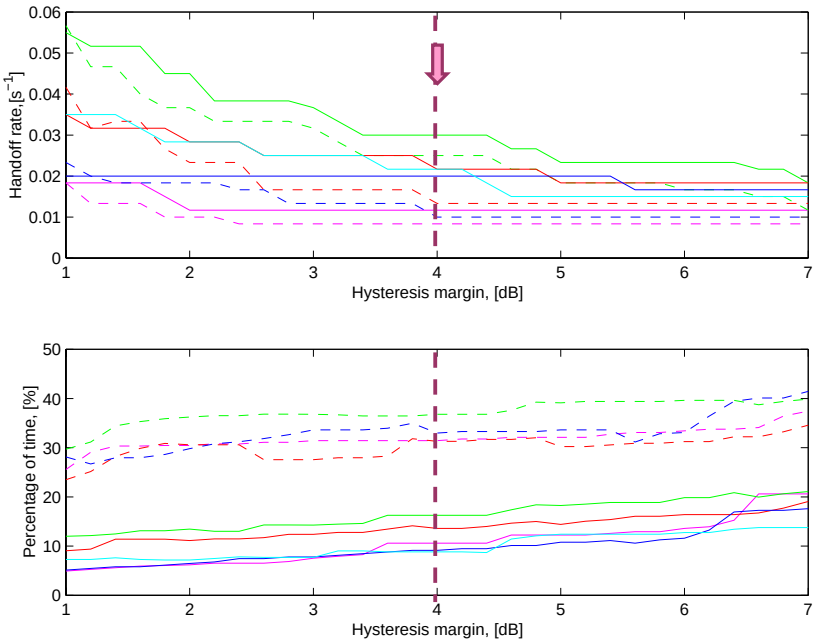

Figure 3.35 *Handoff rate ρ_{HO} and percentage $\Delta\xi$ as functions of the margin ΔM with no combined FMT {solid lines} and with FMT {dashed lines}*

As expected, the handoff rate decreases when the margin gets higher, while the opposite is observed for $\Delta\xi$. The additional fade mitigation significantly increases the percentage $\Delta\xi$ and slightly reduces the number of handoffs. However, the increase of $\Delta\xi$ is actually not significant, because compensated signals from most satellites fluctuate around the target E_b/N_0 value. Hence, the best satellite is probably not much better than the active satellite.

A margin of 4 dB seems to produce a good compromise in the simulated scenarios. For larger margins, no significant shrinkage of the handoff rate is indeed observed. Therefore, this value is used in the following simulations. The same margin is also chosen for implementing diversity techniques.

3.4.6.3 PERFORMANCE FOR THE LONG STRAIGHT STREET CASE

Simulations are carried out in both high-urban and low-urban areas, for satellite locations outlined by $\boldsymbol{T_1}$ and $\boldsymbol{T_2}$, with a street oriented either along a meridian ($\phi_{street} = 90°$), either along a parallel ($\phi_{street} = 0°$), and with d_m = 1 m or 7.5 m. That yields sixteen distinct scenarios to be simulated. For each scenario, eight cumulative density functions (CDF's) of E_b/N_0 are calculated, depending on the technique to be implemented:

- no fade mitigation (FM), no handoff (HO) diversity, no dual diversity {blue dot lines}
- FM, no HO diversity, no dual diversity {blue circles}
- no FM, single-satellite diversity, signal selection (SEL) ≡ HO diversity {blue '+'}
- no FM, 2-satellite diversity, equal gain combining (EGC) {black squares}
- no FM, 2-satellite diversity, maximal ratio combining (MRC) {red stars}
- FM, single-satellite diversity (SEL) ≡ HO diversity {blue solid lines}
- FM, 2-satellite diversity (EGC) {black dot-dashed lines}
- FM, 2-satellite diversity (MRC) {red dashed lines}.

The different techniques are implemented using the following set of parameters:

- <u>for fade mitigation</u>, $(E_b/N_0)_0 = \kappa_0 = 6.5$ dB; $\tau_p = 400$ ms; $T_u = 2$ s; $W = 400$ ms; $\Delta P_{max} = 13$ dB; $\delta = 2$ dB; $M_f = 3$ dB,
- <u>for satellite diversity</u>, $\tau_p = 400$ ms; $S_u = 2$ s; $V = 400$ ms; $\Delta M = 4$ dB.

All curves relative to the non-median scenarios (d_m = 1 m) are shown in Figure 3.36 and Figure 3.37.

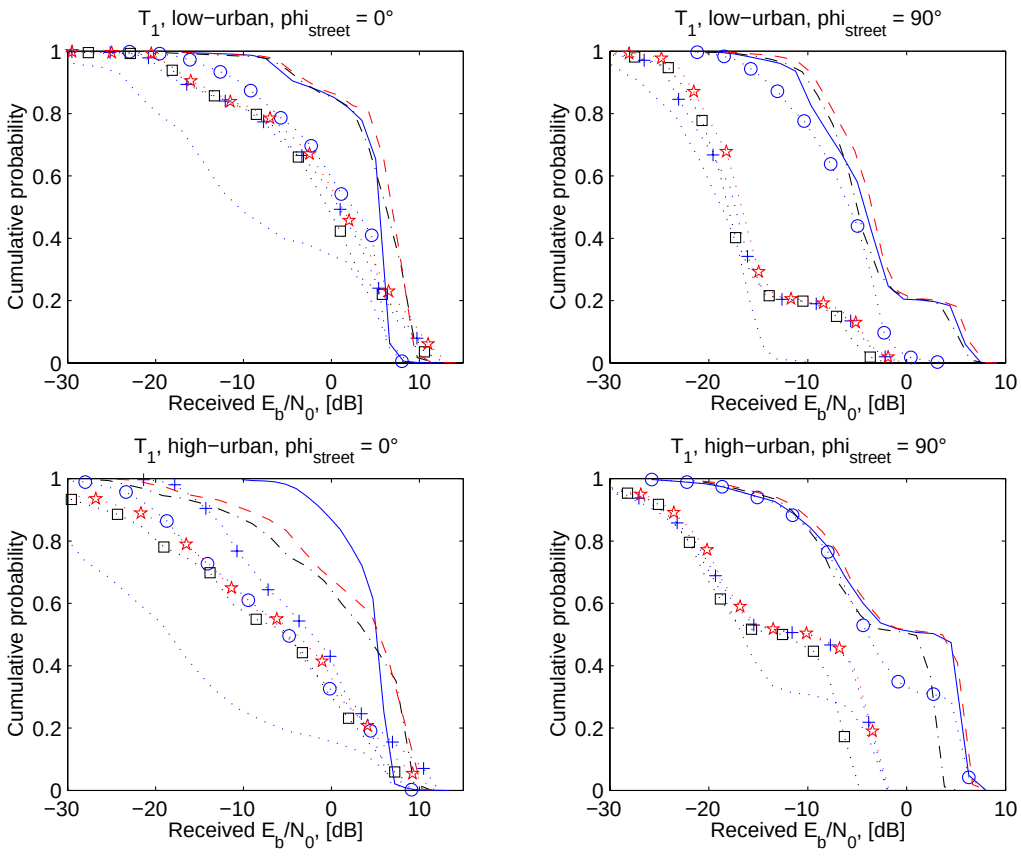

Figure 3.36 *E_b/N_0 CDF's for a communication taking place at time $\boldsymbol{T_1}$ (d_m = 1 m)*

The next remarks highlight the relationships between propagation, satellite motion and system procedures.

- About the original E_b/N_0 CDF's (no FMT, handover based on maximum elevation angle)

(i) For ϕ_{street} = 0°, $\boldsymbol{T_1}$ and $\boldsymbol{T_2}$ scenarios actually produce similar statistical results, especially in low-urban areas. This is to be explained by the quasi-axial illumination of the street (see Figure 3.28); in such cases, CDF's of fade and E_b/N_0 do not depend much on the elevation angle.

(ii) For ϕ_{street} = 90°, the mean E_b/N_0 level is higher for $\boldsymbol{T_2}$ (higher elevation angle) with respect to $\boldsymbol{T_1}$, and for low-urban areas, with respect to urban ones. Indeed, in such situations (quasi-orthogonal illumination), the fade level mainly depends on the LOS ratio. The latter is related to the mean building height and elevation angle, street widths being taken as equal.

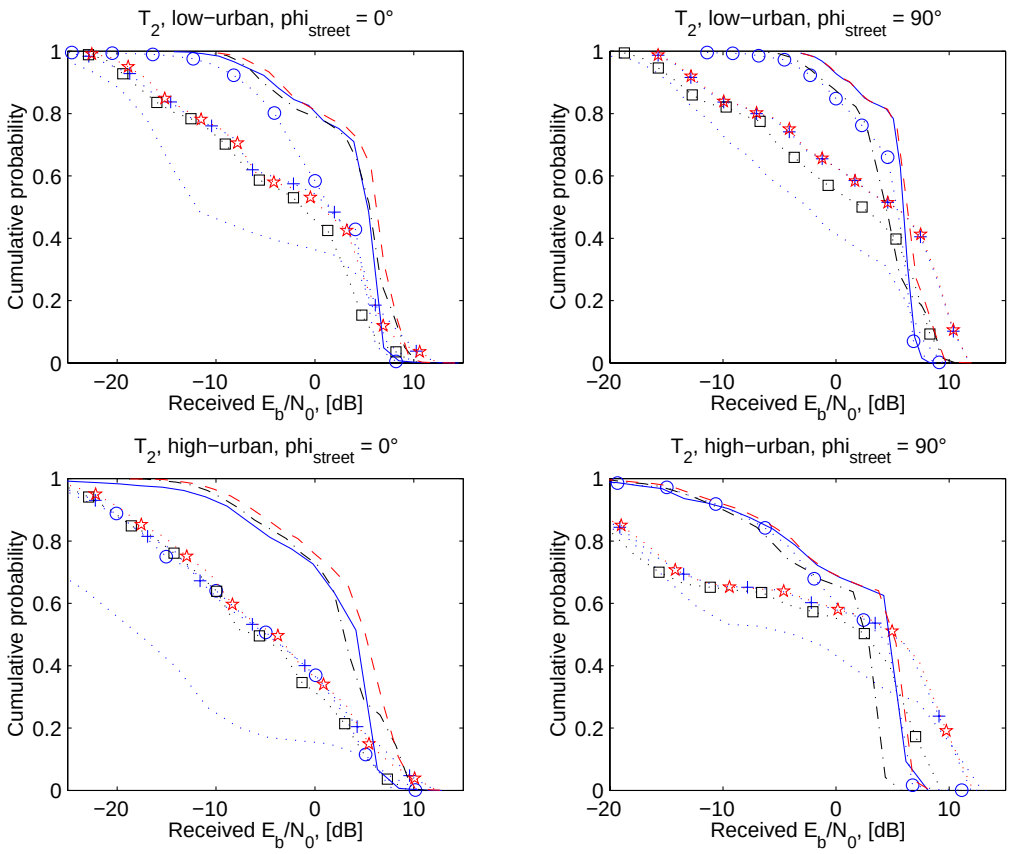

Figure 3.37 *E_b/N_0 CDF's for a communication taking place at time $\boldsymbol{T_2}$ (d_m = 1 m)*

- About fade mitigation and diversity

(i) For ϕ_{street} = 90°, fade mitigation allows achievement of a significant improvement of the expected performance, performing often better than diversity only. For such street orientation, fade depths are moderate on the path from the nearest satellite, and therefore well compensated. Using diversity without FMT yields worse results than using FMT only, since then, the shadowing is not perfectly mitigated by diversity. In other words, the signals from the best satellite(s) or their combination are on average below the power-controlled signal related the nearest satellite.

(ii) For ϕ_{street} = 0°, the fade compensation algorithm does increase the received E_b/N_0 but in the very same way as diversity only (i.e. when diversity is not combined with FMT).

(iii) The best performances are obtained by the combination of diversity and fade mitigation.

- About diversity techniques

(i) Signal selection (handoff diversity) without FMT generally gives good results, which are similar to those achieved by FMT only.

(ii) When no FMT is implemented, EGC appears to be the less efficient method, especially for $\phi_{street} = 90°$. In low-urban areas, even the combination with fade compensation does provide lower E_b/N_0 than other diversity techniques. This can be easily explained. In such situations, the second best satellite may encounter deep fades. Therefore, a low amplitude for one signal significantly decreases the combined level because EGC sums amplitudes, as outlined by (3.18). This is not the case for MRC, that adds the power of both branches.

(iii) When combined with fade mitigation, SEL and MRC perform very similarly.

As a conclusion, for (quasi-)axial illumination cases, the performance does not depend on the maximum elevation angle, and thereby on the period of the communication. For (quasi-) orthogonal cases, the performance is largely imposed by the distribution of physical parameters (building height, street width) and by the period of the communication. Meanwhile, there is a substantial gain of performance (in terms of E_b/N_0) when a combination of FMT with satellite diversity is used. Among diversity techniques, MRC and SEL seem the most adequate techniques. Since it only requires single-satellite diversity, signal selection actually constitutes a good compromise between system management and availability.

Simulations have also been run by increasing the transverse mobile position d_m up to $w_0/2 = 7.5$ m. The related graphs are presented in Appendix G. The conclusions remain globally unchanged, except for two noticeable differences.

(i) For $\phi_{street} = 90°$, EGC diversity is not really efficient.

(ii) For $\phi_{street} = 0°$, the fade mitigation algorithm still increases the performance, but much less than diversity only (remember that performance figures are very similar for $d_m = 1$ m). This is because diversity is very efficient in the case of a non-symmetric position of the receiver in the street (i.e. $d_m << w_0$). This advantage is reduced in the case of a median position in the street.

It has to be added that the obtained CDF's of E_b/N_0 could easily be transformed into cumulative distributions of BER, taking into account system link parameters (modulation, coding, etc.).

3.4.6.4 COMPARISON BETWEEN A LONG STREET AND A CROSSROAD

1° The crossroad problem

A specific approach has to be set up in order to compare the impact of propagation in a street and a crossroad. Simulations based on a static receiver are no longer relevant, since the location inside the crossroad actually matters. Consequently, simulations are run assuming a mobile receiver, which moves up along the dashed line as indicated in Figure 3.30-b. The mobile speed is fixed to 1 m/s. The path length is 55 m, going from – 27.5 m up to 27.5 m (the origin of coordinates is located in the centre of the cross). Simulations represent thereby 55 s. These seconds are taken out from scenario $\boldsymbol{T_1}$, around the maximum elevation angle (see Figure 3.29). Neither fade compensation nor diversity is considered in the simulations.

2° Simulation results

Three scenarios are examined, each being simulated for both street orientations:

- *low-urban* I – all heights = 7.5 m, all street widths = 15 m, d_m = 7.5 m
- *low-urban* II – all heights = 7.5 m, all street widths = 15 m, d_m = 1 m
- *high-urban* I – all heights = 17 m, all street widths = 15 m, d_m = 7.5 m
- *high-urban* II – all heights = 17 m, all street widths = 15 m, d_m = 1 m.

Simulation results are shown in Figure 3.38. Apart from the different shadowing values, the analysis of all simulated cases highlights other significant differences between the crossroad and the street. A particular attention is namely paid to the amplitude of fast fluctuations with and without crossroad. The log-variance (expressed in logarithmic scale) of amplitude fluctuations is denoted as σ^2 (note that σ^2 is not the variance of the log-amplitude).

(i) In low-urban area I, the LOS-field always exists. The received amplitude follows a Gaussian distribution (σ^2 = – 27 dB for ϕ_{street} = 0°; σ^2 = – 30 dB for ϕ_{street} = 90°). The crossroad has no significant influence on the path-loss.

(ii) In low-urban area II and high-urban areas (I and II), for ϕ_{street} = 0° (thus mainly in LOS conditions), the crossroad has a very small influence when the receiver is crossing the road. The distribution of the received amplitude is again Gaussian (for example, σ^2 = – 22 dB in scenario high-urban I).

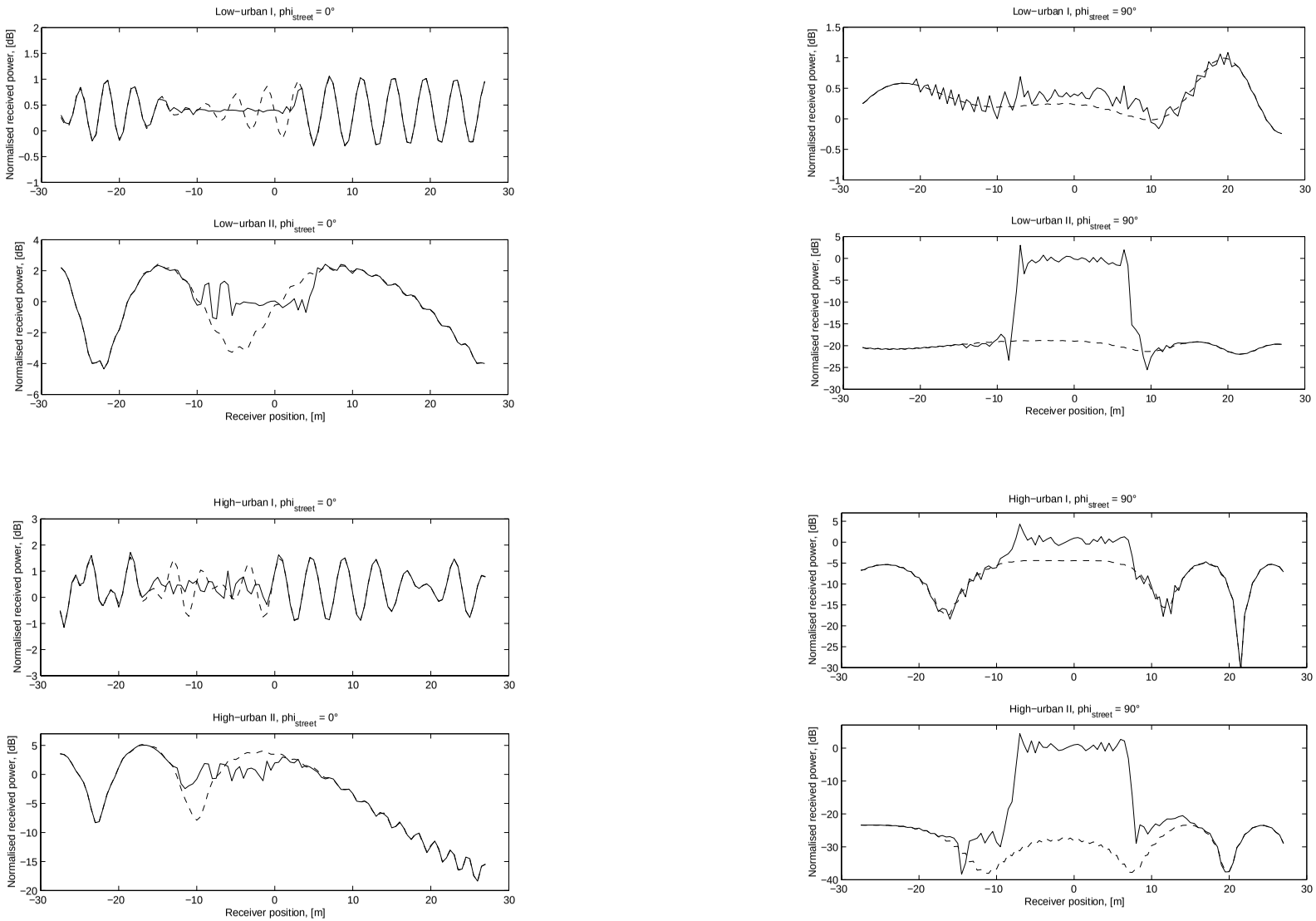

Figure 3.38 *Comparison between street {dashed lines} and crossroad {solid lines} cases for both orientations of the main street: ϕ_{street} = 0° (left) and ϕ_{street} = 90° (right)*

(iii) In low-urban area II and high-urban areas, for ϕ_{street} = 90°, the street scenario is characterized by a continuous shadowing. The passage through the crossroad results obviously in unshadowed conditions. Outside the crossing (i.e. in shadowed conditions), there are only few differences between the street and the crossroad cases. The distribution of the LOS-amplitude in the crossroad is still Gaussian, but σ^2 can be as large as – 18 dB, what is much larger than the above-mentioned values. The increase of σ^2 is caused by side effects, which are particularly well modelled by edge equivalent currents for calculating diffracted fields. These effects, at the simulated frequency (1.6 GHz), seem to spread over some 7 metres. For crossroads wider than this value, the variance of the LOS-amplitude inside the crossroad tends to decrease (it would reach values observed in (i) for a crossroad of infinite width).

(iv) The received-field level in shadowed regions is highly related to the ratio d_m / h_b . This ratio indeed determines the diffraction angle and thereby the level of diffraction.

To summarize, the impact of a crossroad can be roughly described by the following conclusions.

(i) When a line-of-sight exists outside the crossroad (e.g. for high d_m / h_b), the crossroad has no significant influence on the path-loss.

(ii) If this is not the case, the crossroad modifies the path-loss since it allows a direct transmission path.

(iii) A narrow crossroad cannot be modelled by a purely open-area section, since corner effects cause the variance of the received amplitude within the crossroad to be larger than the variance that would have been observed in open areas. When the width of the crossroad increases, then the relative part over which corner and vertical edges do have an impact is reduced; the variance tends to the asymptotic open-area value.

Owing to these results, the validity of equation (3.20) (see p. 172) should be slightly moderated, although one should not forget that (3.20) is used for a global prediction, and not for a precise prediction of what the field really is inside the crossroad.

3.5 S BAND SATELLITE-IMT 2000

3.5.1 IMT 2000 and low earth-orbit satellites

The communication system that is investigated is based on ESA proposal submitted to the ITU as a candidate technology for the satellite component of IMT 2000 [18]. IMT 2000 stands for International Mobile Telecommunications 2000. It is the name assigned to an ITU effort to implement a uniform standard for the new generation of high-speed wireless systems, often called third-generation mobile. As IMT 2000 standard, the satellite-IMT 2000 (S-IMT 2000) project is aimed to provide subscribers with mobile voice and data as well as broadband multimedia service. IMT 2000 has been allocated spectrum worldwide in the 2 GHz band.

Using *wideband CDMA* as the multiple access technique and operating in FDD mode, the proposed satellite system is characterized by a bandwidth of either 2.5 MHz or 5 MHz and provides bearer data rates up to 64 kbps. It has many similarities with the UTRA proposal emerging from the ETSI expert group. It will support fixed, transportable and vehicular terminals for all data rates as well as handheld receivers for data rates below 16 kbps included.

3.5.2 System description

The original ESA proposal does not specify any particular satellite constellation. As proposed in [1], the Deligo network, with 64 satellites in 8 orbital planes at 1626 km in altitude [19], is used for simulating S-IMT 2000 service. Performance is simulated at two particular locations, namely Rome and London, with elevation statistics provided by the orbit generator (see Chapter 2, Figure 2.28). Diversity schemes are also investigated by means of the shadowing correlation model described in Chapter 2.

Table 3.12 details the system specifications to be used by the simulations. The system margin is only 6 dB, thanks to a powerful error-correcting code (R_c = 1/3). Moreover, shadowing is mitigated by means of a power-control algorithm. Since S-IMT 2000 is a wideband CDMA system, simulations must account for the multiple access interference (MAI). The inter-symbol interference is neglected because its effect seems to be not significant with respect to MAI. Multiple access interference is integrated as described in Section 3.2.4.2. On the other hand, the closed-loop power-control is implemented with a maximal correction of ΔP_{max} of 10 dB, an update period T_u of 100 ms and a computation delay τ_p of 100 ms, as suggested in [1].

SW-CDMA characteristics	
Orbit type (altitude)	Circular (1626 km)
Antenna	Omnidirectional
Frequency	2.1 GHz
Modulation scheme	QPSK
Polarisation	Right circular
Error protection	Convolutional $R_c = 1/3$, $K = 9$
Required effective E_b/N_0	2 dB for BER 10^{-3}
Chip rate	4096 Mcps
Channel bandwidth	5 MHz
Bit rate	32 kbps
Fade margin	6 dB

Table 3.12 *SW-CDMA main specifications*

3.5.3 Long-term performance prediction

3.5.3.1 Simulation method

The COST 255 approach is used to carry out simulations [15]. Again, typical urban and suburban areas are featured by a lognormal distribution (median μ, standard deviation σ) for building height, and a constant value w_0 for street width (see Table 3.7). As already mentioned, distributions of elevation angle have been described in Chapter 2. Spatial series of the received signal are generated for given elevation angles. The mobile terminal is assumed to move down long straight built-up streets, which are consecutively oriented following random azimuth angles relative to the satellite link [15].

3.5.3.2 Performance for a pedestrian speed

A pedestrian speed is first assumed (1 ms^{-1}). The distributions of coded BER as a function of the spatial coverage are shown in Figure 3.39 in both urban and suburban areas, at two latitudes (London and Rome).

In a similar way as in Figure 3.21, the various curves on the graphs are associated with the following percentages of time (from left to right):

- 100.00, 100.00, 96.79, 89.35, 78.52 (indicated by a star), 68.25, 57.83, 46.04, 31.95, 16.50 and 7.64 % of time while considering the London latitude,
- 100.00, 96.97, 89.63, 75.57, 58.29 (indicated by a star), 44.07, 31.54, 21.23, 13.44, 7.72 and 3.61 % of time at the Rome latitude.

For instance, in urban environment at Rome latitude, the mean coded BER (including power-control) is less than 10^{-3} during:

$$\left.\begin{array}{l} 96.97\,\%\ \text{of time on}\ 96.31\,\% \\ 75.57\,\%\ \text{of time on}\ 96.53\,\% \\ 44.07\,\%\ \text{of time on}\ 97.24\,\% \\ 21.23\,\%\ \text{of time on}\ 97.35\,\% \\ 7.72\,\%\ \text{of time on}\ 99.37\,\% \end{array}\right\} \text{of the considered area.}$$

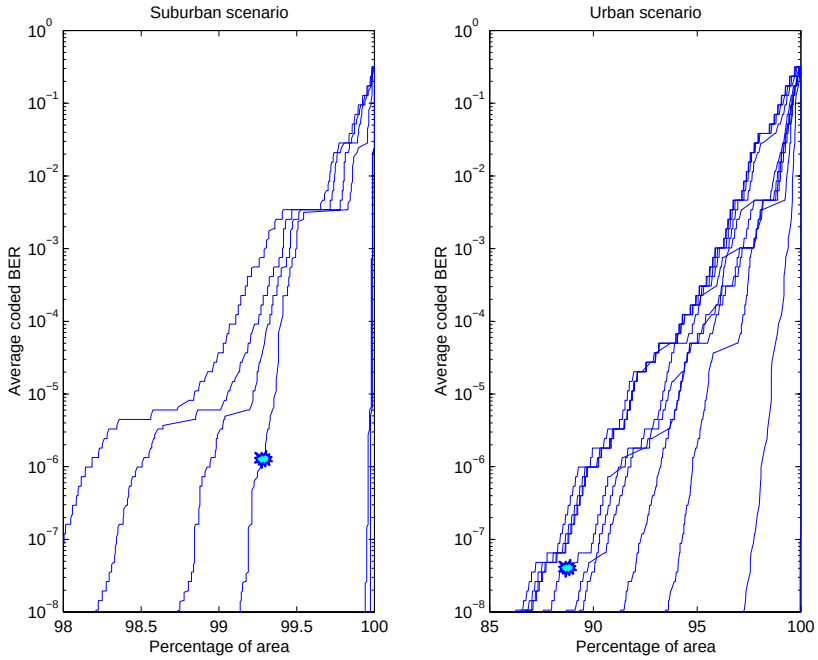

Figure 3.39 *Percentage of area over which the coded BER is less than ordinate, in suburban (left) and urban (right) areas, for several percentages of time*

Although the fade margin is much lower for this test case than for the LEO-66 system, results are not worst. This is due to

- the power-control, which, in the case of a pedestrian speed, appears to be quite efficient,

- the satellite constellation: Deligo constellation provides indeed higher elevation angles than Iridium.

However, results may still seem too optimistic. It can partly be explained by the fact that only three azimuth angles (0, 45 and 90 degrees relative to the street axis) were simulated in the time series. Since the axial case (0°) is actually a line-of-sight case, its contribution in the averaging process might cause the performance to be overestimated.

Figure 3.40 compares the performance at both latitudes (upper graph) as well as for both environments (lower graph).

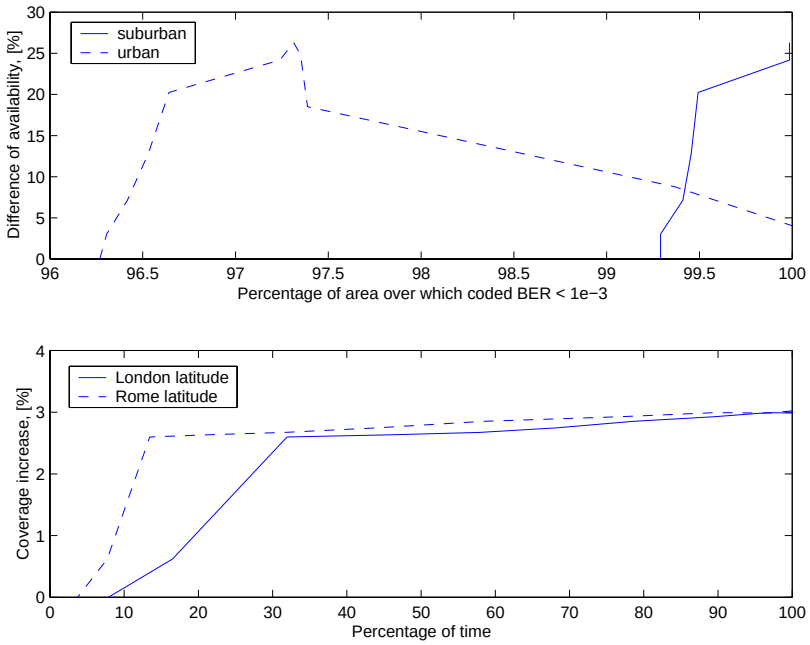

Figure 3.40 *Comparison between availability for both latitudes as a function of coverage (upper graph), and between coverage for both areas, as a function of availability (lower graph)*

Some 25 % are gained in terms of time availability between the two simulated latitudes. This is much greater than the value obtained for the LEO-66 test case. On the lower graph, the coverage is increased by only 3 % when comparing suburban to urban areas.

Finally, Figure 3.41 highlights the effect of power-control on the performance. For all simulated scenarios, the gain of performance is plotted against the availability when comparing coverage achieved with and without power-control. In suburban areas, the gain of

1 % is quite constant. Meanwhile, the gain in urban areas decreases for high percentages of time, what could be explained by the deeper fades encountered at low elevation angles in such areas.

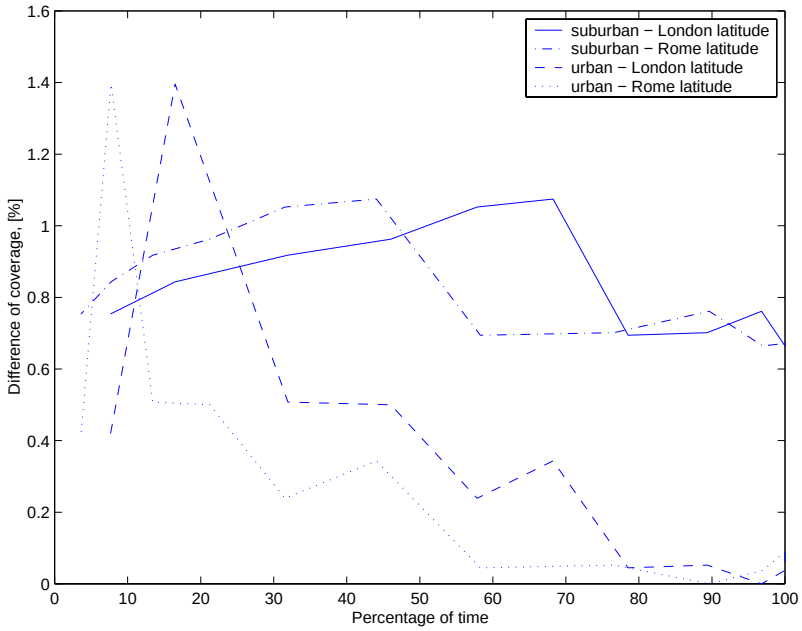

Figure 3.41 *Effect of power-control in all simulated cases: performance gain (increase of coverage)*

3.5.3.3 HIGH-SPEED SCENARIOS

A high-speed scenario (15 ms^{-1}) is also investigated, all other parameters remaining the same as before.

Figure 3.42 depicts the degradation of coverage as a function of the percentage of time. It is actually quite limited (0.5 to 1.5 %), despite significant signalling delays in the power-control process. It has however been noticed that these results are very sensitive to the power-control parameters (update rate, correction step).

Considering a mobile speed of 30 ms^{-1}, Figure 3.43 illustrates that the degradation is again somewhat reduced (1 to 1.8 %). Such reduced degradations of performance that result from the increase of the mobile speed have also been reported in other simulations described in [1], using a ray-tracing model in non built-up areas or a Markov chain approach. The system, as simulated, appears therefore to be overdesigned.

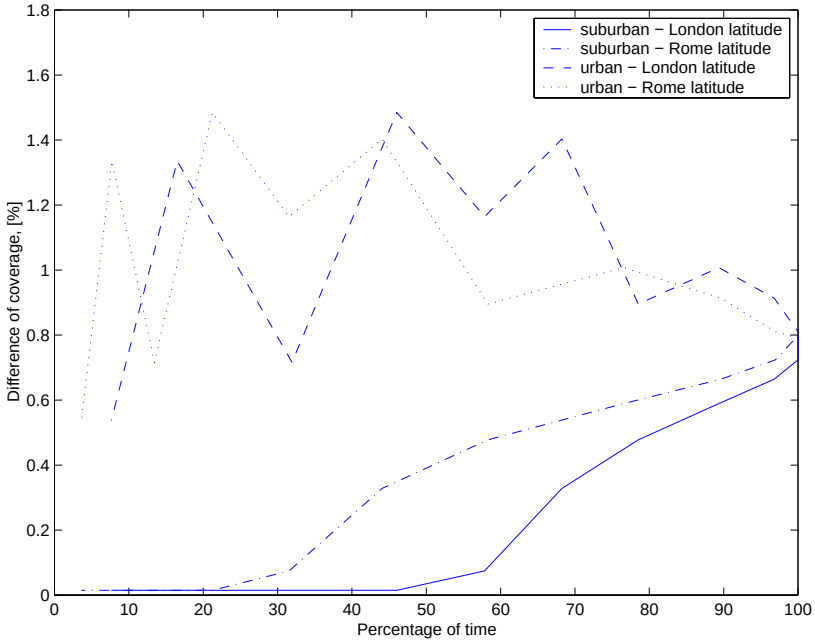

Figure 3.42 *Degradation of performance for a high-speed (15 ms^{-1}) scenario relative to a pedestrian case*

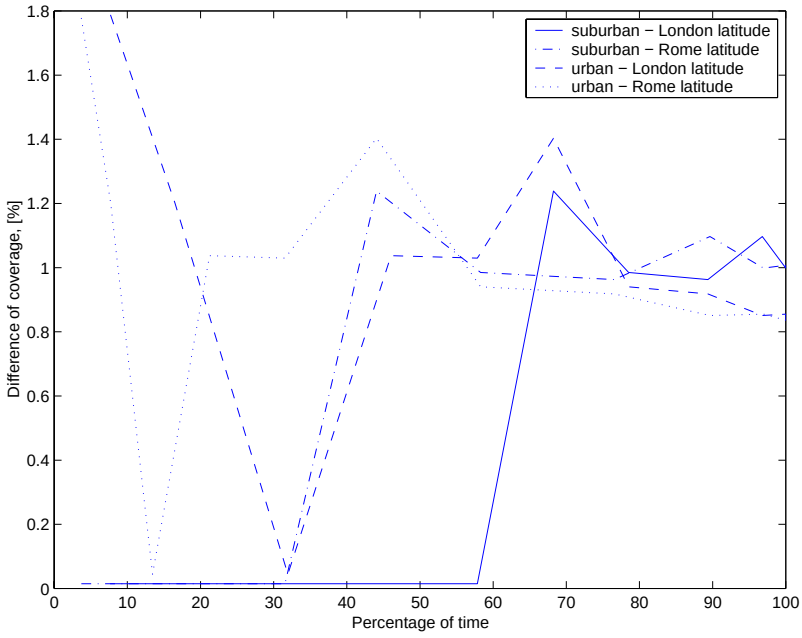

Figure 3.43 *Degradation of performance for a high-speed (30 ms^{-1}) scenario relative to a pedestrian case*

3.5.4 Shadowing correlation in dual-diversity schemes

The Deligo constellation has been designed with the aim of optimising dual diversity, in the sense that if one path is blocked, there is a high probability of the other being less so. This section is another illustration of the capability of the physical-statistical approach to deal with shadowing correlation, as well as a demonstration of the good anti-correlation properties achieved by the Deligo constellation.

To begin with this analysis, Figure 3.44 depicts the average values of ϑ_1, ϑ_2 and $\Delta\phi$ against latitude. The elevation angles of the two nearest satellites peak at latitude of about 52°, and then rapidly decrease. The mean azimuth separation oscillates, going from 65° up to 100°. Also, the variation of azimuth separation around the mean value is quite large.

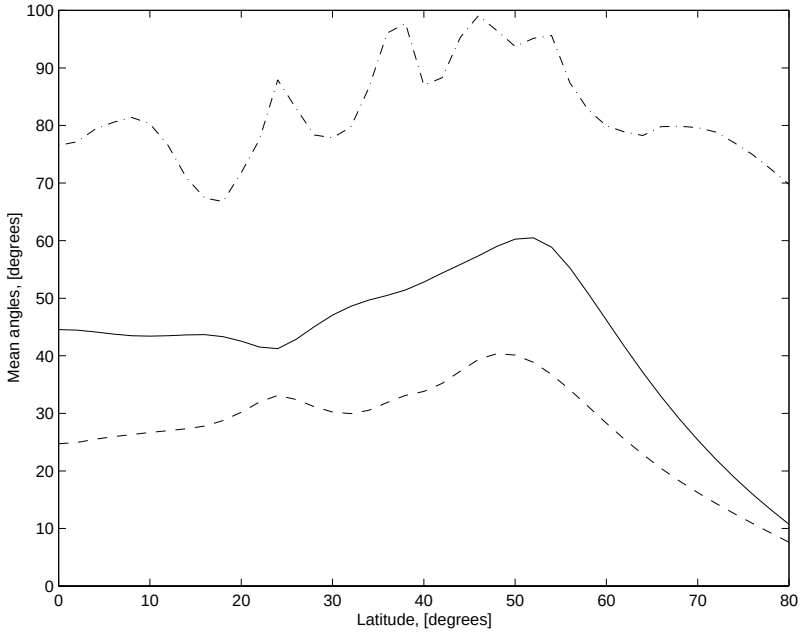

Figure 3.44 *Average values for highest elevation angles ϑ_1 {solid line}, ϑ_2 {dashed line} and azimuth separation $\Delta\phi$ {dot-dashed line} versus latitude, for the Deligo constellation*

The mean log-shadowing correlation coefficient against latitude between the paths from the two highest satellites is shown in Figure 3.45 for the areas defined in Table 3.8 (assuming $d_m = w_0/2$).

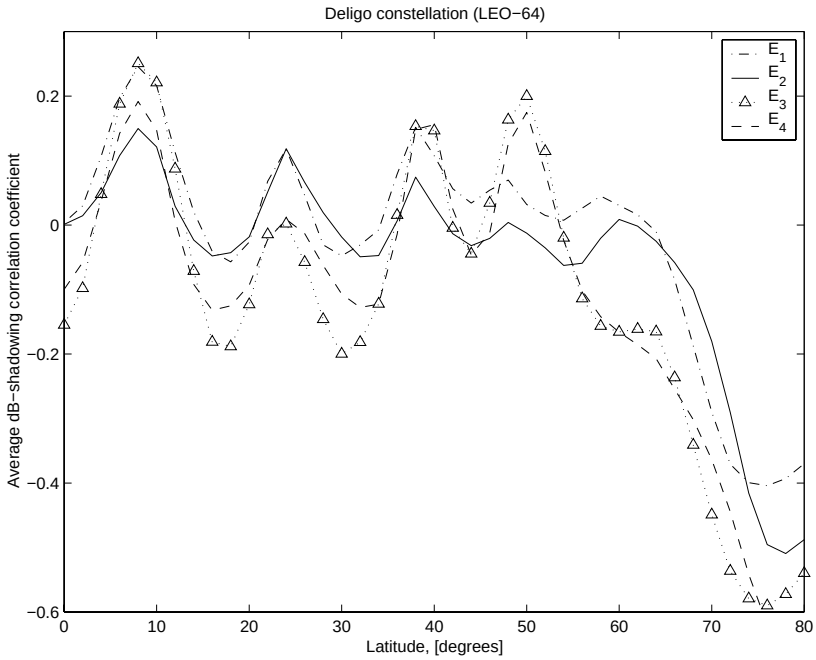

Figure 3.45 *Average log-shadowing correlation versus latitude for the Deligo constellation in four areas ($d_m = w_0/2$):*

- *E_1 – suburban building height distribution, w_0 = 12 m*
- *E_2 – suburban building height distribution, w_0 = 20 m*
- *E_3 – urban building height distribution, w_0 = 12 m*
- *E_4 – urban building height distribution, w_0= 20 m*

Already, it can be noticed that a negative average correlation is obtained for a significant range of latitudes. Also, the correlation oscillates for latitudes less than around 50° and then decreases at higher latitudes in the same way as the elevation angles up to latitude of 75°. Indeed, results obtained in Chapter 2 show that the negative correlation peaks for smaller elevation angles, at least up to a certain limit. For very low elevation angles, the mean correlation grows again (see Figure 2.31).

However, as mentioned earlier, the average correlation coefficient is not the most significant indicator of the achieved diversity gain, since the correlation may vary significantly around its mean.

The distribution of the correlation coefficient must therefore be investigated. Figure 3.46 presents the percentage of time against latitude for which the correlation is negative (≤ 0) in the four simulated areas.

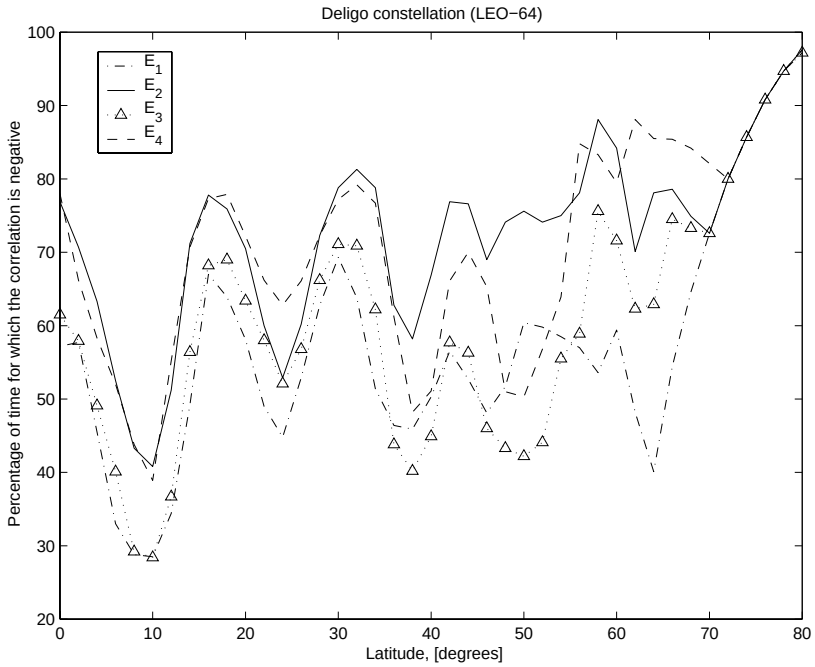

Figure 3.46 *Percentage of time against latitude for which the correlation is negative, in the four areas ($d_m = w_0/2$)*

This percentage, and therefore also the diversity gain, are larger in areas E_2 and E_4, although the negative correlation is in average smaller in areas E_3 and E_4. The larger the street width, the higher this percentage. Indeed, for narrow streets, the probability for diversity paths to be simultaneously blocked is very high, even for large azimuth separations. Hence, the diversity gain is the smallest in areas E_1 and E_3. The impact of the mean building height on the diversity gain depends on the latitude and thereby, on the constellation characteristics.

The case of a receiver placed close to a building ($d_m = 1$ m << w_0) is ultimately analyzed.

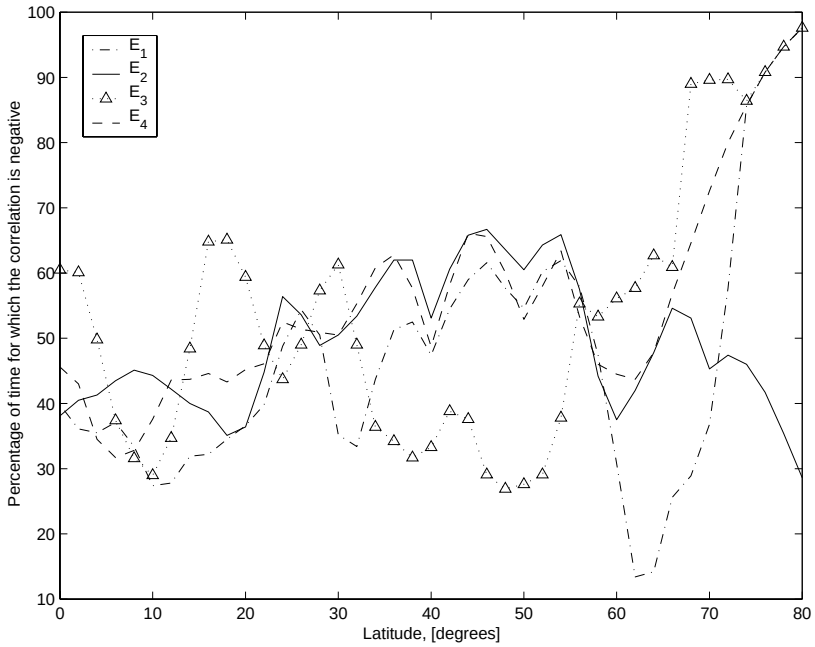

Figure 3.47 *Percentage of time against latitude for which the correlation is negative, in the four areas (d_m = 1 m << w_0/2)*

Although the achieved percentages, in Figure 3.47, are on average smaller than previously, the conclusions remain globally similar. Note, however, that the percentage of negative correlation in area E_2 at high latitudes (> 65°) is reduced with respect to the other environments (that has already been observed for the Globalstar constellation, see Table 3.11).

3.6 KA BAND MULTIMEDIA LEO SATELLITE SYSTEM

3.6.1 "Internet-in-the-sky"

In the context of multimedia transmission by LEO satellites, two systems are currently being developed, respectively at Ku band (Skybridge, 32 satellites) and K/Ka band (Teledesic, 288 satellites). Both constellations will provide a high-speed access to Internet and other interactive broadband services. Nevertheless, a significant difference must be pointed out. On one hand, Skybridge will be complementary to existing terrestrial networks, which means that the space segment only fills gaps in the terrestrial infrastructure. Subsequently, the Skybridge network does not require links between satellites, all traffic routing functions being managed by terrestrial gateways (local connection stations). On the other hand, Teledesic has been designed to totally bypass the terrestrial telecommunication infrastructure, realising a global "Internet-in-the-sky". Therefore, the network includes onboard processing and inter-satellite links. Because the system used as a third test case is very similar to the Teledesic network, the latter is described in details in the following.

The Teledesic network will consist of 288 operational satellites, divided into 12 planes, each containing 24 satellites. To make efficient use of the radio spectrum, frequencies are allocated dynamically and reused many times within each satellite footprint. Within any circular area of 100 km radius, the Teledesic network can support more than a total of 500 Mbps of data to and from all user terminals by allocating bandwidth-on-demand. The system is planned to operate in a portion of the high-frequency K and Ka bands (18.8-19.3 GHz downlink and 28.6-29.1 GHz uplink).

The low orbit enables the use of small, low-power terminals and antennas. The compact terminals will be mounted on a rooftop and connect inside to a computer network or a PC. They will communicate directly with the satellite network and support a wide range of data rates. The terminals also interface with a wide range of standard network protocols, including IP, ISDN, ATM and others. Although optimised for service to fixed-site terminals, the Teledesic network shall be able to serve transportable and mobile terminals as well, such as those for maritime and aviation applications. Most users will have two-way connections that provide up to 64 Mbps on the downlink and up to 2 Mbps on the uplink. Broadband terminals will offer 64 Mbps of two-way capacity.

Communication links at K and Ka bands are degraded by rain and blocked by obstacles in the line-of-sight. To avoid obstacles and limit the portion of the path exposed to rain requires that the satellite serving a terminal be at a high elevation angle above the horizon. The Teledesic

constellation assures a minimum elevation angle (mask angle) of 40º within its entire service area. Based on this design, the system should be able to achieve availability of 99.9 % or greater.

3.6.2 System specifications

Table 3.13 summarizes the specifications of a Teledesic-like system. Regarding the fade margin, the actual values for Teledesic are not known, so the indicated values are only reasonable assumptions. The system includes fade mitigation. Therefore, the margin is divided into a fixed (clear-sky) part and a variable part.

Ka band multimedia satellite system characteristics	
Orbit type (altitude)	Circular (1375 km)
User's terminal	Satellite dish (0.4-0.8 m diameter)
Downlink frequency	18.8 -19.3 GHz
Uplink frequency	28.6-29.1 GHz
Satellite EIRP	50 dBW
User data rate	2 to 64 Mbps
Availability	99.9 % for BER 10^{-9}
Assumed fade margin (around 29 GHz)	2 to 3 dB (fixed) + 8 to 12 dB (variable)

Table 3.13 *Main specifications of a Ka band multimedia satellite system*

3.6.3 Statistical long-term performance

Due to the very high elevation angle, building multipath effects are neglected in the following. Hence, the long-term performance is expressed by means of the cumulative density function of tropospheric attenuation. The latter is calculated by an appropriate statistical combination of gas, cloud and rain attenuation as well as scintillation. The cumulative density functions of the total attenuation are then combined with statistical distributions of the elevation angle at any point on the earth (see Chapter 1, Figure 1.8), in order to provide long-term attenuation statistics.

Figure 3.48 illustrates the clear-sky and total attenuation exceeded during 0.1 % of time over Europe for both up- and downlinks of Teledesic network [20].

Considering the K band downlink in Europe, the clear-sky attenuation exceeded during 0.1 % of time is of about 1.2 dB for a ground-based receiver, while the total attenuation reaches 6 and 8 dB respectively for ground-based and maritime use.

Regarding the 29.1-GHz uplink, the clear-sky margin should be at least 2 dB, while the total attenuation is as high as 12 to 14 dB. These simulation results meet the assumed fade margins of Table 3.13.

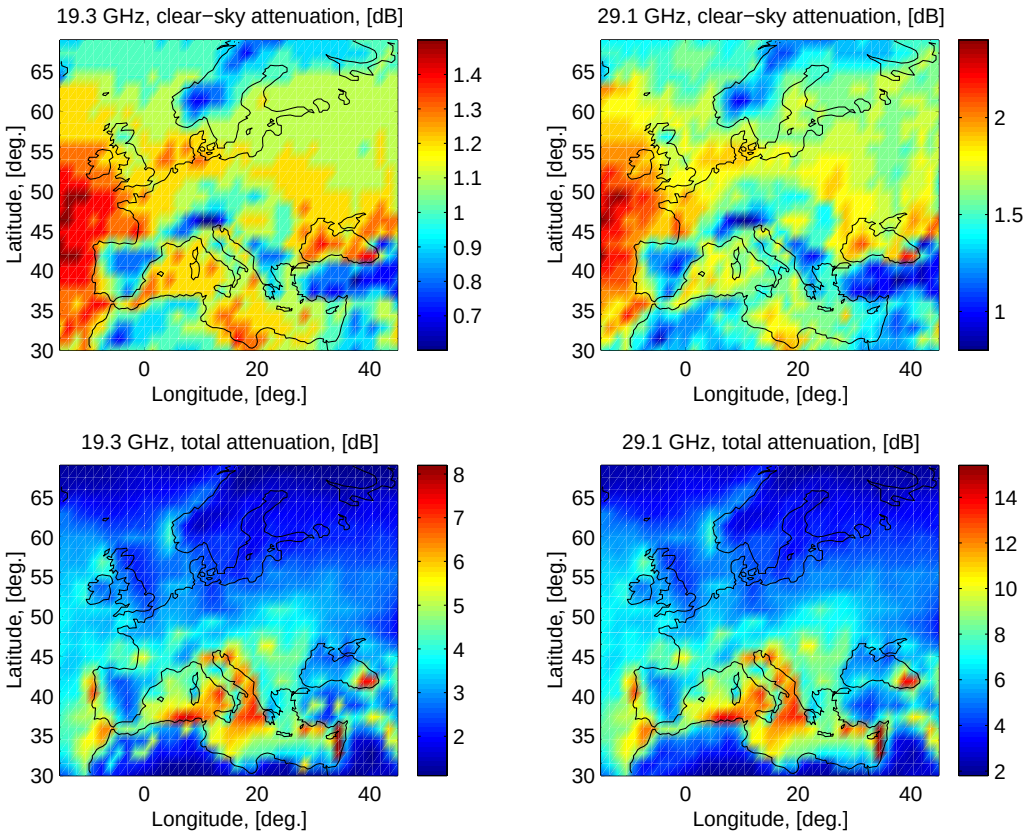

Figure 3.48 *Attenuation exceeded during 0.1 % of time for Teledesic*

3.6.4 Short-term performance

3.6.4.1 TIME SERIES MODELLING

The deterministic attenuation of each atmospheric mechanism is estimated by means of instantaneous models. Only gas, clouds and rain are accounted for, due to the lack of all the necessary input data. The total instantaneous impairment is determined by a coherent addition

of individual attenuation levels (in dB). Real-time simulations are consequently carried out within so-called canonical scenarios, characterized by specific propagation conditions.
A real meteorological satellite map (see Figure 1.9) is converted into a spatial distribution of rain cells. The cells are described by means of exponential profiles similar to EXCELL model. Clouds are located in the very same place as individual rain cells, and are given cumulus properties (see Table 1.1). A constant wind (typically 10 knots) is also assumed in order to simulate the geographical evolution of rain zones and clouds. Three receiving locations are considered:

- L_1 (65° N. latitude, 14° E. longitude),
- L_2 (43.2° N. latitude, 25.4° E. longitude),
- L_3 (61° N. latitude, 6° E. longitude).

Rain cells are represented in Figure 3.49, together with the mentioned locations.

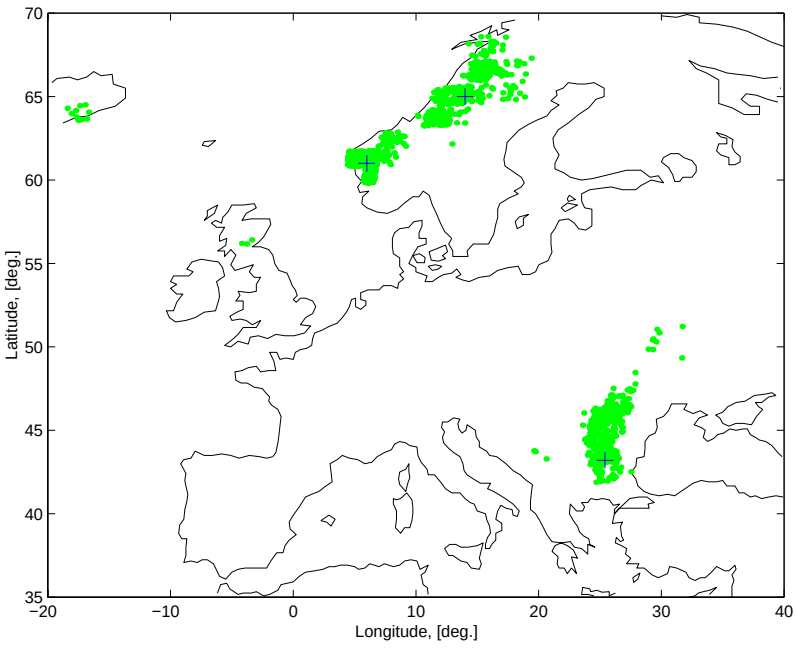

Figure 3.49 *Rain cells {circles} and simulated receiving locations {+}*

Simulated time periods last 60 minutes, the initial time being the same for each of the three locations. For instance, Figure 3.50 depicts the variation of the elevation angle in location L_1, for all satellites the elevation of which is above 15 degrees.

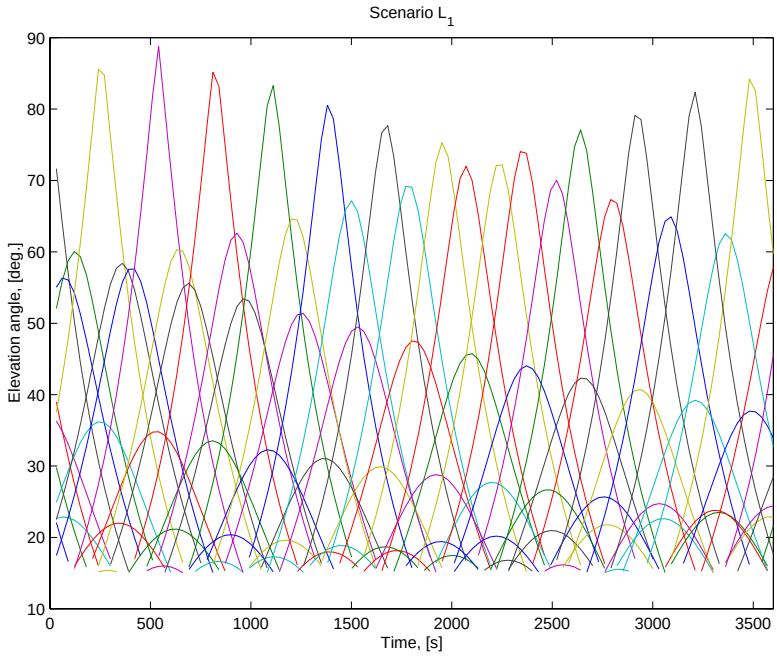

Figure 3.50 *Elevation angles above 15° versus time (location **L1**, Teledesic constellation)*

3.6.4.2 PRELIMINARY RESULTS AT KA BAND

The following simulations deal with the design of fade mitigation and diversity techniques. They are only concerned with the Ka band link (29.1 GHz), which is the most constraining link.

The number of unknown system parameters related to fade mitigation and satellite diversity (M_f, T_u, W, δ, ΔP_{max}, N, S_u, V, ΔM) is quite large. In order to estimate these parameters, a step by-step procedure is applied. Clear-sky conditions are firstly analyzed. For such conditions, the fade mitigation is rarely switched on. Hence, values for the handover parameters can be found. Then, a rainy situation is investigated, so the remaining parameters are determined. Two constraints are simultaneously considered: a low percentage of outage together with a large dwell time (denoted as t_{HO}). For example, 4 1/2 minutes (270 s) is a typical value for the mean dwell time [21]. This value is considered as a reference value in the following.

1° Clear-sky conditions

The clear-sky fade margin has to be fixed. It has been observed in Figure 3.48 that a margin from 2 to 4 dB is a reasonable value in Europe. Using the canonical scenario $\boldsymbol{L_1}$, time series of fade are simulated. The handoff procedure include the *a posteriori* condition on the elevation angle. That means that, among best satellites, the choice is made in favour of the best satellite with increasing elevation angles. For gaseous absorption only and fixing the delay τ_p = 1 s as well as the detection margin δ = 0.5 dB, reasonable dwell times are obtained for 30 s < [V, S_u] < 60 s. For example,

- V = 40 s, S_u = 60 s, M_f = 2 dB, 0.5 dB < ΔM < 3 dB $t_{HO} \cong$ 293 s,
- V = 60 s, S_u = 60 s, M_f = 2 dB, 0.5 dB < ΔM < 3 dB $t_{HO} \cong$ 283 s.

Note that the dwell time does not necessarily increase with the update period owing to the forced handoff procedure. It should also be mentioned that the values found for t_{HO} do not depend upon the value of the hysteresis margin, at least for the simulated values.

When cloud attenuation is added, the dwell times fall down, for the two above cases, to 234 s and 220 s respectively, with ΔM = 0.5 dB. However, these values can be increased by increasing the hysteresis margin ΔM from 0.5 dB to 1 dB: V = 40 s, S_u = 60 s, M_f = 2 dB, ΔM = 1 dB $t_{HO} \cong$ 270 s.

2° Rainy conditions

In rainy weather, the attenuation signal can present deep fades, as illustrated in Figure 3.51. Hence, the fade compensation algorithm is often switched on.

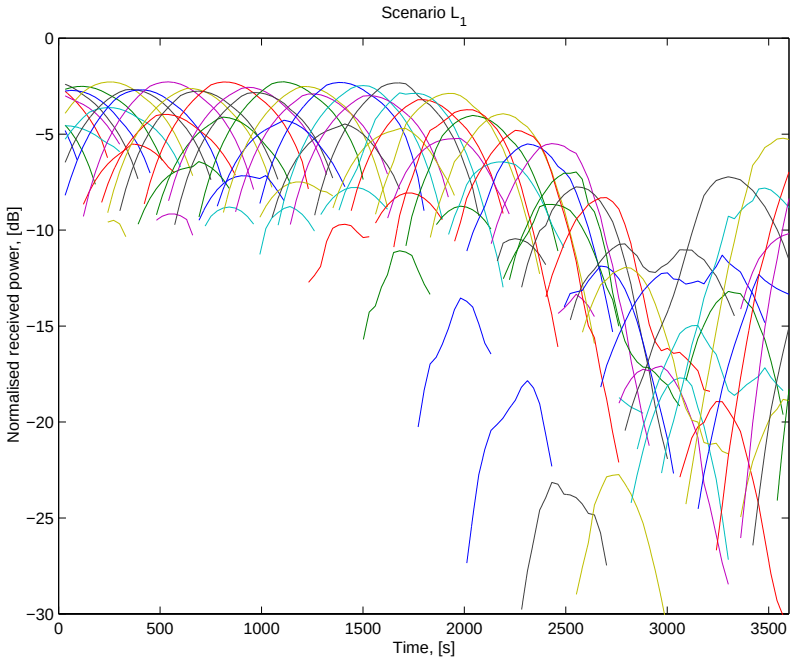

Figure 3.51 *Normalized power (relative to free-space) received from all satellites with elevation angles above 15 degrees*

The impact of three parameters is analyzed:

(i) the hysteresis margin ΔM

(ii) the maximal power correction ΔP_{max}

(iii) the fade compensation update period T_u (it is assumed that T_u and S_u are always given identical values).

When not investigated, the parameters are assigned the following default values [20]:

- ΔP_{max} = 10 dB (since the clear-sky margin is 2 or 4 dB and the total necessary fade margin has been found to be around 12 to 14 dB, see Figure 3.48),
- $T_u = S_u = 60$ s,
- $W = V = 40$ s, $\tau_p = 1$s, $\delta = 0.5$ dB and $N = 20$.

Figure 3.52 illustrates the impact of ΔM for three different clear-sky margins (ΔM = 2, 3 and 4 dB).

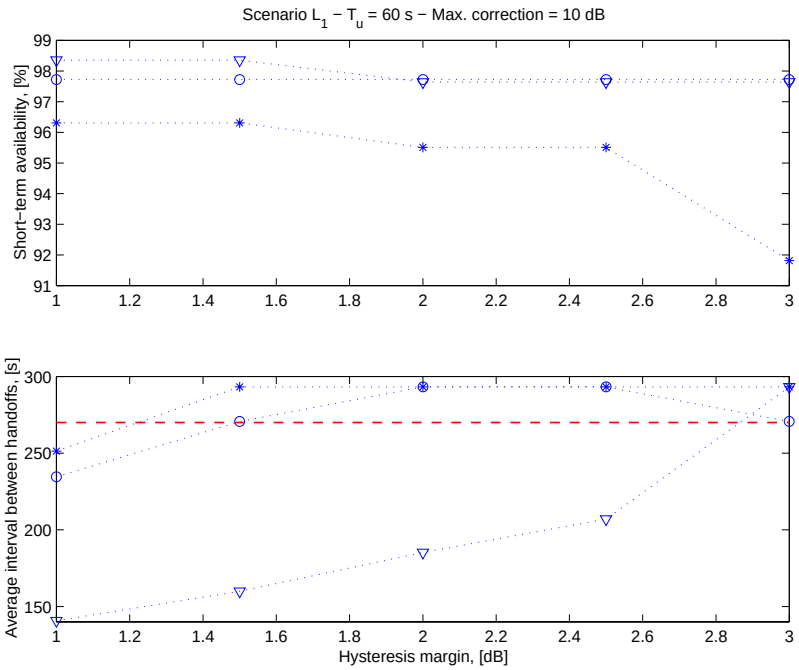

Figure 3.52 *Impact of hysteresis margin, considering three clear-sky margins: 2 dB {*}, 3 dB {o} and 4 dB {∇} (the target value t_{HO} = 270 s is indicated by a dashed line)*

A large dwell time is achieved by a high hysteresis margin ΔM. In contrast, a large availability is obtained for low values of ΔM. If the highest availability is desired under the constraint that t_{HO} remains larger that 270 s, it comes:

- for M_f = 2 dB, $\Delta M \cong$ 1.5 dB
- for M_f = 3 dB, $\Delta M \cong$ 1.5 dB to 2 dB
- for M_f = 4 dB, $\Delta M \cong$ 3 dB.

Once the hysteresis margin is fixed with respect to the clear-sky margin, the effect of the maximal compensation is investigated, as illustrated by Figure 3.53. For all clear-sky margins, the availability generally increases with increasing ΔP_{max}. Nevertheless, a saturation effect seems to appear for corrections higher than 10 dB. The average interval between handoffs also tends to increase for high corrections. Regarding the observed fluctuations, it should be remembered that for an observation length of 60 minutes and a dwell time $t_{HO} \cong$ 270 s, the relative accuracy on simulated t_{HO} is of 7.5 %. For all margins, a dwell time larger than 270 s is achieved for corrections higher than 8 to 10 dB. The pre-fixed value ΔP_{max} = 10 dB, which has been deduced from the long-term analysis, appears subsequently to be appropriate.

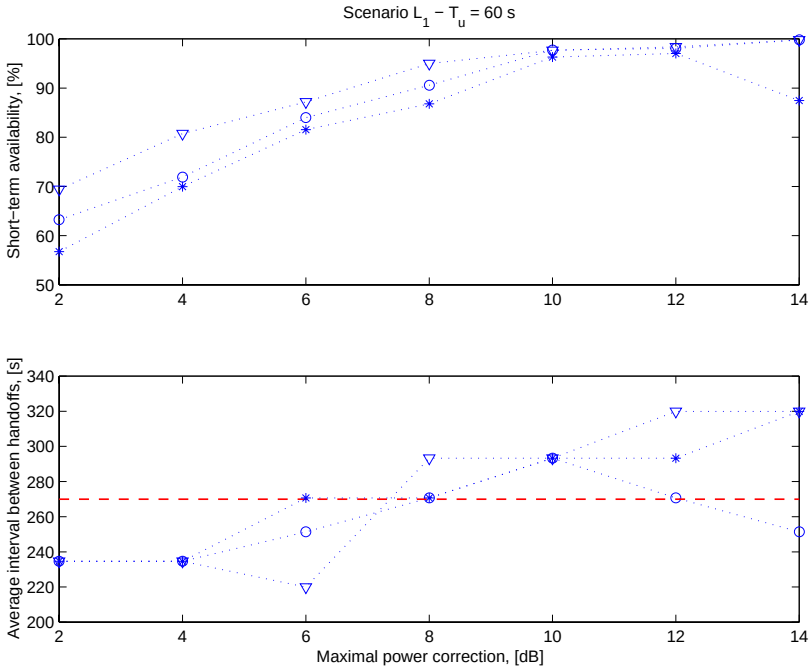

Figure 3.53 *Impact of maximal power correction, considering three clear-sky margins: 2 dB {*}, 3 dB {o} and 4 dB {∇}*

The variation of availability and dwell time with the update period is actually less clear, as observed in Figure 3.54.

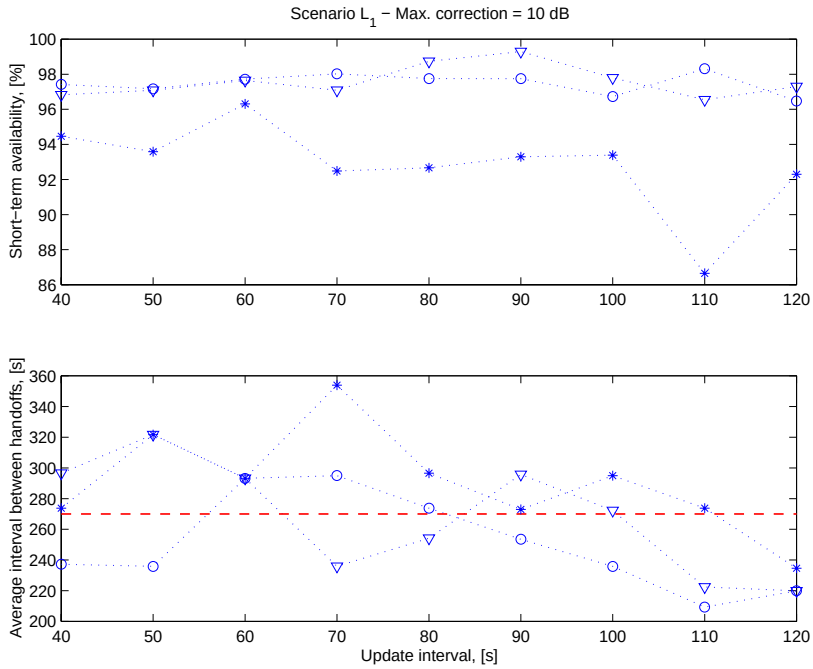

Figure 3.54 *Impact of update period, considering three clear-sky margins: 2 dB {*}, 3 dB {o} and 4 dB {∇}*

However, the availability is generally not very affected by a variation of the update rate, while the dwell time slightly decreases for higher update periods.

3.6.4.3 SIMULATION RESULTS

For each scenario, Table 3.14 summarizes the simulated performance in terms of dwell time and short-term availability, considering three values for the clear-sky fade margins (2, 3 and 4 dB), together with the associated hysteresis margins (1.5, 2 and 3 dB respectively). The system parameters are given the following values, as suggested by the preliminary analysis:

- ΔP_{max} = 10 dB, δ = 0.5 dB and N = 20
- $T_u = S_u$ = 60 s
- $W = V$ = 40 s, τ_p = 1s.

	Single satellite diversity						**MRC-Diversity**		
	t_{HO}, [s]			**Availability, [%]**			**Availability, [%]**		
L1	293	293	293	91.4	97.7	97.6	100	100	100
L2	293	220	293	96.3	96.2	97.1	100	100	100
L3	293	235	320	80.6	73.8	71.9	85.5	87.4	90.2

Table 3.14 *Performance for each scenario, considering three clear-sky margins (each column is realted to a different fixed margin: ΔM = 2, 3 and 4 dB)*

Regarding ***L1*** and ***L2***, the dwell time is clearly acceptable, except for one simulation. The MRC diversity (including fade mitigation) allows for a good improvement of the short-term availability, although its implementation might be too complex with respect to the actual gain. Multi-satellite diversity also increases the handoff rate, as illustrated in Figure 3.55. The latter compares indeed the received signal after various handoff and diversity procedures, namely three of the methods detailed in Sections 3.3.3 and 3.3.4 (including fade compensation): satellite handover with maximum elevation strategy, single satellite diversity (3.16) and MRC-diversity (3.19).

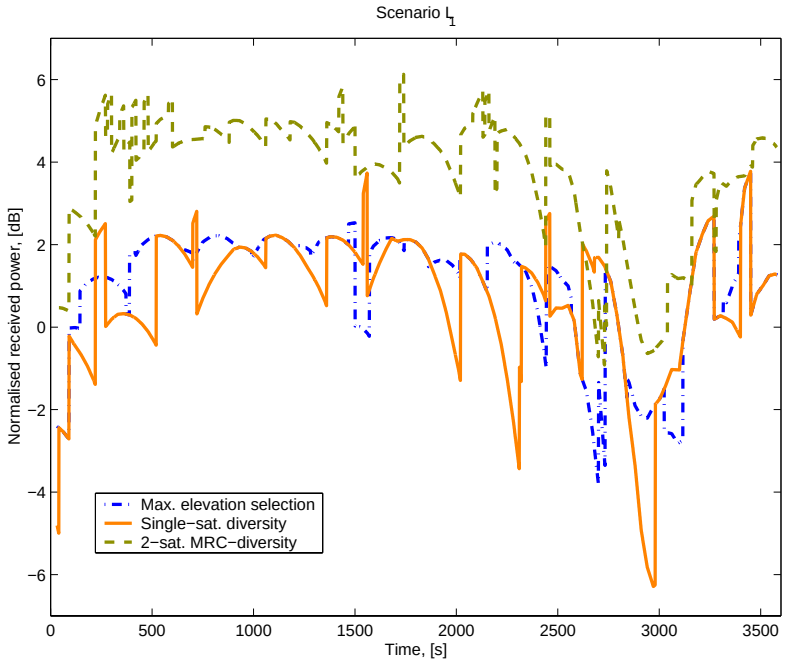

Figure 3.55 *Received signal (L_1) for three handover strategies*

The increase of dwell time comparing the maximum elevation strategy and the single-satellite diversity (3.16) is clearly visible. Moreover, the MRC-diversity, although providing a gain of 3 dB, also decreases significantly the average dwell time.

On the other hand, simulation results for scenario L_3 are severely degraded. This can be explained by the presence of a rain cell at the zenith of this particular location, which is characterized by a heavy rain rate (up to 22 mm/h). During a significant part of the time, the maximal power correction is then largely exceeded. In this case, the MRC-diversity gain provides a significant improvement (up to 20 %) of the availability.

Finally, the relationships between the local rain rate and the dwell time or the outage percentage are investigated over a larger area around location L_1. Maps are represented in Figure 3.56. Although it seems difficult to establish basic relationships between the rain rate and the performance parameters, it is worth noting several points.

(i) In the non-rainy zones, the dwell time is of about 270 s, meaning that the system is properly designed.

(ii) The dwell time remains in all places above 200 s. This is a very reasonable value. In several locations, the dwell time is as high as 500 s. There is no strong correlation between R and t_{HO}.

(iii) Regarding the outage figure, it is very low in the clear areas, but grows up to 20 % in various places. There is obviously a relationship between outage percentage and local rain rate, although is difficult to find it on a point-by-point basis.

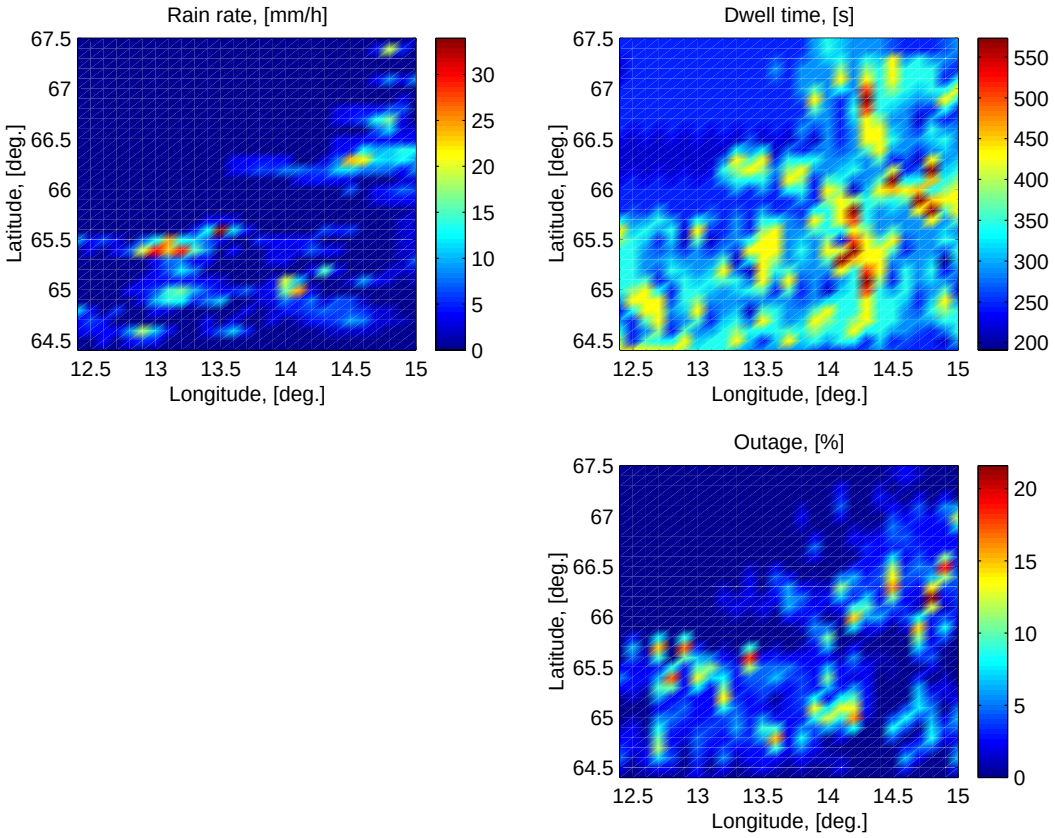

Figure 3.56 *Local rain rate, dwell time and percentage of outage around* L_1

The above remarks point out that the local rain rate is generally not a good indicator of the system performance. This is not very surprising. Indeed, the local rain rate only represents the rain in the zenith direction, and not the amount of rain encountered along the satellite-to-receiver path. Hence, clear zones that are surrounded by rain cells may be characterized by bad performance, and vice-versa. Anyway, in general, a heavy rain rate causes the outage figure to increase.

3.7 Stratospheric communication system

3.7.1 High-altitude platforms

Stratospheric communication systems constitute a proposed alternative to LEO satellite systems [22][23]. Therefore, it seems interesting to analyze a platform-based communication system as last test case. Another reason is that stratospheric platforms, although fixed and considered by ITU-R as a pure terrestrial system, have actually many similarities with satellite communication systems, mainly because of the platform height.

Utilising lighter than air technology, a network of platforms will act as a high-speed telecommunication relay to dense metropolitan areas. Platforms equipped with a telecommunication payload will be held in a geo-stationary position in the stratosphere, over major cities and their suburbs. Each platform shall provide high speed, high capacity wireless broadband service to an area of some 19,000 square kilometres (150-km diameter). The system is described in Figure 3.57. Various applications are planned, such as high-speed Internet access, video conferencing or fixed wireless telephony. Subscribers will transmit at V band directly to the platform, where onboard switching will route traffic directly to other subscribers within the same platform coverage area. Traffic destined for subscribers outside the platform coverage area will be routed through ground stations to the public networks or to other platforms serving nearby cities.

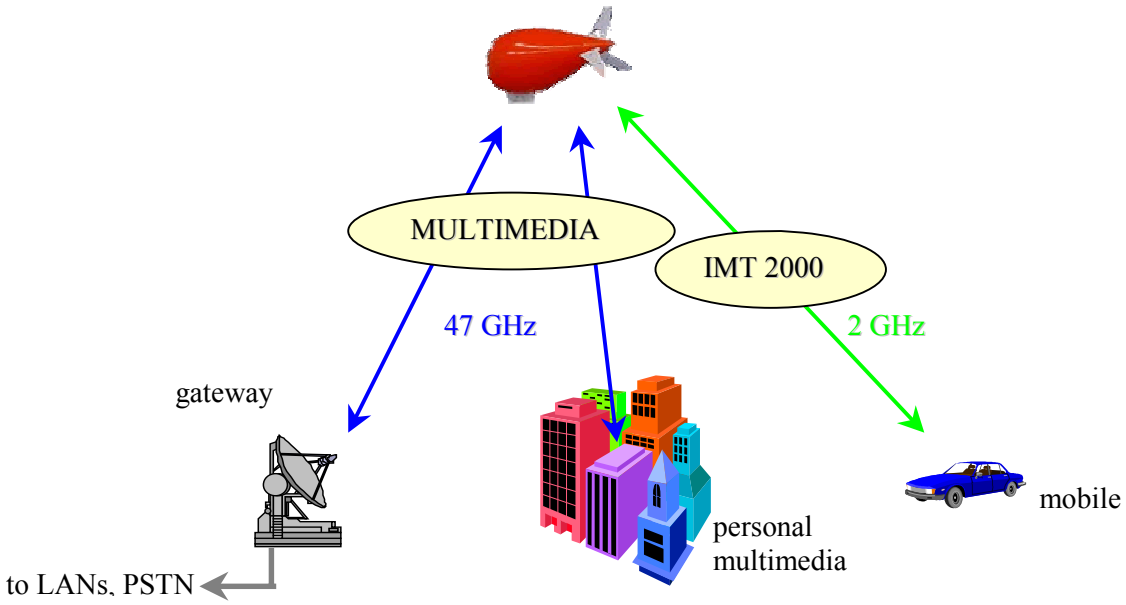

Figure 3.57 *HAP system overview*

Subscribers will also have the possibility to communicate through a terrestrial gateway that will redirect the traffic to wireless LANs. Meanwhile, the stratospheric network should offer the capacity to be used at S band as a base station for the third generation cellular service (IMT 2000). In this study case, the feasibility of direct transmission between individual users and a platform is investigated, regarding both fixed broadband V band applications and mobile S band service.

3.7.2 System specifications

High-altitude platforms (HAP's) are located in a stratospheric geostationary position 21 km above the earth by means of ionic propulsion engines.

Consider in a first stage the V band service. With a 27.1 dBW EIRP, the system generates 691 spot beams over a 150-km diameter coverage area out to 15 degrees elevation angle [22]. It is assumed that variable antenna gains are used to compensate for the different path losses from innermost to outermost cells on the downlink. Users' antennas are assumed to be typical horns, the beamwidth of which is around 15 degrees. Planned systems envision a total bandwidth of 300 MHz in each direction in the 47.2-47.5 GHz and 47.9-48.2 GHz bands, with a QPSK modulation scheme and FDMA/TDMA (uplink) and TDM (downlink) protocols.

As far as the IMT 2000 service is concerned, realistic specifications are chosen in accordance with the IMT 2000 standard and basic recommendations. They are summarized in Table 3.15.

HAPS-IMT 2000 characteristics	
Mobile antenna	Omnidirectional
Frequency	2.1 GHz
Modulation scheme	QPSK
Multiple access	Wideband CDMA
Polarisation	Right circular
Error protection	Convolutional $R_c = 1/3$, $K = 9$
Required E_b/N_0	2 dB for BER 10^{-3}
Chip rate	4096 Mcps
Channel bandwidth	5 MHz
Net bit rate	from 8 kbps (voice) up to 384 kbps (data)

Table 3.15 *Typical IMT 2000 system based on high-altitude platforms*

3.7.3 Performance prediction

3.7.3.1 SIMULATION APPROACH

Although it has been developed for LEO satellite systems, the approach detailed in Section 3.2.2 can easily be applied to stratospheric services. It has however to be slightly rewritten, since the LEO satellites are now replaced with fixed platforms. As a consequence, the temporal variation is exclusively given by the variation of the conditional channel, all physical parameters being related to the receiver location. It is demonstrated in the following that the distribution over *time* and *area* can be transformed into a distribution over the *area* conditional upon the *area size*. The performance parameters to be predicted are for example the average BER as well as the fade level or BER exceeded with a given percentage of *time*. Hence, the performance criterion can be expressed in a general fashion as a given value of parameter x (exceeded during τ % of time or averaged over time) over β % of a ρ_S-kilometre diameter area [24][25].

Two stratospheric applications are simulated in the next sections. Regarding the use of HAP's for mobile applications, building shadowing and multipaths are the only effects to be encountered at IMT 2000 frequency band (around 2 GHz). On the other hand, multimedia transmissions at 47 GHz suffer mainly from rain and other atmospheric effects, but also from terrestrial multipath effects. All these effects can conditionally be modelled by cumulative distributions over time. Since the elevation angle of the HAP-to-terminal link no longer depends on time, but well on the receiver location, there is no need in dividing the set of physical parameters $\overline{\eta}$ into two contributions. Hence, the distribution over the area (conditional upon the area size) of the fade level or BER exceeded during τ % of time can be easily estimated, the distribution over *time* being given by the various percentiles of tropospheric/building attenuation. After some discussion about the distributions of the physical parameters, the physical-statistical prediction method is applied to both V band multimedia transmission and IMT 2000 mobile service.

3.7.3.2 DISTRIBUTION OF PHYSICAL PARAMETERS

Thus, consider a stratospheric system delivering telecommunication services to a given built-up area. The area is defined as a circular zone of diameter ρ_S, the centre of which is located right below the platform. The value of ρ_S determines the minimum elevation angle within the area.

Two types of environments constitute the area: the centre ($\rho < \rho_U$) is taken as urban, while farther parts ($\rho_U < \rho < \rho_S$) are featured by suburban parameters. Analytical distributions of the physical parameters have to be assumed for both urban and suburban parts. The building height probability density is estimated by a lognormal distribution, with median μ and standard deviation σ depending on the type of environment (see Section 2.3.2.1). The street width is assigned a constant value over the whole area and the azimuth angle relative to the street axis is taken as uniformly distributed over [0, 2π]. The elevation angle probability density function is outlined assuming that the receiver is randomly located inside the zone of diameter ρ_S, so the distribution is given, as detailed in [25] by:

$$T_{\Theta}(\vartheta) = 8 \left(\frac{h_S}{\rho_S}\right)^2 \frac{tan^2\,\vartheta + 1}{tan^3\,\vartheta}, \qquad \vartheta \geq tan^{-1}\left(\frac{2\,h_S}{\rho_S}\right) \tag{3.21}$$

where h_S is the platform altitude.

In (3.21), the distribution of the elevation angle, and therefore the distribution of $\overline{\eta}$, clearly vary according to the size of the area.

In the simulations, the various parameters are assigned the following values (see Table 3.6, [22]):

- (μ, σ) = (15.0 m, 0.30) in urban area
- (μ, σ) = (7.1 m, 0.25) in suburbs
- w_0 = 20.0 m
- ρ_U = 20 km
- h_S = 21 km.

The height and location of the terminal actually depend on the kind of application to be simulated. As far as the V band multimedia service is concerned, a value h_m = 10 m is assumed for the horn antenna height. For the mobile application, the omnidirectional antenna is placed at 2 metres in height above street level.

3.7.3.3 ATTENUATION STATISTICS FOR THE V BAND MULTIMEDIA SERVICE

At 47 GHz, the degradation of performance is caused by atmospheric effects as well as by building shadowing and multipaths (local effects). Indeed, the V band system being portable, antennas can be installed everywhere, e.g. at windows or preferably on rooftops. Such

locations, though higher than street level, may still suffer from diffraction and reflection by taller buildings. The present section consequently accounts for both tropospheric and local mechanisms, using an appropriate combination method.

The conditional distribution of building attenuation A_B is calculated from $T_{R|\overline{N}}$ as given by equation (2.62). Bold fonts are used when the attenuation is expressed in [dB], so that it can be written: $\boldsymbol{A_B} = 10\ log(A_B)$. The distribution $T_{\boldsymbol{A_B}|\overline{N}}(\boldsymbol{A_B} \mid \overline{\eta})$ is then easily inferred.

Regarding tropospheric effects, the following models (detailed in Chapter 1) are utilised:

- Liebe-Salonen model for water vapour attenuation,
- ITU-R model for oxygen attenuation (ITU-R Rec. PN.676-2),
- ITU-R model for rain attenuation (ITU-R Rec. PN.618-5),
- Salonen-Uppala model for cloud attenuation (ITU-R Rec. PN.840-1),
- ITU-R model for scintillation (ITU-R Rec. PN.618-5),
- Castanet-Lemorton model for the combined attenuation.

These models estimate the cumulative distribution of each attenuation, as well as of the total attenuation conditional upon the physical parameters (i.e. the elevation angle). The cumulative distribution of attenuation due to atmospheric effects is denoted as $P_{atm}(\boldsymbol{A} \mid \overline{\eta})$.

Atmospheric and building effects are clearly not correlated. Hence, the cumulative density function $P(\boldsymbol{A} \mid \overline{\eta})$ of the total attenuation in [dB] is given by [24]:

$$P(\boldsymbol{A} \mid \overline{\eta}) = \int_{-\infty}^{\boldsymbol{A}} T_{\boldsymbol{A_B}|\overline{N}}(\boldsymbol{A_B} \mid \overline{\eta})\ P_{atm}(\boldsymbol{A} - \boldsymbol{A_B} \mid \overline{\eta})\ d\boldsymbol{A_B} \tag{3.22}$$

where $T_{\boldsymbol{A_B}|\overline{N}}(\boldsymbol{A_B} \mid \overline{\eta})$ is the conditional distribution of building attenuation.

Knowing $P(\boldsymbol{A} \mid \overline{\eta})$, it is easy to determine the total attenuation $\boldsymbol{A_1} \mid \overline{\eta}$ exceeded during 1 % of time. For simplicity, the following notation is used: $\boldsymbol{A_1} \mid \overline{\eta} \equiv F(\overline{\eta})$.

Figure 3.58 and Figure 3.59 compare the attenuation levels caused by each effect as a function of the elevation angle.

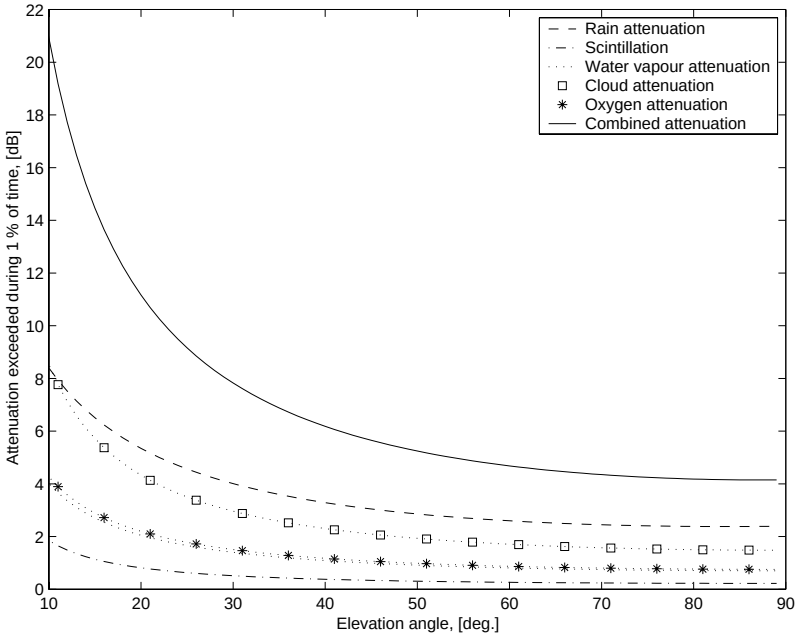

Figure 3.58 *Conditional attenuation exceeded during 1 % of time due to various tropospheric mechanisms versus elevation angle*

Considering first tropospheric mechanisms (Figure 3.58), rain and clouds are the major source of impairment, especially at low elevation angles. The contributions due to oxygen and water vapour are similar and scintillation, though less important, is significant. As expected, the combined attenuation is actually less than the sum of individual attenuation levels.

Figure 3.59 superimposes the attenuation exceeded during 1 % of time caused by tropospheric effects and local effects, together with the combined attenuation level. Note that the building attenuation is averaged over building heights and azimuth angles. It can be observed that the fading caused by local effects is of the same order of magnitude as the tropospheric attenuation.

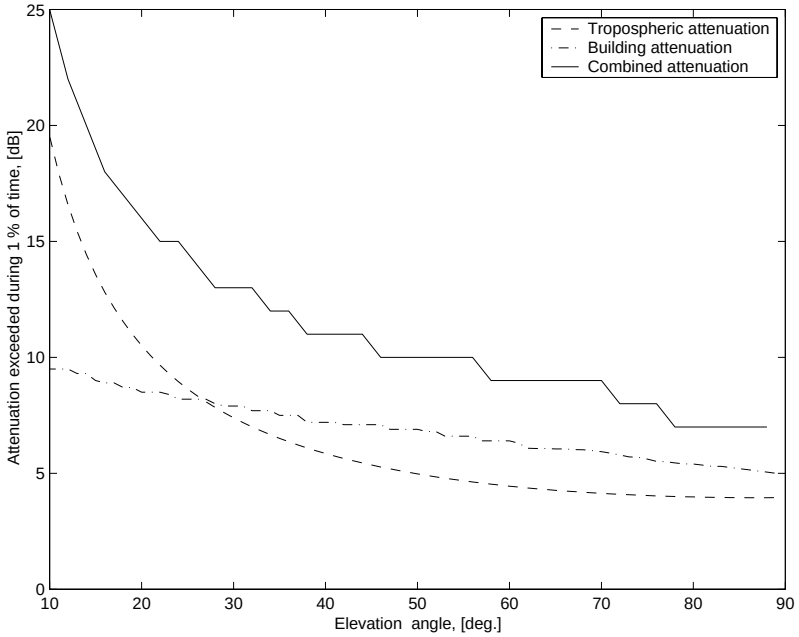

Figure 3.59 *Attenuation exceeded during 1 % of time: tropospheric mechanisms, local effects and combined level*

For a given size ρ_S of the service area, $T_{\overline{N}}(\overline{\eta})$ is completely defined. The distribution of attenuation within the area limited by $\rho < \rho_S$ is finally given by an expression similar to (3.6):

$$T_{\mathbf{A_1}|\overline{\eta}}(\mathbf{A_1} \mid \overline{\eta}) = T_{\overline{N}}\left[F^{-1}(\mathbf{A_1} \mid \overline{\eta})\right]\left|\frac{\partial F^{-1}(\mathbf{A_1} \mid \overline{\eta})}{\partial \mathbf{A_1} \mid \overline{\eta}}\right| \tag{3.23}$$

The method yields the attenuation distribution for any given size of the area, as depicted in the following graphs (Figure 3.60 and Figure 3.61). The combined (total) attenuation exceeded during 1 % of time is significantly increased if compared to each single attenuation but is less than their sum. For example, it reaches 12.8 dB over 90 % of a 79-km diameter area versus 7.5 dB and 8 dB for tropospheric and building attenuation levels respectively.

(a)

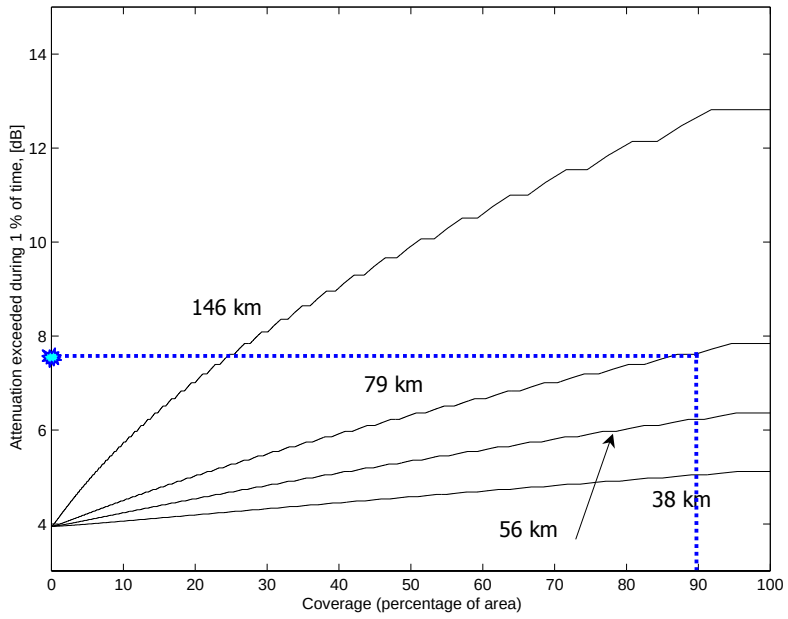

(b)

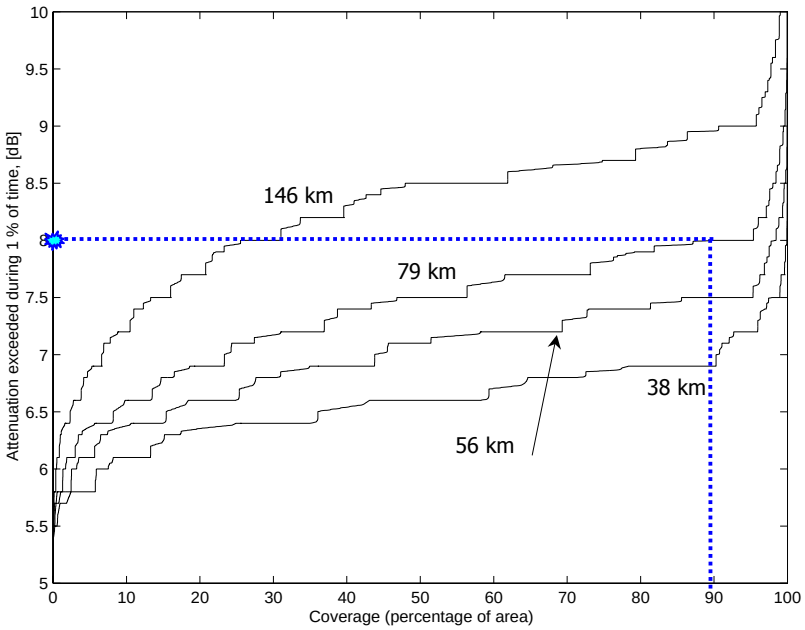

Figure 3.60 *Tropospheric (a) and building (b) attenuation exceeded during 1 % of time as a function of the percentage of area, for several diameters (146, 79, 56 and 38 km)*

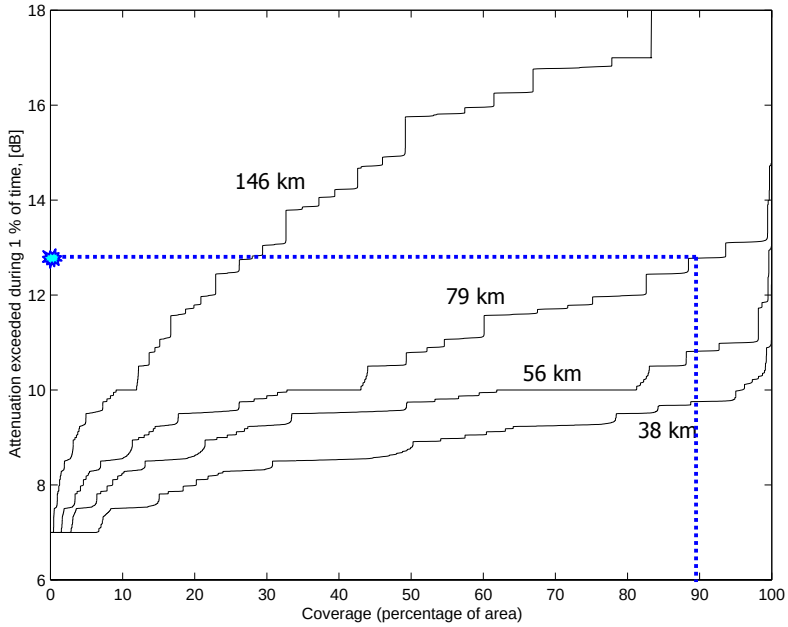

Figure 3.61 *Combined attenuation exceeded during 1 % of time as a function of the percentage of area, for several diameters (146, 79, 56 and 38 km)*

As a conclusion, building shadowing and multipaths cannot be neglected, at least for moderate antenna heights. For very high antenna heights, local effects should become less significant.

3.7.3.4 RAW AND CODED BER PREDICTION FOR IMT 2000 SERVICE

1° Prediction method

The IMT 2000 stratospheric service operates around 2.1 GHz. At such frequencies, the troposphere has no influence and only local mechanisms must be accounted for. This section particularly highlights the impact of error-correcting code and power-control on the performance evaluated through the distribution over the area of the BER exceeded during 1 % of time.

It has already been described how the conditional raw/coded BER can be calculated as a function of the physical parameters (see Chapter 2, Section 2.3.6). The method outlined by equation (3.8) can then be applied taking into account the rewriting of Section 3.7.3.1. The distribution over the area of the average BER is given by:

$$T_{P_E|\overline{N}}(P_E \mid \overline{\eta}) = T_{\overline{N}}\left[G^{-1}(P_E \mid \overline{\eta})\right]\left|\frac{\partial G^{-1}(P_E \mid \overline{\eta})}{\partial P_E \mid \overline{\eta}}\right| \tag{3.24}$$

with $P_E(E_b/N_0) \mid \overline{\eta} \equiv G(\overline{\eta})$. The same processing can of course be applied to the BER exceeded during any percentage of time.

2° Simulation results

In a first time, the impact of the fade margin on the coverage has been investigated with regard to the raw BER without power-control. The system margin is defined as the difference between the simulated received SNR (i.e. E_S/N_0) and the minimum E_S/N_0 required to achieve a BER of 10^{-3}. Simulation results are depicted in Figure 3.62 for several coverage area diameters [25].

For a fade margin less than approximately 10 dB, the performance is highly dependent on the margin. When the latter is above 10 dB, a saturation effect appears and the coverage only slightly increases with increasing margins. Meanwhile, for areas larger than 80 km in diameter, the saturation value of the coverage is less than 80 % (77% for ρ_S = 95 km; 53 % for ρ_S = 146 km).

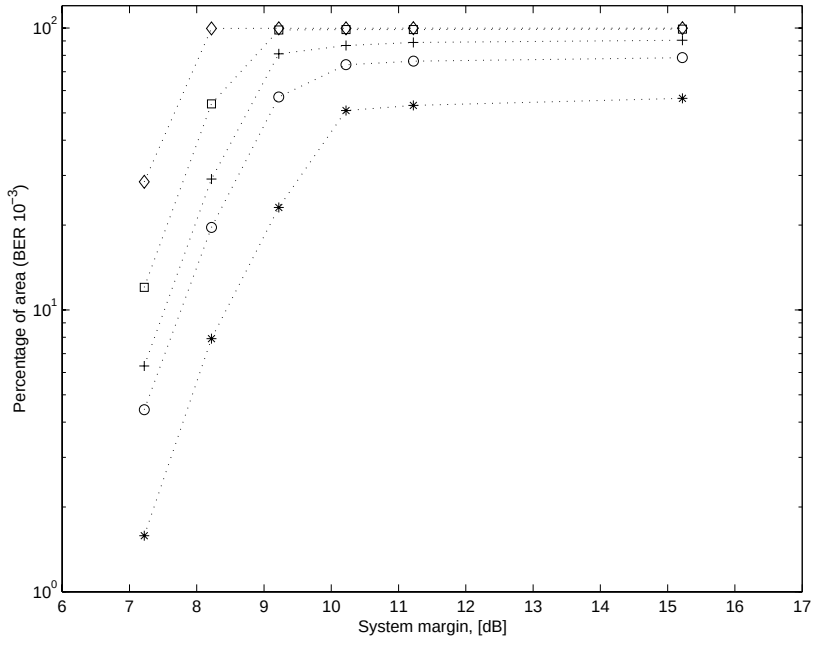

Figure 3.62 *Coverage achieved for BER 10^{-3} as a function of the system margin for several area diameters: 146 km {*}, 95 km {o}, 79 km {+}, 56 km {squares} and 38 km {diamonds}*

Figure 3.63 presents similar results, but the error-correcting code defined by the specifications is now accounted for.

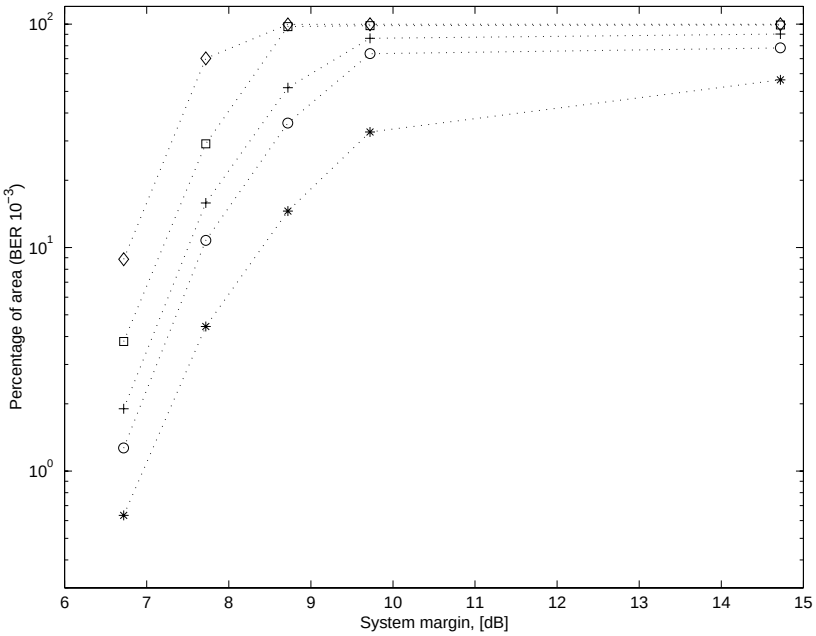

Figure 3.63 *Coverage achieved for BER 10^{-3} (using a convolutional code) as a function of the system margin for several area diameters: 146 km {*}, 95 km {o}, 79 km {+}, 56 km {squares} and 38 km {diamonds}*

The BER is estimated by the tight upper bound given by (2.67-a). The minimum required fade margin seems to be the same as before, i.e. at least 10 dB. However, thanks to the coding gain, the required nominal SNR will be strongly reduced. For instance, using the specified code (R_c = 1/3) and identical fade margins, the nominal received SNR, and thereby the transmitted power, should be some 9 dB smaller when the correcting code is used.

Figure 3.64 summarizes several predictions such as the fade level exceeded during 1 % of time, as well as the BER exceeded during 1 % of time and the mean BER. Values of BER are calculated using a nominal SNR of 11 dB and the convolutional encoding.

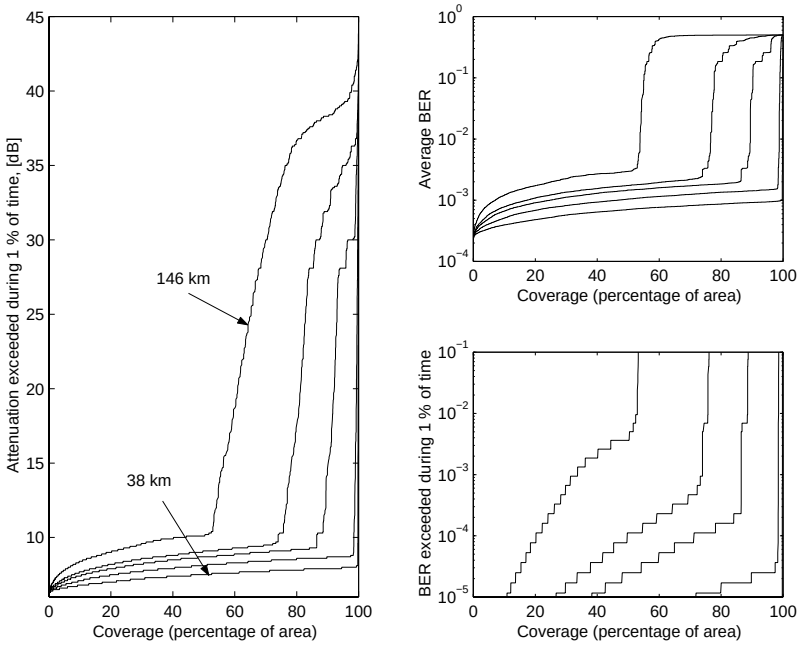

Figure 3.64 *Fade level and BER exceeded during 1 % of time as well as average BER as a function of the percentage of area, for several diameters (from left to right): 146, 95, 79, 56 and 38 km*

In IMT 2000 specifications, the use of a correcting code is usually paired with a power-control mechanism. The latter would indeed ensure for increasing the received SNR, in order to take a better advantage of the convolutional coding. Simulations have consequently been carried out considering a fade mitigation strategy. Since the global approach is statistical, a perfect compensation has to be implemented, i.e. neglecting signalling delays, estimation of E_b/N_0 and quantification errors. A maximal power correction of 10 dB is assumed [25].

In Figure 3.65, the required fade margin is strongly reduced when the compensation algorithm is implemented. For equal performance, the margin is intuitively decreased by nearly 10 dB, i.e. the maximal fade compensation.

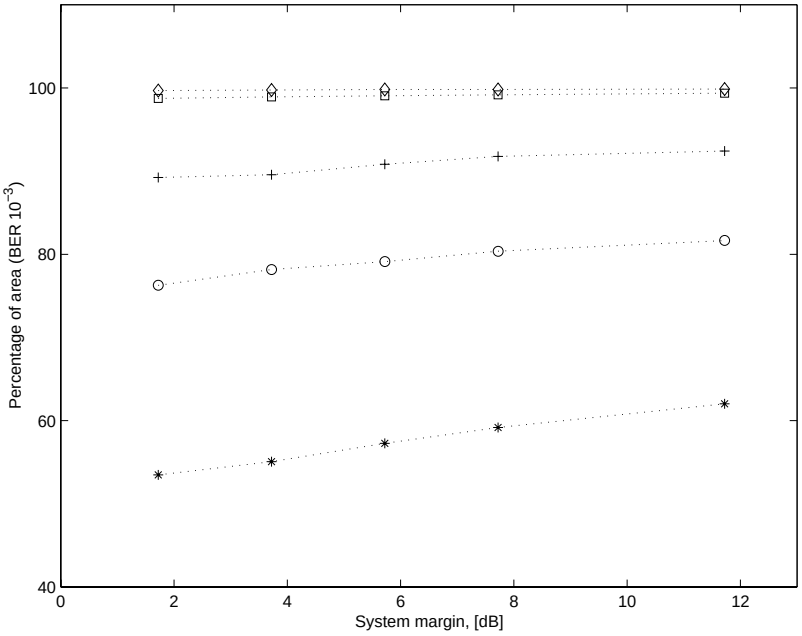

Figure 3.65 *Coverage achieved for BER 10^{-3} (using a convolutional code and power-control) as a function of the system margin for several area diameters: 146 km {*}, 95 km {o}, 79 km {+}, 56 km {squares} and 38 km {diamonds}*

However, the performance achieved at large distances from nadir remains strongly degraded. In order to improve the coverage of portable links at elevation angles less than some 30 degrees, directive antennas should be used to meet the quality requirements.

3.8 SUMMARY

This final chapter aims at setting up prediction methods that have then been applied to various existing or future systems.

A distinction between long- and short-term performance has firstly been introduced. While long-term availability is concerned with statistical predictions and models, short-term analysis is better carried out based on deterministic models.

Regarding long-term performance, a new and original method has been presented that differentiates temporal availability with spatial coverage, in the field of mobile satellite communication systems. The method fully exploits both the physical model and the physical-statistical modelling described in Chapter 2.

The short-term analysis relies on instantaneous physical models and scenarios, such as a ray-tracing tool or a meteosat map. It is based on the combination of these models with an orbit generator used in *real time* simulations. Time series results can therefore be used to demonstrate the effectiveness of several system procedures in canonical scenarios. Models of various system strategies such as fade mitigation, satellite handover and diversity have been described.

The developed prediction methods have been applied to four study cases, covering a large range of applications and frequency bands. These examples stress the capabilities of the theoretical models to yield system-oriented results, when they are used in combination with the prediction tools.

A first test case has been dedicated to mobile-satellite systems. The feeder link has firstly been analyzed on a long-term basis, and several constellations have been compared, in order to emphasise the impact of the link frequency and the constellation.

The L band user link has then been investigated. The long-term analysis is based on the mentioned new method, which allows to predict the fade level exceeded during a given percentage of time over a given percentage of area. Also, the shadowing correlation model has been applied to Iridium and Globalstar constellations.

Regarding the short-term performance, two canonical built-up scenarios have been studied in a deterministic way: a long straight street and a crossroad. In the crossroad scenario, the

effects of corner and vertical edge diffraction on the simulated path-loss have been pointed out.

As a second case, a S-IMT 2000 system has been considered, applying the COST 255 methodology and the shadowing model to Deligo constellation. On one hand, the impact of receiver speed and power-control has been simulated. On the other hand, it has been shown that the correlation coefficient is highly dependent on the latitude, even for an optimised constellation.

A Ka band multimedia LEO satellite system constitutes the third test case. Tropospheric models have been applied to predict the long-term availability over Europe. The design of fade mitigation and diversity techniques has also been discussed in the framework of typical dynamic scenarios.

Finally, the prediction tools have been adapted to a V band/S band terrestrial system based on high-altitude platforms. It has been demonstrated that such systems accommodate very satisfactorily with a physical-statistical analysis.

3.9 REFERENCES

[1] COST 255, *Radiowave propagation modelling for new SatCom services at Ku band and above*, European Commission, Brussels, to be published.

[2] DÖTTLING, M., SAUNDERS, S.R., Bit error rate calculation for satellite communication systems, Joint International Workshop COST 252/253/255 (Toulouse, France), pp. 51-55, May 1999.

[3] OESTGES, C., System-level simulation for land mobile satellite services, Joint International Workshop COST 252/253/255 (Toulouse, France), pp. 59-63, May 1999.

[4] DE GAUDENZI, R., GIANNETTI, F., DS-CDMA satellite diversity reception for personal satellite communication: satellite-to-mobile link performance analysis, *IEEE Trans. Veh. Tech.*, vol. 47, n° 2, pp. 658-672, 1998.

[5] OESTGES, C., VANHOENACKER-JANVIER, D., Physical-statistical prediction of performance for land mobile satellite systems, *IEE Proc.-Microw. Antenn. Propagat.*, vol. 146, n° 5, pp. 362-368, 1999.

[6] MOTOROLA SATELLITE COMMUNICATIONS, INC., *Iridium system application before the Federal Communication Commission*, Washington, 1990.

[7] DÖTTLING, M., ZWICK, T., WIESBECK, W., Investigation of satellite diversity and handover strategies in Land Mobile Satellite systems based on a ray-tracing propagation model, 6th Int. Mobile Satellite Conf., Proc. IMSC '99 (Ottawa, Canada), pp.128-133, 1999.

[8] KERSCHAT, K., KOUDELKA, O., RIEDLER, W., TOMLINSON, M., HUGHES, C.D., HOERLE, J., A variable spread-spectrum fade countermeasure system for the DICE video conference system, Olympus Utilisation Conference, ESA WPP-60, (Sevilla, Spain), pp. 555-560, 1993.

[9] CORAZZA, G.E., DEGLI-ESPOSTI, V., FRULLONE, M., RIVA, G., A characterization of indoor space and frequency diversity by ray-tracing modelling, *IEEE J. Selected Areas Commun.*, vol. 14, n° 3, pp. 411-419, 1996.

[10] HESS, G.C., *Land-mobile radio system engineering,* Artech House, Boston-London, 1993.

[11] MILLER, B., Satellites free the mobile phone, *IEEE Spectrum*, pp. 26-35, March 1998.

[12] TRONCHE, C., Satellite systems for multimedia and mobile telecommunications, 28th European Microwave Conf., Proc. EuMC '98 (Amsterdam, The Netherlands), pp.374-383, 1998.

[13] AGIUS, A.A., SAUNDERS, S.R., EVANS, B.G., Antenna design for the ICO handheld terminal, 10th Int. Conf. on Ant. and Prop., ICAP '97 (Edinburgh, UK), IEE Conf. Publication 436, pp. 1.385-1.389, April 1997.

[14] CORAZZA, G.E., VATALARO, F., A statistical model for land mobile satellite channels and its application to nongeostationary orbit systems, *IEEE Trans. Veh. Tech.*, vol. 43, n° 3, pp. 738-742, 1994.

[15] DÖTTLING, M., OESTGES, C., VÁZQUEZ-CASTRO, M.A., Test cases involving mobile links: simulation results, COST 255 Final Workshop (Bech, Luxemburg), October 1999.

[16] ITU-R, *ITU-R Recommendations – Propagation in non-ionized media,* PN series vol., ITU, Geneva, 1994.

[17] KANATAS, A.G., CONSTANTINOU, P., City center high-elevation angle propagation measurements at L band for land mobile satellite systems, *IEEE Trans. Veh. Technol.*, vol. 47, n° 3, pp. 1002-1011, 1998.

[18] CAIRE, G. et al., Development and validation of wideband-CDMA IMT 2000 physical layer for satellite applications, 6th Int. Mobile Satellite Conf., Proc. IMSC '99 (Ottawa, Canada), pp.213-219, 1999.

[19] MEENAN, C., SAMMUT, A., TAFAZOLLI, R., EVANS, B.G., Deligo: Repetitive ground track 100 % dual-diversity LEO satellite constellation for S-PCN, *Electronics Letters*, vol. 31, n° 17, pp. 1407-1408, 1995.

[20] OESTGES, C., MAUFROID, X., VANHOENACKER-JANVIER, D., Performance simulation of a Ka band multimedia LEO satellite system, 6th Ka Band Utilization Conference (Cleveland, U.S.A.), pp. 605-612, June 2000.

[21] MONTPETIT, M.J., Internet transmission over Teledesic: simulations studies, Joint International Workshop COST 252–253–255 (Toulouse, France), pp. 77-88, May 1999.

[22] LEE, Y.C., ROTHBLATT, M., Le service de télécommunications stratosphériques, ou la possibilité de corriger des déséquilibres, *Nouvelles de l'UIT*, vol. 3, pp. 25-29, 1997.

[23] SILANSKY, S., Using the Sky Station service, *Stratospheric News*, vol. 2, pp. 4-5, 1998.

[24] OESTGES, C., VANHOENACKER-JANVIER, D., Performance prediction of a 47 GHz stratospheric communication system, Millennium Conference on Antennas and Propagation, AP2000 (Davos, Switzerland), April 2000 (on CD-ROM).

[25] OESTGES, C., VANHOENACKER-JANVIER, D., Coverage analysis of a stratospheric communication system, *IEE Proc.-Microw. Antenn. Propagat.*, accepted for publication.

CONCLUSIONS

In the framework of this thesis, channel models and performance prediction methods are developed in view of non-geostationary orbit systems. For the last decade, low earth-orbit constellations have indeed been considered as a valuable global solution in the design of satellite personal communication networks (S-PCN's). Such systems, operating from L band to high-frequency Ka band, are planned to offer mobile telephony or multimedia applications with worldwide cellular coverage.

However, tropospheric and local mechanisms strongly affect the static and dynamic behaviour of non-geostationary S-PCN's. Owing to the constant motion of satellites and the "megacellular" coverage, new channel models and prediction methods are required. Yet, it is believed that a combination of existing models, valid for geostationary links and mobile terrestrial cellular networks, is not really appropriate. New approaches must also meet the growing need for system-oriented tools, which could help in system design.

The study is divided in three chapters. Chapters 1 and 2 present electromagnetic models of the satellite-to-receiver channel. Then, Chapter 3 describes several prediction tools, together with a number of realistic exemplary applications.

Chapter 1 deals with models of tropospheric attenuation and scintillation, caused by rain, clouds, gas and turbulences. The main difference between low-orbit and geostationary channels is the satellite motion, resulting in varying elevation and azimuth angles. Therefore, existing tropospheric models are simply used in combination with an orbit generator. With time series modelling in mind, particular attention is paid to EXCELL rain model, because it allows for a spatial description of rain cells. Also, the first steps of a new time series modelling technique, accounting for system dynamic procedures, are introduced, although finalisation of the approach is beyond the scope of this work.

Chapter 2 is dedicated to the mobile satellite channel. In built-up areas, local effects are caused by reflection on ground and walls, diffraction by wedges and scattering from obstacles. These are mainly buildings and trees that are located in the vicinity of the receiver. Two models are outlined: a deterministic ray-tracing tool and a physical-statistical approach.

The deterministic ray-tracing tool is based on geometrical optics. Buildings and trees are featured by parallelepipeds. The Fresnel theory, the Uniform Theory of Diffraction and the ITU-R vegetation loss model are used to represent the electromagnetic ray-based mechanisms. Moreover, in order to cope with wedges of finite length, an incremental diffraction coefficient is derived from equivalent currents. Although the method is more time-consuming than the classical UTD, it presents several redundant advantages:

- every visible wedge is accounted for, even if the UTD diffraction point is located outside the edge,
- corner effects are properly modelled,
- the solution for the diffracted field is continuous, so that unrealistic abrupt field variations are avoided,
- in contrast to classical UTD simulations, time series results, which are based on equivalent currents, look more authentic, because they always include some multipath component,
- the software implementation of equivalent currents is quite straightforward, since the process is a simple integration.

Multiple interactions are also discussed. Reflection is accounted for up to the second order. Double diffraction might be significant at very low elevation angles, i.e. when it constitutes the only existing interaction. However, for mobile satellite systems, elevation angles are far from grazing incidence, and single contributions are likely to be preponderant.

Models of rough surface scattering are finally briefly approached. This mechanism should be most of the time negligible, except for directive high frequency links (above 10 GHz). Note that the software implementation is still possible in such cases.

An advantage of ray-tracing tools consists in their intrinsic wideband nature. Subsequently, transfer functions and impulse responses are easily inferred. However, any ray technique has to be carefully used in a wideband context. Indeed, parameters, such as the RMS delay spread, are highly dependent upon the description of the area, mainly its geographical extension and the location of near obstacles.

The deterministic model has been successfully validated at 12.5 and 30 GHz by narrowband measurements.

Although a deterministic analysis is necessary when prediction results are required in specific dynamic scenarios, some statistics must be introduced as soon as coverage predictions are needed. Therefore, an innovative approach, known as physical-statistical, is developed in this thesis. Based on a combination of physical ray-tracing and statistical modelling, the new model is capable of producing satellite system outage calculations over very large geographic areas, with short computation time. Additionally, the effect of multiple satellite diversity is predicted statistically as an integral part of the model, using a novel and highly flexible approach. Finally, simulation results are presented for a number of practical cases and are found to be in good agreement with measurements.

The physical-statistical approach offers several advantages, summarised below.

(i) The model is based on a physical description of electromagnetic mechanisms. Hence, it performs very well at extrapolating results in a wide parameter range.

(ii) Like statistical models, it is easy to use and the computational load is reduced. A number of calculations are indeed carried out a priori, regardless of the characteristics of the simulated area.

(iii) Although it produces statistical results, the approach integrates a quantitative description of the area, thereby avoiding usual classification problems and meeting current designers' needs. Coverage area are based on statistical distributions of objective parameters, such as building height, street width, link elevation and azimuth angles, etc.

(iv) Numerous underlying models are already included in the approach: wideband characterisation (thanks to the ray-tracing), statistical shadowing correlation model, prediction of fade dynamics (level-crossing rate, fade duration).

That concludes the modelling part of the work. In Chapter 3, system-oriented prediction tools are investigated. A distinction is introduced between long- and short-term performance. Long-term performance is outlined by statistical annual availability and global coverage. In contrast, short-term predictions rely on short time periods and specific scenarios. They take into account the complex and dynamic interactions between very different parameters, such as shadowing correlation, satellite motion, mobile speed, imperfect fade compensation or handover procedure.

In the field of long-term performance for mobile satellite systems, both the receiver and the satellite are mobile. Therefore, a new analytical prediction approach is considered. The formalism is very general, so that it can easily be applied in other communication fields. Being based on the physical-statistical modelling, the model differentiates the temporal availability (in the sense of GEO links) with the spatial coverage (in the sense of terrestrial cellular networks). Hence, the performance is featured by two values, which stand respectively for availability and coverage. For example, the model provides the cumulated percentages of area over which the availability is a given value (95 %, 99 %, 99.9 %, etc.). This new prediction model is analytical. It is also compared with the COST 255 methodology, which is based on time series:

- being analytical, the new model requires a smaller computation load than the COST 255 approach,
- in counterpart, the time series nature of the COST 255 method allows to integrate, up to a certain point, several considerations, such as imperfect power-control, etc.

In the short-term analysis, the design of various dynamic strategies, like fade mitigation algorithm, handoff and multiple satellite diversity, is discussed. Simple relationships are given to model such procedures in view of time series simulations.

Finally, a number of test cases are investigated by means of the described tools. They cover a large spectrum of frequency and future applications: L band land mobile satellite systems (Globalstar, Iridium), S band SW-CMDA system (IMT 2000), Ka band multimedia satellite network (Teledesic), V band stratospheric system.

For LMS systems, the long-term analysis reveals that the performance in built-up areas is strongly related to the global line-of-sight ratio, which is expressed by basic geometrical relationships as a function of:

- environmental parameters (open-area percentage, distributions of building height, receiver position, street width and orientation),
- constellation parameters (frequency, distributions of azimuth and elevation angles).

The shadowing correlation model also points out that the design of Globalstar seems very promising in terms of dual diversity, unlike that of late Iridium.

In the short-term analysis of LMS links, exemplary simulation results firstly highlight the necessity of using fade mitigation techniques in combination with a diversity scheme, such as single-satellite handoff diversity or maximal-ratio-combining dual diversity. Secondly, a crossroad scenario illustrates the significant impact of corner effects, which have therefore to be suitably modelled.

The second test case (IMT 2000) emphasises the COST 255 approach. Also, an investigation into dual-path shadowing correlation and its relationship with the constellation design is presented.

In the Teledesic-like test case (Ka band Internet transmission), an innovative method for dealing with tropospheric dynamic and short-term effects is applied, especially in the design of fade mitigation and diversity techniques. Based on a real meteosat map, simulations show that acceptable performance is achieved by using handoff diversity (single satellite diversity) in combination with power-control. They also point out the limitations of a time series analysis based on a restricted number of events.

Finally, the long-term prediction method is applied to a non-satellite case, namely a V band stratospheric communication system. Relying on high-altitude platforms, such systems are planned to establish personal communication networks over dense urban areas. Simple analytical relationships stress the capability of the developed approach to combine, in an original fashion, tropospheric and local effects. Simulations highlight that, at 47 GHz, local effects could play a certain role, at least for moderate antenna height with respect to average building height. This last test case also demonstrates that physical-statistical predictions could be extended to non-LEO systems, such as terrestrial mobile networks.

Work has of course to be done, the megacell channel being quite a new field of study. In order to conclude, a personal review of interesting open issues is provided in the following.

(i) Scintillation is increasingly considered as a significant effect. Models, though, are scarce. The UCL model should be adapted to low-orbit propagation, in order to provide a deterministic tool accounting for real-time scintillation effects.

(ii) In the context of tropospheric propagation, the new time series method, the first steps of which have been proposed in this thesis, should valuably be developed. Such tool

would therefore model the complex interaction between short-term effects within a long-term point of view.

(iii) The ray-tracing tool can still be improved, and not only in terms of acceleration techniques. For example, the impact of vegetation should deserve a particular attention. Indeed, only the attenuation effect has been modelled, although trees also induce scattering effects, which are likely to impair high-frequency wideband communications. Both theoretical work and experiments are needed in this field.

(iv) The promising physical-statistical channel modelling should be extended in order to provide predictions over very large regions, such as a continent. That would certainly require the analysis of more generic configurations, as well as an appropriate statistical description of the area.

(v) This technique is also believed to be attractive in terrestrial applications. For example, when vehicles, people or other scatterers move near the receiver, time-varying channels must be considered. In such cases, the physical-statistical analysis is seen as an appropriate compromise between the easy-of-use of empirical models and the physical insight of deterministic models.

(vi) The Doppler effect is only briefly approached along this work. Its estimation as well as the analysis of its impact on performance might raise interesting issues.

(vii) Solutions to fill the gap between propagation research and system design are proposed. A lot of work still remains. For instance, system procedures should be investigated more deeply. Links with network issues (multiple access and protocols, adaptive resource sharing), communication techniques (coding, modulation, filtering delays, adaptive signal processing, loop control) and antenna design (active or smart antennas, multibeam antennas) must be established more precisely.

APPENDICES

APPENDIX A ABOUT THE 1999 VERSION OF ITU-R RECOMMENDATIONS

This appendix examines the new ITU-R recommendations regarding oxygen, water vapour and rain attenuation. The focus is on the frequency range from L band to V band only. The detailed recommendations can be found in [1], for any frequency.

1° Oxygen attenuation

The specific attenuation γ_o [dB/km] estimated by ITU-R Rec. 676-4, for $f < 54$ GHz, by:

$$\gamma_o = \left[\frac{7.34}{f^2 + 0.36} + \frac{0.6951}{(54 - f)^{1.2289} + 0.9527} \right] f^2 \; 10^{-3} \qquad \text{(A.1)}$$

where f is the frequency expressed in [GHz].

Relationship (A.1) is valid at ground level (pressure equal to 1013 hPa) and at a temperature of 15 °C. Expressions valid for other temperature and pressure conditions are detailed in [1]. Figure A.1 compares the specific attenuation obtained from ITU-R Rec. 676-2, Rec. 676-4 and the Liebe model in the same conditions (temperature: 15 °C; pressure: 1013 hPa).

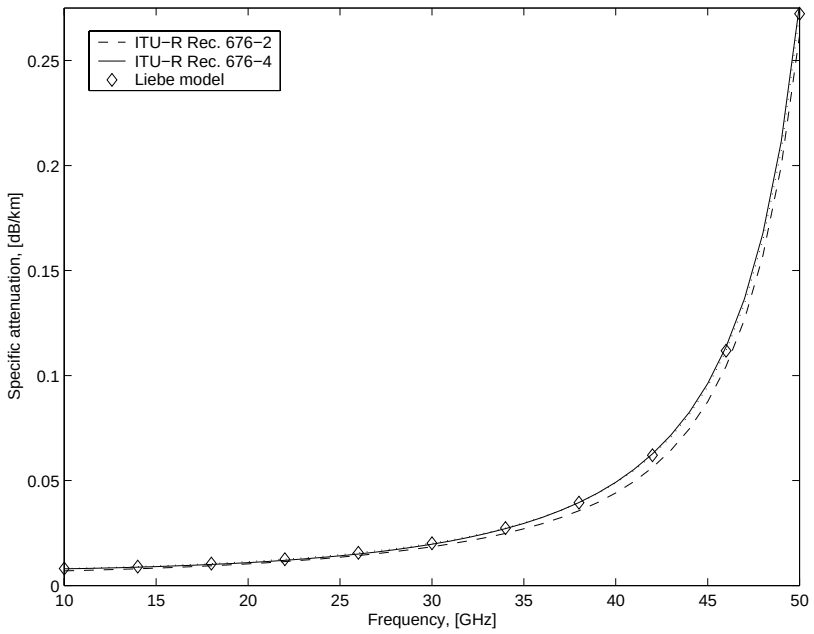

Figure A.1 *Oxygen specific attenuation as a function of frequency*

It can be observed that the new recommendation is actually a close approximation of the Liebe model. Therefore, Liebe model and its approximation (A.1) should preferably be used in place of the 1997 version of ITU-R Rec. 676. However, it must be remembered that the oxygen attenuation is usually very small.

Note also that, for the calculation of the slant-path attenuation A_o [dB], the equivalent height of oxygen h_o [km] is now outlined for $f < 56.7$ GHz, by:

$$h_o = 5.386 - 3.32734\,10^{-2} f + 1.87185\,10^{-3} f^2 - 3.52087\,10^{-5} f^3 + \frac{83.26}{(f-60)^2 + 1.2} \quad \text{(A.2)}$$

2° Water vapour attenuation

The new ITU-R Rec. 676-4 for water vapour attenuation is actually a close approximation of the Liebe-Salonen model, which is always used in this work.

3° Rain attenuation

The new rain attenuation model is the model known as the DAH model [2]. All details regarding ITU-R Rec. 618-6 can be found in [1]. Figure A.2 compares ITU-R Rec. 618-5 and 618-6 for a 30-GHz link characterised by an elevation angle of 30 degrees and circular polarisation.

The point rainfall intensity exceeded during 0.01 % of time in Saint-Hubert (Belgium) in 1992 is 21.73 mm/h (see Chapter 1, Figure 1.6). It is observed that a significant discrepancy is found between the old and new versions of ITU-R recommendation for rain attenuation. However, it should be remembered ITU-R Rec. 618-5 is still reported from Olympus and Italsat experiments as well as from ACTS to perform satisfactorily in most of the cases.

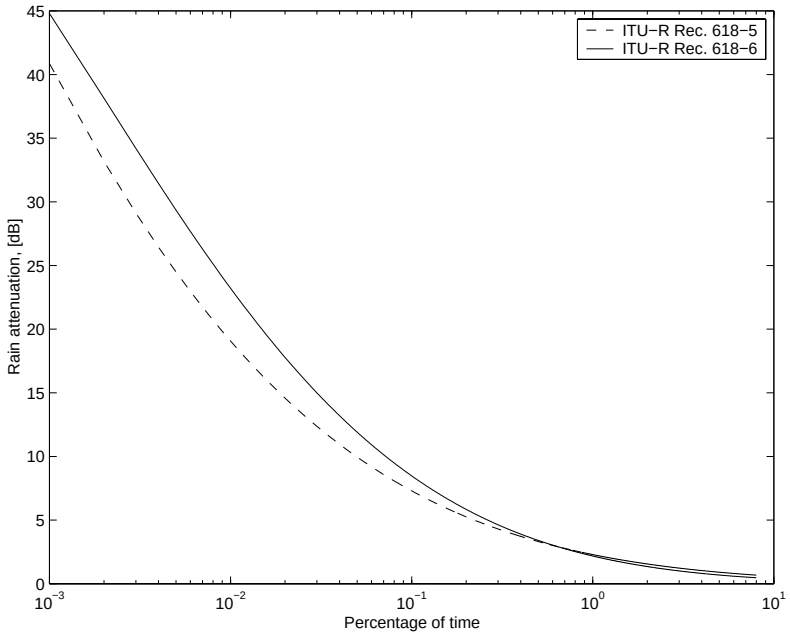

Figure A.2 *Distribution of rain attenuation in Saint-Hubert (30 GHz, elevation of 30 degrees)*

APPENDIX B DESCRIPTION OF THE ORBIT GENERATOR

This appendix examines various aspects concerning the motion of satellite vehicles around the earth: orbit parameters, perturbations and geometric relationships between satellites and earth stations. As a result, an orbit generator is also presented. Although orbits of communication satellites are in general elliptic, this study is restricted to the case of circular low-earth orbits, such as the orbits of Iridium or Teledesic networks.

1° Orbit parameters

Any circular orbit the radius of which is a can be described by a number of parameters [1].

- Velocity. The velocity V of the satellites is constant and given by:

$$V = \sqrt{\frac{\mu}{a}} \tag{A.3}$$

  where μ = 3.986 10^{14} m^3 s^{-2} is the product of the mass of the earth and the universal gravitational constant.
- Period of the orbit. The period T is the duration of rotation of the satellites in the orbit, given by:

$$T = 2\pi\sqrt{\frac{a^3}{\mu}} \tag{A.4}$$

- Inclination of the plane of the orbit (i). This is the angle that defines the position of the ascending node; it is counted positively in the forward direction from 0 and 180°, between the orbit plane and the equatorial plane. The ascending node N_A is thereby the intersection of the orbit with the equatorial plane, the satellite crossing this plane from south to north.
- Right ascension of the ascending node (Ω). This is the angle measured positively from 0 to 360° in the forward direction, between a reference direction (defined in the equatorial plane) and that of the ascending node.
- Nodal angular elongation (u). This angle is used to define the position of the satellite in its orbit. It is measured positively from 0 to 360° between the direction of the ascending node and the direction of the satellite. If the initial elongation ($t = t_0$) is denoted as u_0, the elongation at time t is given by:

$$u = n(t - t_0) + u_0 \tag{A.5}$$

where $n = 2\pi/T$ is the angular velocity of the satellite.

The three parameters (a, i, Ω) completely define the trajectory of the satellite in space. The motion of the satellite in its orbit is then specified by the nodal elongation u. Regarding constellations of LEO satellites, the number of satellites and the number of orbital planes complete the set of characteristic parameters.

2° Earth-satellite geometry

Consider a communication between a given satellite, its latitude and longitude (relative to a reference meridian) being denoted as φ_{sat} and λ_{sat}, and a terrestrial gateway P. The coordinates of the latter are ψ for the latitude and l for the longitude, with respect to the same reference meridian. The latitude of the satellite does not depend on the earth rotation and is given [1] by:

$$\varphi_{sat} = arcsin\left[\sin i \, \sin u\right] \tag{A.6}$$

where u, and therefore φ, vary with time according to (A.3).

The longitude of the satellite vary with both the movement of the satellite and the rotation of the reference meridian, so that it is given by:

$$\lambda_{sat} = arctan\left[\tan u / \cos i\right] - n_E (t - t_0) \tag{A.7}$$

where $n_E = 2\pi/T_E$ is the angular velocity of the earth (T_E = 86164 s).

Let us define the relative longitude of the satellite by $L = \lambda - l$. The distance R from the satellite to P, as well as the elevation and azimuth angles of the link, ϑ and ϕ, are then given by:

$$R = \sqrt{R_E^2 + a^2 - 2\,a\,R_E \cos\gamma} \tag{A.8-a}$$

$$\cos\vartheta = \frac{a}{R}\sin\gamma \tag{A.8-b}$$

$$\left|\sin\phi_{sat}\right| = \left|\frac{\sin L \cos\varphi}{\sin\gamma}\right| \tag{A.8-c}$$

where

- R_E is the earth radius, R_E = 6378 km,
- the intermediate angle γ is defined by $cos\,\gamma = cos\,L\,cos\,\varphi_{sat}\;cos\,\psi + sin\,\varphi_{sat}\;sin\,\psi$,
- the azimuth is completely determined following the position of the sub-satellite point relative to *P*.

Note that equations (A.8-a,b,c) are valid for an earth receiver situated at sea-level. For an earth station at height h_s, a correction must be applied.

3° Perturbations

The movement of the satellite in its orbit has been described assuming that the only acting force is the terrestrial attraction, the earth being considered as a spherical homogeneous body. However, other forces than the latter are exerted on the satellite, resulting in perturbations of the orbit. These forces consist mainly of:

- the contribution of non-spherical components of the terrestrial attraction,
- the attraction by the sun and the moon,
- other non-conservative forces due to solar radiation pressure, etc.

The perturbations result e.g. in a precession of the orbit plane, affecting the right ascension of the ascending node, which must be accounted for in determining the position of a satellite. The variation of Ω is given by:

$$\begin{aligned} \frac{d\Omega}{dt} &= -\frac{3\sqrt{\mu}}{2\,J_2\,R_E^{1.5}}\left[\frac{R_E}{a}\right]^{3.5} cos\,i \quad [rad/s] \\ &= -9.964\left[\frac{R_E}{a}\right]^{3.5} cos\,i \qquad [°/day] \end{aligned} \tag{A.9}$$

where J_2 is the zonal harmonic function of longitude corresponding to the flattening of the earth, $J_2 = 1.0827\ 10^{-3}$. Polar orbits (i = 0°) are not submitted to the precession of the orbital planes, since Ω remains constant over time.

4° The orbit generator

A package has been developed in order to simulate the motion of all vehicles in a LEO constellation. It must be used with MATLAB 5.3 and is constituted of three functions: **SATPOS**, **ANGLES** and **MAX_ELEV**.

SATPOS generates a non-geostationary satellite constellation at a given time, from its parameters described by an input file:

```
function sat_pos = satpos(input_file, time)
```

Input parameters

input_file: system file

Filenames must be MATLAB-files *<name>.mat*, so that **input_file** = '*<name>*'. The file is organised in three structured fields. The field *<name>.data* is a single column vector containing:

(i) the year *yyyy* of the initial time t_0
(ii) the month *MM* of the initial time t_0
(iii) the day *dd* of the initial time t_0
(iv) the hour *hh* of the initial time t_0
(v) the minutes *mm* of the initial time t_0
(vi) the seconds *ss* of the initial time t_0
(vii) the altitude *h* of the constellation [km]
(viii) the orbital period *T* [s]
(ix) the number N_{sat} of satellites
(x) the number N_{pl} of orbital planes
(xi) the inclination of the orbital planes *i* [°]

The field *<name>.Omega* is a (N_{pl} x 1) vector containing the initial right ascension of the ascending node Ω for each plane. The last field *<name>.u* is a (N_{sat} x 1) vector containing the initial nodal angular elongation for each satellite.

time: time at which the position of all satellites is to be calculated

Variable **time** is a vector the form of which is [*yyyy MM dd hh mm ss*].

Output parameters

sat_pos: longitude and latitude of all satellites

The output is defined by two fields, **sat_pos.lat** (N_{sat} x 1) and **sat_pos.long** (N_{sat} x 1), containing respectively the latitude and longitude of all satellites.

ANGLES calculates the azimuth and elevation angles (ϕ, ϑ) for all visible earth-space links, considering a given location on earth (latitude ψ, longitude l). This function is outlined by equations (A.8-9).

```
function [teta, phi] = angles(earth_lat, earth_long, sat_pos, h_s, h)
```

Input parameters

earth_lat: latitude ψ of the earth station, [°]
earth_long: longitude l of the earth station, [°]
sat_pos: position (longitude and latitude) of all satellites at a given time, as calculated by function **SATPOS**
h_s: height of the earth station above sea level, [km]
h: altitude of the orbit above sea level, i.e. $a - R_E$

Output parameters

teta: (N_{sat} x 1) vector containing the elevation angle of all satellites relative to the earth station

Note that a negative value is assigned to elevations corresponding to non-visible satellites

phi: (N_{sat} x 1) vector containing the azimuth angle of all satellite links, relative to the parallel of the earth station

MAX_ELEV determines the maximum elevation angle (i.e. related to the nearest satellite) as a function of time over a time range to be specified. It uses both functions **SATPOS** and **ANGLES**.

```
function teta_max = max_elev(earth_lat, earth_long,h_s, system, time)
```

Input parameters

earth_lat: latitude ψ of the earth station, [°]
earth_long: longitude l of the earth station, [°]
h_s: height of the earth station above sea level, [km]
system: system file

Filenames must be MATLAB-files <*name*>.*mat*, so that **system** = '<*name*>'. The file is organised in three structured fields, as already described.

time : time specifications

This input is a (2 x 1) vector containing the time duration (from initial time) to be simulated, in [s], as well as the time increment, in [s].

Output parameter

teta_max: (**duration** x 1) vector containing the maximum elevation angle at each time step

5° Some examples

Several constellations are used throughout this thesis. Table A.1 summarises the main characteristics of four low-earth-orbit constellations. While Teledesic and Iridium's orbits are nearly polar and offer therefore a worldwide coverage, Globalstar and Deligo only cover some 80 % of the earth's surface (i = 52° and 54°).

	Globalstar	Teledesic	Iridium	Deligo
Number of satellites	48	288	66	64
Number of orbital planes	8	12	6	8
Orbital inclination, [°]	52	84.3	86.4	54
Orbit altitude, [km]	1414	1375	780	1626
Orbital period	1 h 55 m 45 s	1 h 53 m 14 s	1 h 40 m 27 s	1 h 58 m 36 s

Table A.1 *Characteristic parameters of several LEO constellations*

In order to illustrate the results provided by the orbit generator, the single tracks of a single satellite from three of these constellations are depicted in Figure A.3. The effect of the inclination of the orbit is clearly visible, as well as the non-global coverage of Globalstar. Finally, Figure A.4 shows the tracks of all Globalstar satellites for a period equalling the orbital period. Again, the partial coverage of Globalstar is clearly illustrated. At the end of the period, every satellite occupies the same latitude as initially, the difference in longitude resulting from the earth rotation. In fact, the latitude is not exactly identical, owing to the

effect of the asymmetry of the earth potential. Nevertheless, the orbital period is too short to really illustrate the precession of the orbital planes due to perturbations.

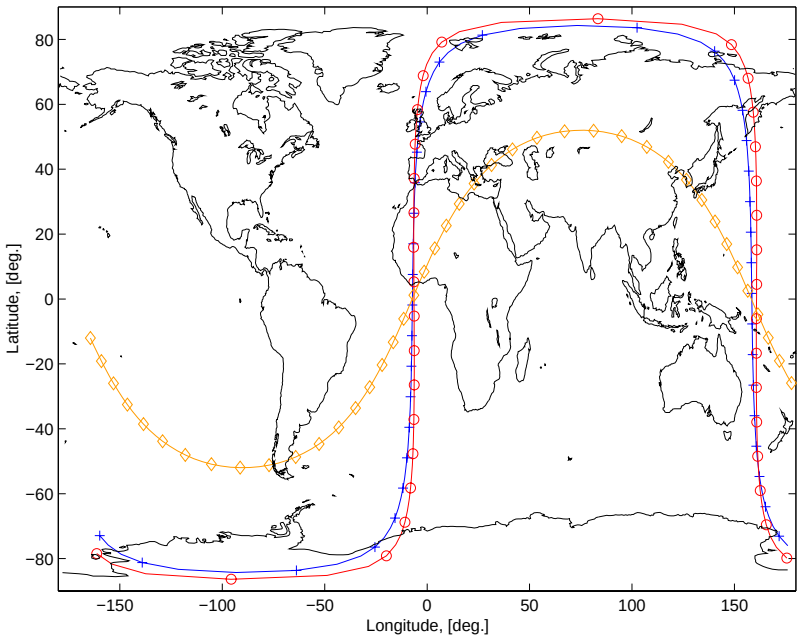

Figure A.3 *Track of a single satellite from each constellation: Globalstar {diamonds}, Teledesic {+} and Iridium {circles}*

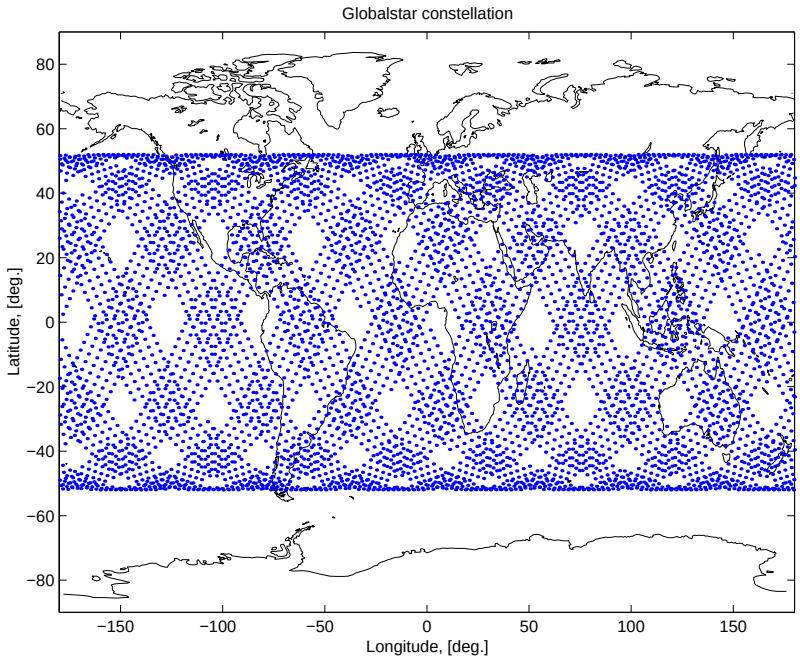

Figure A.4 *Tracks of all satellites from the Globalstar constellation*

APPENDIX C RAY-TRACING SOFTWARE FOR LAND MOBILE SATELLITE SYSTEMS

A ray-tracing software, called **COMSAT**, has been developed in the framework of this thesis, to characterise the propagation channel in built-up areas. It is written in C and its input is a single ASCII file that contains all necessary parameters. A brief description of input data and output results, together with a flow-chart, are given in the following.

Input parameters (described by means of the input file)

link parameters

1) carrier frequency f_0 (and eventually bandwidth B)

2) orbit altitude

3) elevation/azimuth angles

- **fixed values: $\vartheta_0, \phi_{sat,0}$**
- **varying values: $\vartheta(t_i), \phi_{sat}(t_i)$**

Three link parameters must be defined. The carrier frequency is expressed in [GHz]. When a frequency bandwidth is specified, a wideband analysis is realised with a frequency resolution that must be given with the bandwidth (see Outputs). If this analysis is not needed, the default value is $B = 0$. Regarding the elevation and azimuth angles, these can be fixed to constant values (e.g. in a physical-statistical model) or increment at each time t_i, as given by an orbit generator.

receiver characteristics

1) antenna pattern and orientation

2) position P

- **fixed receiver: P_0**
- **mobile receiver: $P(t = t_{initial})$, $P(t = t_{end})$, speed**

The antenna pattern is assumed to be symmetric around its axis and must be specified in [dB] for all angles between 0° and 180° (but the step does not need to be constant). The antenna orientation is described by two directions (in azimuth and elevation). When the receiver is mobile, then a constant speed is assumed from the initial position up to the final position.

building database

The latter specifies the area in a Cartesian coordinate system. The built-up area is constituted by parallelepipeds with smooth planar faces. These blocks represent either buildings either slabs of vegetation. Lateral faces do not need being orthogonal, but rooftop and basement as well as the ground surface have to be horizontal. Building blocks are associated with electrical properties (relative permittivity and conductivity) at the given frequency band. Foliage slabs must be related to a vegetation attenuation model (A, β and ν in Section 2.2.4.4).

Options

calculation methods **1) reflection order**

2) evaluation of diffracted fields

- **classical UTD**
- **edge equivalent currents**

Regarding the reflected contribution, the order of reflection must be specified. In order to keep a reasonable computation time, it is highly recommended to limit the order to 3. The evaluation of the diffracted contribution can be carried using either the classical UTD, either an incremental method based on equivalent currents.

Outputs

narrowband results **1) total complex field $E(t_i, f_0)$**

2) contributive complex fields and delays

- **$E_{LOS}(t_i, f_0)$ and τ_{LOS}**
- **$E_{ref,m}(t_i, f_0)$ and $\tau_{ref,m}$ for each reflection path m**
- **$E_{diff,m}(t_i, f_0)$ and $\tau_{diff,m}$ for each diffraction path m**

When no bandwidth is specified, the software applies a ray-tracing method to determine at each time t_i all paths from the satellite to the receiver, assuming that the incoming wave is planar. The outputs are therefore the scalar complex field for each contribution, together with its delay. A total field is obtained following (2.3) by the complex addition of all individual contributions.

wideband results **channel transfer function $H(t_i, f_j)$ for $f_j \in [f_0 - B/2, f_0 + B/2]$**

When a bandwidth is specified, the calculation outlined by (2.36-37) is applied for each time t_i and each frequency f_j in order to obtain the transfer function over the bandwidth B. The result is therefore a two-dimensional complex matrix.

Flow-chart

The ray-tracing software is globally divided in two parts. In a first part, all geometrical inputs are used in order to provide the existing unmasked paths between the satellite and the receiver. In a second part, all contributions related to individual paths are computed, following the propagation mechanisms, and combined.

geometrical calculations

for each time t_i

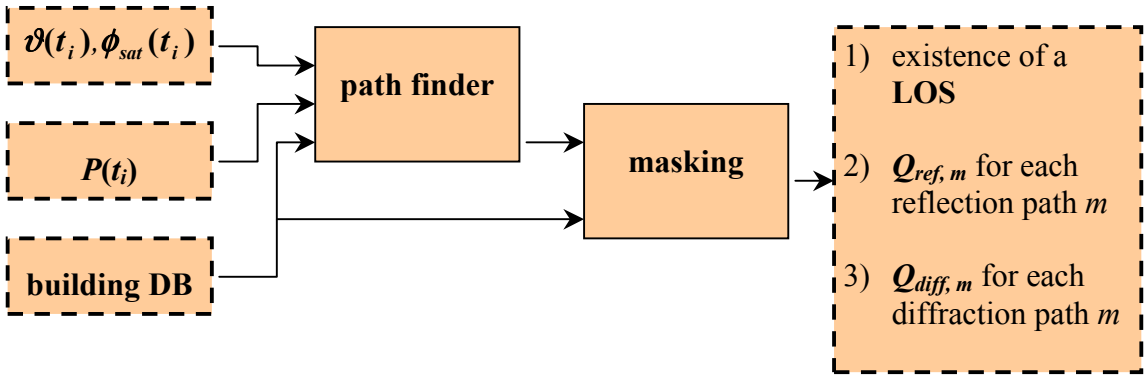

This calculation must be conducted for every time t_i (since the satellite and the receiver may have moved), but does not depend upon the frequency. The path-finder determines all possible reflection and diffraction paths from the satellite to the receiver, using equation (2.10) and (2.17). Then, a sub-routine eliminates the paths that are blocked by buildings on their way to the receiver.

electromagnetic calculations

for each time t_i

if $B \neq 0$,

for each frequency f_j (only one frequency f_0 when $B = 0$)

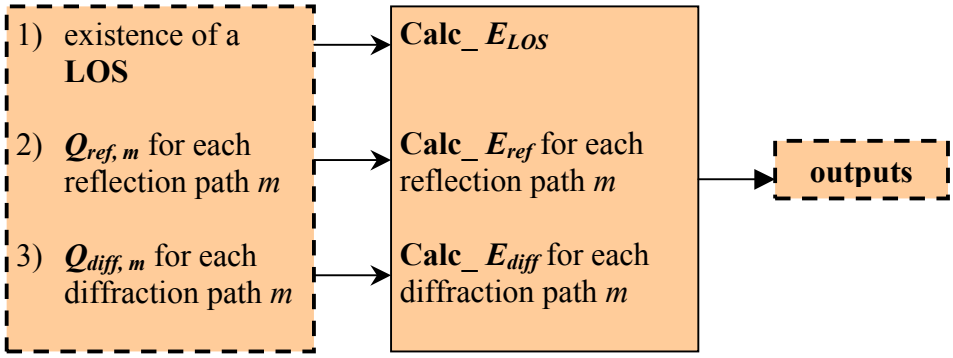

For each individual path, the received complex field is evaluated using the formalism of (2.6) and equations (2.11), (2.19) and (2.23). Each ray undergoes therefore the free-space loss, the foliage attenuation, the interaction due to reflection/diffraction and the effect of antenna pattern and polarisation. The paths are then summed to provide the total path-loss or the transfer function, depending on the desired output.

The field calculation outlined by **Calc_E_m** is given by the following scheme, which can easily be related to equation (2.1). For a line-of-sight field, the expression is considerably simplified, as given by (2.4).

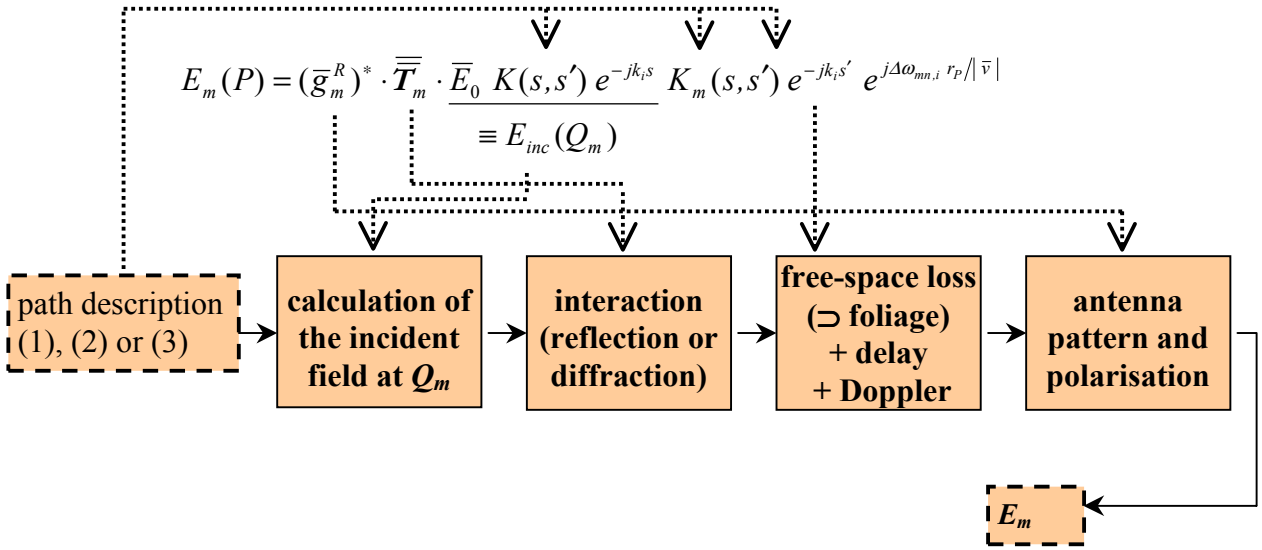

APPENDIX D EQUIVALENT CURRENTS FOR EDGE DIFFRACTION

In Section 2.2.4.2, expressions have been presented for evaluating the single-diffracted field on the basis of equivalent currents. It is shown hereafter how these expressions are inferred.

The incident and diffracted fields can be resolved into edge-fixed components by means of edge-fixed coordinate systems ($\bar{s}_{inc}$, $\bar{\beta}_{0,inc}$, $\bar{\phi}_{inc}$) and ($\bar{s}_{diff}$, $\bar{\beta}_{0,diff}$, $\bar{\phi}_{diff}$). We get:

$$\begin{aligned} \bar{E}_{inc} &= E_{inc,\bar{\beta}_0}\,\bar{\beta}_{0,inc} + E_{inc,\bar{\phi}}\,\bar{\phi}_{inc} \\ \bar{E}_{diff} &= E_{diff,\bar{\beta}_0}\,\bar{\beta}_{0,diff} + E_{diff,\bar{\phi}}\,\bar{\phi}_{diff} \end{aligned} \tag{A.10}$$

The $\bar{\beta}_0$ -polarised component of the field is considered in a first time. Let us assume that an electric current flows along an edge of infinite length:

$$\bar{I}_e(r') = I_e(r')\,\bar{t} \tag{A.11}$$

where $\bar{t}$ is a unit vector tangential to the edge and r' is the position of any point on the edge.

The magnetic vector potential at the field point P due to the current is given by:

$$\bar{A}(P) \overset{\Delta}{=} A(P)\,\bar{t} = \int_{-\infty}^{\infty} \bar{I}_e(r')\,\frac{e^{-jkr''}}{4\pi r''}\,dr' \tag{A.12}$$

where r'' *is* the path length between the point defined by r' and the observation point P.

The integral in (A.12) can be evaluated using the method of the stationary phase. The stationary point happens to be the Keller's diffraction point, denoted as Q_{diff}. That yields:

$$\bar{A}(P) = I_e(Q_{diff})\,\frac{e^{-j\pi/4}}{\sin\beta_0\sqrt{8\pi k}}\,\frac{e^{-jks'}}{\sqrt{s'}}\,\bar{t} \tag{A.13}$$

where s' is the distance from Keller's diffraction point to the observation point.

The far-zone diffracted field along $\bar{\beta}_0$ caused by $\bar{A}$ can finally be expressed as:

$$\bar{E}_{diff,\bar{\beta}_0}(P) = -j\,k\,Z\,\bar{A}^T \tag{A.14}$$

where

- $\overline{A}^T$ is the transverse component of $\overline{A}$ relative to the direction of propagation of the diffracted field. Hence, $\overline{A}^T = \overline{A} - (\overline{A} \cdot \bar{s}_{diff})\ \bar{s}_{diff} = A\left[\bar{t} - (\bar{t} \cdot \bar{s}_{diff})\ \bar{s}_{diff}\right]$
- Z is the wave impedance.

Yet, for edges of infinite length, the UTD allows to obtain an expression of the vectorial diffracted field (2.19-21):

$$\overline{E}_{diff,\bar{\beta}_0}(P) = -\overline{E}_{inc,\bar{\beta}_0}(Q_{diff})\ D_s(Q_{diff})\ \frac{e^{-jks'}}{\sqrt{s'}} \tag{A.15}$$

Combining (A.14) with (A.15), the expression for the equivalent electric current at the diffraction point is obtained:

$$\bar{I}_e(Q_{diff}) = -\frac{\overline{E}_{inc,\bar{\beta}_0}(Q_{diff})}{Z}\sqrt{\frac{8\pi}{k}}\ e^{-j\pi/4}\ D_s(Q_{diff}) \tag{A.16}$$

For any point on the edge referenced by r', the equivalent current is written similarly:

$$\bar{I}_e(r') = -\frac{\overline{E}_{inc,\bar{\beta}_0}(r')}{Z}\sqrt{\frac{8\pi}{k}}\ e^{-j\pi/4}\ D_s(r') \tag{A.17}$$

The diffraction coefficient D_s must be evaluated at any point r' lying on the edge, even though these points violate the Keller cone concept. Therefore, $\beta_{0,diff}(r') \neq \beta_{0,inc}(r')$. The angle β_0 appearing in the calculation of D_s (2.22) should be replaced [5] by: $sin\,\beta_0 = \sqrt{sin\,\beta_{0,inc}\ sin\,\beta_{0,diff}}$.

The whole demonstration might seem to be a pointless exercise of going around in circles. However, it enables to decompose the diffraction process, originally defined as an infinitely long process, into an infinitesimal phenomenon. The $\bar{\beta}_0$-polarised component of the diffracted field for a wedge of finite length l is then given by:

$$\begin{aligned}
&\overline{E}_{diff,\bar{\beta}_0}(P) = -j\,k\,Z\,A(P)\left[\bar{t} - (\bar{t} \cdot \bar{s}_{diff})\ \bar{s}_{diff}\right] \\
&A(P) = \int_0^l I_e(r')\,\frac{e^{-jkr''}}{4\pi r''}\,dr'
\end{aligned} \tag{A.18}$$

Regarding the $\bar{\phi}$ -polarised component of the diffracted field, the same procedure can be applied, starting with equivalent magnetic current I_m. The electric vector potential at the observation point P is given for a wedge of finite length by:

$$\bar{F}(P) = \int_0^l I_m(r') \frac{e^{-jkr''}}{4\pi r''} dr' \, \bar{t} \tag{A.19}$$

In the far-zone, the diffracted electric field is expressed as:

$$\bar{E}_{diff,\bar{\phi}}(P) = -j\,k \left[\bar{F}(P) \times \bar{s}_{diff} \right] \tag{A.20}$$

Because of the cross product, there is no need to calculate the transverse component of $\bar{F}$. The expression of the equivalent magnetic current is found by equalling the UTD expression for the $\bar{\phi}$ -polarised component of the diffracted field with the result of the integration of the current along an infinite wedge. The following formula is obtained:

$$\bar{I}_m(r') = \bar{E}_{inc,\bar{\phi}}(r') \sqrt{\frac{8\pi}{k}} \, e^{-j\pi/4} \, D_h(r') \tag{A.21}$$

Combining (A.19), (A.20) and (A.21) finally allows to get an expression for the total diffracted field, which can be expressed by means of a dyadic coefficient $\bar{\bar{C}}$:

$$\bar{E}_{diff}(P) = \int_0^l \bar{\bar{C}} \cdot \bar{E}_{inc}(r') \frac{e^{-jkr''}}{4\pi r''} dr' \tag{A.22}$$

where $\bar{\bar{C}}$ is given by:

$$\bar{\bar{C}} = -C_s \, \bar{\beta}_{0,inc} \left[\bar{t} - (\bar{t} \cdot \bar{s}_{diff}) \bar{s}_{diff} \right] - C_h \, \bar{\phi}_{inc} \left[\bar{t} \times \bar{s}_{diff} \right] \tag{A.23}$$

$$C_s = -j\sqrt{8\pi k} \, e^{-j\pi/4} \, D_s(r') \tag{A.24}$$

$$C_h = j\sqrt{8\pi k} \, e^{-j\pi/4} \, D_h(r') \tag{A.25}$$

APPENDIX E DOUBLE DIFFRACTION COEFFICIENT

For a pair of parallel lossy wedges, the double diffraction $\boldsymbol{D}^d$ defined in Section 2.2.4.2 can be evaluated as described in this appendix [6]. The two wedges are represented by variables n and m, so that the exterior angles of the wedges are respectively $n\pi$ and $m\pi$, as described in Figure A.5.

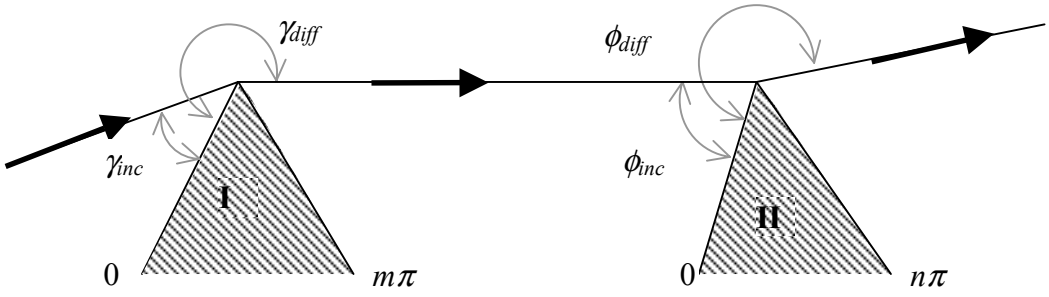

Figure A.5 *Geometry of double diffraction configuration*

The diffraction coefficient is given by:

$$\boldsymbol{D}^d_{s,h} = \frac{-j}{4\pi\, n\, m}\sqrt{BC}\sum_{M=1}^{4}\sum_{N=1}^{4}(-1)^{N+M}\, exp\left\{-jk\left[(B+C\delta^2)\,a_2(M)+C\,a_1(N)\right]\right\} \cdot\left[(I_1+I_2)\,\Gamma+(I_1-I_2)\,\widetilde{\Gamma}\right] \tag{A.26}$$

where the upper sign applies to the soft boundary condition with

$$\Gamma(N,M) = cot\left[\frac{\Pi(M)+\beta(M)}{2n}\right]\left|\sqrt{a_2}\right|\; cot\left[\frac{\Pi(N)+\gamma_0(N)}{2m}\right]\left|\sqrt{a_1}\right| \tag{A.27}$$

$$\widetilde{\Gamma}(N,M) = -\frac{\chi\, a_2}{\sqrt{2}\, n\; sin^2\left[\dfrac{\Pi(M)+\beta(M)}{2n}\right]}\; cot\left[\frac{\Pi(N)+\gamma_0(N)}{2m}\right]\left|\sqrt{a_1}\right| \tag{A.28}$$

$$I_1 = exp(-2\,jkC\sqrt{a_1}\sqrt{a_2}\,\delta)\int_{S_{1+}}^{\infty}\int_{S_{2+}}^{\infty} e^{j(s^2+t^2)}\,dt\;ds \tag{A.29}$$

$$I_2 = exp(+2\,jkC\sqrt{a_1}\sqrt{a_2}\,\delta)\int_{S_{1-}}^{\infty}\int_{S_{2-}}^{\infty} e^{j(s^2+t^2)}\,dt\;ds \tag{A.30}$$

where

- $S_{1\pm} = \psi\sqrt{kC}\ (\sqrt{a_1} \pm \sqrt{a_2}\ \delta)$
- $S_{2\pm} = -\psi\,\chi\sqrt{\frac{C}{B}}\left[\psi\sqrt{kC}\,(\sqrt{a_1} \pm \sqrt{a_2}\ \delta) - s\right]\delta + \left|\sqrt{kB\,a_2}\right|$
- $B = \frac{s''s'}{s''+s'}$, $C = \frac{(s''+s')s}{s+s'+s''}$, $\delta = \frac{s''}{s''+s'}$
- $a_1 = a_1(N)$, $a_2 = a_2(M)$
- $\psi = sign(\sqrt{a_1})$, $\chi = sign(\sqrt{a_2})$

All variables appearing in (A.26-30) are defined in Table A.2 and Table A.3. In these tables, $M^{\pm}$ and $N^{\pm}$ are different from M and N and are the integers that most nearly satisfy $2n\pi M^{\pm} - \beta = \pm\pi$ and $2n\pi N^{\pm} - \gamma_0 = \pm\pi$ respectively.

Term *M*	***Π***	***β***	**$\sqrt{a_1}$**
1	$-\pi$	$\phi_{diff} + \phi_{inc}$	$\sqrt{2}\cos\frac{2n\pi M^{-} - (\phi_{diff} + \phi_{inc})}{2}$
2	$-\pi$	$\phi_{diff} - \phi_{inc}$	$\sqrt{2}\cos\frac{2n\pi M^{-} - (\phi_{diff} - \phi_{inc})}{2}$
3	π	$\phi_{diff} + \phi_{inc}$	$\sqrt{2}\cos\frac{2n\pi M^{+} - (\phi_{diff} + \phi_{inc})}{2}$
4	π	$\phi_{diff} - \phi_{inc}$	$\sqrt{2}\cos\frac{2n\pi M^{+} - (\phi_{diff} - \phi_{inc})}{2}$

Table A.2 *Variables of double diffraction coefficient*

Term *N*	***Π***	***γ_0***	**$\sqrt{a_2}$**
1	$-\pi$	$\gamma_{diff} + \gamma_{inc}$	$\sqrt{2}\cos\frac{2n\pi N^{-} - (\gamma_{diff} + \gamma_{inc})}{2}$
2	$-\pi$	$\gamma_{diff} - \gamma_{inc}$	$\sqrt{2}\cos\frac{2n\pi N^{-} - (\gamma_{diff} - \gamma_{inc})}{2}$
3	π	$\gamma_{diff} + \gamma_{inc}$	$\sqrt{2}\cos\frac{2n\pi N^{+} - (\gamma_{diff} + \gamma_{inc})}{2}$
4	π	$\gamma_{diff} - \gamma_{inc}$	$\sqrt{2}\cos\frac{2n\pi N^{+} - (\gamma_{diff} - \gamma_{inc})}{2}$

Table A.3 *Variables of double diffraction coefficient*

APPENDIX F SYSTEM-LEVEL SOFTWARE FOR ESTIMATING LONG-TERM PERFORMANCE FROM TIME SERIES (COST 255 METHOD)

This appendix outlines the system-level software, which is based on the approach detailed in Section 3.2.4 [7].

The software is written to be used with MATLAB 5.3. The main function **SYSTSIM** is associated with two files (containing orbit data). The output is mainly graphical, providing plots of cumulative distributions over the area of E_b/N_0 or coded BER for given percentages of time.

SYSTSIM performs the system-level simulation for land mobile systems. It uses time-series of effective E_s/N_0 values for several elevation angles as input, and generates statistics of coded BER as a function of percentages of area and time. The function is given by:

```
function [percentile, err] = systsim(input_file, teta, sys, lat, str, nx)
```

Input parameters

input_file: generic name of ASCII files

Filenames must be of the form <*name_xx*>, where *xx* is the corresponding elevation angle in degrees. Then, the variable **input_file** = '<*name*>'. The files <*name_xx*> must contain two columns:

(i) sampling time [s]

(ii) effective E_s/N_0 value, including fade margin [dB]

where

- E_s/N_0 values are assumed to include all effects of thermal noise, MAI and ISI, no further consideration within this function,
- E_s is the symbol energy at radio channel data rate.

teta: vector of elevation angle in degrees (the zenith corresponding to **teta** = 90 deg.)

A typical step of 5° is suggested (it does not need to be constant).

sys: string that controls the constellation to be considered

This parameter can receive two values: **sys** = 'LEO66' for Iridium-like system
'SUMTS' for S-UMTS system (Deligo)

lat: string that indicates the latitude where the simulations are performed

There are two possible latitudes: **lat** = 'london' or 'rome'

str: string indicating the parameter to be displayed

Again, there are two possibilities: **str** = 'eb' for E_b/N_0 distribution
'cb' for coded BER distribution.

nx: number of points on x-axis of PDF and CDF graphical results

A typical value **nx** = 20 is recommended.

Output parameters

percentile: vector of percentages of *time* (time is associated with the elevation angle)

Each percentage is associated with a curve of the graphical output.

err: error flag

If **err** = 0: no error
< 0: fatal error
> 0: warning

APPENDIX G LEO-*N* TEST CASE: SHORT-TERM PERFORMANCE IN BUILT-UP AREAS (MEDIAN RECEIVING POSITION)

Appendix F presents two additional graphs, dealing with short-term CDF's of E_b/N_0 in built-up areas (see Section 3.4.4). These graphs illustrate the case of a median receiving position in the street (the graphs for the non-median position have been presented in details in the text). Remember that the nominal E_b/N_0 (denoted as κ_0) equals 6.5 dB.

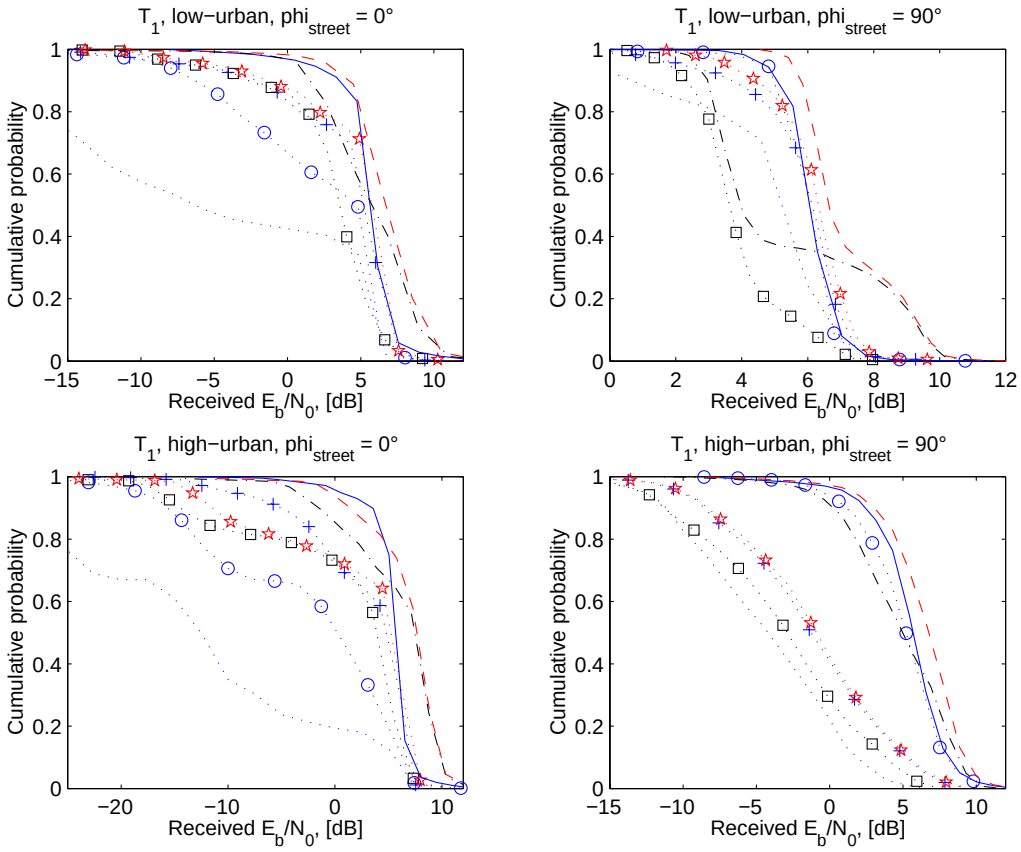

Figure A.6 *E_b/N_0 CDF's for a communication taking place at time T_1 ($d_m = w_0/2$):*

- *no FMT, no diversity {blue dot lines}*
- *FMT, no diversity {blue circles}*
- *no FMT, single satellite diversity (SEL) {blue '+'}*
- *no FMT, satellite diversity (EGC) {black squares}*
- *no FMT, satellite diversity (MRC) {red stars}*
- *FMT, single satellite diversity (SEL) {blue solid lines}*
- *FMT, satellite diversity (EGC) {black dot dashed lines}*
- *FMT, satellite diversity (MRC) {red dashed lines}*

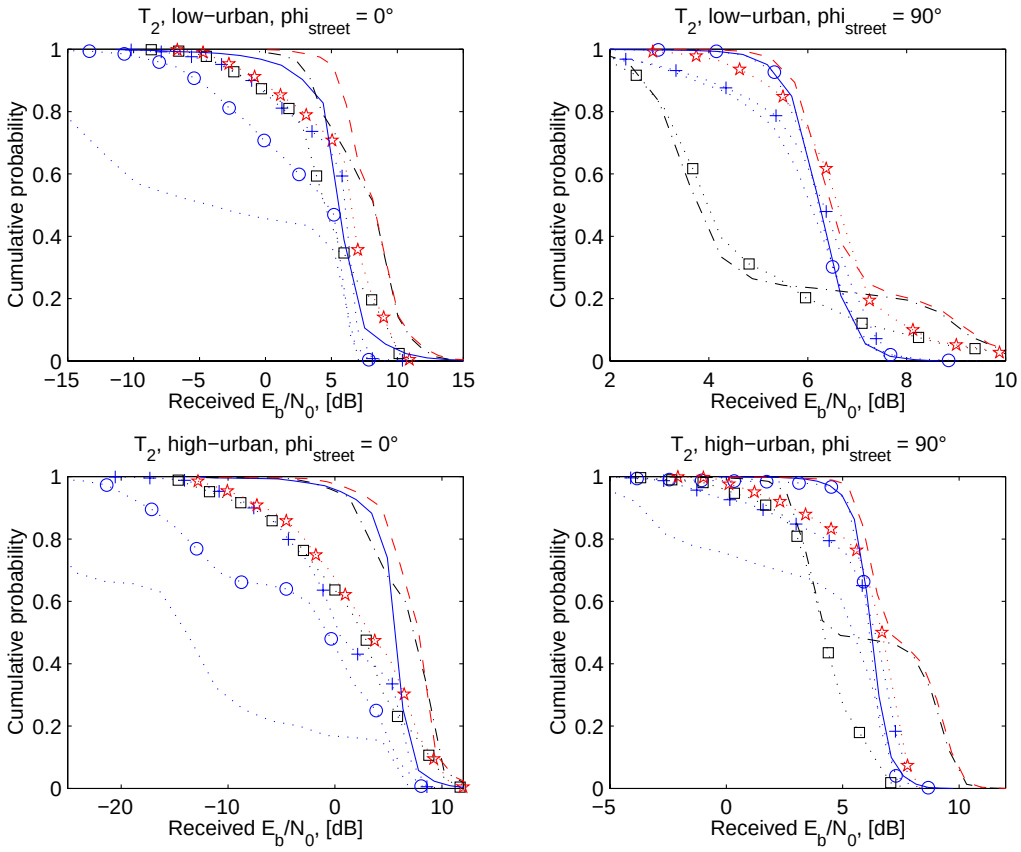

Figure A.7 *E_b/N_0 CDF's for a communication taking place at time **T_2** ($d_m = w_0/2$):*

- *no FMT, no diversity {blue dot lines}*
- *FMT, no diversity {blue circles}*
- *no FMT, single satellite diversity (SEL) {blue '+'}*
- *no FMT, satellite diversity (EGC) {black squares}*
- *no FMT, satellite diversity (MRC) {red stars}*
- *FMT, single satellite diversity (SEL) {blue solid lines}*
- *FMT, satellite diversity (EGC) {black dot dashed lines}*
- *FMT, satellite diversity (MRC) {red dashed lines}*

As already mentioned, two noteworthy differences appear with respect to the non-median scenarios.

(i) For $\phi_{street} = 90°$, EGC diversity is really not efficient.

(ii) For $\phi_{street} = 0°$, the fade mitigation algorithm still increases the performance, but largely less than diversity only (remember that performance are very similar for $d_m = 1$ m). This is because diversity is very efficient in the case of a non-symmetric position of the receiver in the street (i.e. $d_m << w$). This advantage is reduced in the case of a central position in the street.

REFERENCES

[1] ITU-R, *ITU-R Recommendations – Propagation in non-ionized media,* PN series vol., ITU, Geneva, 1999.

[2] DISSANAYAKE A., ALLNUT, J, HAIDARA, F., A prediction model that combines rain attenuation and other propagation impairments along earth-satellite paths, *IEEE Trans. Antennas Propagat.,* vol. 45, n° 10, pp. 1546-1558, 1997.

[3] MARAL, G., BOUSQUET, M., *Satellite communication systems*: *systems, techniques and technology,* 2nd ed., J. Wiley, Chichester, 1993.

[4] MCNAMARA, D. A., PISTORIUS, C.W.I., MALHERBE, J.A.G., *Introduction to the Uniform Geometrical Theory of Diffraction*, Artech House, London, 1990.

[5] KNOTT, E.F., SENIOR, T.B.A., Comparison of three high-frequency diffraction techniques, *Proc. IEEE,* vol. 62, n° 11, pp. 1468-1474, 1974.

[6] SCHNEIDER, M., LUEBBERS, R.J., A general, uniform double wedge diffraction coefficient, *IEEE Trans. Antenn. Propagat*., vol. 39, n°1, pp. 8-14, 1991.

[7] COST 255, *Radiowave propagation modelling for new SatCom services at Ku band and above*, European Commission, Brussels, to be published.